

Engineering Materials

Gagan Kumar Bhargava

Sumit Bhardwaj

Mahavir Singh

Khalid Mujasam Batoo *Editors*

Ferrites and Multiferroics

Fundamentals to Applications

 Springer

Engineering Materials

This series provides topical information on innovative, structural and functional materials and composites with applications in optical, electrical, mechanical, civil, aeronautical, medical, bio- and nano-engineering. The individual volumes are complete, comprehensive monographs covering the structure, properties, manufacturing process and applications of these materials. This multidisciplinary series is devoted to professionals, students and all those interested in the latest developments in the Materials Science field, that look for a carefully selected collection of high quality review articles on their respective field of expertise.

Indexed at Compendex (2021)

More information about this series at <https://link.springer.com/bookseries/4288>

Gagan Kumar Bhargava · Sumit Bhardwaj ·
Mahavir Singh · Khalid Mujasam Batoo
Editors

Ferrites and Multiferroics

Fundamentals to Applications

 Springer

Editors

Gagan Kumar Bhargava
Physics
Chandigarh University
Mohali, India

Mahavir Singh
Physics
Himachal Pradesh University
Shimla, India

Sumit Bhardwaj
Physics
Chandigarh University
Mohali, India

Khalid Mujasam Batoo
King Saud University
Riyadh, Saudi Arabia

ISSN 1612-1317

Engineering Materials

ISBN 978-981-16-7453-2

<https://doi.org/10.1007/978-981-16-7454-9>

ISSN 1868-1212 (electronic)

ISBN 978-981-16-7454-9 (eBook)

© The Editor(s) (if applicable) and The Author(s), under exclusive license to Springer Nature Singapore Pte Ltd. 2021

This work is subject to copyright. All rights are solely and exclusively licensed by the Publisher, whether the whole or part of the material is concerned, specifically the rights of translation, reprinting, reuse of illustrations, recitation, broadcasting, reproduction on microfilms or in any other physical way, and transmission or information storage and retrieval, electronic adaptation, computer software, or by similar or dissimilar methodology now known or hereafter developed.

The use of general descriptive names, registered names, trademarks, service marks, etc. in this publication does not imply, even in the absence of a specific statement, that such names are exempt from the relevant protective laws and regulations and therefore free for general use.

The publisher, the authors and the editors are safe to assume that the advice and information in this book are believed to be true and accurate at the date of publication. Neither the publisher nor the authors or the editors give a warranty, expressed or implied, with respect to the material contained herein or for any errors or omissions that may have been made. The publisher remains neutral with regard to jurisdictional claims in published maps and institutional affiliations.

This Springer imprint is published by the registered company Springer Nature Singapore Pte Ltd.

The registered company address is: 152 Beach Road, #21-01/04 Gateway East, Singapore 189721, Singapore

Preface

Ferrites or Magnetic materials are an important class of materials as they possess high resistivity, high saturation magnetization and initial permeability and negligible eddy current losses. The high resistivity of ferrites makes them suitable for microwave applications and with the tremendous increase in the development of microwave and millimeter wave-based communication technologies, the production of dielectric resonators has emerged as one of the most rapid growth areas in electro-ceramic manufacturing. High saturation magnetization of ferrites is a prerequisite condition for making them useful in storage sectors. In ferrites, the electrical and magnetic properties mainly depend on the synthesizing technique, type of metal ions and their distribution between the tetrahedral (A) and octahedral (B) sites. So due to the ability of ferrite materials to distribute the metal ions over A- and B-sites, material scientists became very much curious far a long time and are still working on the synthesis and characterization of various possible ferrites substituted with different metal ions to cope with the advanced technologies and applications. At the other end, multiferroic materials, i.e., coexistence of ferroelectric and ferromagnetic character have attracted much interest in their potential applications in information storage, the emerging field of spintronics, and sensors. The magnetization can be rotated or even reversed by the reversal of external electric field. The polarization can also be reversed by the reversal of external magnetic field. One of the main aim in preparing this book was to highlight the complex magnetic behavior along with unique coupled magneto electric behavior. This book highlights the fundamentals of ferrites and multiferroic materials with special attention to their structure, types, and properties. The book will provide a platform for critical evaluation of many aspects of dielectric, ferromagnetic coupled electromagnetic issues at the forefront of material science today. It highlights a comprehensive survey about the ferrite and multiferroic materials. There are 12 chapters organized in a systematic way. The first chapter takes the broad view of ferrites and their structures. Second chapter describes the effect of synthesizing techniques on the properties of ferrites. The third and fourth chapter deals with the substitution effects on the electric and magnetic properties of the ferrites. The fifth, sixth and seventh chapters explore the role of ferrites in bio-medical, high frequency antenna and water purification applications

respectively. Chapter eight takes the broad view of multiferroic materials. The chapter nine describes the effect of synthesis on the properties of BFO multiferroic while the chapter ten deals with the multiferroic phenomenon in different forms of materials. The chapter eleven describes the synthesis and properties of $\text{BiFeO}_3\text{-BaTiO}_3$ multiferroic while the twelfth chapter deals with the various applications of multiferroic materials. We hope that the book will emerge as the primary text dealing with general aspects of ferrite and multiferroics and will prove useful for all the various people interested in ferrites and multiferroics: from graduate level to advanced specialists in both academic and industrial settings. At the end we are thankful to Sh. Jagdish Chand and Mrs. Ritika Bhargava for constant encouragement and suggestions during the entire process.

Mohali, India
December 2021

Dr. Gagan Kumar Bhargava

Contents

Basics of Ferrites: Types and Structures	1
Pooja Dhiman, Garima Rana, Dipanshi Goyal, and Ankush Goyal	
Synthesis Routes for Ferrites and Their Impact on the Properties of Ferrites	27
Garima Rana, Pooja Dhiman, Rajesh Kumar, Ankush Chauhan, Anjana Sharma, and Indu Sharma	
Effect of Substitution on the Electric and Magnetic Properties of Ferrites	49
Harshal B. Desai and Ashish R. Tanna	
Substitution Consequences on Electric and Magnetic Behaviour of Nanoferrites	71
Meenakshi Dhiman, Balwinder Kaur, Shikha Rana, and Baljinder Kaur	
The Role of Nanoferrites in Bio-medical Applications	91
Sarveena	
Ferrite Materials for Microwave and High Frequency Antenna Applications	107
Pankaj Sharma, Vineet Sharma, Nikhil Thakur, Pawan Kumar, and Ashok Kumar	
Ferrites for Water Purification and Wastewater Treatment	117
Pankaj Chamoli, Ravi K. Shukla, Achintya N. Bezbaruah, Kamal K. Kar, and K. K. Raina	
Basics of Multiferroic Materials and Their Types	129
Samta Manori and Ramesh Chandra	
Multiferroic Material Bismuth Ferrite (BFO): Effect of Synthesis	143
Ritesh Verma, Ankush Chauhan, Neha, and Rajesh Kumar	

Multiferroic Phenomenon in Bulk, Nanostructures and Thin Films 167
Samta Manori and Ramesh Chandra

Lead-Free BiFeO₃–BaTiO₃ Ceramics: An Overview 181
Naveen Kumar, Gulshan Dhillon, Ranvir Singh Panwar, Indu Sharma,
and Anupreet Kaur Bhatia

Applications of Multiferroics 195
Rohit Jasrotia, Suman, Rohit Khargotra, Ankit Verma, Indu Sharma,
and Ritesh Verma

About the Authors

Dr. Gagan Kumar Bhargava is currently working as a Professor at the Department of Physics, Chandigarh University, Gharuan, Mohali, Punjab, India. He has obtained his Ph.D. degree in Physics from Himachal Pradesh University, Shimla, India. His current research interests are synthesis of nanomaterials for antenna, EMI shielding, electromagnet and bio-medical applications. He has more than 14 years of teaching and research experience. Before joining the Chandigarh University, he was the Head of the Applied Science Department at Green Hills Group of Institutes, Solan, India and also served as an Associate Professor at IEC University, Solan, India. He has published more than 50 research papers in different peer-reviewed international journals and 6 book chapters. He has guided 2 Ph.D's, 1 M.Phil and 12 M.Sc. dissertations. He was the former Editorial Board Member of American Journal of Nanosciences and acted as Editor for American Institute of Physics Conference Proceedings in 2018 for AMDFA-2018.

Dr. Sumit Bhardwaj is currently working as an Assistant Professor at the Department of Physics, Chandigarh University, Gharuan, Mohali, Punjab, India. He has obtained his M.Tech. degree in Metallurgical and Materials Engineering from Thapar University, India and Ph.D. degree in Materials Science and Engineering from National Institute of Technology, Hamirpur, India. His current research interests are in the field of ferrite, multiferroic and composite materials. He has more than 12 years of research and teaching experience. Before joining to Chandigarh University, he has worked at Punjab Engineering College (Deemed to be University), Chandigarh, India. He has published more than 23 research papers in different peer-reviewed international journals and 3 book chapters. He has supervised two M.Tech. dissertations, and currently he is supervising three Ph.D. students.

Dr. Mahavir Singh is a Professor at the Department of Physics and Dean Physical Science Himachal Pradesh University, Shimla, India. He has more than 30 years of teaching experience. He remains head of the department during 2007-2009, 2015 and Dean Engineering Himachal Pradesh University 2017-2018. He was Common Wealth Fellow, UK (2006-2007), Visiting Fellow, Faculty of Engineering, University

of Dundee, UK (2006-2007), Visiting Professor at, Faculty of Engineering University De Bretagne Occidentale, Brest France (2007-2008) and Vice Chancellor at IEC University, Solan, India (2015-17). He was awarded with 100 Most Influential Vice Chancellor Award 2016 by World Education Congress, Global Achiever Award 2014 by Indian Heritage Institute and Calcutta Bharat Excellence Award 2015 from Friendship Forum New Delhi. He has authored book chapter Complex magnetic nanostructure (Springer), The Basis of Nanomagnetism: An Overview of Exchange Bias and Spring Magnets CRC Press, more than 5 textbooks on different areas of physics. He has published more than 190 research papers in different peer-reviewed international journals and about 100 Invited lectures delivered in International conferences. He has guided 23 Ph.D. students and evaluated 60 Ph.D. thesis. He was among Top 2% Scientist Globally as per Stanford University USA 2020 lists.

Dr. Khalid Mujasam Batoo is an Associate Professor at King Abdullah Institute for Nanotechnology, King Saud University, Riyadh, Saudi Arabia. He has authored more than 145 research papers published in peer-reviewed Journals of International commendation and conference papers. He is currently serving as the editorial board member of more than 13 international Journals. Among his various research interests include the study of magnetic nanomaterials, graphene materials, solar cells, batteries, e-textiles, magnetic tunnel Junctions and spintronic materials with an emphasis to understand micro and nano-structural properties of these materials. He has authored several book chapters published by Bentham Science Publishers and Materials Research foundation.

Basics of Ferrites: Types and Structures



Pooja Dhiman, Garima Rana, Dipanshi Goyal, and Ankush Goyal

Abstract This chapter summarizes the detailed introduction, types of magnetism, classifications of ferrites and their crystal structure. In addition, this chapter has the main focus on the magnetic properties possessed by ferrites on the basis of the soft and hard nature of ferrite materials. This chapter summarizes the recent work on the magnetic and dielectric properties of ferrites. Ferrites are primarily known for their high resistivity and highly magnetic nature which makes them suitable material over a wide range of applications like magnetic storage devices, antennas, transformers and other high-frequency devices. A great benefit of ferrites nanoparticles is the porosity, mandatory for sensor applications too. In short, ferrites belong to the materials which are a potential candidate for widely spread applications.

Keywords Ferrites · Nanomaterials · Soft and hard ferrite

1 Introduction

A ferrite ‘a ceramic substance’ composed primarily of iron oxide (Fe_2O_4), with a small number of metals like barium, manganese, nickel, and zinc etc. [1–3]. The term “ferrite” comes from the Latin word “Ferrum,” this is meant for “iron.” Both the iron oxide and the metal are ferrimagnetic. Ferrite, a ceramic substance created by combining iron oxide with a metal. It is thought that ferrites were first found in ancient Greece around 800 BC. Ferrite belongs to iron oxide-based magnetic oxide. Forestier used a heat treatment procedure to manufacture ferrites in 1928 [4]. Snoek [5] developed many ferrites as commercially important materials in 1947. Ferrimagnetic materials have uneven opposing magnetic moments, which allows them to keep their spontaneous magnetization [6, 7]. Chemical composition, particle size, and particle

P. Dhiman (✉) · G. Rana · D. Goyal · A. Goyal
School of Physics & Materials Science, Shoolini University of Biotechnology and Management Sciences, Bajhol, Solan 173229, H.P., India

P. Dhiman
International Research Centre of Nanotechnology for Himalayan Sustainability (IRCNHS),
Shoolini University, Solan, India

interaction with the neighbouring matrix all influence the properties of ferrite NPs. Ferrite NPs have a wide range of applications in various fields ranging from biomedical to industrial applications [8, 9]. Ferrites NPs are commonly used magnetic materials and have substantial scope in the field of biomedical sciences, such as tumour treatment, drug delivery [10, 11], magnetic resonance imaging (MRI) [12–14], biomagnetic separation [15], controlled drug release, cellular therapy, tissue repair, cell separation, purifying of cells, magnetoception, severe inflammation, disability [16–18]. In industrial applications, ferrite nanoparticles are often used as adsorbents and catalysts [19–25], manufacturing of electronic materials [26–28], and wastewater treatment [29–32]. These materials attracted a lot of attention as magnetic nanoparticles due to their unique structural features, surface reactivity, electrical, and magnetic properties, all of which are impacted by the nano-structured phase [2, 33], and these features of nanomaterials differ from bulk materials. The particle sizes of nanoparticles are the range of 1–100 nm. At the nano-scale, nanoparticles have distinctive physical, chemical, and biological properties as compared to their counter parts at larger dimensions. This is due to a greater surface area to volume ratio, increased chemical reactivity or stability, increased mechanical strength, and so on. The macro-structured parameters are the same as the bulk material's. As the abundance of surface particles increases, the particle size decreases. Surface atoms have a minor coordination number than inside atoms, allowing them to move freely. Quantum size effects are observed when the NPs' size is closer to the de-Broglie wavelength limit and their width is less than the quasiparticle interaction [34]. Controlling and manipulating the properties of nanomaterials is attainable by controlling their size during production using various approaches. A metal's electronic areas are characterised by its electronic band structure. The confirmation of band structure is determined by particle size. The delocalized bands can be seen in the molecular states. The energy gap between consecutive lines is determined by the particle size. The distance between the energy levels rises when the size decreases. There are various classifications of magnetic materials, i.e. dia, para, ferro, antiferro, and ferromagnetic materials [35]. In 1831, Faraday published a novel disciplinary law of magnetic induction [36]. Following that, in the nineteenth and twentieth centuries, the Bohr model of the atom and the Dirac hypothesis explained the circulation of currents in atoms. Weiss introduced the next domains theory to explain ferromagnetic behaviour [37]. Neel proposed the next radical approach. Neel suggested a theory to explain the hysteresis loop and magnetism. In almost every field, magnetic materials are extremely popular. Magnetic materials are used in soft magnets, permanent magnets, recording, magnetic storage, and alluring levitation, among other things [38]. All of the properties of nanomaterials are primarily resolute by their shape and size. Controlling and manipulating the properties of nanomaterials has become achievable by monitoring the particle size distribution by varying the synthesis methods [39, 40].

1.1 Advantages of Ferrite NPs

In terms of electrical resistivity, ferrites nanoparticles outperform other magnetic materials, resulting in reduced eddy current losses over a high frequency. The application of ferrites in quality filter circuits, transformers which works at high frequencies, wide-band transformers, and adjustable inductors has increased due to additional properties such as high permeability and temperature constancy. Ferrites nanoparticles are regularly utilized to fabricate the electrical circuits used for low frequency applications and devices operating at the high-frequency efficiency of other circuit components improve. Ferrites nanoparticles are the finest interior material option for frequencies between 10 kHz and 50 MHz because they provide the best arrangement of high Q, low cost, high stability, and low volume. In terms of magnetic and mechanical parameters, ferrites are unrivalled flexibility.

- High resistivity
- High Q/small package
- High permeability low loss achieved
- Low cost
- Large selection material
- Shape versatility
- Flexibility in the choice of core shapes
- Economical assembly
- Wide frequency range
- Temperature and time stability.

2 Magnetic Material and Types of Magnetism

The electronic structure of an atom within a compound is used to classify its magnetic behaviour. The main significant property of a magnetic material, magnetic susceptibility which is expressed by:

$$\chi = M/H \quad (1)$$

where M is used for the magnetization value and H corresponds to the applied magnetic field, with units of A/m . Magnetic susceptibility is dissimilar for a piece of material and depends upon the temperature and is given by:

$$\chi = C/(T - \theta) \quad (2)$$

Here, C and θ are constants that are dissimilar for each material [41]. Figure 1 shows the classification of magnetism. There are different types of magnetism.

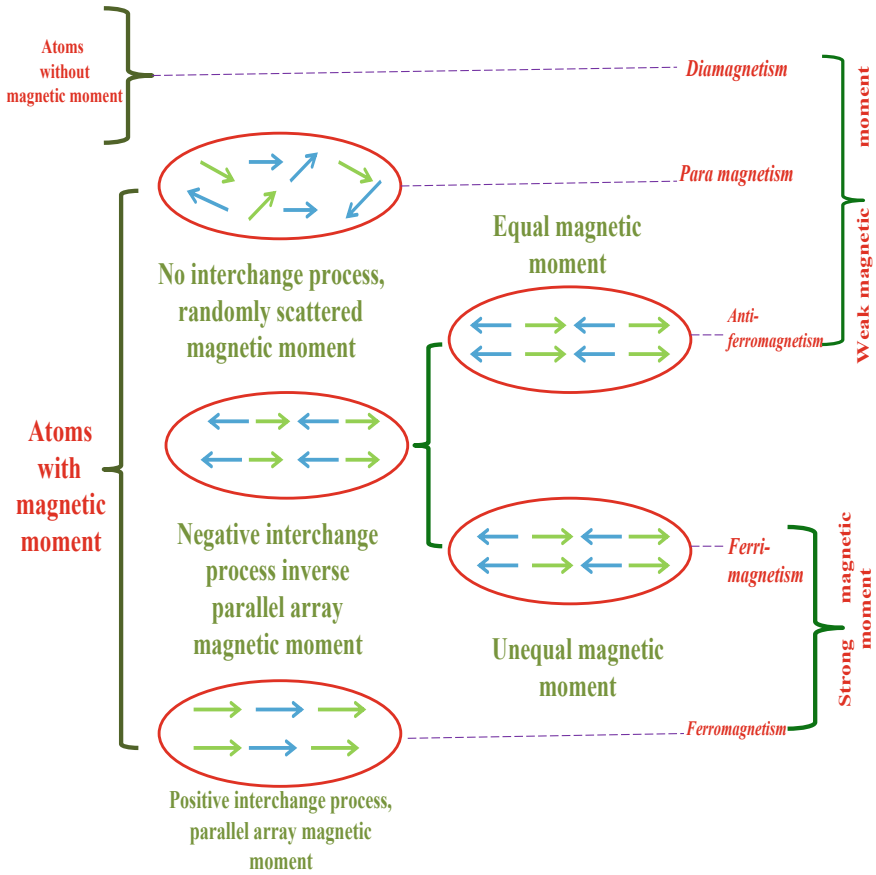


Fig. 1 Schematic presentation of classification of magnetism

2.1 Diamagnetism

The spin and orbital moments of electrons in an enclosed shell in an atom are normally aligned in such a way that the atom as a whole has zero net moment. Diamagnetic materials exhibit magnetic permeability values of ≤ 1 , as susceptibility is expressed as $\chi \cdot \nu = \mu \cdot \nu - 1$, and the values lie between -10^{-6} and -10^{-5} . If the material contains a net magnetization and long-ranged arrangement of magnetic moments, the impacts of these atomic current loops are mitigated.

2.2 Paramagnetism

The number of electrons which are not paired and reside in atomic shells, particularly the '3d' and '4f' shells of every other atom, is responsible for all other sorts of magnetic activity found in materials. When the applied magnetic field is eliminated, however, fluctuations which occur thermally cause the magnetization of paramagnetic atoms to shift arbitrarily. These materials have a comparative magnetic permeability of ≥ 1 i.e. $\mu > \mu_0$ indicating that their susceptibility is +ve and tiny, on the scale of 10^{-3} to 10^{-5} , and so are influenced to magnetic fields. Curie's law describes this phenomenon in the availability of a particularly poor magnetic field.

$$\chi = \frac{M}{H} = \frac{C}{T} \quad (3)$$

Here C is known as the Curie constant.

2.3 Ferromagnetism

Ferromagnetic materials contain 'atomic magnetic moments which are oriented ones' of comparable size, and their crystalline structure facilitates direct coupling contacts between the moments, which can boost flux density significantly. Moreover, the oriented moments in magnetic particles can impart magnetic behaviour in the absence of an exterior magnetic field. Hard magnets are those materials that maintain permanent magnetization even when no magnetic field is applied. Ferromagnetic materials have very high magnetic susceptibilities and the atom has a parallel aligned magnetic moment, which produces strong magnetization. The value of susceptibility (χ) is large and lies below the Curie temperature.

$$\chi = \frac{C}{T - \theta} \quad (4)$$

where C is known as the Curie temperature, which is the temperature at which exchange forces are present, i.e., randomization happens because of thermal energy, as it happens in a paramagnetic system.

2.4 Ferrimagnetism

In zero applied fields beyond a certain temperature is called Neel temperature. Ferrimagnetism is a property of the material whose atoms or ions interact to congregate an order, but not a parallel arrangement. The antiparallel alignment of ions leads in

a significant net magnetization within a magnetic region in most cases. In comparison to ferromagnetic materials, these have a higher saturation magnetization. The value of susceptibility (χ) is large and exists below the Curie temperature. The value of susceptibility (χ) is large and exists below the Curie temperature. Ferrites (for example, Fe_3O_4) are ferrimagnetic minerals in which metal cations and oxygen anions are arranged in the crystal lattice.

2.5 Antiferromagnetism

Antiferromagnetism belongs to a type of magnetism in which neighbouring ions act as minuscule magnets and impulsively align them into opposing or antiparallel configurations throughout the material at relatively low temperatures, resulting in a material with essentially zero external magnetism. Very feeble magnetic susceptibility (χ) of the order of paramagnetic materials is the characteristics of these materials. Above the Neel temperature (TN), thermal energy is sufficient to randomize the atomic moments aligned in the opposite direction, causing their long-range order to vanish. The material shows paramagnetic behaviour in this state (Table 1).

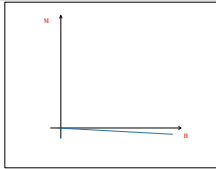
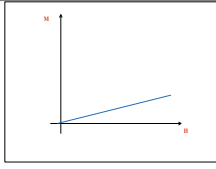
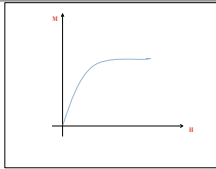
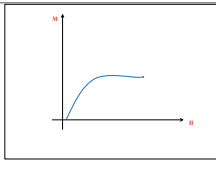
3 Classifications of Ferrite NPs According to Magnetic Behavior

Soft and hard ferrites are classified according to their potential to be magnetized and/or demagnetized instead of their capacity to withstand penetration or erosion [42, 43]. Coercive force (H_c) is the prime essential qualities of magnetic substances, and it distinguishes both types of ferrites from each other. Figure 2 shows the hysteresis loop of soft ferrite and hard ferrite (Table 2).

3.1 Soft Ferrites

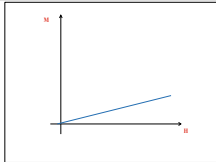
Soft ferrites are easily magnetized and demagnetized because they have low resistivity. A small hysteresis loop occurs in soft ferrite. These materials have soft magnetic properties like high permeability, low coercive value and high saturation magnetization value. Soft ferrites have diverse applications in the electronic industry, including the development of transformer cores, high frequency inductors, and microwave components [6]. Soft ferrites are those that contain Ni, Zn, or Mn and are utilized in transformers or electromagnetic cores. Because at high frequency, the soft ferrites possess very low losses therefore can be commonly used in RF transformers and also in inductors.

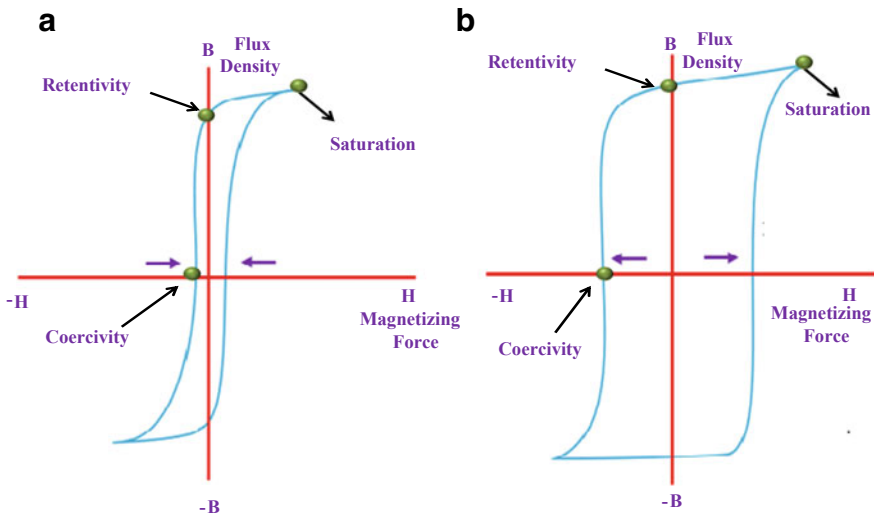
Table 1 Comparison of different types of magnetism

Type	Temperature dependence	M-H loops	Value of χ	Example
Diamagnetic	Temperature independent		-10^{-6} to -10^{-5}	As in covalent solids such as Au, Cu, and Ag, the atoms' shells are enclosed
Paramagnetic	Follows Curie's law $\chi = \frac{M}{H} = \frac{C}{T}$		$+10^{-5}$ to $+10^{-3}$	As in transition metal ions, atoms possess arbitrarily oriented magnetic moments
Ferromagnetic	Below Curie's temperature		Positive and large Fe $\sim 100,000$	In some transition metals and rare earths, such as cobalt and nickel, atoms with identically induced magnetic moments process substantial persistent magnetization without an external magnetic field
Ferrimagnetic	Below Curie's temperature		Positive and large Ba ~ 3	Atoms having antiparallel aligned magnetic moments, such as magnetite and ferrite, have high magnetism in the absence of a magnetic field

(continued)

Table 1 (continued)

Type	Temperature dependence	M–H loops	Value of χ	Example
Anti-ferromagnetic	Below Neel temperature		$+10^{-5}$ to $+10^{-3}$	Magnetic moments are present in both parallel and antiparallel oriented atoms. The most frequent transition metal oxides and salts are MnO and NiO

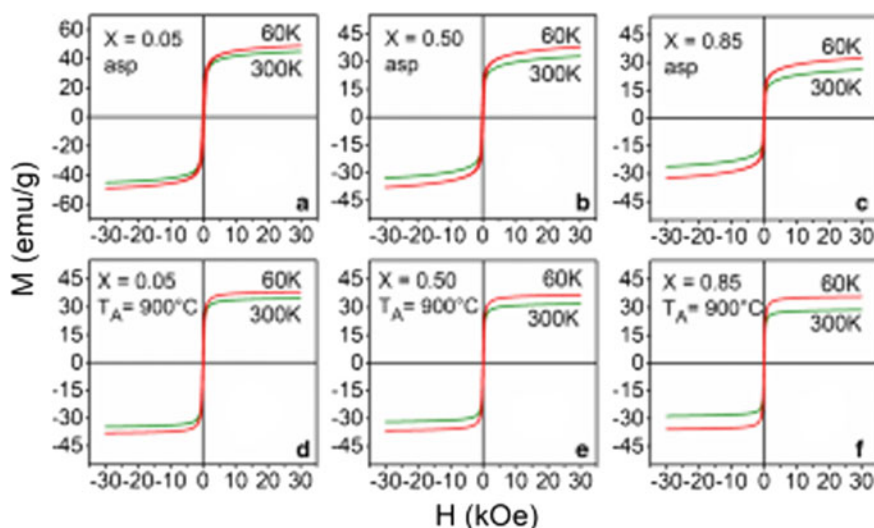
**Fig. 2** Depicts the hysteresis loop of **a** soft ferrite, **b** hard ferrite

3.1.1 Magnetic Property of Soft Magnet: Nickel Ferrite (NiFe_2O_4)

Magnetic materials, depending on the spin orientation, exhibit various kinds of magnetic ordering. The magnetization of ferrites is due to the interaction of the spins with the exchange of neighbouring atoms. Anumol et al. [44] used the sol-gel process to make magnesium-substituted Ni-ferrite ($\text{Mg}_x\text{Ni}_{1-x}\text{Fe}_2\text{O}_4$; $0 \leq x \leq 1$) nanoparticles, which were then annealed at 550 and 900 °C. Figure 3 shows the (as prepared and annealed at $T = 900$ °C) $\text{Mg}_x\text{Ni}_{1-x}\text{Fe}_2\text{O}_4$ nanoparticles samples with

Table 2 Essential properties of both type of magnetic ferrites (soft and hard)

Soft ferrite	Hard ferrite
Low coercivity	High coercivity
High electrical resistivity	Not important
High Curie temperature	High Curie temperature
Low anisotropy	High anisotropy
Low magnetostriction	Not important
High permeability	Low permeability
High saturation magnetization (1–2 T)	High saturation magnetization (0.3–6 T)
High Curie temperature	High Curie temperature

**Fig. 3** Hysteresis loop of the **a–c** as-prepared and **d–f** annealed ($T_A = 900\text{ }^\circ\text{C}$) Mg–NiFe₂O₄ nanoparticles sample [44]. Reprinted with permission from Springer Nature

$x = 0.05, 0.50,$ and 0.85 magnetic hysteresis (M–H) loops. The hysteresis loops did not drencheven at a maximum magnetic field strength of 30 kOe, as shown in Fig. 3. Furthermore, the annealed samples' loops seem to be more saturated than the as prepared samples. The corresponding magnetization values were calculated by extending the M–H loop from high field to zero applied fields. At 300 and 60 K with an increase in the concentration of Ca²⁺, the values of magnetic saturation increase. At room temperature, Chavan et al. [45] found that the highest M_S of 64.5 emu/g for $x = 0$, i.e. Nickel ferrite NPs. At room temperature, Moradmard et al. [46] registered a maximum M_S value of 28.8 emu/g for $x = 0$. For $x = 0.05$, the maximum M_S values were 42 and 46 emu/g at 300 and 60 K, respectively. In addition, the M_S value of the annealing temperature at 550 °C is smaller than that of the asp sample. The M_S

value for annealed at 900 °C samples declined gradually from the value of 37 emu/g ($x = 0$) to 29 emu/g ($x = 0.25$) at 300 K.

The M_S value increased marginally to 31 emu/g as the x value increased to 0.50, but then decreased as the Mg^{2+} concentration increased. However, for the samples which were annealed at 900 °C, a similar pattern was observed at 60 K. The bare Mg-ferrite sample, annealed at 550 °C, had the lowest M_S values of 21 emu/g and 26 emu/g at 300 and 60 K respectively. At both 300 and 60 K, H_C decreased as Mg^{2+} doping (%) increased. It's important to note that at 300 K, the H_C values for the 900 °C-annealed samples were consistently higher than those for the as prepared and 550 °C-annealed samples. Though the H_C values were higher at 60 K, they were the lowest of the 900 °C-annealed samples. The as-prepared and 550 °C-annealed samples with $x = 1$ had the lowest H_C of 10 Oe at 300 K, while the asp sample with $x = 0$ had the maximum H_C of 340 Oe at 60 K. The non-saturated magnetization of samples increased with increasing Mg^{2+} content for the as-prepared samples and the samples annealed at 550 °C with substitution values between 0.05 and 1, i.e. for $0.05 \leq x \leq 1$, where as it did not change for the samples annealed at 900 °C [44]. The observed magnetic behaviour in these nanoparticles samples is explained by crystallite size distribution. Another factor is decreased ionic magnetic moment, and the most important cation distribution in the spinel type of ferrites, and decreased anisotropy with increasing Mg^{2+} concentration [47].

According to Maaz et al., nickel ferrite coercivity increases with particle size (for microscopic particles) when the particle changes its behaviour from a super-paramagnetic type, i.e. from blocked to unblocked. This happens for very narrow sized particles because thermal energy overcomes the anisotropy, which is volume dependent. While the coercivity reduces with size for larger particles because of two unique mechanisms; first one is that bulky particles can maintain domain wall motion, and the second one is that surface role varies and bulk anisotropies are observed as the size is reduced [48]. Atif et al. prepared Zn doped nickel ferrite by the sol-gel method and the highest magnetic saturation values were found, i.e. 76 emu/g. The saturation magnetization increases with an increase in the zinc content [49]. The value of magnetic saturation and coercivity increase with an increase in the concentration of dopant [50].

3.1.2 Electrical Property of Soft Ferrite

The ferrite system acts as a heterogeneous system with various conducting properties of grains and grain boundaries. Koop believed that both the grains and the limits were parallel to R.C. Circuit loops. When an A.C. is exposed to a dielectric material, the series arrangement of these parallel circuits replicates the conduct of the inhomogeneous dielectrics as a whole, due to the comparable current flow through grains and grain boundaries. There is a relative movement of positive and negative ions in the electric field, which results in an electric dipole moment. Atif et al. prepared Zn doped $NiFe_2O_4$ nanoparticles by sol-gel technique and the value of dielectric permittivity ranged from 2.77 to 12.2 kHz [49]. Moradmard et al. magnesium doped

nickel ferrite nanoparticles are fabricated by co-precipitation technique and study the various parameters like dielectric loss, dielectric constant, and ac conductivity with frequency range 1–12GHz [46]. The related dielectric pictures are shown in Fig. 4 (Fig. 5).

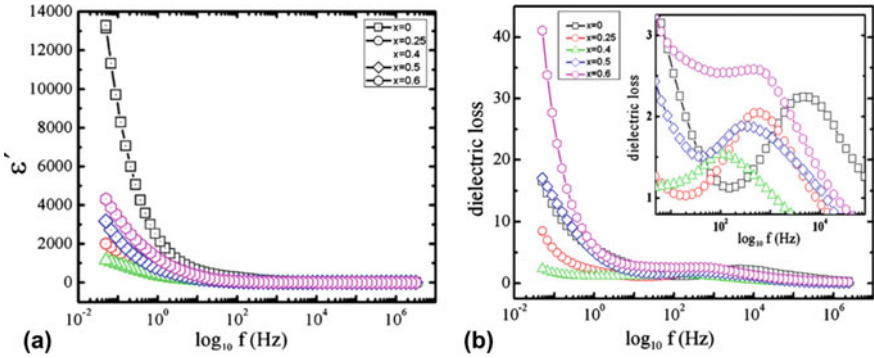


Fig. 4 a Variation of dielectric for the Ni_{1-x}Zn_xFe₂O₄. b Variation of dielectric loss for the Ni_{1-x}Zn_xFe₂O₄ [49]. Reprinted with permission from Elsevier

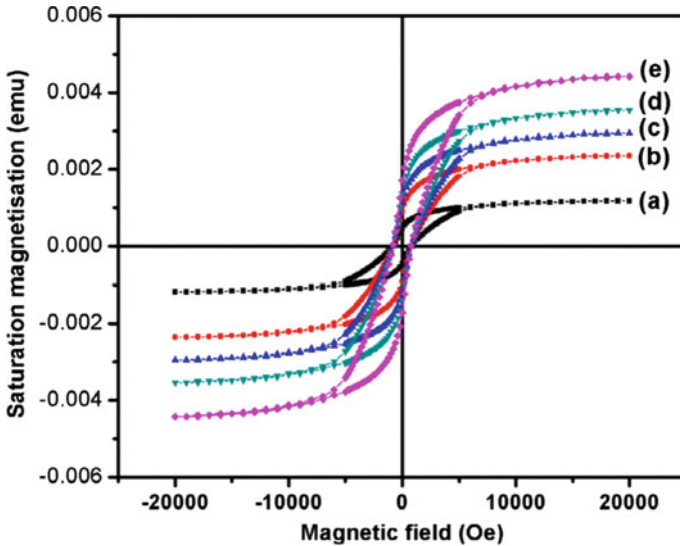


Fig. 5 M–H curve of a Pure barium ferrite and b Cu-2 mol%, c Cu-4 mol%, d Cu-6 mol%, and e Cu-8 mol% doped barium ferrite [51]. Reprinted with permission from Elsevier

3.2 Hard Ferrite

Permanent ferrite magnets, which are composed of Fe, Ba, and/or Sr oxides, have a high remanence upon magnetization. Hard ferrites materials are characterized by their hexagonal structure. The high value of H_c is known as hard ferrites. Because of this feature, hard ferrites are employed as permanent magnets once magnetised. Hard ferrites possess a broad hysteresis loop and a strong coercive force [52]. They are used to make permanent magnets for applications such as refrigerator magnets, washing machines, TVs, communication systems, switch mode power supplies, loudspeakers, and small electric motors [6]. When magnetically saturated, they achieve good magnetic flux and have high magnetic permeability. As a result, these “ceramic magnets” can store magnetic fields that are greater than iron. These are the most commonly used magnets in radios. The magnetic field strength H is approximately 30–160 kA turns per meter (400–2,000 Oe), and the greatest magnetic field B is about 0.35 T. M-, W-, U-, X-, Y-, and Z-type ferrites have a hexagonal structure.

3.2.1 Magnetic Property of Hard Magnet: Barium Ferrite ($BaFe_{12}O_{19}$)

Iqbal et al. [53] prepared $BaFe_{12}O_{19}$ NPs by using the sol–gel method and the annealing temperatures of these nanomaterials were 700 and 850 °C for 3 h. The magnetic nature of $BaFe_{12}O_{19}$ NPs is studied and plotted between magnetic moment and the applied magnetic field. These annealed nanomaterials (B-400, B-700, and B-850) have magnetic moments of 16.58, 23.39, and 31.32 emu/gm at 5 kOe, respectively, and coercivity values of 1.5, 2.1, and 2.7 kOe, respectively. According to this research, as the annealing temperature rises, the magnetic nature of these nanomaterials (B-400 to B-850) increases. B-850 was discovered to have the maximum value of a magnetization of 31.32 emu/g and coercivity of 2.7 kOe. This may be attributed to the growth of magnetic domains and an increase in crystallite size in the untainted phase of ferrite nanoparticles, which were verified by XRD study [54]. Furthermore, the high uniaxial anisotropy along the c-axis of M-type hexaferrite of B-850 [55] can be due to the increase in magnetic properties. The magnetic behaviour of B-850 is established to be consistent with the M-type $BaFe_{12}O_{19}$'s hard-magnetic functionality [53].

The citrate modified sol–gel approach was utilised by Kumar et al. [56] to create the rare earth La^{3+} doped BaM ($Ba_{1-Y}La_YFe_{12}O_{19}$, $Y = 0.00–0.20$), because it would be cost-effective and the precursors could be blended homogeneously [57]. The samples were annealed for 2 h at 50 °C and later annealed for 2 h at 1200 °C. At room temperature, with a maximum applied field of 20 kOe, the magnetic hysteresis (M–H) loops of Lanthanum (La^{3+}) doped barium hexaferrite ($Ba_{1-Y}La_YFe_{12}O_{19}$, $Y = 0.00–0.20$) ceramics were measured. All of the samples have a ferromagnetic signature with a strong coercive field. By increasing La in the BHF lattice up to $Y = 10\%$, the saturation magnetization ($M_s = 58.8$ to 63.6 emu/g) increases while the coercive field (H_c) decreases. For $Y > 0.10$, M_s decreases and H_c rises [56]. Vadivelan et al., fabricated

pure barium ferrite and copper-doped barium ferrite by co-precipitation technique at different ratios. The coercivity value increased dramatically from 851.128 to 856.651 Oe as the dopant ratios of copper increased at 300 K, according to magnetic properties studies. The increased value of coercivity are increase the magnetic storage capacity of this material [58].

3.2.2 Electrical Property of Hard Ferrite

The major qualities of interest for numerous applications are resistivity and permittivity (the dielectric constant ϵ and relative permittivity ϵ_r , which is a reflection of how easy it is to create an electric flux through a material, both of which should have a high frequency). It is feasible to calculate a complex permittivity with real (ϵ') and imaginary (ϵ'') elements, as well as dielectric resonance and losses. Dielectric polarisation occurs when metal cations and oxygen anions form dipoles. Metal cations and oxygen anions form dipoles, resulting in dielectric polarization. Electron hopping between Fe^{2+} and Fe^{3+} is the most common conduction mechanism in ferrites. The best sintered samples of barium, strontium and calcium M-type hexaferrite and further doped with 4 mol% (La_2O_3) were found to have ϵ_r of ~ 10 , ~ 20 and ~ 15 respectively. The values of the Co_xTi_x -substituted versions were nearly identical, with ϵ_r decreasing slightly as x increased. $\text{CaCo}_x\text{Ti}_x\text{Fe}_{12-2x}\text{O}_{19}$ (with 4 mol% La_2O_3) appeared to exhibit a direct dielectric resonance at 10 GHz for $x = 0.8$ and 8.75 GHz for $x = 1$. This was determined using measurements of ϵ' and ϵ'' [59]. Electron and hole conduction with two activation energies explain electrical conductivity. In addition, the sample has a high dielectric constant as well as a low dielectric loss value (Fig. 6). As a result, milling time, speed, and sintering temperature all play a role in improving dielectric properties.

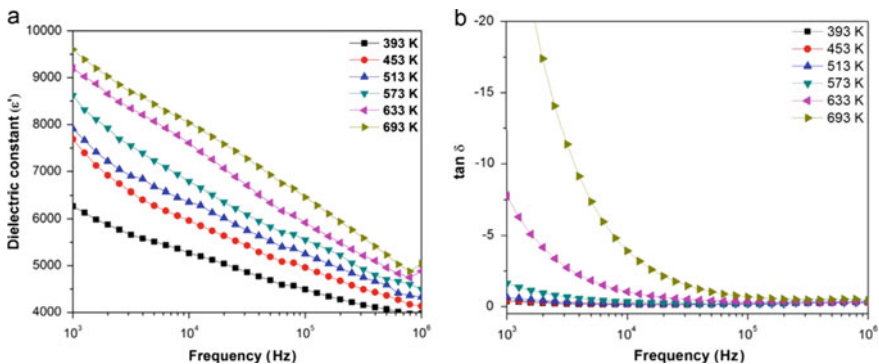


Fig. 6 Frequency dependency of **a** dielectric constant and **b** dielectric loss of $\text{BaFe}_{12}\text{O}_{19}$ within the temperature range of 393–693 K [60]. Reprinted with permission from Elsevier

These findings suggest that synthesised $\text{BaFe}_{12}\text{O}_9$ is suitable for electronic and microwave applications [60]. The enhancing impact of $\text{Ba}_{0.5}\text{Sr}_{0.5}\text{TiO}_3$ on the multifaceted permeability and permittivity was seen in the 1 MHz–1 GHz region. BST is a dielectric perovskite with an incredibly high ϵ_r of 1000 [61] that is employed in a capacitor or frequency filter for various electronic purposes at MW frequencies.

Mn–Zn ferrite and Ni–Zn ferrite are soft ferrites, whereas hard ferrites include $\text{BaFe}_{12}\text{O}_{19}$ and $\text{SrFe}_{12}\text{O}_{19}$. Various synthesis methods, magnetic properties, dielectric properties and applications of soft and hard ferrites are shown in Table 3. A recovered sintered, and therefore denser, ferrite has extra magnetic moments per unit volume, and thus a higher M_s , but the heat treatment required to achieve maximum densification also causes grain growth, resulting in a multi-domain particle with a lower coercivity because some of the domains will oppose one another. The magnetic characteristics of ferrites are known to be influenced by chemical composition, crystal structure, particle size, microstructure, and the material's surface. These properties are heavily influenced by the methods of material processing. The values of dielectric permittivity and ac conductivity are highly temperature dependent, and increase with temperature. With substitutions in M-type hexaferrite, there are a few cases where the saturation magnetization increased while the coercivity decreased. High enough coercivity (above 600 Oe) and saturation magnetization (as high as possible) are needed for the recording medium. Ferrites NPs investigate a number of applications in a range of biomedical to industrial shown in Table 3.

4 Classifications of Ferrites NPs According to Crystal Structure

Ferrites are ceramic materials that are mostly made up of iron oxide. The preparation of oxygen anions in the region of metal cations can alter, resulting in various crystal forms. Spinel, Pervoskite (ortho ferrites), Garnets, and Magneto-plumbites (hexagonal) are the different types of ferrites shown in Fig. 7. Table 4 summarizes the type of ferrite and its characteristics.

4.1 Spinel Ferrites

Spinel ferrite has a cubic structure with the chemical formula AFe_2O_4 , where A and Fe cations occupy tetrahedral and octahedral lattice sites [75]. Spinel ferrite can be defined as a closed cubic structure with 56 atoms: 24 cations occupying 8 of 64 cations are available at A sites and 16 of 32 cations are available at B sites and 32 oxygen anions [76]. Ni, Zn, Co, Mg is divalent cations and irons (Fe^{3+}) are trivalent cations in the cubic spinel structure. Various anions, such as sulphur (thiospinels), chlorine (halospinels), and oxygen, can create the spinel structure. Both size and

Table 3 Various synthesis methods, magnetic property, dielectric property and applications of soft and hard ferrites

Composition	Methods	Particle size (nm)	Temperature (°C)	Magnetic property	Dialectical property	Applications	References
$Zn_xMg_{1-x}Fe_2O_4$	Sol-gel	40–50	750 at 4 h	$M_s = 16.31-4.07$	-	Drug delivery	Powar et al. [62]
				$H_c = 61.96-130.81$			
$Zn_xMg_{1-x}Fe_2O_4$	Co-precipitation	30.18–42.85	650–750 at 4 h	$M_s = 0.071-0.293$	-	Gas sensing device	Thankachan et al. [63]
				$H_c = 58-194$			
$MgFe_2O_4$	Sol-gel	9	500–24 h	$M_s = 25.33, 4.34$	-	Transformers	Battoo et al. [64]
	Co-precipitation	12		$H_c = 306.988, 371.43$			
$Mg_{0.9}Mn_{0.1}Ag_xFe_{2-x}O_4$	Combustion	17.51–21.81	700–4 h	$M_s = (16.9-22.7$	$dc = 6.32 \times 107$ to $2.27 \times 107 \Omega$ cm	Electromagnet and microwave	Gul et al. [65]
				$H_c = 17.78-90.50$			
$Al_xZnFe_{2-x}O_4$	Co-precipitation	31.4–36.1	600–8 h	$M_s = 6.743-11.276$	Resivity = 4.25×10^5 to 9.90×10^5	Photocatalytic	Das et al. [66]
				$H_c = 0.01-0.068$			
$MgFe_2O_4$	Ultrasonic spray pyrolysis	4.05	600	$M_s = 5.50, 16.8, 18.5, 33.0$	-	Hyperthermia	Vignesh et al. [67]
				$H_c = 9.1, 12.53, 82.13, 98.37$			
$MnFe_2O_4$	Combustion method (glycine)	30–35	-	$M_s = 46$	-	Gas sensor	Cui et al. [68]
				$H_c = 64$			

(continued)

Table 3 (continued)

Composition	Methods	Particle size (nm)	Temperature (°C)	Magnetic property	Dialectical property	Applications	References
MnFe ₂ O ₄ and Mn/Fe ₃ O ₄ nanowires	Thermal decomposition of Fe–Mn–NA organometallic polymer precursors	5–10	450–4 h	$M_s = 45.9\text{--}48.7$	–	Water treatment	Amiri et al. [69]
NiFe ₂ O ₄	Hydrothermal process	~56 ± 1	200–2 h	$M_s = 16.10$	–	Cancer biomedical	Dumitrescu et al. [70]
NiFe ₂ O ₄	Sol gel auto combustion method	65	500, 700, 900 °C	–	$\rho = 4.1 \times 10^7$ to 5.3×10^7	Humidity sensors	Karaagac et al. [71]
CoFe ₂ O ₄	Co-precipitation	6.0 ± 1.7	–	$M_s = 35.3\text{--}41.0$ $H_c = 2\text{--}5$	–	Biomedical	Sulaiman et al. [72]
CaFe ₂ O ₄	Sol–gel method	13.59	550–2 h	$H_c = 85.331$	–	Targeted drug delivery	Vadivelan Jaya [51]
BaFe ₁₂ O ₁₉	Sol–gel method	46.67	400, 700, 850–3 h	$M_s = 16.58, 23.39, 31.02$ $H_c = 1.5, 2.1, 2.7$	$\epsilon' \& \epsilon'' = 6.53/11.5 \& 0.4/0.1$	EMI shielding	Iqbal et al. [53]
BaCu _x Fe _{12-x} O ₁₉	Co-precipitation	33.6–37.8	1200–6 h	$M_s = 11.7\text{--}34.9$ $H_c = 851.128\text{--}856.651$	–	Recording	Narang and Hudhara [59]
BaFe ₁₂ O ₁₉ fibers and hollow fibers	Electro-spun and coaxial electrospun	–	800–2 h	$M_s = 45\text{--}61$ $H_c = 102\text{--}3761.57$	–	Switching and sensing	Liu et al. [58]

(continued)

Table 3 (continued)

Composition	Methods	Particle size (nm)	Temperature (°C)	Magnetic property	Dialectical property	Applications	References
SrZr _x Cd _x Fe _{12-2x} O ₁₉	Co-precipitation	28–39	920–1 h	$M_s = 84-88$	$\epsilon' = 22-34$ $\tan\delta = 0.33-0.41$	Recording media	Ashiq ad Iqbal [73]
				$H_c = 137-60$			
Co _{1-x} Zr _x Fe ₂ O ₄	Co-precipitation	16–26	700–4 h	$M_s = 0.33\ 47.9$	–	Consumer electronics, aerospace, catalysis and bio surgical	Kavitha and Kurian [74]
				$H_c = 1144.10-896.29$			

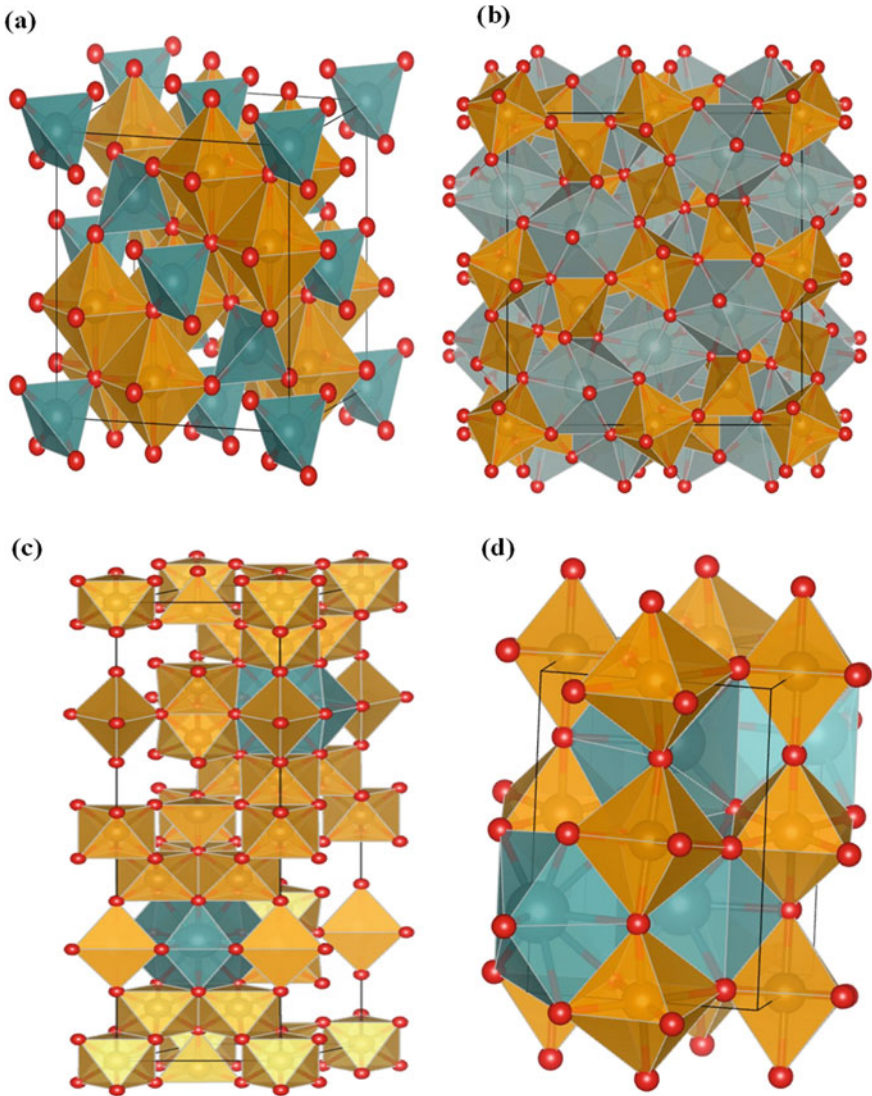


Fig. 7 Shows the crystal structure of **a** Spinel ferrite, **b** garnet ferrite, **c** hexagonal ferrite and **d** perovskite ferrite

Table 4 Summarized the type, formulas, and crystallographic sites of ferrites

S. no	Types	Chemical formula	Structure	Examples
1	Spinel ferrite	MFe_2O_4	Cubic	$M = Mn, Zn$ etc
2	Garnet ferrite	$Mn_3Fe_5O_{12}$	Cubic	$Mn = Y, Sm$ etc.
3	Ortho ferrite	$MnFeO_3$	Perovskites	$Mn = La, Dy$ etc.
4	Hexagonal ferrite	$MFe_{12}O_{19}$	Hexagonal	$M = Ba, Sr$ etc.

charge neutrality considerations must be met by the cations in the structure. Spinel structures are classified as follows based on the arrangement of metal cation M^{2+} :

- (i) **Normal spinel structure**, $A[B_2O_4]$ where all Me^{2+} ions occupy A (tetrahedral) sites and Fe^{3+} ions in B (octahedral) sites; the structural formula of such ferrites is $Me^{2+}[Fe_2^{3+}]O_4^{2-}$. This type of distribution takes place in $ZnFe_2O_4$ and $CdFe_2O_4$.
- (ii) **Inverse spinel structure**, $B[ABO_4]$ with Me^{2+} ions occupying the B octahedral sites and Fe^{3+} ions distributed over both B octahedral and A tetrahedral sites [77, 78]. The A-sites are completely occupied by Fe^{3+} cations and the B-sites are randomly occupied by Me^{2+} and Fe^{3+} cations; the structural formula of these ferrites is $Fe^{3+}[Me^{2+}Fe^{3+}]O_4^{2-}$. Magnetite Fe_3O_4 , ferrites $MgFe_2O_4$, $NiFe_2O_4$ and $CoFe_2O_4$ include inverted spinel structure [79].
- (iii) **Mixed spinel structure**, $A_{1-x}B_x[A_xB_{2-x}O_4]$ or $(Me_{1-x}Fe_x)[Fe_{2-x}Me_x]O_4$ with Me^{2+} and Fe^{3+} ions scattered over both octahedral and tetrahedral sites e.g. $MnFe_2O_4$, where x is the degree of inversion. The cation dispersion in spinel is inverted to a medium degree, with a fraction of Me^{2+} and Fe^{3+} cations present at both sites.

The gap between tetrahedral and octahedral site expansion is defined by a parameter which is known as the parameter oxygen or the parameter anion (u). The oxygen parameter (u) is a quantity that describes the O^{2-} ion movement due to cation replacement at the site of tetrahedral A. As u increases, oxygen ions move such that the distance between A and O ions (r_A) increases while that between B and O ions (r_B) decreases. When ' u ' parameter reduces, the O^{2-} ions are displaced so that r_A decreases and r_B increases. The parameter u has a neighbourhood value of 0.375 ($u = 3/8$) for all ideal spinels. But this ideal pattern is slightly deformed in the real spinel lattice and typically corresponds to $u > 0.375$. The theoretical lattice constant (a_{th}), octahedral site ion radius (r_B), and tetrahedral site ion radius (r_A) for spinel systems were determined based on the cation distribution by the following ratio:

$$a_{th} = \frac{8}{3\sqrt{3}} \left[(r_A + R_o) + \sqrt{3(r_B + R_o)} \right] \quad (5)$$

where, R_o is the oxygen ion radius of O^{2-} (1.38 Å); r_A and r_B are the ionic radii of A (tetrahedral) and B (octahedral) sites respectively, and u is the parameter of the anion (oxygen).

Spinel ferrites with nanoscale dimensions have potential applications in the field of great-performance materials. Magnetic ferro-fluids, microwave absorbers, and magnetically guided drug carriers are all examples of high-density magnetic recording media.

4.2 Perovskite Ferrites

The standard chemical formula for cubic perovskite or ortho ferrites is ABX_3 , where A and B are cations with differing oxidation values and X is an anion. The A-cation is located in the unit cell's centre, whereas the B cation and X anions are located in the unit cell's corners and edges, respectively. Two of the most investigated materials are orthoferrites ($RFeO_3$) compounds such as lanthanum and samarium [80]. The bandgap absorption of perovskite ferrites nanoparticles caused high absorption at 590 nm, which has applications in environmental cleansing and/or water splitting.

4.3 Garnet Ferrites

The garnet ferrites possess an $X_3Y_2(SiO_4)_3$ type structure, in which X site is generally captured by divalent cations e.g. Ca^{2+} , Mg^{2+} , Fe^{2+} and similarly, the Y sites are occupied by trivalent cations in an octahedral and /or tetrahedral environment with $[SiO_4]^{4-}$ producing the tetrahedral. Examples of trivalent ions are Al^{3+} , Fe^{3+} , Cr^{3+} etc. Garnet ferrites are specified by the general formula $(A_3B_5O_{12})$, which belongs to rare-earth cations. Garnet ferrites feature three crystallographic lattices (a, b, and c) in their crystal structure. Garnet ferrites have dodecahedral (12-coordinated) sites along with the octahedral and tetrahedral sites present in spinels. It was discovered that $24Fe^{3+}$ ions reside at tetrahedral sites, while $16Fe^{3+}$ ions prefer octahedral sites, and $24R^{3+}$ ions occupy dodecahedral sites, whereas oxygen ions are spread over the interstitial sites [81]. Garnets are magnetically hard as well. As a result of the antiparallel spin alignment among all types of sites, net ferrimagnetism is a complicated consequence. Despite the fact that spinels have better magnetic qualities, garnets have better dielectric qualities because they are more stress sensitive. Because of their ferrimagnetic characteristics, the rare earth iron garnets $M_3Fe_5O_{12}$ [$M = Y, Dy, Sm$] have attracted a lot of attention.

4.4 Magneto-Plumbites

The magnetic mineral magneto plumbite $PbFe_{12}O_{19}$ was first described in 1925. It has a hexagonal structure, so it is named as hexagonal ferrites and with the general composition, $MeFe_{12}O_{19}$ where ($Me = Ba, Pb, Sr$). In interaction with divalent oxides ($BaO, PbO, or SrO$), these ferrimagnetic oxides have a main component of Fe_2O_3 . These ferrites have a lot of uniaxial anisotropy, more magnetization, and better chemical stability; therefore, they are perfect for recording technology. $BaFe_{12}O_{19}$ hexa-ferrite films are interesting options for high density recording media as well as microwave/millimeter wave devices [82, 83]. M-, W-, U-, X-, Y-, and Z-type ferrites have a hexagonal structure. The hexa-ferrites are classified into six categories based

Table 5 Shows the information of chemical formula and building blocks of all hexa-ferrites

Types	Chemical formula	Building blocks	Unit cell	Spinel plates and hexagonal layers
M	[(Ba,Sr)Fe ₁₂ O ₁₉]	SRS*R*	2M	2M ₅ = B ₁ S ₄ B ₁ S ₄
W	[(Ba,Sr)Me ₂ Fe ₁₆ O ₂₇]	SSRS*S*R*	2W	2W ₇ = B ₁ S ₆ B ₁ S ₆
Y	[(Ba,Sr) ₂ Me ₂ Fe ₁₂ O ₂₂]	3(ST)	3Y	2Y ₆ = B ₂ S ₄ B ₂ S ₄ B ₂ S ₄
Z	[(Ba,Sr) ₃ Me ₂ Fe ₂₄ O ₄₁]	STSRs*T*S*R*	2Z	2Z ₁₁ = B ₂ S ₄ B ₁ S ₄ B ₂ S ₄ B ₁ S ₄
X	[(Ba,Sr) ₂ Me ₂ Fe ₂₈ O ₄₆]	SSRS*S*R*	3X	3X ₁₂ = B ₁ S ₄ B ₁ S ₆ B ₁ S ₄ B ₁ S ₆ B ₁ S ₄ B ₁ S ₆
U	[(Ba,Sr) ₄ Me ₂ Fe ₃₆ O ₆₀]	SRS*R*S*T*	U	U ₁₆ = B ₁ S ₄ B ₂ S ₄ B ₁ S ₄

on chemical formula and crystal structure [84]. All are closely related to hexagonal ferrite, a highly complex crystal structure that can be described in a variety of ways, as seen in Table 5.

4.4.1 M-Type Structure

One ‘S’ as well as an ‘R’ block constitutes an M-type hexagonal ferrite. The blocks are overlapped with hexagonal and cube pack layers and, as well, the plane containing the Ba atom is called the mirror plane. Where block S and R rotate 180° around the c-axis, therefore, providing the mirror block ‘R’, R* gives the unit formula SRS*R*, where * indicates a rotation of 180° of the corresponding building unit with respect to the c-axis. Furthermore, it was shown that barium M-type hexa-ferrite made of a spinel stack such as ferrite block and substituted M-type ferrite was extensively investigated such as BaFe₁₂O₁₉ [85, 86]. It has been discovered to improve the magnetic properties of BaM ferrite. It was also documented that in the case of M-type barium hexa ferrite, the lattice parameter $c = 23.17 \text{ \AA}$ and $a = 5.89 \text{ \AA}$, but in the case of SrM ferrite, the lattice parameters $c = 23.03 \text{ \AA}$ and $a = 5.86 \text{ \AA}$ for PbM ferrite, the lattice parameters are $c = 23.02 \text{ \AA}$ and $a = 5.88 \text{ \AA}$ the cross-section view of the M-type ferrite structure. BaM has almost the same structure and unit cell ordering [83]. Ba²⁺ is greater than Pb²⁺, with lattice constants of $c = 23.02 \text{ \AA}$, $a = 5.88 \text{ \AA}$ for PbM [87].

4.4.2 W-Type Structure

The molecular unit of W-type ferrite is made up of 2 S-blocks and 1 R-block, making it comparable but not identical to the M structure. There are mainly 2S blocks on top of and under the R block, but the R block still has a mirror plane, and the unit cell is made up of 2 molecular W-units, resulting in SSRS/S/R. Fe₂W belongs to the space group *P63/mmc* and has a cell length of 32.84 \AA [88].

4.4.3 X-Type Structure

The X structure is kind of related to that of the W structure, consisting of one M and one W molecular unit, resulting in the structure SRS/S/R, with the blocks of the W segment rotated through 180° relative to those of the M section. The crystal structure 3(SRS/S/R), $c = 84.11 \text{ \AA}$, is a class of the $R3M$ space group and is made up of three identical units [88].

4.4.4 Y-Type Structure

Y-type ferrite contains molecular units with 1 T and 1 S unit, with a total 6 layers, and the unit cell is formed from 3 of these components, with a c-axis length of 43.56 \AA , and it belongs to the $R3m$ space group [88]. Because the T block excludes a mirror plane, the overlap of hexagonal and cubic close-packed layers needs three T blocks, with the relative placements of the Ba atoms recurring every 3 T blocks. As a result, the formula for the unit cell is simply 3(ST).

4.4.5 Z-Type Structure

The Z unit is made up of Y + M, therefore it's ST + SR, with a mirror plane in the R block and 11 layers of oxygen layer recurrence distance. As a result, two molecular units are required to construct a single Z ferrite unit cell, one of which is rotated 180° in the c-axis region relative to the other, generating STSRS/T/S/R, that has a c-axis length of 52.30 and belongs to the space group P63/mmc [88].

4.4.6 U-Type Structure

The molecular units Z + M, or M + Y + M, are contained in the U ferrite structure, resulting in the block structure 'SRS/R/S/T'. Firstly, the unit cell is made up of just 1 molecular unit, where $c = 38.16 \text{ \AA}$ [89], in which the 'R' as the well as 'S' blocks of the Z section are rotated through 180° relative to the M section. It is now more commonly claimed that it is made up of 3 molecular units, with $a = 5.88 \text{ \AA}$ and $c = 113 \text{ \AA}$ [90]. From HRTEM images of U ferrite, MMY stacking sequence and stacking faults are clearly visible, in which the crystal structure was disrupted by the inclusion of additional Y blocks [90]. In HAADF-STEM, the repetition of 'R', 'S', as well as the T blocks of $\text{Sr}_4\text{Co}_2\text{U}$ can be clearly seen. The Sr^{2+} ion has less radii than Ba^{2+} ions, and the lattice constants for $\text{Sr}_4\text{Co}_2\text{U}$ with the $R3m$ space group are $a = 5.86 \text{ \AA}$ and $c = 112.3 \text{ \AA}$.

5 Conclusions

The rapid advancement of magnetic materials research has revolutionized a variety of applications. This chapter covers the fundamentals of ferrite properties as well as the various forms of ferrites. It also highlights the types of ferrites and types of magnetism. The dielectric permittivity values and ac conductivity depend upon temperature, and increase with the increase in temperature. With doping in M-type hexaferrites, there are a few cases where the saturation magnetization increased while the coercivity decreased. The elevated coercivity more than above 600 Oe and saturation magnetization is needed for the recording medium. Chemical composition, crystal structure, particle size, microstructure, and the material's surfaces are all believed to impact ferrites' magnetic properties. The methods of material processing have a big impact on these attributes.

References

1. Q. Song, Z.J. Zhang, *J. Am. Chem. Soc.* **134**, 10182–10190 (2012)
2. S. Gnanam, V. Rajendran, *J. Alloy. Compd.* **735**, 1854–1862 (2018)
3. N.J. Vickers, *Curr. Biol.* **27**, R713–R715 (2017)
4. V.V. Jadhav, R.S. Mane, P.V. Shinde, *Electrochemical Supercapacitors* (Springer, 2020), pp. 37–45
5. J.L. Snoek, Elsevier Publishing Company (1947)
6. P. Thakur, D. Chahar, S. Taneja, N. Bhalla, A. Thakur, *Ceram. Int.* (2020)
7. S. Sharma, N. Dhiman, A. Kumar, M. Singh, P. Dhiman, *Integr. Ferroelectr.* **204**, 38–46 (2020)
8. K.K. Kefeni, T.A. Msagati, T.T. Nkambule, B.B. Mamba, *Mater. Sci. Eng. C* **107**, 110314 (2020)
9. P. Dhiman, N. Dhiman, A. Kumar, G. Sharma, M. Naushad, A.A. Ghfar, *J. Mol. Liq.* **294**, 111574 (2019)
10. L.H. Reddy, J.L. Arias, J. Nicolas, P. Couvreur, *Chem. Rev.* **112**, 5818–5878 (2012)
11. S.V. Spirou, M. Basini, A. Lascialfari, C. Sangregorio, C. Innocenti, *Nanomaterials* **8**, 401 (2018)
12. C.-H. Sohn, S.P. Park, S.H. Choi, S.-H. Park, S. Kim, L. Xu, S.-H. Kim, J.A. Hur, J. Choi, T.H. Choi, *Nanomedicine: nanotechnology. Biol. Med.* **11**, 127–135 (2015)
13. X. Zhu, J. Zhou, M. Chen, M. Shi, W. Feng, F. Li, *Biomaterials* **33**, 4618–4627 (2012)
14. H. Lee, T.-H. Shin, J. Cheon, R. Weissleder, *Chem. Rev.* **115**, 10690–10724 (2015)
15. M.A. Gijs, F. Lacharme, U. Lehmann, *Chem. Rev.* **110**, 1518–1563 (2010)
16. A.K. Gupta, M. Gupta, *Biomaterials* **26**, 3995–4021 (2005)
17. S.J. Soenen, U. Himmelreich, N. Nuytten, M. De Cuyper, *Biomaterials* **32**, 195–205 (2011)
18. J. Estelrich, M.J. Sánchez-Martín, M.A. Busquets, *Int. J. Nanomed.* **10**, 1727 (2015)
19. M.G. Mahfouz, A.A. Galhoum, N.A. Gomaa, S.S. Abdel-Rehem, A.A. Atia, T. Vincent, E. Guibal, *Chem. Eng. J.* **262**, 198–209 (2015)
20. A. Barre, R. Culerrier, C. Granier, L. Selman, W.J. Peumans, E.J. Van Damme, F. Bienvenu, J. Bienvenu, P. Rougé, *Mol. Immunol.* **46**, 1595–1604 (2009)
21. J. Wei, X. Zhang, Q. Liu, Z. Li, L. Liu, J. Wang, *Chem. Eng. J.* **241**, 228–234 (2014)
22. L. Tan, Q. Liu, X. Jing, J. Liu, D. Song, S. Hu, L. Liu, J. Wang, *Chem. Eng. J.* **273**, 307–315 (2015)
23. I. Ibrahim, I.O. Ali, T.M. Salama, A. Bahgat, M.M. Mohamed, *Appl. Catal. B* **181**, 389–402 (2016)

24. G. Sharma, A. Kumar, S. Sharma, M. Naushad, P. Dhiman, D.-V.N. Vo, F.J. Stadler, *Mater. Lett.* **278**, 128359 (2020)
25. A. Kumar, G. Sharma, M. Naushad, T. Ahamad, R.C. Veses, F.J. Stadler *Chem. Eng. J.* **370**, 148–165 (2019)
26. M.A. Carpenter, M.A. Geletkanycz, W.G. Sanders, *J. Manag.* **30**, 749–778 (2004)
27. S.C. Tang, I.M. Lo, *Water Res.* **47**, 2613–2632 (2013)
28. M. Hasanzadeh, N. Shadjou, M. de la Guardia, *TrAC Trends Anal. Chem.* **72**, 1–9 (2015)
29. N. Van. Quy, N.D. Hoa, M. An, Y. Cho, D. Kim, *Nanotechnology* **18**, 345201 (2007)
30. X. Qu, J. Brame, Q. Li, P.J. Alvarez, *Acc. Chem. Res.* **46**, 834–843 (2013)
31. S.K. Brar, M. Verma, R. Tyagi, R. Surampalli, *Waste Manag.* **30**, 504–520 (2010)
32. K.K. Kefeni, B.B. Mamba, T.A. Msagati, *Sep. Purif. Technol.* **188**, 399–422 (2017)
33. P. Dhiman, N. Dhiman, A. Kumar, G. Sharma, M. Naushad, A.A. Ghfar., *J. Mol. Liq.* **294**, 111574 (2019)
34. E. Roduner, *JCSR Size matters: why nanomaterials are different* **35**, 583–592 (2006)
35. C. Heck, (Elsevier, 2013)
36. B. Viswanathan, V.R.K. Murthy, (Springer, 1990)
37. L. Bouet, P. Tailhades, I. Pasquet, C. Bonningue, S. Le Brun, A. Rousset, *Jpn. J. Appl. Phys.* **38**, 1826 (1999)
38. A. Kaur, G.K. Bhargava, *Mater. Today: Proc.* **37**, 3082–3086 (2021)
39. A.M. Ealias, M. Saravanakumar, *IOP Conf. Ser. Mater. Sci. Eng.* 032019 (2017)
40. W.S. Galvão, D. Neto, R.M. Freire, P.B. Fechine, *Solid State Phenomena. Trans. Tech. Publ.* 139–176 (2016)
41. D. Jiles, *Introduction to Magnetism and Magnetic Materials* (CRC press, 2015)
42. J. Chatterjee, Y. Haik, C.-J. Chen, M. Materials, *J. Magn.* **257**, 113–118 (2003)
43. O. Masala, D. Hoffman, N. Sundaram, K. Page, T. Proffen, G. Lawes, R. Seshadri, *Solid State Sci.* **8**, 1015–1022 (2006)
44. C. Anumol, M. Chithra, S. Rout, S.C. Sahoo, *J. Supercond. Novel Magn.* **33**, 1611–1617 (2020)
45. P. Chavan, L. Naik, P. Belavi, G. Chavan, C. Ramesha, R. Kotnala, *J. Electron. Mater.* **46**, 188–198 (2017)
46. H. Moradmard, S.F. Shayesteh, P. Tohidi, Z. Abbas, M. Khaleghi, *J. Alloy. Compd.* **650**, 116–122 (2015)
47. T. Vigneswari, P. Raji, *J. Mol. Struct.* **1127**, 515–521 (2017)
48. K. Maaz, S. Karim, A. Mumtaz, S. Hasanain, J. Liu, J. Duan, *J. Magn. Magn. Mater.* **321**, 1838–1842 (2009)
49. M. Atif, M. Nadeem, R. Grössinger, R.S. Turtelli, *J. Alloy. Compd.* **509**, 5720–5724 (2011)
50. H. Liu, Z. Yu, B. Fu, M. Ran, C. Wu, X. Jiang, R. Guo, Z. Lan, K. Sun, *Ceram. Int.* **47**, 1318–1324 (2021)
51. S. Vadivelan, N.V. Jaya, *Results Phys.* **6**, 843–850 (2016)
52. R. Srivastava, B. Yadav, *Int. J. Green Nanotechnol.* **4**, 141–154 (2012)
53. S. Iqbal, G. Kotnala, J. Shah, S. Ahmad, *Mater. Res. Express* **6**, 055018 (2019)
54. P. Xu, X. Han, M. Wang, *J. Phys. Chem. C* **111**, 5866–5870 (2007)
55. S. Choopani, N. Keyhan, A. Ghasemi, A. Sharbati, R.S. Alam, *Mater. Chem. Phys.* **113**, 717–720 (2009)
56. S. Kumar, M.K. Manglam, S. Supriya, H.K. Satyapal, R.K. Singh, M. Kar, *J. Magn. Magn. Mater.* **473**, 312–319 (2019)
57. S. Kumar, S. Supriya, M. Kar, *J. Appl. Phys.* **122**, 224106 (2017)
58. G-F. Liu, Z.-D. Zhang, F. Dang, C.-B. Cheng, C.-X. Hou, *J. Magn. Magn. Mater.* **412**, 55–62 (2016)
59. S.B. Narang, I. Hudiara, *J. Ceram. Process. Res.* **7**, 113–116 (2006)
60. R.C. Pullar, Y. Zhang, L. Chen, S. Yang, J.R. Evans, P.K. Petrov, A.N. Salak, D.A. Kiselev, A.L. Kholkin, V.M. Ferreira, *J. Eur. Ceram. Soc.* **27**, 4437–4443 (2007)
61. A. Nigam, S. Pawar, *Ceram. Int.* **46**, 4058–4064 (2020)
62. R.R. Powar, V.D. Phadtare, V.G. Parale, S. Pathak, K.R. Sanadi, H-H. Park, D.R. Patil, P.B. Piste, D.N. Zambare, *Mater. Sci. Eng.: B* **262**, 114776 (2020)

63. S. Thankachan, S. Xavier, B. Jacob, E. Mohammed, J. Exp. Nanosci. **8**, 347–357 (2013)
64. K.M. Batoo, E.H. Raslan, S.F. Adil, I. Sharma, G. Kumar, J. Mater. Sci.: Mater. Electron. **31**, 7880–7888 (2020)
65. S. Gul, M.A. Yousof, A. Anwar, M.F. Warsi, P.O. Agboola, I. Shakir, M. Shahid, Ceram. Int. **46**, 14195–14205 (2020)
66. H. Das, N. Sakamoto, H. Aono, K. Shinozaki, H. Suzuki, N. Wakiya, J. Magn. Magn. Mater. **392**, 91–100 (2015)
67. R.H. Vignesh, K.V. Sankar, S. Amaresh, Y.S. Lee, RKJS. Selvan, Sens. Actuators B: Chem. **220**, 50–58 (2015)
68. H.-J. Cui, J.-W. Shi, B. Yuan, M.-L. Fu, J. Mater. Chem. A **1**, 5902–5907 (2013)
69. M. Amiri, M. Salavati-Niasari, A. Akbari, Adv. Colloid Interface Sci. **265**, 29–44 (2019)
70. A. Dumitrescu, G. Lisa, A. Jordan, F. Tudorache, I. Petrila, A. Borhan, M. Palamaru, C. Mihailescu, L. Leontie, C. Munteanu, Mater. Chem. Phys. **156**, 170–179 (2015)
71. O. Karaagac, B.B. Yildiz, H. Köçkar, J. Magn. Magn. Mater. **473**, 262–267 (2019)
72. N. Sulaiman, M. Ghazali, B. Majlis, J. Yunas, M. Razali, Bio-Med. Mater. Eng. **26**, S103–S110 (2015)
73. M.N. Ashiq, M.J. Iqbal, I.H. Gul, J. Alloy. Compd. **487**, 341–345 (2009)
74. S. Kavitha, M. Kurian, J. Alloy. Compd. **799**, 147–159 (2019)
75. S. Atiq, M. Majeed, A. Ahmad, S.K. Abbas, M. Saleem, S. Riaz, S. Naseem, Ceram. Int. **43**, 2486–2494 (2017)
76. S.B. Narang, K. Pubby, J. Magn. Magn. Mater. 167163 (2020)
77. P. Dhiman, M. Patial, A. Kumar, M. Alam, M. Naushad, G. Sharma, D.-V.N. Vo, R. Kumar, Mater. Lett. **284**, 129005 (2021)
78. J. Chand, S. Verma, Pooja, Sarveena, M. Singh, AIP Conf. Proc. **1591**, 1518–1520 (2014)
79. P. Dhiman, T. Mehta, A. Kumar, G. Sharma, M. Naushad, T. Ahamad, G.T. Mola, Adv. Powder Technol. (2020)
80. A.A.S. Hassan, W. Khan, S. Husain, P. Dhiman, M. Singh, M.M. Alanazi, J. Mater. Sci.: Mater. Electron. **32**, 3753–3765 (2021)
81. M.N. Akhtar, M.A. Khan, M. Ahmad, G. Murtaza, R. Raza, S. Shaukat, M. Asif, N. Nasir, G. Abbas, M. Nazir, J. Magn. Magn. Mater. **368**, 393–400 (2014)
82. E. Pollert, Prog. Cryst. Growth Charact. **11**, 155–205 (1985)
83. R.C. Pullar, Prog. Mater. Sci. **57**, 1191–1334 (2012)
84. A. Goldman, (Springer Science & Business Media, 2006)
85. V.P. Singh, R. Jasrotia, R. Kumar, P. Raizada, S. Thakur, K.M. Batoo, M. Singh, World J. Condens. Matter Phys. **8**, 36 (2018)
86. G. Albanese, A. Deriu, Ceram. Int. **11**, 137 (1985)
87. V. Adelskold, Arkiv Kemi MinerGeol (1938).
88. P. Braun, J. Hornstra, J. Leenhouts, Philips Res. Rep. **12**, 491–548 (1957)
89. J. Kohn, D. Eckart, C.F. Cook, Science **172**, 519–525 (1971)
90. D. Lisjak, D. Makovec, M. Drogenik, J. Mater. Res. **19**, 2462–2470 (2004)

Synthesis Routes for Ferrites and Their Impact on the Properties of Ferrites



Garima Rana, Pooja Dhiman, Rajesh Kumar, Ankush Chauhan, Anjana Sharma, and Indu Sharma

Abstract Nano ferrites have piqued interest owing to their numerous uses in biomedical, wastewater remediation, and electronic devices. This chapter is primarily concerned with the various fabrication techniques for ferrite nanoparticles. This chapter presents various methods used for ferrites preparation with distinctive examples, their advantages as well as limitations in detail. The fabrication techniques used to achieve ferrites nanoparticles of various structures and morphologies, such as hydrothermal, microemulsion, solvothermal, solution combustion, microwave, chemical vapor deposition, sol–gel, chemical bath deposition, or wet chemical synthesis, sonochemical, thermal decomposition, and electrochemical methods, are briefly described. This chapter summarizes the recent work on the influence of synthesis techniques on the properties of ferrites in nanoform. Ferrites belong to the materials which are a potential candidate for widely spread applications.

Keywords Ferrites · Nano materials · Synthesis techniques

1 Introduction

The three major targets of magnetic nanomaterials are synthesis, knowledge of novel advanced materials, and relationships between them. Nanomaterials are those materials whose particle size lies between the range of 10–100 nm in at least one or more dimensions, as defined by their nanometric equivalents. A large number of atoms are present at or near the surface of particles at this length scale, giving the materials their specific properties. Nanomaterials have a high surface-to-volume ratio which

G. Rana · P. Dhiman (✉) · R. Kumar · A. Chauhan
School of Physics & Materials Science, Shoolini University of Biotechnology and Management Sciences, Bajhol, Solan, HP, India

A. Sharma
Department of Physics, Chandigarh University, Gharuan, Mohali, Punjab, India

I. Sharma
Department of Physics, Career Point University, Hamirpur, HP, India

provides them with extraordinary properties in comparison to their bulk counterparts. Ferrites are ceramic compounds that contain metal oxides, such as iron oxide, as their primary ingredient. Ferrites are classified into three types based on their crystal structure:

- (1) Spinel type, which includes spinel ferrites,
- (2) Garnet type, which includes garnet ferrites.
- (3) Magneto-plumbite type, which includes hexagonal ferrites.

The spinel ferrites are commonly known as soft ferrites which are being utilized in microwave communication systems, transformers, and inductors, etc. Another class of ferrites i.e. hard magnetic ferrites usually hexagonal ferrites, are widely employed in most electrical–mechanical devices being used for energy conversion. Because of the widespread applications of ferrites in the electronics, and telecommunication sector, plenty of soft magnetic materials including Ni ferrite, Mn, or Zn ferrite, are requisites magnetic materials for day-to-day usable devices. Spinel ferrites have some unique properties like they are highly thermally and chemically durable, possesses minimum eddy current losses, have high resistivity, and most important low coercivity [1–3], these magnetic materials can be used for high-frequency applications, they also find a role in information storage devices, antenna applications, sensors and in many power transfer system [4–7]. On the other hand, hexaferrite is used in a variety of electronic devices today, including mobile and wireless communication at GHz frequencies, EMI shielding, multiferroics, microwave absorbers, and antenna applications [8, 9].

Ferrites nanoparticles have electrical and magnetic properties that are intuitive to microstructure features and volatility of composition, which are impacted by the methods used to synthesize them [10–13]. Verma and Chatterjee et al. [10] synthesized Zn doped Mn–Ni nanoferrites ($\text{Mn}_{0.2}\text{Ni}_{0.8-x}\text{Zn}_x\text{Fe}_2\text{O}_4$) through the citrate precursor method and studied the structural, electrical, and magnetic properties by varying the Zn concentration on Ni sites, with $x = 0.4, 0.5, \text{ and } 0.6$. Results revealed that AC resistivity values lie between 10^5 and $10^7 \Omega \text{ cm}$ and decrease with the increase in Zn doping and also with the increase in sintering temperature. In another work, Zhang et al. [11] used the sol–gel process to make $\text{Ni}_{0.5}\text{Zn}_{0.5}\text{Fe}_2\text{O}_4$ with the size of grains varying from 9 to 96 nm. The magnetic observations demonstrate that the compositions with grains of less than 30 nm size show super-paramagnetic, while for the samples with grain size above 30 nm, ferromagnetic behavior dominates.

2 Fabrication of Ferrite Nanoparticles

The development of numerous dependable techniques to manufacture nanoparticles by manipulating their size distribution, shape, morphology, and chemical composition have recently been a fascinating subject of research area for many researchers working in the field of nanotechnology. When these nanoparticles are combined with the organic molecules, then due to their collective nature, it is possible to create

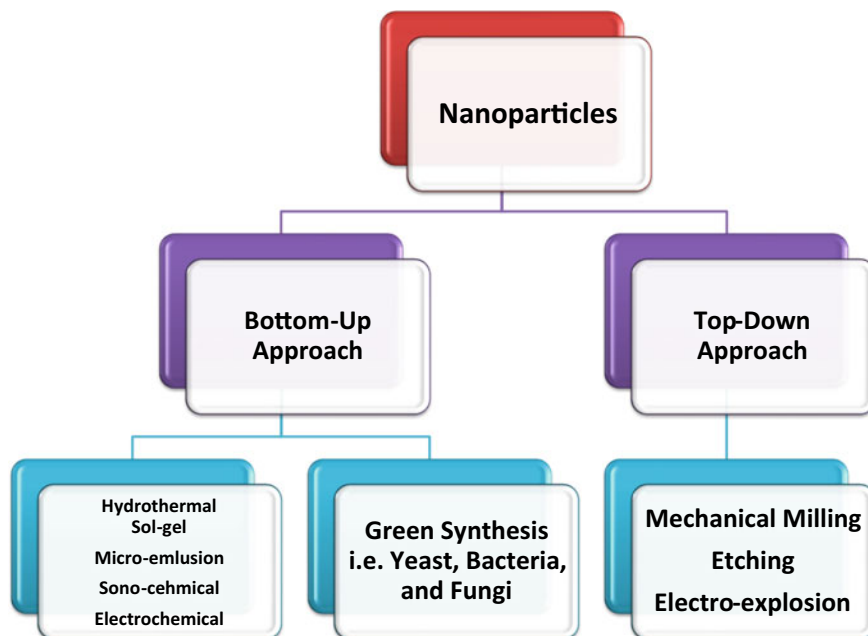


Fig. 1 Pictorial representation of bottom-up and top-down approach

various dimensional (1-D, 2-D, 3-D) mesostructures. As indicated in Fig. 1, nanoparticles synthesis techniques are essentially classified into two types: top-down and bottom-up [14]. Physical processes such as milling, crushing, and other methods in which bulk particles are broken down into smaller and smaller particles, resulting in the formation of nanoparticles, are included in the top-down approach. Though crystallographic damage during the production of the nanostructure has a negative effect on the surface structure. Contrarily, the bottom-up technique includes the sol-gel route, laser pyrolysis method, plasma spraying, aerosol-based processes, green synthesis methods, and much more. These all belong to chemical and biological techniques. In these techniques, nano-systems are generated by adding atoms to atoms, molecules to molecules, or clusters to clusters. When it comes to producing nanostructured materials with homogeneous structures and distributions, the bottom-up technique is far superior to the top-down approach [15].

2.1 Mechanical Milling Method

Mechanical milling is a powder-making technique in which narrow-sized particles are formed from bulk materials that are subjected to rubbed against each other with the help of an agitator medium. This technique employs high-speed air jets to create

huge pressure and friction [14]. It's a high-energy method that introduces structural faults, chemical disorders, and elastic strain to the source bulk material throughout the procedure. As a result, nanostructures are generated [15]. Mechanical milling is best exemplified by ball milling. The particle size of raw bulk material, the gas environment, and intentional additives may influence the entire process [16]. The technique is simple and inexpensive, and it has high efficiency and selectivity [17]. The mechanical milling process was used to make Nb⁵⁺/Ti³⁺-doped NiFe₂O₄, MnFe₂O₄, and NiZnFe₂O₄ [18]. The particle sizes decreased as the doping percentage is raised. The size of the ferrite grain has a significant influence on saturation magnetization and coercive area. After a high-energy milling procedure, cobalt ferrite nanoparticles were generated in this study by post calcination. The entire development of the CFO phase was confirmed by the appearance of all diffracting planes of cobalt ferrite in the HRTEM picture (Fig. 2). The samples which are obtained through high energy milling are the ones with maximum coercivity values of 2090 Oe were obtained. Particle size reduction, the development of a magnetic dead layer on the sample's surface, and cation re-distribution might be used to explain the variation in saturation magnetization behavior as milling energy was increased. A greater Co²⁺ concentration on the octahedral site was found at medium milling energy, along with higher saturation magnetization values (78 emu/g) [19]. The solid-state approach has been used to make zinc ferrite [20], cobalt ferrite [21], and LiZn ferrite (Li_{0.4}Zn_{0.2}Fe_{2.4}O₄) [22].

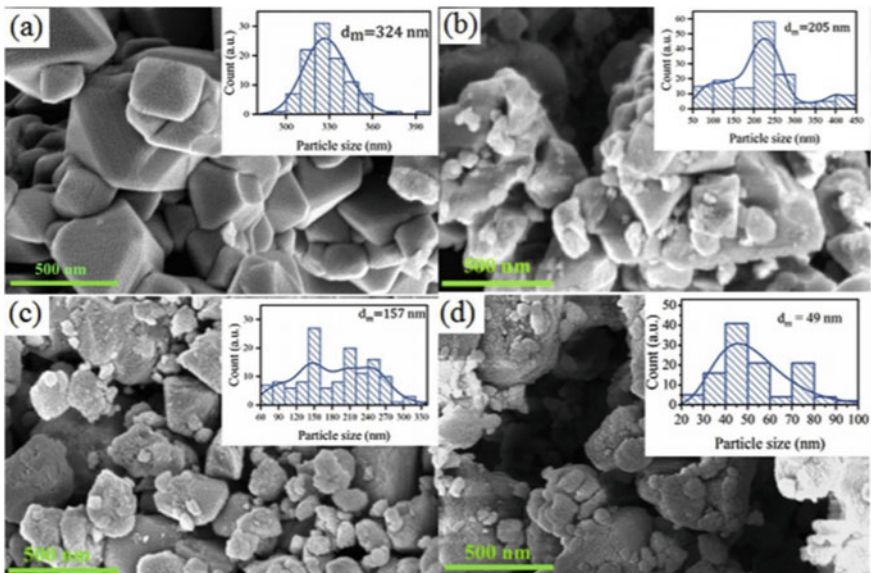


Fig. 2 FESEM images of **a** un-milled sample, **b** low energy milled, **c** medium energy milled and, **d** high energy milled samples, insets show the histograms of size distribution [19]. Reprinted with permission from Elsevier

Ahmed et al. [23] used various ways to synthesize Mn ferrite. They reported the effects of various preparation procedures on morphological parameters. The results show that the citrate approach yields the smallest lattice parameter and particle size (14.1 nm), whereas the ceramic approach yields the greatest values. The citrate and flash approaches yielded the smallest nanosizes (14.1 and 40.7 nm, respectively). Mechanical alloying is a perfect substitute for the solid-state approach, with the additional benefit of reducing milling time. Apart from its practicality, this technology allows for the rapid manufacturing of nanocomposites, advanced ceramics, amorphous alloys, metastables, and other significant powders in large quantities are obtained. The procedure is simple and quick to get the desired outcome in a short amount of time [24–28]. As a result, it can help you save time and energy. Because of these advantages, we determined to use this method to make ferrite nanoparticles [26–28].

2.2 Sol–Gel Method

The sol–gel synthesis technique is a wet chemical synthesis method in which reaction starts with precursor solution and chelating agents which results in the formation of gel (an interconnected network). Metal nitrates and metal alkoxides are commonly utilized as precursors. Metal hydroxide chains are formed in solution connecting metal centers with hydroxo (M–OH–M) or oxo (M–O–M) links, resulting in metal-hydroxo or metal-oxo chains. As a result, the sol develops into a gel-like diphasic system that includes both solid and liquid phases with morphologies ranging from discrete particles to extensive polymer networks. Temperature, pH, the concentration of metal ions precursor solution, and other chemical conditions influence the relative rates of hydrolysis and condensation. Because of the change in porosity of the gel, a change in pH has a significant impact on the surface properties of the synthesized samples. Srivastava et al. [29] used sol–gel and hydrothermal techniques to make nickel ferrite nanoparticles. The NiFe_2O_4 nanoparticles were manufactured using a hydrothermal method at a low temperature of 160 °C, and their particle size was smaller (9 nm) than that of the sol–gel method (~27 nm). As demonstrated in Fig. 3, NiFe_2O_4 nanoparticles synthesized by the sol–gel technique have a ferromagnetic behavior with a saturation magnetization of 31 emu/g, but those synthesized by the hydrothermal process have a superparamagnetic behavior with a saturation magnetization of 46 emu/g. Using a simple one-pot sol–gel auto-combustion method, a series of $\text{SrFe}_{10}\text{Al}_2\text{O}_{19}/\text{Co}_{0.8}\text{Ni}_{0.2}\text{Fe}_2\text{O}_4$ hard/soft nanocomposite ferrites with different weight percent of soft phase have been effectively fabricated. They had a single smooth hysteresis loop, according to the magnetic data. A linear increase in the Mr/Ms ratio for nanocomposites formed from the one-pot sol–gel technique with soft phase content up to 15% wt% indicates the strongest exchange coupling in this specimen. However, as the soft phase content, as well as composites, is manufactured using the physical mixing approach, this ratio is reduced and indicating that the exchange coupling between the hard and soft phases is not completely understood.

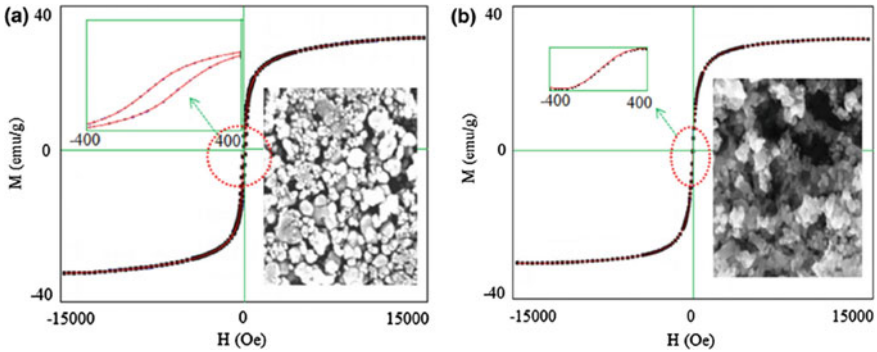


Fig. 3 M versus H for NiFe₂O₄ nanoparticles synthesized by a sol-gel method and b hydrothermal technique [29]. Reprinted with permission from Elsevier

The dominance of dipolar contact in the soft phase over exchange interaction between hard-soft phases in nano-composites resulted in a continual drop of coercivity as the soft phase incremented. The one-pot sol-gel autocombustion approach appears to be a straight forward but effective way for producing hard/soft ferrite nanocomposites with good magnetic properties [30]. In comparison to its solid-state equivalent, nano-sized NiFe₂O₄ particles manufactured by the sol-gel technique could be sintered at a lower temperature [31]. When compared to coarse-grained powder produced from the solid-state reaction procedure, NiFe₂O₄ nanoparticles have a substantially better sintering performance. On the other side, the Ms value of NiFe₂O₄ nanoparticles was lower than that of the coarse-grained equivalents and reduced the grain size. When the grain size was 15 nm, the coercivity of the samples reached a maximum value, and then reduced when the grain size was increased further.

2.3 Hydrothermal Method

In the hydrothermal synthesis method, soluble salts containing both types of cations i.e. divalent and trivalent (Fe³⁺) transition metal salts are macerated and combined in a 1:2 mol ratio. To produce a homogenous solution, an organic solvent such as ethylene glycol is introduced drop-wise into the combination of the aqueous solution while vigorously stirring.

The solution is then subjected to a high-pressure autoclave. The type of ferrite nanoparticles required influences the heating time and temperature. The following is an example of Fe₃O₄ nanoparticles synthesis: A solution of ferrous and ferric salt in sodium oleate was used to make Fe₃O₄ nano-particles. The various mole ratios of SO: Fe is employed in a hydrothermal method at 230 °C for 3 h [32]. With the smallest oleate concentration, i.e., SO: Fe of 0.05, homogeneity in size distribution and shape of NPs was obtained. The loss of magnetization (Ms value) and when

the SO: Fe mole ratio rises from 0 to 0.5, an average particle size appears. The hydrothermal synthesis method is a potential method for producing FNPs on a big scale. Using an adequate solvent mixture and changing factors like time, temperature, and pressure, high-quality NP synthesis might be produced. Koseoglu et al. fabricated $Mn_xCo_{1-x}Fe_2O_4$, where $x = 0.0, 0.2, 0.4, 0.6, 0.8$ and 1.0 by hydrothermal method. With sizes ranging from 14 to 22 nm, $CoFe_2O_4$ nanoparticles contain a single spinel structure[33]. On the other hand, Wang et al. reported that at a low temperature of 160 °C, well-crystallized BFO nanoparticles (hard ferrite) with an average size of around 10 nm were successfully produced using a hydrothermal technique aided by PVA. Three different processes were used to make manganese ferrite nanoparticles ($MnFe_2O_4$): co-precipitation, sol–gel, and hydrothermal method [34]. The average size of sol–gel is 45, 36 nm for co-precipitation, and 16 nm for hydrothermal samples was determined using X-ray diffraction data, which was consistent with FESEM pictures. They reported the effect of the different preparation methods on the particle size and magnetic properties. Safi al. [35] prepared $CoFe_2O_4$ nanoparticles by co-precipitation, sol–gel auto-combustion, and hydrothermal method (Fig. 4). For the co-precipitation and combustion techniques, FE-SEM micrographs demonstrated the creation of particles with average sizes of 39 nm and 617 nm, respectively. In the FE-SEM micrograph of a hydrothermal sample, there are rod-like grains with a maximum size of 139 nm and a breadth of 35 nm. In addition to this spherical nanoparticle with a particle size of 34 nm can be seen. Also, it is found that crystallite size has a greater impact on magnetic properties.

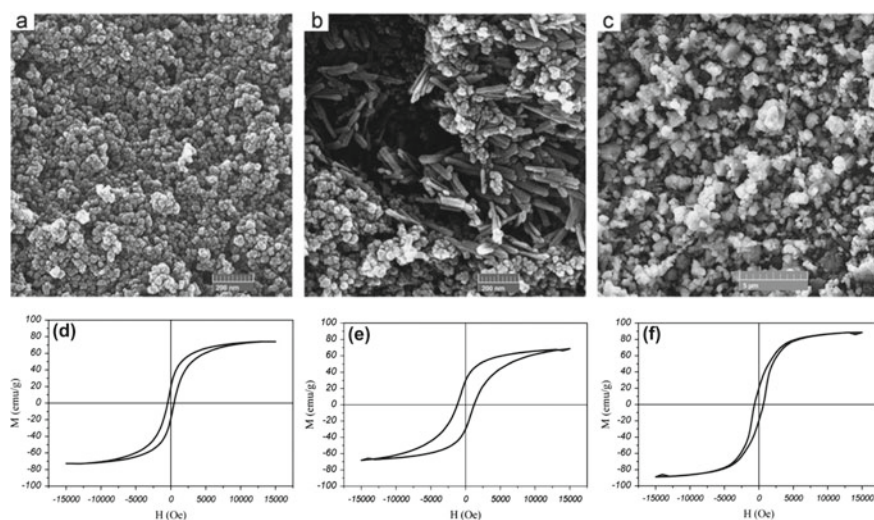
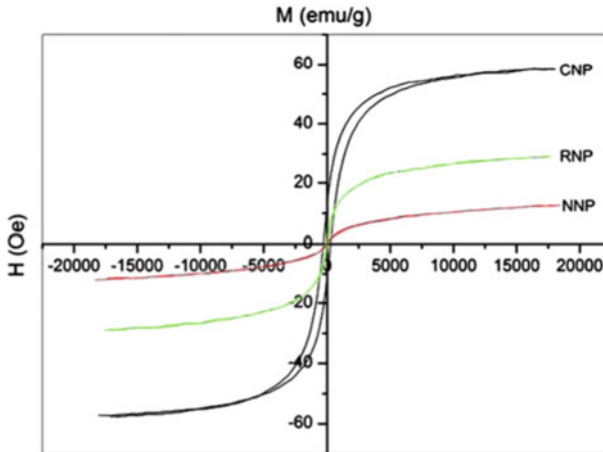


Fig. 4 FE-SEM and VSM micrograph of $CoFe_2O_4$ nanoparticles synthesis by **a, d** co-precipitation, **b, e** hydrothermal, **c, f** combustion methods [35]. Reprinted with permission from Elsevier

2.4 Co-precipitation Method

Precipitation is the settling down of ordinarily soluble chemicals under the circumstances used by a precipitate. It entails precipitating needed hydroxides from a solution simultaneously for the precipitate to contain the required metals in the desired proportion. The synthesized solution is a mixture of dispersed precipitation agents like ammonium hydroxide or ammonium oxalate and oxalic acid that is used to precipitate the blended hydroxide or oxalate out of the solution. The final crystalline oxide is obtained by heating the precipitates at higher temperatures [31]. Many researchers have used the precipitation approach to make ferrites nanoparticles but were not limited to the following [31, 36, 37]. This method was used by Jahanbin et al. [37] to make a high-purity nickel-zinc ferrite. They claim that by using this process, they can create a spinel ferrite in a fraction of the time it takes to do so using the traditional method. In their studies, Gopal Reddy et al. [38] used a co-precipitation approach to manufacture nanoparticles Ni ferrite as a gas sensor to specifically detect chlorine in the air. A similar product was then manufactured by the citrate method. The single-phase Ni ferrite was generated at 600 °C for 4 h in both cases, according to their findings. In comparison to the sample developed by the citrate approach (crystallite size $\sim 275 \text{ \AA}$), the ferrite developed by the co-precipitation approach had a smaller crystallite size ($\sim 175 \text{ \AA}$). This implies that the sensitivity of the sensor made from Ni ferrite developed by co-precipitation is higher.

This is due to the fact that a smaller crystallite size means a bigger surface area exposed to the test gas, which enhances the possibility of gas–solid contact and hence the sensitivity. In another study, Sharifi et al. [39] prepared cobalt ferrite nanoparticles by three methods i.e. Normal micelles, Reverse micelles, and co-precipitation method and study their magnetic properties as shown in Fig. 5. In the co-precipitation process and nanoparticles are sintering at 1000 °C to make Cobalt ferrite; the ferrite crystallite size was determined to be in the 11.70 nm range. On the other hand, by using the normal micelles method crystallite size are 5.58 nm and in the case of the reverse micelles method, crystallite size is 7.63 nm. The coprecipitation sample's increased crystallinity could be another factor contributing to the higher saturation magnetization. The size of the nanoparticles has a significant impact on the sample's magnetic properties. To create ferrites nanoparticles using this approach, the chemical procedure must be carefully required to make sure that the hydroxides precipitate at the same time. Another disadvantage of this procedure is that the precipitates may form in a state that makes filtration or decantation problematic, causing contaminants by adsorbing some ions in the precipitate.



Method	M_s (emu/g)	M_r (emu/g)	H_c (Oe)	H_{max} (kOe)	t_{shell} (nm)
CNP	58.4	12.45	286.0	18.0	0.74
NNP	12.6	0.17	23.7	18.4	0.80
RNP	29.4	0.84	25.2	17.6	0.87

Fig. 5 Shows the M–H curve of cobalt ferrite nanoparticles by three different methods (Normal micelles, Reverse micelles, and co-precipitation method) [39]. Reprinted with permission from Elsevier

2.5 Chemical Vapor Deposition Method

Chemical vapor deposition, popularly known as CVD is an economic industrial technology technique for mass-producing carbon nanotubes, known for outstanding performance in a variety of sectors, particularly in green technologies such as energy storage devices, green composites, and solar cells also. To manufacture a very pure nanostructural thin film with great performance, a chemical vapor deposition approach is applied. The precursor is located on the surface of a substrate by heating followed by evaporation to generate vapor, and the condensation happens through a chemical reaction under vacuum, resulting in a chemical difference between the precursor material and the product. After introducing the surface of a substrate to the vaporized precursor, a template is generated on the surface, which is then followed by the formation of nanostructures on that template [40]. The reaction temperature, reaction rate, and precursor concentration all facilitate the development of the nanostructure during the deposition process [41]. Ultimately, this technology allows for homogeneous nanostructure coating on the substrate surface, albeit there are certain limitations due to the process’s greater temperature requirement. For the synthesis of nanoparticles, iron, cobalt, and Fe–Co catalysts were produced using a traditional precipitation approach using CO₂ as the carbon precursor by catalytic chemical vapor

deposition [42]. The Fe–Co nanoparticles were synthesized in a thermogravimetric analyzer at temperatures ranging from 450 to 1000 °C. At various temperatures, pebble-like nanoparticles with some connected forms were discovered for Fe, Co, and Fe–Co. It was also discovered that increasing the temperature not only increased the size of the nanoparticles while vastly improving their sphericity and crystallinity. The sizes of nanoparticles in Fe–Co alloy were found to be 51 ± 1 nm, 54 ± 1 nm, 72 ± 1 nm, and 165 ± 1 nm at 500, 600, 700, and 800 °C, respectively, using FESEM (Fig. 6). The results of TEM and FESEM are very comparable. Increased temperature leads to larger particle size, sphericity, and crystallinity on Fe, Co, and Fe–Co catalysts in FESEM. On the other side, particles at low temperatures are small and amorphous. In a CVD reaction carried out directly on spinel ferrite nanoparticles MFe_2O_4 ($M = Co, Cu, Ni, Mn, Fe, \text{ or } Zn$) supported on a 316 grade SS foil, several morphologies of carbon nanomaterials were generated [43]. Polymorphic carbons (PNCs) with varying forms and sizes were discovered to be the acquired components in each ferrite. The creation of spherical carbon nanoparticles was not catalyzed by zinc and cobalt zinc ferrites, according to the findings.

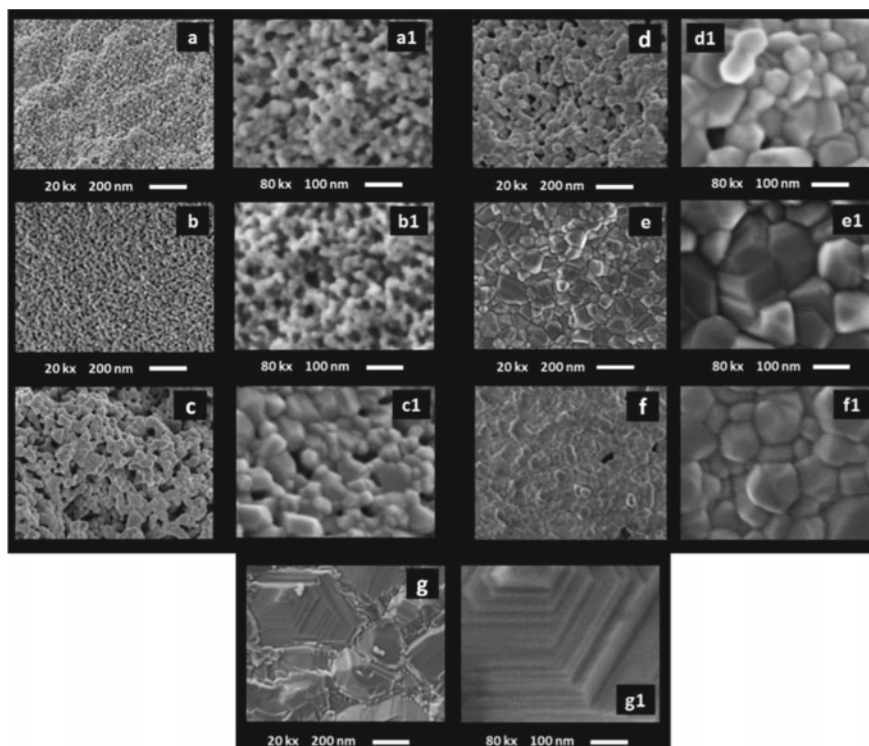


Fig. 6 FESEM images (20 & 80 kx) of the carbon-encapsulated Fe–Co nano-particles synthesized under CO_2 environment at **a** 450 °C, **b** 500 °C, **c** 600 °C, **d** 700 °C, **e** 750 °C, **f** 800 °C, **g** 1000 °C [42]. Reprinted with permission from Elsevier

2.6 Microwave-Assisted Method

The newly established microwave-assisted approach can be used to make multi-functional nanoparticles [44]. Energy is given directly to specified materials in this method via chemical interactions with electromagnetic radiations (EMR). Heat is formed when electromagnetic energy is converted to thermal energy. The temperature of the technique typically varies from 100 to 200 over a short period. A Teflon vessel is linked to an exhausting drain to remove the vapors released during the heating process [45–47]. The narrow-sized distribution of FNPs can be manufactured in a short period, with great consistency and high quality at a low cost for industrial use. CoFe_2O_4 , $\gamma\text{-Fe}_2\text{O}_4$, and Fe_2O_4 are some of the FNPs made with this approach. In the microwave-assisted approach, improved multimode equipment has been developed. Microwave-assisted synthesis of FNPs is commonly utilized on a large scale, however, it results from slow growth when compared to hydrothermal, thermal decomposition, and co-precipitation techniques [48]. The microwave-assisted method was used to create ferrite nanoparticles of various particle sizes by adjusting the reaction temperature which is highly magnetic in nature [49]. The iron oxide nanoparticles were made at two distinct temperatures, 45 and 85 °C. The average size of FeO nanoparticles generated at 45 and 85 °C was found to be 10 and 13.8 nm, respectively, with superparamagnetic activity at ambient temperature. The decrease in supersaturation at high temperatures is responsible for the increase in particle size and saturation magnetization values with increasing reaction temperature. The size of the nanoparticles can be controlled by adjusting the reaction temperature within the microwave reactor, according to Kalyani et al. [49].

2.7 Solution Combustion Method

The combustion process has the advantage of ensuring less energy and time. This strategy is both quick and adaptable. This process has been used by several researchers to make ferrites nanoparticles. In the basic approach, metal nitrate and iron nitrate are used as oxidizers, and glycine is used as a fuel [50]. In 50 mL of distilled water, a sufficient amount of nitrates and glycine were dissolved and allowed to combine magnetically with the solution. The oxidizer to fuel ratio was kept constant at 1:1, and the mixture was heated to 80 °C with constant stirring. After 4 h of active stirring at 80 °C, a brownish gel was generated. The gel was dried at 120 °C before being burned into a loose gigantic powder by self-propagating combustion. The gigantic powder was ground with an agate motor and pestle, and the fine powder was calcined at 750 °C [51]. Dhiman et al. fabricated $\text{Mg}_{0.5-x}\text{Cu}_x\text{Zn}_{0.5}\text{Fe}_2\text{O}_4$ ($x = 0, 0.01 \text{ \& } 0.02$) by solution combustion method. Cu Doped Mg–Zn ferrites have lower recombination and higher charge flow, according to PL and EIS studies [52]. Mazroueiet al. [53] prepared cobalt ferrite nanoparticles by solution combustion technique using glycine and urea as a fuel. Tad increased the procedure of the solution combustion method by

raising the weight % of additional fuel, according to thermodynamic calculations, resulting in the formation of crystallites in products and a rise in crystallite size. As predicted, raising the weight percentage of additional fuel extended the range of saturation magnetization in the samples. The percentage of magnetism in urea-produced samples was lowered due to the superparamagnetic behavior of the particle fraction. The glycine-derived samples also exhibited a hard ferrimagnetic property. It can be observed that the solution combustion method should be utilized to make cobalt ferrite nanoparticles with a particle size less than 100 nm and that if glycine is employed, the minimum quantity of fuels must be two times the stoichiometric amount [53].

2.8 *Electrochemical Method*

The electrochemical manufacturing approach is related to the coprecipitation approach, except that the ion sources are created by scarification of anode electrodes during oxidation. The ions react through the interface between two electrodes and create the appropriate ferrite nanoparticles when the anode electrode is firstly oxidized and discharged into the surfactant solution. Several of the advantages of electrochemical synthesis over other fabrication techniques are the high purity of the reagent and command of particle size. The purity and desired particle size can be accomplished by adjusting the active power or regulating the distance between the electrodes. By minimizing the difference between the electrodes, the crystallinity of the particles might be maintained. The particle size continues to rise when the current density and the distance between electrodes are increased at the same time [54]. This is attributed to the reason that the closer the electrodes are, the quicker the reduction-oxidations take place, releasing more oxidized metal ions into the solvent, resulting in a higher rate of nanoparticles production. Electrochemical synthesis is a straightforward, low-cost, ecologically friendly, and cost-effective approach [55]. Cabrera et al. employed pure iron as the anode and an amine as the surfactant to preclude agglomeration in the fabrication of Fe_3O_4 nanoparticles with size between 20 and 30 nm and obtained a yield of over 80% [56]. Mazario et al. [57] fabricated cobalt ferrite nanoparticles by electrochemical method. The relationship between structure, composition, and magnetic characteristics has been studied as a function of synthesis temperature. Temperature is an essential variable that has a direct relationship with cobalt alteration in the spinel structure. The CoFe_2O_4 was obtained with a Fe: Co ratio of 2 at the greatest temperature; in fact, the proportion of inverse of this sample is quite close to 100%. As a result, the structure so created was an inverse spinel cobalt ferrite, with larger particles as the synthesis temperature rises [57].

2.9 Sonochemical Method

The sonochemical approach has been demonstrated to be an effective way to synthesize Fe_3O_4 and $\gamma\text{-Fe}_2\text{O}_3$ FNPs [58, 59]. Bubbles are formed in the solvent medium throughout ultrasonic irradiation and can successfully concentrate the diffuse energy of ultrasound; when the bubble collapses, a large amount of energy is released, which heats the contents of the bubble. This results in a temporary localized hot spot with an equivalent temperature and pressure inside the bubbles of around 5000 K and 1000 bars, respectively, and heating and air conditioning rates of $>10^{10} \text{ K}_S^{-1}$. These unusual circumstances allow access to a variety of chemical processes that are ordinarily unavailable [60]. The particle content predicted to be synthesized using the sonochemical approach is equivalent to the content of the vapor in the bubbles, which aids in NP purity control [44]. Various types of NPs, such as alloys, FNPs, carbides, and catalysts, are widely synthesized using this approach. For example, air-stable $\text{Fe}_3\text{O}_4/\text{Au}$ [61], Fe_3O_4 [62–64], monodisperse non-aggregated $\text{Fe}_3\text{O}_4@\text{SiO}_2$ [65], $\gamma\text{-Fe}_2\text{O}_3$ [66], and $\text{Cu Fe}_2\text{O}_4$ [67] have all been synthesised using this technique. The sonochemical approach was used to successfully produce NiFe_2O_4 NPs. Reversible electrode reactions and significant charge transfer resistance were observed in the NiFe_2O_4 electrode. For sensor experiments, the NPs can be easily formed into a robust electrode to monitor paracetamol oxidation and reduction. The electrode's strong conductivity in 0.1 M HCl and low charge-transfer resistance were validated by electrochemical impedance tests (Fig. 7). The findings indicate that NiFe_2O_4 produced via sonochemistry is an excellent content for energy storage devices, batteries, sensors, and organic dye degradation [68].

2.10 Thermal Decomposition

Hydrothermal [69–76], microwave [74, 77, 78], solvothermal [77, 79–82], mechano-thermal [83, 84], and seed-hydrothermal [83] are just a few of the chemical techniques that have been used to create the thermal chemical treatment for manufacturing ferrite nanoparticles. Iron salts, such as iron nitrate nono-hydrated or iron chloride Hexa-hydrated are utilized in each of these procedures. Salt is mixed in water or another suitable solvent with help of magnetic stirring. The pH of the solution is controlled between 7 and 12 based on the metal salt. The sample is poured in an autoclave and heated for 12–24 h, then allowed to cool to room temperature naturally. Purification or centrifugation is used to collect the solid, which is then cleaned and dried overnight at 60 °C. Rather than dissolving, the precursor compounds are crushed in a ball mill, using a similar mechano-thermal processing mechanism. Metal oxide (M_2O_3) with iron salt is used in the seed-hydrothermal process. The two compounds are placed in an autoclave and heated according to the preceding process.

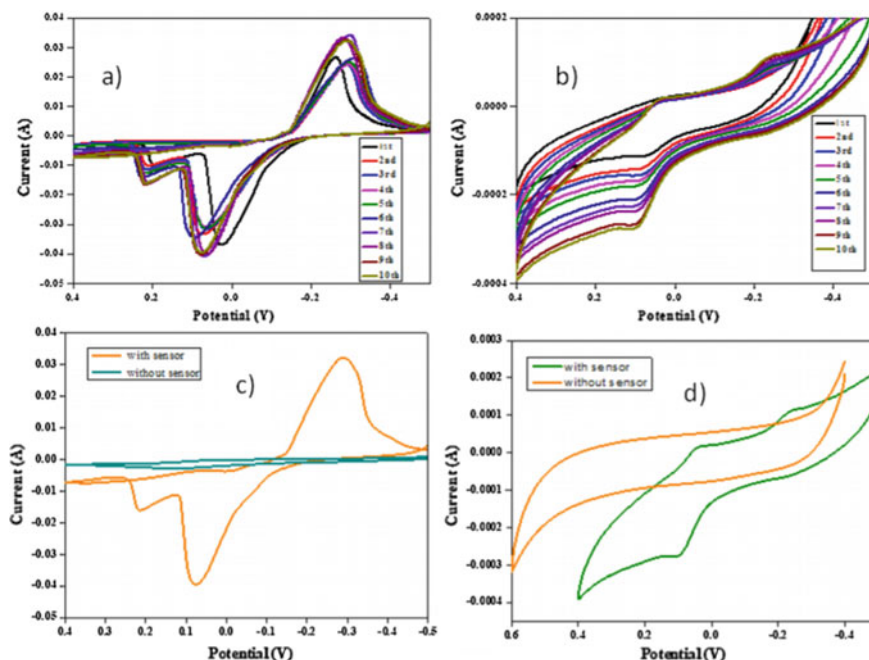


Fig. 7 a) 0.1 M HCl, b) 0.1 M NaOH, c) comparison of CV for NiFe_2O_4 electrode with and without paracetamol in 0.1 M HCl and d) 0.1 M NaOH cyclic voltammetry sensitivity for the NiFe_2O_4 electrode at various sensors concentrations [68]. Reprinted with permission from Elsevier

Adriana et al. [85] prepared Co-ferrite nanoparticles with the help of thermal decomposition technique, oleate was used as a precursor. Figure 8a–c shows exemplary pictures of fabricated cobalt ferrite nanoparticles, demonstrating the development of distinct nanoparticles with limited size distribution and sizes of 12 ± 2 nm for sample 2D, 14 ± 2 nm for sample 14D, and 14 ± 5 nm for sample 30D. The ageing period of the iron-cobalt oleate precursor affects the crystallinity of the produced nanoparticles. Magnetic properties are expected to be changed in the same way. The results of the magnetic property are shown in Fig. 8d–f.

2.11 Microemulsion Method

Surfactant molecules stabilized, two thermodynamically isotropic and very immiscible type liquids often utilized in this technique. Polyoxyethylene ethers have been used as a non-ionic surfactant, n-hexane as an oil phase, and n-butanol as a co-surfactant, which have all been identified [86]. The synthesis variety of ferrite nanoparticles by altering the kind of surfactant, co-surfactant, oil–water ratio, and reaction conditions are one of the major benefits of the microemulsion synthesis

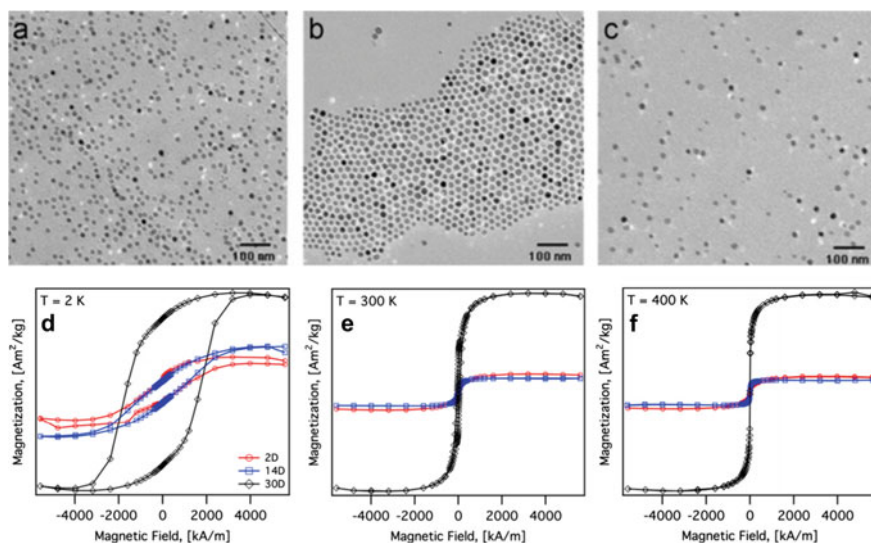


Fig. 8 a–c TEM images and d–f Magnetization of cobalt ferrite nanoparticles [85]. Reprinted with permission from Elsevier

process [87]. Another great benefit of the microemulsion process [88] is the ability to adjust the size of the particles produced. Due to the sluggish nucleation rate at low reaction temperatures, the NPs formed are sometimes less crystalline and more polydispersed, which is a major disadvantage of this process [89].

Ali et al. [90] prepared $\text{Mg}_{1-x}\text{Ca}_x\text{Ni}_y\text{Fe}_{2-y}\text{O}_4$ by microemulsion technique and annealed at 700 °C for 7 h. The synthesized samples had crystallite sizes ranging from 29 to 45 nm (Fig. 9). As seen in Table 1, the saturation magnetization (M_s) rises and subsequently falls, whereas the coercivity (H_c) increases constantly with increasing dopant concentration.

A simple, efficient, and consistent microemulsion approach was used to deposit magnetic monodisperse ferrite $\text{Ni}_{1-x}\text{Co}_x\text{Fe}_2\text{O}_4$ nanostructures on the sidewall of carbon nanotubes. The results showed that a considerable number of high purity magnetic ferrite nanoparticles with sizes ranging from 15 to 25 nm were uniformly adorned on the surface of carbon nanotubes. The $\text{Ni}_{1-x}\text{Co}_x\text{Fe}_2\text{O}_4/\text{CNTs}$ nanocomposites had a maximum saturation magnetization value of 44.21 emu/g. These magnetic ferrite/CNT nanocomposites could be used in a variety of fields, including biomedicine and electromagnetic devices [91].

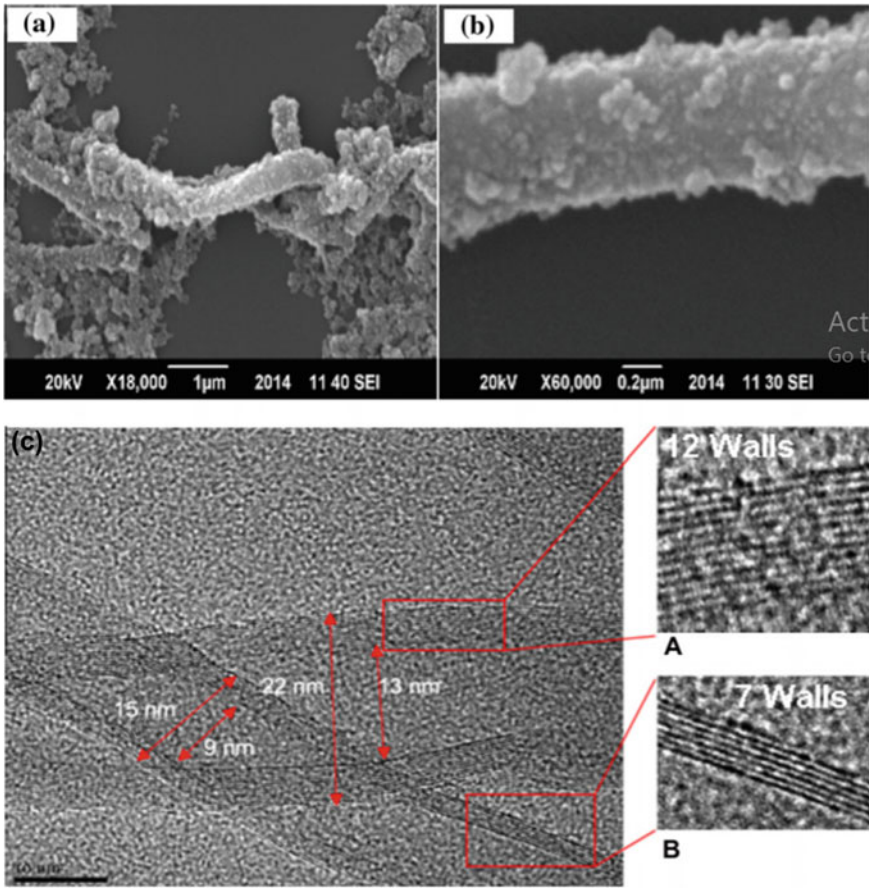


Fig. 9 a–b SEM and c HRTEM image of f $\text{Ni}_{0.5}\text{Co}_{0.5}\text{Fe}_2\text{O}_4$ nanoparticles coated CNTs [91]. Reprinted with permission from Elsevier

Table 1 $\text{Mg}_{1-x}\text{Ca}_x\text{Ni}_y\text{Fe}_{2-y}\text{O}_4$ nano-ferrites with distinct magnetic parameters [90]

Magnetic parameters	$x = 0$ $y = 0$	$x = 0.2$ $y = 0.4$	$x = 0.4$ $y = 0.8$	$x = 0.8$ $y = 1.2$
Magnetization	9.84	24.99	20.44	19.89
Retentivity	1.32	3.65	3.83	3.79
Coercivity	94.44	98.97	136.32	153.08
$R^2 = (Mr/Ms)$	0.13	0.14	0.18	0.19

Reprinted with permission from Elsevier

3 Synthetic Approaches Are Compared

The efficiency of ferrite nanoparticles is influenced by the synthesis methods, the kind of precursor, and the solvent employed. Basically, diverse synthesis strategies are frequently used with varying parameters; hence no well-recommended synthesis method for ferrite nanoparticles has been identified. However, owing to their observations, different researchers' have different view points and perspectives. When the sonochemical, thermal decomposition, sol–gel, and hydrothermal synthesis approaches are compared, the hydrothermal method is proposed as the best choice for ferrite nanoparticles synthesis. This is because of benefits such as achieving desired shape and size, high crystallization, and homogeneous content [92]. Therefore, the hydrothermal approach promotes particle agglomeration reduction and allows for the creation of particles with a restricted size distribution, phase uniformity, and defined shape [44, 93]. According to Biswal et al. [94], the coprecipitation method is found to be the desired choice for manipulating the shape and characteristics of ferrite nanoparticles when compared to the others techniques. In comparison to other techniques, some researchers have praised sol–gel methods. For example, Xu et al. [95] highlighted that the sol–gel approach has numerous advantages over conventional manufacturing techniques for metal oxides, including good uniformity, cheap price, and high purity. The bulk quantity synthesis of monodispersed ferrites nanoparticles at the boundary of water and toluene was reported using a microwave-hydrothermal process under ideal circumstances, working with metal chloride or nitrate salts and oleic acid as a dispersion agent [96]. These techniques are also crucial for the monodisperse fabrication of metal ferrite nanoparticles with a size distribution of 5–10 nm. In comparison to hydrothermal, co-precipitation, and sol–gel procedures, Fajaroh et al. [54] claim that the electrochemical approach is preferred in terms of simply manipulating particle size by modifying the applied electro-oxidation current density or potential to the environment. However, it is problematic to identify one approach as the most optimal for ferrite nanoparticles manufacturing. The target product plays a big role in deciding the method to use for ferrite nanoparticles synthesis. Thermal decomposition method is suggested for shape and size-controlled NPs, while coprecipitation is chosen owing to its simplicity. Microemulsion is also recommended for monodispersed ferrite nanoparticles of diverse morphologies. The good thing about the quick reaction time is increased selectivity, enhanced yield percentage and softer reaction conditions make sonochemical and microwave irradiation emerging approaches. The findings indicate that nickel ferrite nanoparticles produced via sonochemical is an excellent content for energy storage devices, batteries, sensors, and organic dye degradation [68]. In comparative analysis to the other previously mentioned conventional techniques, sonochemical and microwave irradiation are different strategies that have been performed enormously today due to green claims and advantages, including less reaction times, mild process conditions, maximum yields, enhanced selectivity [97]. In general, the researcher's primary concern should be the technique to be used, and the technique to be used is influenced by the yield of NPs, their morphology, the operating circumstances, the size

and form of the NPs, the time and expense of the experiment. Solvent and surfactants choice, pH, and stirring rpm are all essential aspects. Another significant criterion for the high-quality production of ferrite nanoparticles in the desired quantity might be said to be the modification of the synthesis procedure. As a result, the benefits and drawbacks of certain techniques would not just be a criterion for their usage, because the technique's goal could vary. In general, there is still a need for more research into the cost-effective production of ferrite nanoparticles with regulated size and form and that there is no universal or optimum approach for the synthesis of ferrite nanoparticles.

4 Conclusions

Magnetic materials can be fabricated in nanoparticle form before being compacted and sintered, allowing them to be used at higher frequencies. The size, structure, microstructure, magnetic behavior, electrical conductivity, and other characteristics of the desired product all influence by the ferrite synthesis method adopted. One can prepare the desired product by carefully selecting a synthesis strategy and maintaining the necessary circumstances. The qualities of ferrite are largely determined by the method and conditions used to prepare it. As a result, the purpose of this research was to present various ways of producing nano-crystalline ferrites. Furthermore, the microstructure aspects of the sample, such as grain size distribution, strain, and porosity of sample are highly dependent on the type of preparation strategies employed and play a vital role in the sample's magnetic properties, are highlighted. The most frequently used synthesis fabrication with their advantages and some limitations are also discussed.

References

1. P. Ravindranathan, K. Patil, *J. Mater. Sci.* **22**, 3261–3264 (1987)
2. S. Bid, S. Pradhan, *Mater. Chem. Phys.* **82**, 27–37 (2003)
3. A. Verma, O. Thakur, C. Prakash, T. Goel, R. Mendiratta, *Mater. Sci. Eng. B* **116**, 1–6 (2005)
4. R. Kambale, P. Shaikh, S. Kamble, Y. Kolekar, *J. Alloy. Compd.* **478**, 599–603 (2009)
5. V. Šepelák, I. Bergmann, A. Feldhoff, P. Heitjans, F. Krumeich, D. Menzel, F.J. Litterst, S.J. Campbell, K.D. Becker, *J. Phys. Chem. C* **111**, 5026–5033 (2007)
6. S. Patange, S.E. Shirsath, B. Toksha, S.S. Jadhav, K. Jadhav, *J. Appl. Phys.* **106**, 023914 (2009)
7. J. Ding, X. Liu, J. Wang, Y. Shi, *Mater. Lett.* **44**, 19–22 (2000)
8. H. Bayrakdar, *J. Alloy. Compd.* **674**, 185–188 (2016)
9. C.A. Stergiou, G. Litsardakis, *J. Magn. Magn. Mater.* **405**, 54–61 (2016)
10. A. Verma, R. Chatterjee, *J. Magn. Magn. Mater.* **306**, 313–320 (2006)
11. M. George, A.M. John, S.S. Nair, P. Joy, M. Anantharaman, *J. Magn. Magn. Mater.* **302**, 190–195 (2006)
12. A.A. Hossain, S. Mahmud, M. Seki, T. Kawai, H. Tabata, *J. Magn. Magn. Mater.* **312**, 210–219 (2007)

13. P. Gao, X. Hua, V. Degirmenci, D. Rooney, M. Khraisheh, R. Pollard, R.M. Bowman, E.V. Rebrov, J. Magn. Magn. Mater. **348**, 44–50 (2013)
14. N. Ichinose, Y. Ozaki, S. Kashu, *Superfine Particle Technology* (Springer Science & Business Media, 2012)
15. P. Saravanan, R. Gopalan, V. Chandrasekaran, Defence Sci J **58** (2008)
16. C. Rao, J. Gopalakrishnan, E. Banks, Phys. Today **41**, 112 (1988)
17. J. Chand, M. Singh, J. Alloy. Compd. **486**, 376–379 (2009)
18. T. Kundu, S. Mishra, Bull. Mater. Sci. **31**, 507–510 (2008)
19. V. Mahdikhah, A. Ataie, A. Babaei, S. Sheibani, C.W. Ow-Yang, S.K. Abkenar, J. Phys. Chem. Solids **134**, 286–294 (2019)
20. S. Bera, A. Prince, S. Velmurugan, P. Raghavan, R. Gopalan, G. Panneerselvam, S. Narasimhan, J. Mater. Sci. **36**, 5379–5384 (2001)
21. V. Berbenni, C. Milanese, G. Bruni, A. Girella, A. Marini, Zeitschrift für Naturforschung B **65**, 1434–1438 (2010)
22. E.N. Lysenko, E.V. Nikolaev, A.P. Surzhikov, IOP Conf. Ser.: Mater. Sci. Eng. (IOP Publishing), 012092 (2016)
23. M. Ahmed, N. Okasha, S. El-Dek, Nanotechnology **19**, 065603 (2008)
24. X. Jiang, M.A. Trunov, M. Schoenitz, R.N. Dave, E.L. Dreizin, J. Alloy. Compd. **478**, 246–251 (2009)
25. M. Jalaly, M. Enayati, F. Karimzadeh, P. Kameli, Powder Technol. **193**, 150–153 (2009)
26. A. Hajalilou, M. Hashim, H.M. Kamari, J. Mater. Sci.: Mater. Electron. **26**, 1709–1718 (2015)
27. A. Hajalilou, M. Hashim, R. Ebrahimi-Kahrizangi, H.M. Kamari, J. Therm. Anal. Calorim. **119**, 995–1000 (2015)
28. A. Hajalilou, M. Hashim, R. Ebrahimi-Kahrizangi, N. Sarami, Ceram. Int **40**, 5881–5887 (2014)
29. M. Srivastava, S. Chaubey, A.K. Ojha, Mater. Chem. Phys. **118**, 174–180 (2009)
30. S. Torkian, A. Ghasemi, R.S. Razavi, J. Magn. Magn. Mater. **416**, 408–416 (2016)
31. C. Zhang, X. Zhong, H. Yu, Z. Liu, D. Zeng, Phys. B **404**, 2327–2331 (2009)
32. T. Taniguchi, K. Nakagawa, T. Watanabe, N. Matsushita, M. Yoshimura, J. Phys. Chem. C **113**, 839–843 (2009)
33. Y. Köseoğlu, F. Alan, M. Tan, R. Yilgin, M. Öztürk, Ceram. Int. **38**, 3625–3634 (2012)
34. L.A. Kafshgari, M. Ghorbani, A. Azizi, Part. Sci. Technol. (2018)
35. R. Safi, A. Ghasemi, R. Shoja-Razavi, E. Ghasemi, T. Sodaee, Ceram. Int. **42**, 6375–6382 (2016)
36. D. Makovec, A. Kodre, I. Arčon, M. Drogenik, J. Nanopart. Res. **11**, 1145–1158 (2009)
37. T. Jahanbin, M. Hashim, K.A. Mantori, J. Magn. Magn. Mater. **322**, 2684–2689 (2010)
38. C.G. Reddy, S. Manorama, V. Rao, Sens. Actuators B: Chem. **55**, 90–95 (1999)
39. I. Sharifi, H. Shokrollahi, M.M. Doroodmand, R. Safi, J. Magn. Magn. Mater. **324**, 1854–1861 (2012)
40. L. Filippini, D. Sutherland, I.N. Center, NANOYOU teachers training kit in nanoscience and nanotechnologies (2010), (pp. 1–29)
41. C.S. Kim, K. Okuyama, K. Nakaso, M. Shimada, J. Chem. Eng. Jpn. **37**, 1379–1389 (2004)
42. M.F. Irfan, A. Arami-Niya, Nano-Struct. Nano-Objects **18**, 100261 (2019)
43. V. Dhand, G. Mittal, K.Y. Rhee, S.-J. Park, Int. J. Precis. Eng. Manufact-Green Technol. **4**, 441–451 (2017)
44. K.K. Kefeni, T.A. Msagati, B.B. Mamba, Mater. Sci. Eng. B **215**, 37–55 (2017)
45. L. Gonzalez-Moragas, S.-M. Yu, N. Murillo-Cremaes, A. Laromaine, A. Roig, Chem. Eng. J. **281**, 87–95 (2015)
46. A.S. Bhatt, D.K. Bhat, C.-w. Tai, M.S. Santosh, Mater. Chem. Phys. **125**, 347–350 (2011)
47. W. Wu, Z. Wu, T. Yu, C. Jiang, W.-S. Kim, Sci. Technol. Adv. Mater. (2015)
48. M. Zahid, N. Nadeem, M.A. Hanif, I.A. Bhatti, H.N. Bhatti, G. Mustafa, *Magnetic Nanostructures* (Springer, 2019), (pp. 181–212)
49. S. Kalyani, J. Sangeetha, J. Philip, J. Nanosci. Nanotechnol. **15**, 5768–5774 (2015)

50. P. Dhiman, T. Mehta, A. Kumar, G. Sharma, M. Naushad, T. Ahamad, G.T. Mola, *Adv. Powder Technol.* (2020)
51. P. Dhiman, A. Kumar, M. Shekh, G. Sharma, G. Rana, D-VN. Vo, N. AlMasoud, M. Naushad, Z.A. A.L. Othman, *Environ. Res.* **197**, 111074 (2021)
52. P. Dhiman, M. Patial, A. Kumar, M. Alam, M. Naushad, G. Sharma, D-VN. Vo, R. Kumar, *Mater. Lett.* **284**, 129005 (2021)
53. A. Mazrouei, A. Saidi, *Mater. Chem. Phys.* **209**, 152–158 (2018)
54. F. Fajaroh, H. Setyawan, W. Widiyastuti, S. Winardi, *Adv. Powder Technol.* **23**, 328–333 (2012)
55. D. Ramimoghadam, S. Bagheri, S.B. Abd Hamid, J. Magn. Magn. Mater. **368**, 207–229 (2014)
56. L. Cabrera, S. Gutierrez, N. Menendez, M. Morales, P. Herrasti, *Electrochim. Acta* **53**, 3436–3441 (2008)
57. E. Mazario, M. Morales, R. Galindo, P. Herrasti, N. Menendez, *J. Alloy. Compd.* **536**, S222–S225 (2012)
58. K.V. Shafi, A. Ulman, X. Yan, N.-L. Yang, C. Estournès, H. White, M. Rafailovich, *Langmuir* **17**, 5093–5097 (2001)
59. K.V. Shafi, A. Ulman, A. Dyal, X. Yan, N.-L. Yang, C. Estournès, L. Fournès, A. Wattiaux, H. White, M. Rafailovich, *Chem. Mater.* **14**, 1778–1787 (2002)
60. J.H. Bang, K.S. Suslick, *Adv. Mater.* **22**, 1039–1059 (2010)
61. W. Wu, Q. He, H. Chen, J. Tang, L. Nie, *Nanotechnology* **18**, 145609 (2007)
62. S. Zhu, J. Guo, J. Dong, Z. Cui, T. Lu, C. Zhu, D. Zhang, J. Ma, *Ultrason. Sonochem.* **20**, 872–880 (2013)
63. R.A. Mukh-Qasem, A. Gedanken, *J. Colloid Interface Sci.* **284**, 489–494 (2005)
64. A. Pradhan, R.C. Jones, D. Caruntu, C.J. O'Connor, M.A. Tarr, *Ultrason. Sonochem.* **15**, 891–897 (2008)
65. A.-L. Morel, S.I. Nikitenko, K. Gionnet, A. Wattiaux, J. Lai-Kee-Him, C. Labrugere, B. Chevalier, G. Deleris, C. Petibois, A. Brisson, *ACS Nano* **2**, 847–856 (2008)
66. S. Zhang, Y. Zhang, Y. Wang, S. Liu, Y. Deng, *Phys. Chem. Chem. Phys.* **14**, 5132–5138 (2012)
67. W.-Z. Lv, B. Liu, Z.-K. Luo, X.-Z. Ren, P.-X. Zhang, *J. Alloys Compd.* **465**, 261–264 (2008)
68. M.S. Amulya, H. Nagaswarupa, M.A. Kumar, C. Ravikumar, S. Prashantha, K. Kusuma, *Appl. Surf. Sci. Adv.* **1**, 100023 (2020)
69. Y. Li, X.-T. Wang, X.-Q. Zhang, X. Li, J. Wang, C.-W. Wang, *Phys. E: Low-Dimens. Syst. Nanostruct.* **118**, 113865 (2020)
70. K. Wang, X. Xu, L. Lu, H. Wang, Y. Li, Y. Wu, J. Miao, J.Z. Zhang, Y. Jiang, *ACS Appl. Mater. Interfaces* **10**, 12698–12707 (2018)
71. J.A. Darr, J. Zhang, N.M. Makwana, X. Weng, *Chem. Rev.* **117**, 11125–11238 (2017)
72. S-M. Lam, M-W. Kee, K-A. Wong, Z.H. Jaffari, H-Y. Chai, J-C. Sin, *MXenes: Appl.* **51**, 20–60 (2019)
73. X. Wang, W. Mao, Q. Wang, Y. Zhu, Y. Min, J. Zhang, T. Yang, J. Yang, Xa. Li, W. Huang, *RSC Adv.* **7**, 10064–10069 (2017)
74. K. Suzuki, Y. Tokudome, H. Tsuda, M. Takahashi, *J. Appl. Crystallogr.* **49**, 168–174 (2016)
75. Q. Zhang, D. Sando, V. Nagarajan, *J. Mater. Chem. C* **4**, 4092–4124 (2016)
76. S. Li, Y.-H. Lin, B.-P. Zhang, Y. Wang, C.-W. Nan, *J. Phys. Chem. C* **114**, 2903–2908 (2010)
77. K. Chybczynska, M. Blaszyk, B. Hilczer, T. Lucinski, M. Matczak, B. Andrzejewski, *Mater. Res. Bull.* **86**, 178–185 (2017)
78. C. Ponzoni, M. Cannio, D. Boccaccini, C. Bahl, K. Agersted, C. Leonelli, *Mater. Chem. Phys.* **162**, 69–75 (2015)
79. S. Mondal, K. Dutta, S. Dutta, D. Jana, A. Kelly, S. EFW-L. De, *ACS Appl. Nano Mater.* **1**, 625–631 (2018)
80. M.A. Iqbal, A. Tariq, A. Zaheer, S. Gul, S.I. Ali, M.Z. Iqbal, D. Akinwande, S. Rizwan, *ACS Omega* **4**, 20530–20539 (2019)
81. M. Sanna Angotzi, A. Musinu, V. Marnelli, A. Ardu, C. Cara, D. Niznansky, H.L. Xin, C. Cannas, *ACS Nano* **11**, 7889–7900 (2017)
82. X. Sun, Z. Liu, H. Yu, Z. Zheng, D. Zeng, *Mater. Lett.* **219**, 225–228 (2018)
83. J. Rout, R. Choudhary, *Phys. Lett. A* **380**, 288–292 (2016)

84. V.V. Jadhav, R.S. Mane, P.V. Shinde, (Springer, 2020) (pp. 47–67)
85. A.P. Herrera, L. Polo-Corrales, E. Chavez, J. Cabarcas-Bolivar, O.N. Uwakweh, C. Rinaldi, J. Magn. Mater. **328**, 41–52 (2013)
86. F. Foroughi, S. Hassanzadeh-Tabrizi, J. Amighian, A. Saffar-Teluri, Ceram. Int. **41**, 6844–6850 (2015)
87. S.F. Hasany, N.H. Abdurahman, A.R. Sunarti, R. Jose, Curr. Nanosci. **9**, 561–575 (2013)
88. D. Langevin, Annu. Rev. Phys. Chem. **43**, 341–369 (1992)
89. X.-M. Lin, A.C. Samia, J. Magn. Mater. **305**, 100–109 (2016)
90. R. Ali, M.A. Khan, A. Mahmood, A.H. Chughtai, A. Sultan, M. Shahid, M. Ishaq, M.F. Warsi, Ceram. Int. **40**, 3841–3846 (2014)
91. S.T. Hussain, S.R. Gilani, S.D. Ali, H.S. Bhatti, J. Alloy. Compd. **544**, 99–104 (2012)
92. L. Chen, Y. Shen, J. Bai, Mater. Lett. **63**, 1099–1101 (2009)
93. H. Zhang, G. Zhu, Appl. Surf. Sci. **258**, 4952–4959 (2012)
94. D. Biswal, B.N. Peeples, C. Peeples, A.K. Pradhan, J. Magn. Mater. **345**, 1–6 (2013)
95. J. Xu, H. Yang, W. Fu, K. Du, Y. Sui, J. Chen, Y. Zeng, M. Li, G. Zou, J. Magn. Mater. **309**, 307–311 (2007)
96. B. Baruwati, M.N. Nadagouda, R.S. Varma, J. Phys. Chem. C **112**, 18399–18404 (2008)
97. I. Safarik, K. Horska, K. Pospiskova, Z. Maderova, M. Safarikova, IEEE Trans. Magn. **49**, 213–218 (2012)

Effect of Substitution on the Electric and Magnetic Properties of Ferrites



Harshal B. Desai and Ashish R. Tanna

Abstract This chapter summarizes the effect of monovalent, divalent, trivalent, and tetravalent elements substitution on the electric and magnetic properties of spinel ferrites. Due to the doping of different cations, drastic changes take place in the properties of spinel structure. The spinel structure of the ferrite possesses insulating properties at room temperature and magnetic due to the presence of iron in the material. As well as the preparation method plays a crucial role to vary the physical properties of ferrite, in the result, possibility to use these spinel ferrite materials in a variety of applications. By changing the synthesis route of the magnetic ferrite specimens, can be utilized as superparamagnetic materials for specific biomedical applications. The temperature can affect the electrical properties as more than one valence state of the ions in the interstitial sites of ferrite by hopping mechanism. The various dopants modify the exchange interaction, spin canting, cation distribution, Curie temperature, saturation magnetization, nuclear hyperfine field, ac resistivity, dc resistivity, and many other properties of spinel ferrite materials.

Keywords Magnetic properties · Electrical properties · Spinel ferrites · Superparamagnetic

1 Introduction

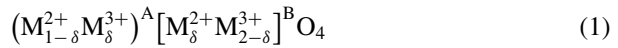
Ferro-spinels are electrical insulators therefore there is very little charge transport under the influence of the external electrical field. The electrical conductivity depends on the product of the charge carrier density and the carrier mobility at finite fields rather than independent values of these quantities. The electrons in solids conduct electricity as well as heat. In fact, the thermal conductivity and electrical conductivity are coupled since electrical conduction transports energy and thermal conduction transports charge. The result gives rise to thermo-electricity. The magneto-transport properties can give information on the carrier mobility and carrier density separately.

H. B. Desai · A. R. Tanna (✉)

Department of Physics, School of Science, RK University, Rajkot 360020, India

e-mail: ashish.tanna@rku.ac.in

For example, magneto-resistance helps to find out the carrier mobility and density through Hall Effect. The electromagnetic transport properties are sensitive to the grain microstructure. The microstructure of the ferrite is determined by a variety of factors: raw material quality, calcination temperature, high energy milling procedure, and sintering regime. Moreover, the concentration of substitution and impurities effectively regulates the densification process and the grain boundary properties and thus their electric and magnetic properties. The spinel oxide with formula AB_2O_4 can have different metal cations at the place of A and B. If Fe^{3+} are represented as B ions and any divalent cations M^{2+} as A ion, then the formula is $M^{2+}Fe^{3+}_2O_4$ and the examples are: $ZnFe_2O_4$; $NiFe_2O_4$; $CuFe_2O_4$, etc. These are called ‘2–3’ spinels. If B ion is any divalent ion and A any tetravalent ion the they are known as ‘2–4’ spinels, for example, $GeCo_2O_4$, $TiMgO_4$, etc. Likewise, there would be ‘6–1’ spinels also, for example, Na_2WO_4 , Li_2MoO_4 , etc. In the case of ‘2–3’ spinel the degree of inversion (fraction of divalent metal ion occupying B site) δ can be shown in the following manner:



If the $\delta = 0$ then, it is known as the “normal” spinel, and if $\delta = 1$ then, it is known as an “inverse” spinel. These are the two extreme cases. For example, $ZnFe_2O_4$ is normal ferrite whereas $NiFe_2O_4$ is an inverse ferrite, but $MgFe_2O_4$ is a partially inverse ferrite with $\delta \sim 0.9$. The cation distribution depends upon various factors, viz. electrostatic energy, anion polarization energy, crystal field stabilization energy (CFSE), and magnetic ordering energy. The spinel ferrites allow a special kind of magnetic order called ferrimagnetism [1]. There are two types of crystallographically in equivalent sublattices: A-site (tetrahedral site) and Octahedral site (B-site). The ferrimagnetism occurs due to the antiparallel orientation of the two-sub lattice magnetization M_A and M_B provided that the inter-sub lattice exchange interaction (A–B exchange interaction) is antiferromagnetic. It was pointed out by Neel [2] that the cations in spinel ferrites are separated by larger oxygen ions which practically excludes a direct contact between the cation orbitals making any direct exchange very weak instead of it, superexchange interaction appear i.e. indirect exchange via oxygen p orbital that may be strong enough to order the magnetic moments. The oxygen plays an important role, so, negative interaction can be obtained, viz. super exchange, has been suggested by Kramers [3], Anderson [4], and Van Vleck [5]. It is generally assumed that the interaction diminishes rapidly with an increase in metal ions-oxygen ion distances. The dumbbell shape of the 2p orbital makes it a reasonable assumption that the interaction for given ionic separation can be greatest when the M–O–M angle is 180° and very small indeed when this angle is 90° . With these two assumptions, it is concluded that the A-B interaction probably intermediates between these two extremes [6]. Therefore, the cations substitution in the ferrites plays a vital role to modulate the magnetic properties according to their need in technological applications. The spinel ferrites are good insulators of electricity at room temperature [1] when without transition cations. This is due to a huge energy band gap and this can be controlled by activation energies and electrical conductivity of

doped elements. While cations are doped in the spinel ferrite materials energy levels are modulated. Thus, the spinel oxides with $3d^n$ elements in the A (tetrahedral) sites can possess high resistivity. A similar type of behavior has been observed for pure spinel ferrite systems i.e. zinc ferrite ($ZnFe_2O_4$), cadmium ferrite ($CdFe_2O_4$), and lithium spinel ferrite ($Li_{0.5}Fe_{2.5}O_4$). Hence, the rise in the electrical resistivity is due to valence states generated by cations and disorders associated with the spinel oxides. The known examples for this type of coexistence are divalent and trivalent iron or cobalt ions in the octahedral sites. This causes the charge transfer and hopping of electrons/holes or valency exchange in the ions of mixed spinel ferrites. The ferrites are extremely useful electro-ceramics or electronic materials as they exhibit excellent magnetization like ferromagnetic metals but at the same time, unlike ferromagnetic metals, they possess very high electrical resistivity reducing the detrimental effect of eddy currents. This outstanding combination of magnetic and electrical properties makes them excellent and indispensable magnetic materials for high-frequency applications. The study of electrical conductivity provides the information about conduction mechanism which is the important property of ferrites. On the other hand, the dielectric constant of these materials is very high at low frequencies. The values of dielectric constants are 10^5 – 10^4 for Mn–Zn, 10^4 – 100 for Cu–Zn, and 10^3 – 10 for Ni–Zn ferrites within the frequency range from 100 Hz to 100 MHz. The dielectric constant decrease with an increase in frequency [7]. The electrical and dielectric properties of ferrites depend upon several factors i.e. the synthesis process, dopant elements, grain size, and chemical composition. The polarization studies of ferrite ceramics are understood and microscopically explained the theories by comparing with the different materials in the present scenario. Researchers have extended dielectric theories further to understand the low-frequency dielectric properties of these types of ceramic materials like ferrites. Also, the dielectric constant is dependent on the average grain size of the specimens of similar compositions of polycrystalline ferrites [8]. Ferrites have a different mechanism of conduction for semiconductors. In a basic ferrite structure, the cations are surrounded by closely packed oxygen ions and to the first impression can be treated as isolated, though there may be a little overlap of the charge anion clouds. However, there is the transfer of electrons from one ion to another ion with high probability, whenever the ions occasionally come closer to each other under the presence of lattice vibrations. Among various spinel ferrites, the Cu^{2+} ferrite has exciting physical properties, and it is distinguished from the other ferrites due to structural phase transition under various conditions. This result in a reduction in the crystal symmetry caused by the Jahn–Teller ion as well as temperature dependency of Cu^{2+} spinels is crucial with the synthesis process of the samples. The substitution of non-magnetic Al^{3+} in $CuFe_2O_4$ can lower the long-range magnetic ordering and the other cations (Cr^{3+}) can generate disorder in the spinel ferrite material [9]. To understand the conduction mechanism for the present case, Cu^{2+} substituted $MnFe_2O_4$ is taken into consideration.

2 Effect of Substitution on Manganese Ferrite

The copper doped manganese ferrite ($\text{Mn}_{1-x}\text{Cu}_x\text{Fe}_2\text{O}_4$ ($x = 0.25, 0.5, 0.75, 1.0$) was synthesized by solid-state reaction. In this oxide precursor-like CuO , Fe_2O_3 , and MnCO_3 powders were used. These powders were mixed and grinded well in an agate mortar in stoichiometric proportion.

After the successfully sintering process, copper substituted manganese ferrite was obtained. The electric, dielectric, and magnetic properties of copper substituted manganese ferrite were investigated at room temperature and 77 K. It is evident from Table 1 that Neel temperature increases with the increasing substitution of copper ions. The Mössbauer spectroscopy supports the cations distribution deduced from XRD and hence the electrical and magnetic properties are discussed by Tanna et al. [10]. The conduction mechanism in ferrites is explained by Verway and De Boer [11]. They proposed that electronic exchange among the same ions having different valence states which are randomly distributed over equivalent crystallographic lattice sites is the most apparent source of conduction in ferrites.

Most of the hopping part is impacted by the electronic exchange between Fe^{3+} and Fe^{2+} ion pairs. Factors like sintering conditions and cation distribution are mainly responsible for the increase or decrease of inter ionic distances in these ions' pairs, which further increase or decrease the conduction. For the present system, dc resistivity at different temperatures is determined. Figure 1 shows the DC resistivity as a function of temperature for all the samples which obeys thermally activated behavior given as

$$\rho_{dc} = \rho_0 \exp\left(\frac{E_a}{kT}\right) \quad (2)$$

where, ρ_0 is the pre-exponential factor with the dimensions of $\Omega \cdot \text{cm} \cdot \text{K}^{-1}$, E_a is the activation energy and k are the Boltzmann constant. It is observed that the DC resistivity decreases with Cu^{2+} doping and the activation energy (E_a) increases which is consistent with the AC resistivity results.

Table 1 DC Resistivity (ρ_{dc}), Transition Temperature (T) and Activation Energy (E_a) for the $\text{Mn}_{1-x}\text{Cu}_x\text{Fe}_2\text{O}_4$ ferrite system

X	$\log \rho_{dc} (\Omega \text{ cm})$ (at 318 K)	Transition temperature (T) K	Activation energy (eV)		
			E_f	E_p	ΔE
0.00	7.901	593	0.561	0.584	0.023
0.25	7.617	603	0.592	0.603	0.011
0.50	7.452	623	0.621	0.670	0.049
0.75	7.833	630	0.674	0.698	0.024
1.00	7.882	648	0.676	0.713	0.037

Fig. 1 Thermal variation of dc resistivity of $Mn_{1-x}Cu_xFe_2O_4$ ferrite system

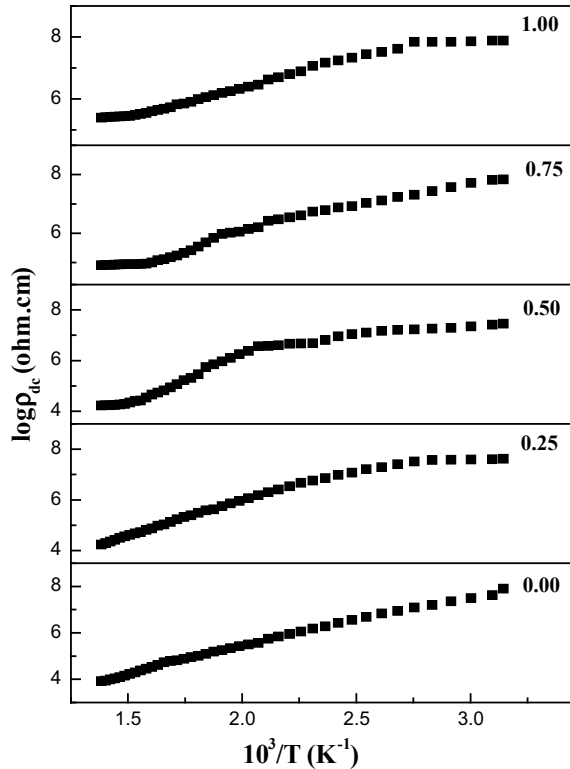


Figure 2a shows the room temperature variation of dielectric constant as a function of frequency for Cu^{2+} doped manganese spinel ferrites. The dielectric constant was observed to decrease with the increase in frequency. This behavior can be understood with the use of Maxwell Wagner’s interfacial polarization model [12] and Koop’s hypothesis [13]. The dielectric ceramics are considered to have heterogeneous structure that acts like a multilayer capacitor according to the presumption of these theories and models. This heterogeneous structure is composed of grain boundaries and grains with low and high conduction, respectively. Due to this, at high frequencies, the conductivity of grains is higher, while at lower frequencies grain boundaries exhibit low conductivity [14]. If the voltage is applied then the drop occurs at grain boundaries in a dielectric specimen and hence, there is a separation of mobile positively and negatively charged particles and an interfacial polarization starts building up. The interfacial polarization may insist high value of dielectric constant at low frequencies. As suggested by Novikova et al. [15] that in ferrites dielectric polarization is a phenomenon like conduction. It is the electronic exchange between Fe^{3+} and Fe^{2+} ions resulting in the local displacement of electrons along the direction of the external field which gives rise to polarization effects in ferrites. The observed changes in dielectric constant i.e. first decreases with increase in frequency and then

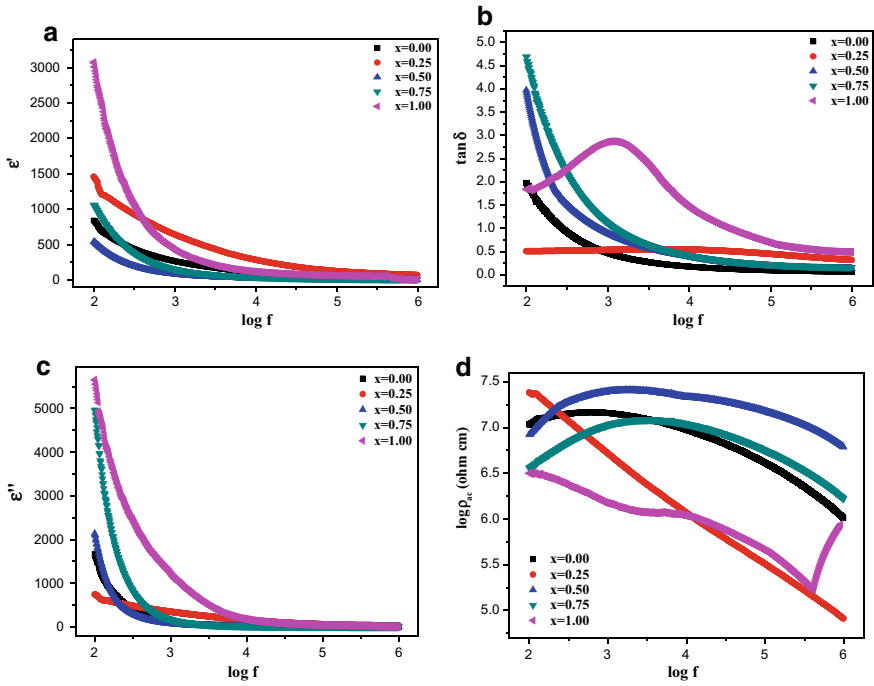


Fig. 2 a Variation of dielectric constant (ϵ') with frequency. b Variation of loss tangent ($\tan \delta$) with frequency for the $Mn_{1-x}Cu_xFe_2O_4$ ferrite system. c Variation of ac resistivity (ρ_{ac}) with frequency. d Variation of complex dielectric constant (ϵ'') with frequency for the $Mn_{1-x}Cu_xFe_2O_4$ ferrite system

remaining almost constant at very high frequencies is due to the lagging behind of electronic exchange between Fe^{3+} and Fe^{2+} ions with the external field at such high frequencies. It is clear from Fig. 2a that the dielectric constant increases with an increase in Cu^{2+} concentration, while for $x = 0.5$ ferrite sample dielectric constant is decreased. The reason for the observed variations in the dielectric constant is based on the cation distributions and is explained by Tanna et al. [10] in detail. This type of variation in dielectric constant due to the cationic migration is also explained earlier by Saafan et al. [16] for other ferrites. The presence of Fe^{3+} ions in the B-site is supposed to be responsible for a decrease or increase in the value of the dielectric constant which in turn is responsible for the low or high resistivity or conductivity in these ferrites. Figure 2b shows the variation of tangent loss tangent ($\tan \delta$) as a function of frequency for all the samples at room temperature. It is observed that the dielectric loss tangent is increased by Cu^{2+} doping while it decreases with frequency. However, for $x = 1.0$ composition, it gives bell shape behavior.

AC conductivity for all five compositions is calculated using the following formula from the dielectric data at room temperature over a frequency range (100 Hz–1 MHz).

$$\sigma_{AC} = \varepsilon' \varepsilon_0 \cdot \omega \cdot \tan\delta \quad (3)$$

where, σ_{AC} is AC conductivity and ε_0 is the permittivity of free space, ε' is the dielectric constant. Using the following formula AC resistivity of the sample can be found.

$$\rho_{AC} = \frac{1}{\sigma_{AC}} \quad (4)$$

Various models and theories exist in literature to explain the AC conduction mechanism in disordered solids like ferrites. Heikes and Johnston [17] suggested that it is the hopping of electrons between two nearest sites in spinel lattice responsible for AC conduction. The random transition of these charge carriers from one to another site incorporates the disorderliness in such solids. The power-law relationship of AC conductivity with frequency is given by the reported formula [18, 19]. It is observed from Fig. 2c that AC resistivity decreases with Cu^{2+} doping. The reason for this characteristic is the presence of a maximum fraction of Fe^{3+} ions for hopping at the B site. The electron polaron hopping models can also account for this type of variation in AC resistivity/conductivity. An attempt is made to calculate the polaron radius (r_p) using the following formula [20, 21].

$$r_p = \frac{1}{2} \left[\frac{\pi}{6N} \right]^{1/3} \quad (5)$$

where N is the number of sites per unit volume = $(96/a^3)$. The calculated values of the polaron radius are given in Table 2. It is observed that r_p is decreased with an increase in Cu^{2+} content. Also, r_p is smaller than interionic distances. Hence, it confirms that AC conductance is mainly dominated by the small polarons hopping. However, a feeble decrease in AC conductivity at high frequencies for some compositions may be due to mixed type polaron conduction i.e. small and large both.

Here, ε'' (dielectric constant-imaginary part) can be calculated by using the following relation and the variation with frequency is displayed as Fig. 2d. This shows the same trend as ε' and $\tan\delta$ graphs.

Table 2 Dielectric constant, AC Resistivity and Polaron radius of ferrite system: $\text{Mn}_{1-x}\text{Cu}_x\text{Fe}_2\text{O}_4$

X	Dielectric constant (ε')	Dielectric loss ($\tan\delta$)	$\log \rho_{ac}$ (Ω cm)	Polaron radius (r_p) Å
	at 1 kHz			
0.00	264	0.4719	7.161	0.7484
0.25	643	0.5362	6.719	0.7455
0.50	80	0.8945	7.399	0.7426
0.75	154	1.1168	7.033	0.7395
1.00	424	2.8618	6.173	0.7379

Table 3 Saturation magnetization (σ_S), magneton number (η_B) and neel temperature (T_N) of $Mn_{1-x}Cu_xFe_2O_4$ ferrite system

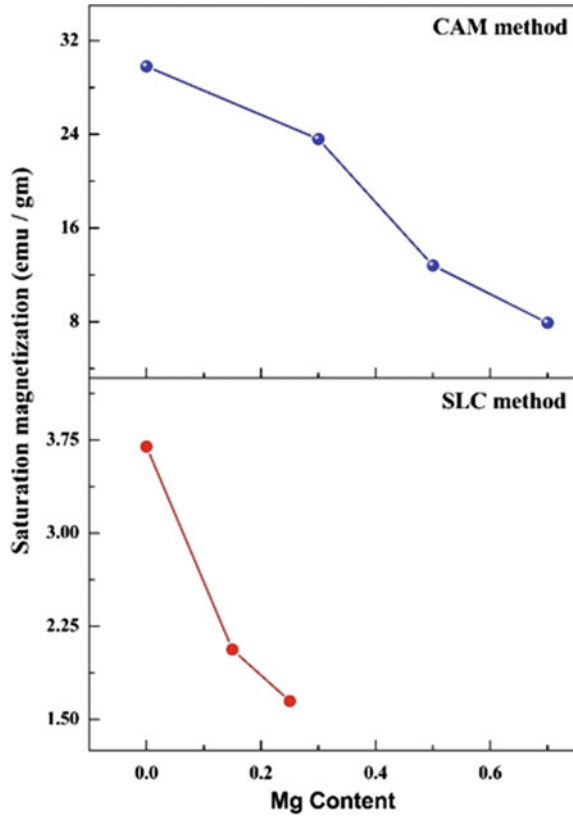
X	σ_S (emu/gm)		$n_B^{obs} \mu_B$	$n_B^{obs} \mu_B$		T_N (K)	
	RT	77 K		RT	77 K	Susceptibility	DC resistivity
0.00	60	81	5	2.48	3.35	580	593
0.25	51	65	4	2.13	2.71	600	603
0.50	40	50	3	1.68	2.10	610	623
0.75	28	35	2	1.19	1.49	615	630
1.00	16	20	1	0.69	0.86	625	648

$$\varepsilon'' = \varepsilon' \tan \delta \quad (6)$$

Magnesium substituted manganese ferrite prepared by co-precipitation assisted microwave method and magnetic properties were studied and found that as the Mg content increased in $Mg_xMn_{1-x}Fe_2O_4$ ferrite, saturation magnetization and coercivity decreased. The change in the value of saturation magnetization occurred because of the discrepancy in the cation distribution at the tetrahedral site and octahedral site. The magnesium content preferred the octahedral site more than the tetrahedral site.

The magnetic Mn^{2+} ($5 \mu_B$) ions had a preference for both tetrahedral and octahedral sites of the spinel lattice. The substitution of the nonmagnetic Mg^{2+} ions into the octahedral sublattices instead of the high magnetic nature of Mn^{2+} ($5 \mu_B$) ions led to a decrease in the octahedral site's magnetic moment when it compared with the tetrahedral site's magnetic moment [22]. Okasha et al. synthesized magnesium substituted manganese ferrite by the simple and low-cost method. The γ -rays were incident on magnesium substituted manganese ferrite using Co^{60} source. The magnetic properties of as-prepared magnesium substituted manganese ferrite and γ -rays irradiated magnesium substituted manganese ferrite were investigated and found that saturation magnetization and coercivity of γ -rays irradiated magnesium substituted manganese ferrite was higher than the as-prepared magnesium substituted manganese ferrite. This occurred due to the irradiation of γ -rays on the ferrite because of the regulated growth of single-domain particles where the lack of domain walls produced the magnetization process more complex [23]. Figure 3 shows the effect of the synthesis method on the saturation magnetization of magnesium substituted manganese ferrite. Attia et al. [22] found that in the series of $Mg_xMn_{1-x}Fe_2O_4$ ($x = 0.0, 0.3, 0.5, 0.7$), the saturation magnetization 29.8 emu/gm at $x = 0.0$ while Okasha et al. [23] found that in the series of $Mg_xMn_{1-x}Fe_2O_4$ ($x = 0.0, 0.15, 0.25$), the saturation magnetization 3.698 emu/gm at $x = 0.0$. It can be concluded that saturation magnetization depends on the synthesis method. Gabal et al. [24] prepared aluminum substituted manganese–zinc ferrites by citrate sol–gel auto-combustion method and the magnetic properties were investigated. They found that with the increase in aluminum content in manganese–zinc ferrite, saturation magnetization as well as coercivity decreased. This happened because non-magnetic Al^{3+} ions occupied B-site by replacing the Fe^{3+}

Fig. 3 Effect of synthesis method on saturation magnetization of magnesium substituted manganese ferrite [22, 23]. Reprinted with permission from Elsevier



ions which led to a decrease in the octahedral site's magnetic moment when matched with the tetrahedral site's magnetic moment. Angadi et al. [25] prepared samarium–gadolinium substituted manganese–zinc ferrite ($\text{Mn}_{0.4}\text{Zn}_{0.6}\text{Sm}_x\text{Gd}_y\text{Fe}_{2-(x+y)}\text{O}_4$ ($x = y = 0.01\text{--}0.05$, step size 0.1)) by combustion route and the magnetic properties were investigated. They reported that the increase in samarium–gadolinium content in manganese–zinc ferrite, resulted a decrease in saturation magnetization, and coercivity because of the presence of an efficiently uniaxial anisotropy in ferrite particle. The Yafet-Kittle angle explained the degree of spin canting effect. The calculated values of the Yafet-Kittle angle were varied between the angles 60 and 70°. The values of Yafet-Kittle angle of the specimen with increasing $\text{Sm}^{3+}\text{--}\text{Gd}^{3+}$ contents was obtained to increase. This increase in Yafet-Kittle angle suggested that there was an increasing tendency for triangular spin arrangement on the octahedral site which resulted in a decrement of A–B exchange interaction [25]. Deraz et al. [26] synthesized the specific sample $\text{Mn}_{0.5}\text{Zn}_{0.5}\text{Fe}_2\text{O}_4$ ferrite by an advanced combustion route and magnetic properties were investigated. They observed the values of saturation magnetization and coercivity as 85.78 emu/gm and 58 Oe respectively. They synthesized MnFe_2O_4 and ZnFe_2O_4 by the same method and obtained the values

of saturation magnetization as 67.18 emu/gm and 52 emu/gm respectively. They reported that the value of saturation magnetization of $\text{Mn}_{0.5}\text{Zn}_{0.5}\text{Fe}_2\text{O}_4$ ferrite was greater than the value of saturation magnetization of MnFe_2O_4 and ZnFe_2O_4 ferrites [26].

3 Effect of Substitution on Magnesium Ferrite

Manikandan et al. [27] synthesized manganese substituted magnesium ferrites ($\text{Mn}_x\text{Mg}_{1-x}\text{Fe}_2\text{O}_4$, $x = 0-0.5$, step sized 0.1) by facile microwave-assisted combustion method and investigated the magnetic properties. They reported that as Mn content increased in $\text{Mn}_x\text{Mg}_{1-x}\text{Fe}_2\text{O}_4$ ferrites, saturation magnetization increased and coercivity decreased. The change in the value of saturation magnetization took place because of the alteration in the cation distribution at the tetrahedral and octahedral sites. The magnesium ferrite is a mixed spinel ferrite. The Mg^{2+} ion concentration at the tetrahedral site was 12%, while the concentration of Mg^{2+} ion at the octahedral site was 88% in the magnesium ferrite. The magnetic Mn^{2+} ($5 \mu_B$) ions preferred both tetrahedral and octahedral sites of the spinel ferrite. The substitution of the high magnetic Mn^{2+} ($5 \mu_B$) ions into the octahedral site instead of Mg^{2+} ions led to an increment in the magnetic moment of the octahedral site when matched with the tetrahedral site. Also, the Mn^{2+} ions' occupancy in the tetrahedral site allowed the Fe^{3+} ions to drift from the tetrahedral to octahedral site and voluntarily increases the net magnetic moment [27]. Ghodake et al. [28] synthesized manganese substituted magnesium-zinc ferrite ($\text{Zn}_{0.4}\text{Mg}_{0.6-x}\text{Mn}_x\text{Fe}_2\text{O}_4$ ($0 \leq x \leq 0.3$)) by oxalate precursor chemical method that with the increase in Mn substitution in Magnesium-Zinc ferrite, the saturation magnetization, coercivity, and Bohr magneton increased. This happened due to the fact that Mg^{2+} and Mn^{2+} both occupied A-site and B-site while Zn^{2+} ions occupied in A-site. So, as Mn content increased in this system, magnetic moment increased and hence saturation magnetization increased at 80 K. Electric properties of $\text{Zn}_{0.4}\text{Mg}_{0.6-x}\text{Mn}_x\text{Fe}_2\text{O}_4$ ($0 \leq x \leq 0.3$) were investigated at room temperature. The increment in dc resistivity suggested that the formation of Fe^{2+} ions increased the electron hopping between $\text{Fe}^{2+} \leftrightarrow \text{Fe}^{3+}$ [28]. Manganese substituted magnesium-zinc ferrite prepared by the glycine-nitrate auto combustion process in which nitrates were used as oxidants and glycine was used as fuel. The magnetic properties of specimens were investigated and found that as the Mn content increased in Mg-Mn-Zn ferrite, the saturation magnetization increased. This happened due to the fact that Mg^{2+} and Mn^{2+} both occupied A-site and B-site while Zn^{2+} ions occupied A-site. So, as Mn content increased in this system, magnetic moment increased and hence saturation magnetization increased [29]. Chhaya et al. [30] reported the maximum value of saturation magnetization in calcium substituted magnesium ferrite (76 emu/gm) for $\text{Mg}_{0.8}\text{Ca}_{0.2}\text{Fe}_2\text{O}_4$ because the orthorhombic phase (Calcium ferrite) was present with face-centered cubic phase. The calcium ferrite possessed antiferromagnetic properties. In this system, a small fraction (20% in $x = 0.35$) of calcium ferrite was covered by the strong ferrimagnetic face-centered cubic phase. As the content of

calcium increased, the saturation magnetic increased from $x = 0.0$ to $x = 0.2$ and then saturation magnetization decreased. The electrical properties of calcium substituted magnesium ferrite were also investigated and found that as calcium content increased in magnesium ferrite, electrical conductivity decreased [30]. Iqbal et al. [31] synthesized cobalt-chromium doped magnesium ferrite ($\text{Mg}_{1-x}\text{Co}_x\text{Cr}_x\text{Fe}_{2-x}\text{O}_4$ with $x = 0.0-0.5$) by polyethylene glycol assisted microemulsion method and then investigated the magnetic properties. They found that saturation magnetization of the specimens increased as content of cobalt-chromium increased up to 0.3 followed by a decrease in saturation magnetization for x greater than 0.3. In the magnesium ferrite, the substitution of Co^{2+} and Cr^{3+} replaced Mg^{2+} and Fe^{3+} ions and thus changed the magnetic properties. Substitution of Mg^{2+} ion by Co^{2+} ion enhanced the magnetic moment of the octahedral site which led to an increment in the overall magnetic moment. On the other hand, the substitution of Fe^{3+} ($5 \mu_B$) by Cr^{3+} ($3 \mu_B$) resulted a reduction of magnetization on the same site. Hence, the competition between two ions at the octahedral site led to an increment in saturation magnetization to a certain specimen level and started to reduce afterward. Electrical properties of cobalt-chromium substituted magnesium ferrite were also investigated and found that room temperature resistivity increased as the contents of cobalt-chromium increased in $\text{Mg}_{1-x}\text{Co}_x\text{Cr}_x\text{Fe}_{2-x}\text{O}_4$ ferrites [31]. Thummer et al. [32] have synthesized aluminum and chromium substituted magnesium ferrite $\text{MgAl}_x\text{Cr}_x\text{Fe}_{(2-2x)}\text{O}_4$ by double sintering method and investigated the magnetic properties. They found that initially, saturation magnetization increased as the content of aluminium–chromium is increased from 0.0 to 0.2 and then decreased as the Al–Cr concentration further increased. The magneton number variation with x was explained by invoking the “canted” spin structure or Neel’s collinear structure. The canted spin structure was stable at lower temperatures and disappeared when approached to the Neel-type collinear spin ordering at all temperatures. The canting angles were related to the magnetic dilution by using the noncollinear spin models based on the molecular field theory [32]. Tanna et al. [33] synthesized zinc substituted magnesium ferrite ($\text{Mg}_{1-x}\text{Zn}_x\text{Fe}_2\text{O}_4$ ($0 \leq x \leq 1.0$, step size 0.1) and aluminum substituted magnesium–zinc ferrites ($\text{Mg}_{0.6}\text{Zn}_{0.4}\text{Al}_x\text{Fe}_{2-x}\text{O}_4$ ($0 \leq x \leq 0.6$, step size 0.1) by double sintering solid-state reaction and found interesting behavior. The magnetic properties of zinc substituted magnesium ferrite were investigated and noticed that as the content of Zn increased in $\text{Mg}_{1-x}\text{Zn}_x\text{Fe}_2\text{O}_4$ from $x = 0.0$ to 0.4, there was an increment in saturation magnetization, and then for a higher value of x , saturation magnetization decreased. The magnetic properties of aluminum substituted magnesium–zinc ferrites were investigated and found that as the content of Al increased in $\text{Mg}_{0.6}\text{Zn}_{0.4}\text{Al}_x\text{Fe}_{2-x}\text{O}_4$ up to 0.1, saturation magnetization increased, and then for higher values of x , saturation magnetization decreased. The discrepancy between Neel’s moment and observed moment increase in $\text{Mg}_{1-x}\text{Zn}_x\text{Fe}_2\text{O}_4$ after $x = 0.4$ suggested the canted spin structure or non-collinear structure. The initial composition $\text{Mg}_{0.6}\text{Zn}_{0.4}\text{Fe}_2\text{O}_4$ of other system $\text{Mg}_{0.6}\text{Zn}_{0.4}\text{Fe}_{2-x}\text{Al}_x\text{O}_4$ showed the onset of canted spin structure. The electrical properties of $\text{Mg}_{0.6}\text{Zn}_{0.4}\text{Fe}_{2-x}\text{Al}_x\text{O}_4$ were also investigated and found that the value of electrical resistivity increased with an increase in Al-concentration. This occurred due to electron hopping between Fe^{2+} and Fe^{3+}

ions. This process was expected between the two adjoining octahedral sites in spinel ferrite. Thus, the increment in the electrical resistivity with Al-substitution is due to fact that Al^{3+} replaced the Fe^{3+} which diluted the conduction at octahedral sites [33]. Farid et al. [34] synthesized Praseodymium substituted magnesium ferrite by sol–gel auto combustion method. The magnetic properties of synthesized specimens were investigated and found that saturation magnetization depends on praseodymium content in magnesium ferrite. This happened due to the fact that Mg^{2+} ions occupied the A-site, but the Fe^{3+} ions were resided on A-site as well as B-site, while praseodymium ions were occupied the B site because of large ionic radius than Fe^{3+} ions. So, there was a lesser probability of praseodymium ion resided on an A-site. As praseodymium is a non-magnetic element, therefore, the net magnetic moment of the B site was less than the magnetic moments of the A site. This was the main cause for the decrement of magnetization at the octahedral site. The decrement in saturation magnetization may be due to the migration of Fe^{3+} ions from octahedral site to tetrahedral site. The electrical properties of praseodymium substituted magnesium ferrite were also investigated and found that (i) at room temperature, the dc resistivity increased as praseodymium content increased in magnesium ferrite (ii) as the temperature increased, the dc resistivity decreased. This happened due to the hopping of electrons (negative charge carriers) from Fe^{2+} to Fe^{3+} , the transfer of holes (positive charge carriers) and Mg^{1+} to Mg^{2+} were accountable for the conduction mechanism in ferrites [34]. Deraz [35] has prepared $\text{Mg}_{0.5}\text{Mn}_{0.5}\text{Fe}_2\text{O}_4$ ferrite by the sol–gel auto-combustion method and reported the values of saturation magnetization and coercivity as 47.78 emu/gm and 93.36 Oe respectively.

4 Effect of Substitution on Magnesium–Manganese Mixed Ferrite

Lwin et al. [36] have synthesized magnesium–manganese mixed ferrite by solution combustion method by varying the pH values of solutions and magnetic properties were investigated. They observed that the value of saturation magnetization of the specimen ($\text{pH} < 1$) was higher than the specimens synthesized with pH variation. This happened owing to the porosity, crystal structure, and density of synthesized ferrite specimens. When the specimen was sintered, ammonium hydroxide vaporized and the gases were entrapped inside the specimen, therefore the porosity of the specimen increased which led to a decrease in the saturation magnetization [36]. Kumar et al. [37] prepared gadolinium substituted magnesium–manganese ferrite ($\text{Mg}_{0.9}\text{Mn}_{0.1}\text{Gd}_x\text{Fe}_{2-x}\text{O}_4$, $x = 0.0, 0.1, 0.2, 0.3$) by self-ignited solution combustion technique and electrical properties were investigated. They found that as the Gd content increased in Mg–Mn ferrite, dc resistivity increased. Electronic conduction in ferrite specimen was occurred due to the hopping of electrons between ions of the same transition elements present in more than one valence state which were distributed randomly over crystallographically equivalent lattice sites [37].

Lakshman et al. [38] prepared indium substituted magnesium–manganese ferrite ($\text{Mg}_{0.9}\text{Mn}_{0.1}\text{In}_x\text{Fe}_{2-x}\text{O}_4$ ($0.1 \leq x \leq 0.9$)) and chromium substituted magnesium–manganese ferrite ($\text{Mg}_{0.9}\text{Mn}_{0.1}\text{Cr}_y\text{Fe}_{2-y}\text{O}_4$ ($0.1 \leq y \leq 0.9$)) by conventional ceramic technique and the electrical properties of indium substituted magnesium–manganese ferrite and chromium substituted magnesium–manganese ferrite were investigated. They reported that the changes in resistivity can be described by Verwey's hopping mechanism. According to this mechanism, the conduction of electrons in spinel ferrites was occurred due to the hopping of electrons between ions of the same transition element ($\text{Fe}^{3+} \leftrightarrow \text{Fe}^{2+}$) present in more than one valence state which was distributed randomly over crystallographically equivalent lattice sites. As the content of manganese was very low in the synthesized specimens, the total contribution to the hopping mechanism due to $\text{Mn}^{3+} \leftrightarrow \text{Mn}^{2+}$ can be neglected. Though indium (diamagnetic ion) and chromium (paramagnetic ion) ions did not play a role in the conduction mechanism, they influenced the reduction of the number of Fe^{3+} ions according to their privileged site occupancy. As the content of indium or chromium ions increased, the Fe content gradually decreased. Therefore the hopping mechanism between $\text{Fe}^{3+} \leftrightarrow \text{Fe}^{2+}$ get weaken which resulted an increase in resistivity [38]. Tsay et al. [39] prepared aluminum and indium substituted Magnesium–Manganese ferrite ($\text{Mg}_{0.9}\text{Mn}_{0.1}\text{Fe}_2\text{O}_4$, $\text{Mg}_{0.9}\text{Mn}_{0.1}\text{Al}_{0.1}\text{Fe}_{1.9}\text{O}_4$, and $\text{Mg}_{0.9}\text{Mn}_{0.1}\text{In}_{0.1}\text{Fe}_{1.9}\text{O}_4$) by mixed-oxide solid-state reaction method and magnetic properties were investigated. They found that saturation magnetization and Curie temperature of $\text{Mg}_{0.9}\text{Mn}_{0.1}\text{In}_{0.1}\text{Fe}_{1.9}\text{O}_4$ had maximum values. This happened due to the variation in the magnetic moments of the tetrahedral and octahedral sublattices, which depend on their cation distributions in the Al^{3+} and In^{3+} doped magnesium–manganese ferrite. It was a known fact that In^{3+} ions favorably occupied the tetrahedral site at low concentration, thus increased the ratio of $\text{Fe}^{3+}(\text{B})$ to $\text{Fe}^{3+}(\text{A})$ such that the total magnetic moment and saturation magnetization increased. But aluminum ions occupied the B sites, therefore decreased the ratio of $\text{Fe}^{3+}(\text{B})$ to $\text{Fe}^{3+}(\text{A})$ such that the net magnetic moment and saturation magnetization were decreased. The electrical properties were investigated for all synthesized specimens and found that the electrical resistivity of $\text{Mg}_{0.9}\text{Mn}_{0.1}\text{In}_{0.1}\text{Fe}_{1.9}\text{O}_4$ had maximum value. Therefore, the dielectric loss of $\text{Mg}_{0.9}\text{Mn}_{0.1}\text{In}_{0.1}\text{Fe}_{1.9}\text{O}_4$ was minimum. So, concluded that it can be used in microwave applications [39]. Manouchehri et al. [40] prepared aluminum substituted magnesium–manganese ferrite by co-precipitation method, and the magnetic properties were investigated. They reported that replacement of aluminum ions (with $0 \mu_{\text{B}}$) instead of Fe^{3+} ions (with $5 \mu_{\text{B}}$ magnetic moments) led to a reduced magnetization of the octahedral site compared to the tetrahedral site. Consequently, in compliance with Neel's two sublattice models of ferrimagnetism, the net moment reduced. The saturation magnetization (M_s) was increased up to $x = 0.1$ in $\text{Mg}_{0.8}\text{Mn}_{0.2}\text{Al}_x\text{Fe}_{2-x}\text{O}_4$ ferrites and then decreased with Al content. This variation was explained on the basis of three sublattice models suggested by Yafet and Kittle. For aluminum content 0.1, magnetization increased due to a decrease in canting angle between moments in octahedral sites because of decrement in the negative B–B interaction. This decrement led to improve the parallelism of moments in the octahedral site. As the Al^{3+} content increased in B-site, Fe^{3+} content decreased. Aluminum does not

play a role in the exchange interaction to the adjacent neighbor ions, the magnetization of the octahedral site decreased and so the net saturation magnetization decreased [40]. Kumar et al. synthesized cobalt substituted magnesium-manganese ferrite by solution combustion technique and the electrical properties were investigated. They observed that the resistivity of all the samples was decreased with increased temperature. As the temperature increase, the drift mobility of the charge carrier increased, and they participated in the conduction process. Also, as the cobalt content increased, the variation in dc resistivity was observed due to Verwey's hopping mechanism [41]. Kumar et al. [42] prepared cobalt substituted Mg-Mn-Al ferrites ($\text{Mg}_{0.9}\text{Mn}_{0.1}\text{Al}_{0.3}\text{Co}_x\text{Fe}_{1.7-x}\text{O}_4$, $x = 0.3, 0.5, 0.7$) by the citrate precursor technique. The electrical and magnetic properties of cobalt substituted Mg-Mn-Al ferrites were studied and observed that the electrical resistivity was enhanced as the increased substitution of cobalt in Mg-Mn-Al ferrite. This happened because cobalt ions resided mostly on octahedral sites. Therefore, the cobalt ions impeded electron exchange between divalent and trivalent iron ions on octahedral sites, causing a greater value of resistivity. Saturation magnetization was observed to increase with the increment in cobalt content. This happened because cobalt ions gave the large induced anisotropy due to relatively high orbital contribution to the magnetic moment [42]. Jasrotia et al. [43] prepared silver substituted magnesium-manganese ferrites ($\text{Mg}_{1-y}\text{Mn}_y\text{Ag}_x\text{Fe}_{2-x}\text{O}_4$; $y = 0.1-0.5$, step size 0.1 and $x = 0.0-0.4$, step size 0.1) by sol-gel method and magnetic properties were investigated. They found that $\text{Mg}_{0.6}\text{Mn}_{0.4}\text{Ag}_{0.3}\text{Fe}_{1.7}\text{O}_4$ ferrite had the highest value of saturation magnetization and coercivity. The reason for this is that silver ions entered the A-site (tetrahedral site) and replaced Fe^{3+} ions due to which magnetization of tetrahedral sub-lattice decreased. Though, a decrease in saturation magnetization for silver content 0.4 is due to the occupancy of the B site by some of the silver ions due to which it decreased the magnetization at the B site to a small extent and hence an overall magnetization decreased. The variation of saturation magnetization as a function of the applied magnetic field indicated that a small substitution of silver ions made the strengthening of the exchange interaction in the Mg-Mn ferrite [43]. Somnath et al. [44] prepared a series of neodymium substituted magnesium-manganese ferrite powder ($\text{Mg}_{0.9}\text{Mn}_{0.1}\text{Nd}_x\text{Fe}_{2-x}\text{O}_4$ ($x = 0.1, 0.2, 0.3$)) by solution combustion method, and the magnetic properties were investigated. They observed a decrement in saturation magnetization as an increment in substitution of neodymium ions in magnesium-manganese ferrite. This happened due to superexchange interaction. The exchange interaction occurred by the involvement of oxygen 'anions' which was known as super-exchange interaction in the ferrite. The magnetic ions occupied (A) and (B) sites in the ferrite, so three possible super-exchange interactions occurred: A-A super-exchange interaction, B-B super-exchange interaction, and A-B super-exchange interaction. A-B super-exchange interaction heavily predominated over A-A super-exchange and B-B super-exchange interactions. A-B super-exchange interaction aligns all magnetic spins at A-site in one direction and those magnetic spins at B-site align in opposite direction thus constituted two saturated and magnetized sublattices at 0 K. Net magnetization of the lattice was the difference between the magnetization of the B and A sublattices. Since neodymium ions were replaced by the ferric ions

at the octahedral site and due to the smaller magnetic moment of neodymium ions as compared to ferric ions, the magnetization at the octahedral site decreased, and hence net magnetization decreased [44]. Verma et al. [45] prepared indium substituted magnesium-manganese-nickel ferrite ($\text{Mg}_{0.2}\text{Mn}_{0.5}\text{Ni}_{0.3}\text{In}_x\text{Fe}_{2-x}\text{O}_4$, $x = 0.1, 0.2, 0.3$) synthesized by the citrate precursor technique and magnetic properties were investigated. They found that as the indium content increased in magnesium-manganese-nickel ferrite, saturation magnetization decreased because indium is diamagnetic and initially, its ions migrated to A-sites. $\text{Mg}_{0.2}\text{Mn}_{0.5}\text{Ni}_{0.3}\text{Fe}_2\text{O}_4$ spinel ferrite on doped with indium ions, $\text{Fe}^{3+}(\text{A})-\text{O}-\text{Fe}^{3+}(\text{B})$ was replaced by $\text{In}^{3+}(\text{A})-\text{O}-\text{Fe}^{3+}(\text{B})$. Due to this replacement, the magnetic moment at the tetrahedral sites decreased and thus the net magnetic moment increased. The substitution of indium ions in place of ferric ions into A sites and the presence of nickel ions at B sites diluted both the A and B sublattices simultaneously. They reported that, saturation magnetizations should increase up to indium content 0.1 due to the smaller dilution of ferric ions at the B-site. The substitution of indium ions created an increasing distortion in the iron environment due to the next nearby neighbor effect, a distortion that reduced electronic symmetry. However, they observed a decrement in saturation magnetization when indium ions concentration increased from $x = 0.0$ to 0.1 [45].

5 Effect of Substitution on Cobalt Ferrite

Tanna et al. [46] prepared manganese substituted cobalt ferrite $\text{Mn}_x\text{Co}_{1-x}\text{Fe}_2\text{O}_4$ ($x = 0-1.0$ step size 0.1) by chemical co-precipitation method and magnetic properties were investigated. They found that as Mn substitution increased, saturation magnetization increased. This happened due to either existence of spin canting: $Y-K$ type of spiral type or deviation from spin only values of Mn^{2+} $5.0 \mu_B$ and Fe^{3+} due to some spin disorder or valence fluctuations in Mn^{2+} and Fe^{3+} [46]. Panda et al. [47] prepared bismuth substituted cobalt ferrite ($\text{CoFe}_{2-x}\text{Bi}_x\text{O}_4$, $x = 0.00, 0.05, 0.1, 0.15$) by auto-combustion technique. The electric and magnetic properties of Bi substituted cobalt ferrite were investigated. They observed an enhancement of saturation magnetization and reduction in coercivity as an increment in Bi substitution in cobalt ferrite. Also, reported that the dc resistivity increased with the increase in Bi substitution in cobalt ferrite. Cobalt occupied the B site in inverse spinel whereas it occupied the A site and B site in partial inverse spinel. As bismuth substitution in the cobalt ferrite brought regulated particle growth, therefore, cobalt ions migrated towards the B site with increment in bismuth content which led to an increase in saturation magnetization. The magnetic moment of the octahedral site increased and the tetrahedral site decreased, so the net magnetization increased [47]. Amaliya et al. [48] prepared titanium substituted cobalt ferrite by sol-gel method and the magnetic properties were investigated. They found that as the titanium content increased in cobalt ferrite, saturation magnetization increased. Generally, Ti^{4+} preferred octahedral site occupation in ferrite, the magnetic moment of that site reduced and so net magnetic moment $M = M_B - M_A$ decreased. The substitution of Ti^{4+} ions in

cobalt ferrite has increased the saturation magnetization. The electrical properties of synthesized specimens were also investigated and found that as titanium content increased in cobalt ferrite, conductivity decreased. The titanium has valency (+4) and it did not play a role in super-exchange interaction. Electron or hole interaction occurred only between ions of the same transition element which has multiple valences. So, decrement in cobalt concentration and increment in Ti^{4+} concentration affected super-exchange interaction and as a result, conductivity decreased [48]. Pandit et al. [49] prepared aluminum substituted cobalt ferrite ($CoAl_xFe_{2-x}O_4$ ($0.0 \leq x \leq 0.8$, step size 0.2)) by standard solid-state reaction method and magnetic properties were investigated. They found that as the aluminum content increased in cobalt ferrite, saturation magnetization decreased. This happened due to Al^{3+} being occupied in the octahedral site which meant Fe^{3+} was replaced by non-magnetic Al^{3+} which led to a decrease in the magnetic moment of the octahedral site when matched with the tetrahedral site. The measurements of dc conductivity of aluminum substituted cobalt ferrite were also carried out and found that dc conductivity was enhanced with increment in temperature and showed the semiconducting behavior of aluminum substituted cobalt ferrite. This happened due to the exchange of electrons among the same transition element having different valences, which were randomly distributed over equivalent crystallographic lattice sites. Most of the conductive part was mostly provided by the electron hopping between Fe^{3+} and Fe^{2+} ion pairs. The increment or decrement in dc conductivity was dependent on the concentration of charge carriers at B-sites [49]. Kadam et al. [50] prepared dysprosium substituted nickel–cobalt ferrite ($Ni_{0.8}Co_{0.2}Fe_{2-x}Dy_xO_4$ ($0.0 \leq x \leq 0.1$, step size 0.0252)) by standard ceramic technique, and the magnetic properties were investigated. They found that as the content of dysprosium increased in nickel–cobalt ferrite, saturation magnetization decreased. This happened due to Dy^{3+} occupied in B-site which meant Fe^{3+} was replaced by magnetic Dy^{3+} which led to a decrease in the magnetic moment of the octahedral site when compared with the tetrahedral site. Electrical properties of dysprosium substituted nickel–cobalt ferrite were also investigated and found that the resistivity decreased with increasing temperature due to the increment in the drift mobility of charge carriers which were thermally activated according to the hopping conduction mechanism. The electrical resistivity changed with the cation distribution in the $Ni_{0.8}Co_{0.2}Fe_{2-x}Dy_xO_4$ ferrites. The variation of dc resistivity with temperature confirmed the semi-conducting nature of the sample [50]. Dabagh et al. [51] have synthesized $Co_{1-x}Cu_xFe_{2-x}Al_xO_4$, ($0 \leq x \leq 0.8$) by co-precipitation method and the magnetic properties of was investigated. They found that as copper–aluminum content increased in cobalt ferrite, saturation magnetization decreased. This happened due to the substitution by non-magnetic Cu^{2+} and Al^{3+} ions. As the content of Cu^{2+} and Al^{3+} increased, the magnetic moment of the A-site and B-site decreased, owing to which the net magnetization decreased [51]. Hashim et al. [52] prepared cerium and dysprosium in cobalt ferrite ($CoCe_xDy_xFe_{2-2x}O_4$ ($0.0 \leq x \leq 0.05$, step size 0.01)) by auto combustion method and the magnetic properties was investigated. They found that with the increment of cerium and dysprosium content in cobalt ferrite, saturation magnetization decreased. Normally, rare-earth (RE) ions

were preferred to occupy the octahedral B site. As per the magnetic moment of transition and rare earth elements, the magnetization value can be increased by doping them into the cobalt ferrites. But the saturation magnetization value decreased with an increase in dopant concentration because the presence of dysprosium ions resulted in weak super-exchange interactions in specimens. Other matters which were considered are spin-orbit coupling and 3d-4f coupling. The spin-orbit coupling effect dominated in rare-earth ions [52].

6 Effect of Substitution on Lithium Ferrite

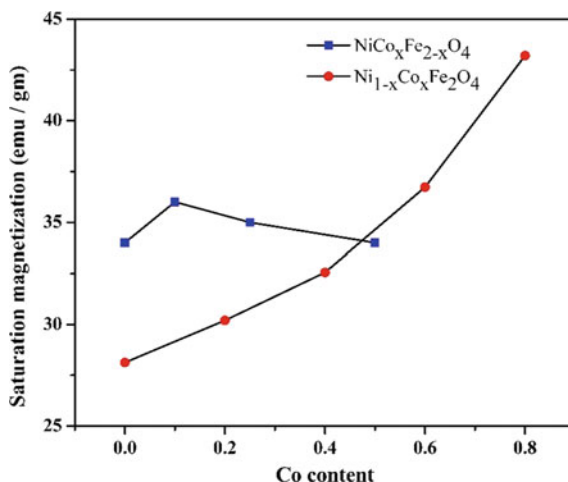
Fu et al. [53] synthesized $\text{Li}_{0.5}\text{Fe}_{2.5-x}\text{Mg}_x\text{O}_{4-\delta}$ ($0 \leq x \leq 1$) ferrite system by standard ceramic method and magnetic properties were investigated. They found that as magnesium content increased in lithium ferrite, magnetization decreased. In the case of Mg^{2+} -substituted lithium ferrite, Li^+ substitution for Fe^{3+} ions at the tetrahedral site led to decrement in the tetrahedral site sublattice magnetization. The Fe^{3+} ions were substituted by non-magnetic Li^+ and Mg^{2+} ions, which led to a decrement in the octahedral site sublattice magnetization. Therefore, the magnetization of tetrahedral and octahedral sublattices decreased. The decrement of the octahedral site magnetization was stronger than one of the tetrahedral sites, which led to a decrease in the net magnetization. The electric properties of magnesium substitute lithium ferrite were also investigated and found that as magnesium content increased in lithium ferrite, electrical conductivity decreased. This happened due to the substitution of magnesium ions for Fe^{3+} ions, Fe^{3+} decreased in magnesium substituted lithium ferrite. Fe^{3+} ions were partially reduced to Fe^{2+} ions in lithium ferrite due to the high-temperature sintering. The content of Fe^{2+} ions was decreased with increased magnesium ions substituted for Fe^{3+} ions. With an increment in the Mg-substituted content, the electrical conductivity was decreased. The Mg^{2+} substituted for Fe^{3+} may restrain the content of Fe^{2+} in lithium ferrite [53]. Simultaneous substitution of 1+, 2+, and 3+ cations in spinel ferrites showed fascinating behavior. Baldha et al. [54] synthesized aluminum-magnesium substituted lithium ferrite ($\text{Mg}_x\text{Al}_{2x}\text{Li}_{0.5(1-x)}\text{Fe}_{2.5(1-x)}\text{O}_4$ ($0.0 \leq x \leq 0.5$, step size 0.1)) by double sintering ceramic technique and investigated magnetic properties at various temperature ranges i.e. 77 and 300 K. It has been observed that saturation magnetization decreased due to increase in magnesium and aluminum content in lithium ferrite. This happened in the synthesized specimens due to Li^+ substitution for Fe^{3+} ions at the tetrahedral site, which led to a decrement in the tetrahedral site sublattice magnetization. The Fe^{3+} ions were replaced by non-magnetic lithium, aluminum, and magnesium ions, which led to a decrement in the octahedral site sublattice magnetization. Hence, the magnetization of tetrahedral and octahedral sublattices decreased. The decrement in the octahedral site magnetization was stronger than the tetrahedral sites, which led to a decrease in the net magnetization [54].

7 Effect of Substitution on Nickel Ferrite

Kambale et al. [55] synthesized cobalt substituted nickel ferrite with a chemical formula $\text{Ni}_{(1-x)}\text{Co}_x\text{Fe}_2\text{O}_4$ by ceramic technique and magnetic properties of this series were investigated. They found that the saturation magnetization and Bohr magneton increased with cobalt content in the NiFe_2O_4 system. This happened due to the replacement of Ni^{2+} ions by Co^{2+} ions on the B site. The magnetic moment per ion for Co^{2+} ions ($3 \mu_B$) was more than that for Ni^{2+} ions ($2 \mu_B$). Therefore, the increment in Co^{2+} substitution on the octahedral sites resulted in an increasing magnetic moment and magnetization enhanced. The electrical properties of synthesized specimens were also investigated and found that the DC resistivity decreased with the increased cobalt concentration. The decrement in DC resistivity happened to the changes in cation distribution, formation of excess Fe^{2+} ions, and the difference in the ionic size of the cations. Due to the higher ionic size of Co^{2+} as compared to Ni^{2+} and Fe^{3+} , its addition distorted the ferrite lattice. The distortions can affect the motion of charge carriers caused by changes in resistivity [55]. The sol-gel auto-combustion method was used to prepare Co^{3+} substituted NiFe_2O_4 [56] by Saffari et al. and magnetic properties were investigated. They found that the saturation magnetization decreased with the increase in cobalt substitution in nickel ferrite. This is because at the initial substitution, a fraction of Co^{2+} ions preferred to occupy the tetrahedral sites, which slightly reduced the magnetic moment of the magnetic ions in tetrahedral sites. With increment in Co^{3+} ions ($x > 0.1$), they were occupied both tetrahedral sites and octahedral sites, which led to a greater reduction in the magnetic moment of octahedral sites than in that of tetrahedral sites. At the initial Co substitution, the Co^{3+} ions of a low magnetic moment ($4 \mu_B$) substituted for Fe^{3+} with a magnetic moment of $5 \mu_B$ in tetrahedral sites led to a slight increase in net magnetization due to the decrease in the tetrahedral site sub-lattice magnetization. In the substitution range of $x > 0.1$, the Fe^{3+} ions of a high magnetic moment ($5 \mu_B$) were replaced with Co^{3+} ions with low magnetic moment values ($4 \mu_B$) in both tetrahedral and octahedral sites and led to a slight decrease at the sub-lattice magnetization at the tetrahedral and octahedral sites. This led to a decrease in net magnetization [56]. Figure 4 shows the effect of Co^{2+} and Co^{3+} on the saturation magnetization of cobalt substituted nickel ferrite. Kamble et al. [55] substituted Co^{2+} in the nickel ferrite while Saffari et al. [56] substituted Co^{3+} in nickel ferrite. As the content of Co^{2+} increased in nickel ferrite, saturation magnetization increased while the content of Co^{3+} increased in nickel ferrite, saturation magnetization decreased.

Patil et al. [57] prepared copper substituted nickel ferrite by standard double sintering ceramic technique. The saturation magnetization was increased with Cu content in $\text{Ni}_{1-x}\text{Cu}_x\text{Fe}_2\text{O}_4$ spinel ferrite. This happened due to a part of copper ions replaced nickel ions and occupied A site while displaced Fe^{3+} ions from A site to B site, increased the content of Fe^{3+} ions in octahedral site, which in turn increased the magnetization in the B site and therefore the net magnetization of the ferrite increased. Cu^{2+} led to improvement in the lattice distortion because Cu^{2+} behaved like a Jahn-Teller ion, which can create a large strain in the spinel ferrite, hence, assuming to

Fig. 4 Effect of Co^{2+} and Co^{3+} on the saturation magnetization of nickel ferrite [55, 56] (Reprinted with permission from Elsevier)



increase the magnetic properties of this spinel ferrite system. As well as temperature-dependent electrical resistivity was decreased due to Cu^{2+} content in $\text{Ni}_{1-x}\text{Cu}_x\text{Fe}_2\text{O}_4$. This happened due to the increase in the thermally triggered drift mobility of charge carriers by the hopping conduction mechanism. In the hopping process, the carrier mobility depended on temperature and was characterized by activation energy. In the case of ferrites, electron hopping between Fe^{2+} and Fe^{3+} and hole hopping between Ni^{3+} to Ni^{2+} and Cu^{2+} to Cu^+ ions in octahedral sites with an activation energy ≈ 0.2 eV was responsible for electrical conduction in bulk $\text{Ni}_{1-x}\text{Cu}_x\text{Fe}_2\text{O}_4$ ferrite. The resistivity and activation energy decreased with increasing copper content. The decrement in resistivity ascribed as the ionic radius of copper (0.72 \AA) was more than the nickel (0.69 \AA) in the copper substituted nickel ferrites. Here, a small amount of Cu^{2+} occupied the A sites displaced Fe^{3+} ions from there to the B sites. This increased in the Fe^{3+} ions in the B sites increased the number of Fe^{2+} and Fe^{3+} pairs in B sites, which increased the conductivity of ferrites. Thus, the conductivity was raised by the substitution of the copper content in this spinel system [57].

8 Conclusion

In Conclusion, the substitution of various cations affects the structural, electrical, and magnetic properties of spinel ferrites. As the spinel ferrite is an insulator and doping of various 1+, 2+ and 3+ cations into their interstitial sites can alter the properties. The simultaneous introduction of nonmagnetic and magnetic ions in the ferrites can change the cation distribution, exchange interaction, nuclear hyperfine field, Curie temperature, spin canting, electrical and dielectric properties of the magnetic oxides. The selective magnetic dilution of either site leads to a non-collinear spin structure. Due to some substitution, there may chance of tetragonal distortion of

cubic spinel ferrites. This interesting behavior can be utilized in many sensor applications. Nonmagnetic doping can raise the possibility of ferrites to use in high-frequency devices. The preparation methods equally play a vital role to modulate the properties of ferrite and hence their applications. By reducing the grain size nanomagnetic ferrites can be produced which are used in biomedical applications. The superparamagnetic behavior of the nano-sized ferrites can be very useful for the hyperthermia process. Nanoferrites can also utilize in waste-water treatment. Altogether, substitution in the spinel ferrites can achieve the choice applications of the prepared materials.

References

1. S. Krupicka, P. Novak, Oxide spinels, in *Ferromagnetic Materials: A Handbook on the Properties of Magnetically Ordered Substances*, vol. 3, ed. by E.P. Wohlfarth (North-Holland, Amsterdam, 1982), pp. 189–304
2. M. Neel, *Ann. Phys.* **12**(3), 137 (1948)
3. H.A. Kramers, *Physica.* **1**, 182 (1934)
4. P.W. Anderson, *Sol. Stat. Phys.* **14**, 99 (1963)
5. J.H. Van Vleck, *J. Phys. Radium* **12**, 262 (1951)
6. J.B. Goodenough, A.L. Loeb, *Phys. Rev.* **98**, 391 (1955)
7. A.K. Jonscher, *Nature* **267**, 673 (1977)
8. M.M. Vijatović, J.D. Bobić, B.D. Stojanović, *Sci. of Sin.* **40**, 235 (2008)
9. D. K. Mehta, M.C. Chhantbar, H.H. Joshi H H, *AIP Conf Proc.* 1665, 050064 (2015)
10. A.R. Tanna AR, H.H. Joshi, *AIP Conf Proc.* 1837, 1(2017)
11. E.J. Verwey, J.H. De Boer, *Rec. Trav. Chim. Phys. Bas.* **55**, 531 (1936)
12. D. Kothari, S. Phanjoubam, J.S. Baijal JS, *J. Mater. Sci.* 25, 5142(1990)
13. C.G. Koops, *Phys. Rev.* **83**, 121 (1951)
14. H. Ismael, M. Nimr, A. Ata, M. Hiti, *J. Magn. Magn. Mater.* **150**, 403 (1995)
15. L.T. Rabinkin, Z.I. Novikova, *Ferrites*, Minsk: Acad. Nauk. (USSR, 1960), 146 I2V
16. S.A. Saafan, A.S. Seoud, R.E. El Shater, *Phys. B* **365**, 27 (2005)
17. R.R. Heikes, W.D. Johnston, *J. Chem. Phys.* **26**, 582 (1957)
18. S.R. Elliott, *Adv. Phys.* **36**, 135 (1987)
19. A. Ghosh, *Phys. Rev. B.* **45**, 11318 (1992)
20. N.H. Vasoya, V.K. Lakhani, P.U. Sharma, K.B. Modi, R. Kumar, H.H. Joshi, *J. Phys. Condens. Matter.* **18**, 8063 (2006)
21. A.J. Bosman, H.J. Van Dall, *Adv. Phys.* **19**, 1 (1970)
22. E.F. Attia, A.H. Zaki, S.I. El-Dek, A.A. Farghali, *J. Mol. Liq.* **231**, 589 (2017)
23. N. Okasha, *J. Alloys Compd.* **490**, 307 (2010)
24. M.A. Gabal, A.M. Abdel-daiem, Y.M. Angari, I.M. Ismail, *Polyhedron* **57**, 105 (2013)
25. V.J. Angadi, B. Rudraswamy, K. Sadhana, S.R. Murthy, K. Praveena, *J. Alloys Compd.* **656**, 5 (2016)
26. N.M. Deraz, A. Alarifi, *Int. J. Electrochem Sci.* **7**(7), 5828 (2012)
27. A. Manikandan, M. Durka, K. Seevakan, S.A. Antony, *J. Supercond. Nov. Magn.* **28**(4), 1405 (2015)
28. U.R. Ghodake, N.D. Chaudhari, R.C. Kamble, J.Y. Patil, S.S. Suryavanshi, *J. Magn. Magn. Mater.* **407**, 60 (2016)
29. H. Mohseni, H. Shokrollahi, I. Sharifi, K. Gheisari K, *J. Magn. Magn. Mater.* 324(22), 3741 (2012)
30. S.D. Chhaya, M.P. Pandya, M.C. Chhantbar, K.B. Modi, G.J. Baldha, H.H. Joshi, *J. Alloys Compd.* **377**(1–2), 155 (2004)

31. M.J. Iqbal, Z. Ahmad, T. Meydan, Y. Melikhov, M.J. Iqbal, Z. Ahmad, J. Appl. Phys. **111**, 033906 (2013)
32. K.P. Thummer, M.P. Pandya, K.H. Jani, K.B. Modi, H.H. Joshi, Mater. Sci. **40**(1), 102 (2004)
33. A.R. Tanna, H.H. Joshi, Int. J. Phys. Math. Sci. **7**(3), 334 (2013)
34. M.T. Farid, I. Ahmad, M. Kanwal, G. Murtaza, I. Ali, J. Magn. Magn. Mater. **428**, 136 (2016)
35. N.M. Deraz, Egypt. J. Chem. **61**(3), 531 (2018)
36. N. Lwin, R. Othman, A.F.M. Noor, S. Sreekantan, T.C. Yong, R. Singh, Mater. Charact. **110**(3), 109 (2015)
37. G. Kumar, J. Shah, R.K. Kotnala, P. Dhiman, R. Rani, V.P. Singh, G. Gurg, E. Shirsath, K.M. Batoo, M. Singh, Ceram. Int. **40**, 14509 (2014)
38. A. Lakshman, M. Province, P.S.V.S. Rao, K.H. Rao, Mod. Phys. Lett. B. **24**(15), 1657 (2010)
39. C. Tsay C, S. Liang, C. Lei, C. Chang, Ceram. Int. **42**(4), 4748 (2015)
40. S. Manouchehri, S. Taghi, M. Benehi, M.H. Yousefi, J. Supercond. Nov. Magn. **29**, 2179 (2016)
41. G. Kumar, S. Sharma, R.K. Kotnala, J. Shah, S.E. Shirsath, K.M. Batoo, M. Singh, Mol. Struct. **1051**, 336 (2013)
42. G. Kumar, J. Chand, A. Dogra, R.K. Kotnala, M. Singh, J. Phys. Chem. Solids. **71**(3), 375 (2010)
43. R. Jasrotia, G. Kumar, K.M. Batoo, S.F. Adil, M. Khan, R. Sharma, A. Kumar, V.P. Singh Phys. B Condens. Matter. **569**, 1 (2019)
44. I. Somnath, R.K. Sharma, M. Kotnala, A. Singh, P. Kumar, V.P. Dhiman, K. Singh, G.K. Verma, J. Magn. Magn. Mater. **444**, 77 (2017)
45. S. Verma, J. Chand, M. Singh, J. Magn. Magn. Mater. **324**(20), 3252 (2012)
46. A.R. Tanna, K.M. Sosa, H.H. Joshi, Mater. Res. Express. **4**, 9393 (2017)
47. R.K. Panda, R. Muduli, D. Behera, J. Alloys Compd. **634**, 239 (2015)
48. P. Amaliya, S. Anand, S. Pauline, J. Magn. Magn. Mater. **467**, 14 (2018)
49. R. Pandit, K.K. Sharma, P. Kaur, R.K. Kotnala, J. Shah, R. Kumar, J. Phys. Chem. Solids **75**(4), 558 (2014)
50. A.A. Kadam, S.S. Shinde, S.P. Yadav, P.S. Patil, K.Y. Rajpure, J. Magn. Magn. Mater. **329**, 59 (2013)
51. S. Dabagh, A.A. Ati, R.M. Rosnan, S. Zare, Z. Othaman, Mater. Sci. Semicond. Process **33**, 1 (2015)
52. M. Hashim, M. Raghasudha, S.S. Meena, J. Shah, E. Sagar, S. Kumar, J. Magn. Magn. Mater. **449**, 319 (2017)
53. Y. Fu, S. Hu, Ceram. Int. **36**(4), 1311 (2010)
54. G.J. Baldha, K.G. Saija, K.B. Modi, H.H. Joshi, R.G. Kulkarni, Mater. Lett. **53**(4–5), 233 (2002)
55. R.C. Kambale, P.A. Shaikh, S.S. Kamble, Y.D. Kolekar, J. Alloys Compd. **478**, 599 (2008)
56. F. Saffari, P. Kameli, M. Rahimi, H. Ahmadvand, H. Salamati, Ceram. Int. **41**(6), 7352 (2015)
57. D.R. Patil, B.K. Chougule, Mater. Chem. Phys. **117**(1), 35 (2009)

Substitution Consequences on Electric and Magnetic Behaviour of Nanoferrites



Meenakshi Dhiman, Balwinder Kaur, Shikha Rana, and Baljinder Kaur

Abstract Although ferrites in bulk as well as in nano dimensions have been extensively studied for more than five decades, still the subject always offers novelty with abundance of potential to be explored and utilized. To understand the behaviour of dopants, scope of enhancement and to achieve desired properties, an attempt has been made to collate various existing theories and understanding of basic and advanced mechanisms. Furthermore, an intensively studied review on the results as reported by many researchers is presented here to assist the readers in assessing the already studied, differently doped ferrites for their magnetic and electrical properties.

Keywords Ferrites · Dielectric constant · Saturation magnetization

1 Introduction

The word “ferrite” is borrowed from “ferrum”, a latin dictionary word which meant iron. Nanoferrite is a class of metal oxide with cubic crystalline arrangement according to the formula $\text{MeO} \cdot \text{Fe}_2\text{O}_3$, where Me is a divalent metal ion [1]. These dopants in various concentrations when introduced by replacing metal ions, produce engineered nanoferrites with specific characteristics. Interestingly, these properties have been found to be closely associated and influencing the magnetic and electric behaviours upon substitution with the suitable metals. Apart from electric and magnetic alterations, these materials exhibit interesting dielectric properties giving

M. Dhiman (✉)

Department of Applied Sciences, Chitkara University, Punjab, India
e-mail: meenakshi.dhiman@chitkara.edu.in

B. Kaur

Government Degree College, R S Pura, Jammu, India

S. Rana

Himachal Pradesh University, Shimla, India

B. Kaur

Wazir Ram Singh, Government College, Dehri, Kangra, India

them a favour in comparison to pure transition metal compounds in various techniques. Magnetite with $\text{Fe}^{2+}\text{Fe}^{3+}\text{O}_4$ ($\text{FeO}\cdot\text{Fe}_2\text{O}_3$) structure is a typical found nanoferrite. In 1909, Hilpert made a first lab made ferrite by a chemical way and later after 1940 various synthesis techniques were developed to control ferrite structure. Snoek and Philips laboratory prepared first economical ferrites and still possessed colossal market share [2]. Afterwards, J. L. Snoek, Kato and Takei organized deliberate studies on industrial uses of ferrites [3]. Later, a few research articles were also published by Snoek and Neel considering basic understanding of structural and ferromagnetic properties [4, 5], focussing on theoretical explanations. These research papers open up the comprehensive analysis in the applicative fields of ferrites to till date.

2 Classification of Ferrites

2.1 Magnetic Classification: Soft and Hard Ferrites

Nanoferrites are distinguished according to their magnetic behaviour as soft and hard nanoferrite. The first class of nanoferrite has high permeability and does not retain countable applied magnetic field however the second class is known for sustained magnetic properties and its flux—multiplication behaviour has increased its applications areas in sensing devices and medical fields. According to internal arrangements of the ions, first group of nanoferrites has cubic inverse spinel structure with a homogeneous arrangement of iron and divalent ions in oxygen lattice as like in the case of Ni–Zn and Mn–Zn ferrites. The second group of nanoferrites possessed permanent magnetism with high coercive field values and generally M-type nanoferrites possess magnetoplumbite arrangement of iron and divalent ions.

2.2 Structural Classification of Ferrites

Researchers classified nanoferrites according to the arrangement of iron and divalent ions positioning in the structure and divided them generally in four major groups: (I) hexagonal, (II) spinel, (III) garnet and (IV) orthoferrite (Table 1).

However, the focus of this chapter is on the study of spinel ferrites related domains only.

Spinel ferrites (Cubic ferrite with inverse spinel structure)

Nanoferrites have typical ferrite structure i.e., $\text{FeO}\cdot\text{Fe}_2\text{O}_3$ and Spinel ferrite is the most commonly investigated class of nanoferrite due to its easy synthesis techniques and diversified applications. The nanoferrite spinel arrangement is similar to the composition of mineral spinel having cubic arrangement of iron oxide and metal

Table 1 Structural classification of ferrites

Type	Structure	General formula	Example
Spinal	Cubic	MFe_2O_4	M = Mn, Cu, Li, Mg, Ni, Zn, Cd etc.
Garnet	Cubic	$Ln_3Fe_5O_{12}$	M = HO, Y, Sm, Gd, Ho, Er etc.
Magnetoplumbite	Hexagonal	$MFe_{12}O_{19}$	M = Ba, Sr
Ortho-ferrites	Pervoskite	$LnFeO_3$	Ln = Same as in garnet

oxide structures. In this spinel arrangement, as suggested by Bragg [6] and Nishikawa [7], the unit cell has 8 molecules of ferrites. The spinel structure has fcc arrangement of oxygen ions in which metal ions are situated at the interstitial sites. The structure has two types of sites according to coordination number i.e., tetrahedral and octahedral sites, also named as A site and B site respectively [8]. In the inverse spinel nanoferrites, the divalent sites occupy octahedral sites and tetrahedral sites are equally occupied by trivalent ions. Generally, Ni and Co doped ferrites have this type of structure which leads to their net magnetization and ferromagnetic nature. Commonly employed ferrites in various fields are mixed spinel structured, which provides excellent electrical and magnetic characteristics to them.

3 Magnetic Interactions

It is well known that the conductivity [9] and the magnetic properties of ferrimagnetic oxides are governed by the Fe–Fe interaction (spin coupling of the 3d electrons). By introducing rare earth ions I into the spinel lattice, the R–Fe interactions appear (3d–4f coupling), leading to changes in both the electrical and magnetic behavior in the ferrites (Fig. 1).

In nanoferrites, commonly two categories of magnetic interplays transpire between two crystallographic sites and are: (i) Direct and (ii) Indirect exchange interactions. The first type of magnetic interactions is associated with the direct overlapping between the magnetic ions orbitals (named as T_{2g} and E_g orbitals in starting transition elements). These interactions explain the Neel molecular field concept by using inter distance between magnetic ions and exclude the concept of powerful Weiss field. The second type of interactions was proposed by Kramers and Anderson [10, 11], which include magnetic interplay between two magnetic ions through the intermediate anions. These interactions are named as superexchange interactions and are generally exhibited by distant located magnetic ions. In nanoferrites, direct and superexchange interactions, both have a significant role to play in governing magnetic behavior. For small distance, direct interactions exist and for large distances, superexchange interactions dominate. Figure 2 shows magnetic interactions in ferrites. The first type of magnetic interactions involves overlapping between T_{2g} or E_g orbitals. This overlapping extent depends on inter orbital distance. The second type of interaction between magnetic ions involves the interaction between T_{2g} and E_g orbitals

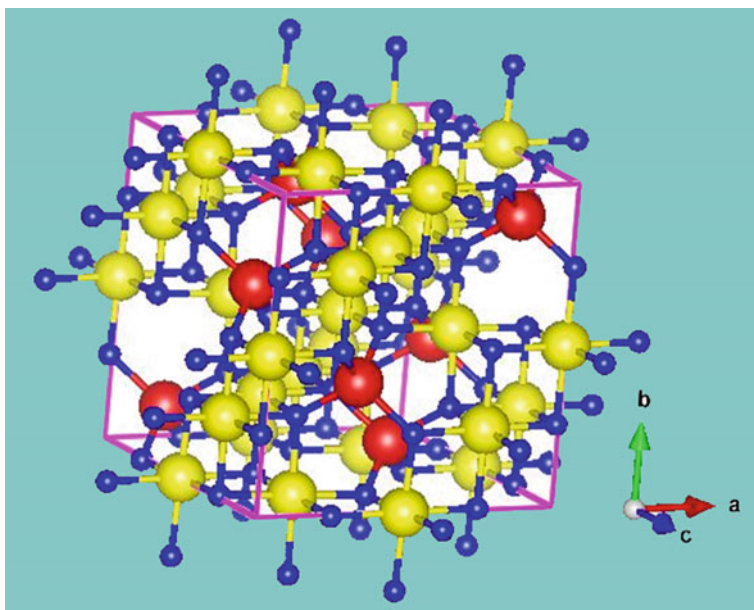
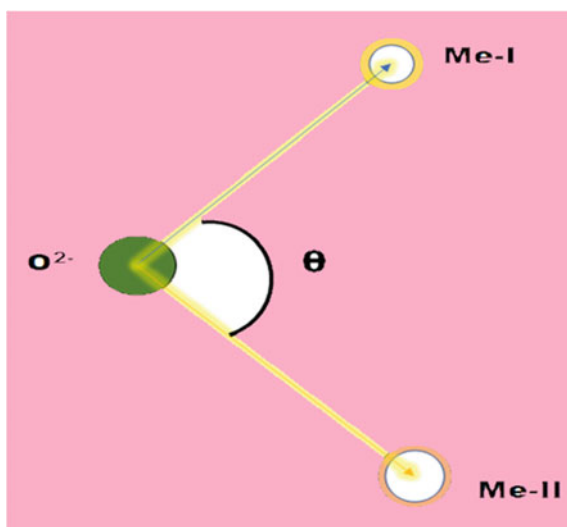


Fig. 1 Unit cell structure depiction of doped Magnesium-Manganese ferrite. (Octahedral sites are represented by yellow balls whereas and the Red coloured balls depict the tetrahedral sites)

Fig. 2 Me(I)–O–Me(II) interaction angles in ferrites



including the 2p orbitals of the anions also. T_{2g} orbitals consist of d_{xy} , d_{yz} and d_{xz} orbitals while E_g orbitals are the d_z^2 and the $d_{x^2-y^2}$. The p orbitals along x, y and z-axis are generally found to take part in these interactions. The nature and stability of these magnetic interactions rely on the inter bond sign and distance present between magnetic ions and involved anions. The semi—empirical rules to calculate these interactions were studied by Goodenough [12] and Kanamori [13]. These interactions were basically developed for two angles (180° and 90°) configurations only. There are generally three interactions namely A–B, B–B and A–A. On the basis of distances (p , q , r) and angle θ , it was concluded that A–B interactions have the greatest magnitude. In these interactions, the distance is small and the angle θ is also high. In B–B interactions, the distance is small as compared to A–A interactions and the angle is also very small. In A–A interactions, the angle is $\approx 80^\circ$, so the interaction is weakest. Therefore $|J_{AB}| > |J_{BB}| > |J_{AA}|$, where J_{AB} , J_{BB} and J_{AA} are the exchange integrals and this situation leads to collinear arrangement in which moments on A sites are antiparallel to the moments on B sites. In order to understand the behaviour of ferrites on substitution on magnetic and electric properties, it is important to understand the underlying theories on magnetic interactions and electric conduction mechanisms.

4 Theories on Magnetic Interactions

4.1 Neel's Theory

In 1948 Neel, explained Ferromagnetic nature of ferrites and provided alterations to Weiss theory by presuming the following points:

- The overall magnetization of the crystal lattice is contributed from both the subparts known as tetrahedral and octahedral sites of the geometrical structure of the ferrites.
- The overall magnetization is the result of A–B and B–A identical interactions between these sites. These identical interactions are predominant over interaction between same sites.
- In ferrimagnets, the similar sites interactions are identical but magnitude wise they differ as the number of neighboring atoms at a particular site varies according to crystal lattice.

According to Neel, the magnetization of ferrites is can be divided as

$$H = H_0 + H_m \quad (1)$$

where, H_0 and H_m are magnetic field applied externally and molecular field internally, which is caused by interatomic interactions between atoms. As there are different

molecular fields at both the crystal sites, the magnetic moment on both the sites is unequal, represented as μ_A and μ_B respectively.

Let us suppose there are 'n' similar ions present per unit volume and 'λ' subpart is situated with A site and rest portion $\nu(1 - \lambda)$ is situated with B sites such that, $\lambda + \nu = 1$.

Now, A site magnetization, $M_A = \lambda n \mu_A$.

If, $n \mu_A = M_a$ then $M_A = \lambda M_a$ and similarly $M_B = \nu M_b$.

Hence, overall magnetization is can be written as,

$$M = M_A + M_B = \lambda M_a + \nu M_b \quad (2)$$

The molecular field acting on sublattice A is

$$H_{mA} = -\gamma_{AB} M_B + \gamma_{AA} M_A \quad (3)$$

Now, the molecular field coefficients, γ_{AB} and γ_{AA} have negative and positive signed interactions if it is present between A and B ions and A and A ions.

$$\text{Similarly } H_{mB} = -\gamma_{AB} M_A + \gamma_{BB} M_B \quad (4)$$

The coefficient γ_{AA} and γ_{BB} are unequal and can be expressed as fractions of γ_{AB} .

$$\alpha = \frac{\gamma_{AA}}{\gamma_{AB}} \text{ and } \beta = \frac{\gamma_{BB}}{\gamma_{AB}} \quad (5)$$

The molecular fields are then

$$H_{mA} = \gamma_{AB} (\alpha \lambda M_a - \nu M_b) \quad (6)$$

$$H_{mB} = \gamma_{AB} (\beta \nu M_b - \lambda M_a) \quad (7)$$

Which are valid above near Curie temperature.

Here γ 's are the appropriate molecular field coefficients. It may be shown that.

$\gamma_{AB} = \gamma_{BA}$ but $\gamma_{AA} \neq \gamma_{BB}$ unless the two sublattice are identical.

Pauthenet confirmed the validity of Neel's theory of sublattice magnetization in ferrites [14].

4.2 Yafet-Kittel Theory of Ferrimagnetism

In some magnetic spinels, Neel's spin ordering model [5] was found inadequate with obtained results. Their magnetic characteristics are explained by the concept of no-collinear spin ordering. Yafet and Kittel [15] suggested a non-collinear spin

ordering concept by ignoring Neel's explanation of parallel spin ions at the both crystallographic axis. Hence, their explanation includes various spin arrangements. Neel's model explanation holds well when A–B site interactions are predominant. However, when A–A and B–B interactions are comparable to A–B interactions, the two sub-lattice model (Neel's model) is no longer applicable and triangular model becomes energetically favorable. Yafet and Kittel [15] proposed that with the doping of non-magnetic dopant in the crystal structure, one sub-lattice leads to canted position of spins on other sublattices. After doping, let us suppose the B sub lattice get divided into two parts as B_1 and B_2 , with similar magnetic moments (θ_{YK}) having the overall magnetization in parallel way of B at 0 K. According to YK theory, the overall magnetic moment can be explained as following

$$\mu(x) = \{ [2(1-x) + 5(1+x)]^B \cos \theta_{YK} - [5(1-x)]^A \} \quad (8)$$

He showed that in a few spinel structures, there exist three sublattices with triangular spin arrangement (Yafet Kittel type Ferrimagnetism) and these structures have low energy in comparison to the general collinear two-sublattice Neel structure (Neel type ferrimagnetism). If ϕ is the angular deviation from the collinear model, the energy is given by

$$E = 8N_0 [6J_{ab}S_aS_b \cos \phi - J_{bb}S_b^2(2 \cos \phi + 1)] \quad (9)$$

where a and b are two sublattices. E is minimum for negative J_{ab} , positive J_{bb} and $\phi = 0$, which is the Neel state. However, if J_{bb} is also negative and if the ratio of the exchange energies ($r_{ex.}$) is

$$r_{ex.} = \frac{J_{bb}S_b}{J_{ab}S_a} > \frac{3}{4} \quad (10)$$

Then the Neel state ceases to be a minimum and the magnetization vectors of the sublattices will be bent from collinear position by angle ϕ such that

$$\cos \phi = \frac{3J_{ab}S_a}{4J_{bb}S_b} \quad (11)$$

Yafet and Kittel proved that Neel model is applicable for $r_{ex.} < \frac{3}{4}$ if the total number of sublattices i.e., the number of different magnetic ion sites, is restricted to 6. A modification of YK theory was proposed by Lotgering [16] to permit A and B sites canting and antiferromagnetism with the usual ferromagnetism order. The YK theory has its interesting features in the possibility of magnetic ordering transition between various possible configurations at temperatures other than that where spontaneous magnetization appears.

5 Electrical Conduction and Mechanism

As it is a known fact that, when the ferrites doped with other suitable dopants such as rare earth ions, there is a significant modification in the structure of the material owing to the stress factor generated due to dopants which leads to enhancement, not only in magnetic but also in electric properties of the material [17]. Apart for having a vast application due to enhanced magnetic nature, these materials are most promising in numerous and versatile applications based on exemplary electrical properties such as in telecommunication, microwave, high frequency transformation, electrochemical energy storage, biomedicines, gas sensing, humidity sensing etc. [18, 19]. Method of preparation composition of the material sintering environment and position of cation distribution that is tetrahedral or octahedral are very essential features and fundamental conditions for the study of ferrites.

6 Theories on Electrical Conduction Mechanism

6.1 Verwey's Hopping Mechanism

E. J. W. Verwey proposed that, the electronic conduction in ferrites is mainly due to hopping of electrons between ions of the same element present in more than one valence state, distributed randomly over crystallographic equivalent lattice sites. It is a thermally activated process and takes place in the presence of lattice vibrations. The hopping probability depends upon the distance between the ions and the activation energy [20]. The distance between two metal ions at B sites is smaller than the distance between a metal ion at B site and other metal ion at an A site because ferrites structurally form cubic close packed oxygen lattices with the cations at the octahedral (B) and the tetrahedral (A) sites, therefore electron hopping between B and A sites under normal conditions, has a very small probability compared with that for B–B hopping. Hopping between A and A sites does not exist for the simple reason that there are only Fe^{3+} ions at the A sites and any Fe^{2+} ions formed during processing, preferentially occupy B sites only [21]. The temperature dependence of electrical conductivity is given by the following relation:

$$\sigma = \sigma_o \exp \frac{-E}{kT} \quad (12)$$

where, ' k ' = Boltzman's constant, ' E ' = activation energy and ' σ_o ' = a constant.

In ferrites, the activation energy denotes the lattice deformation energy. When electrons and holes both participate in the conduction mechanism, then the total conductivity will be as follows;

$$\sigma = q\{n\mu_n + p\mu_p\} \quad (13)$$

In this, q denotes the charge on electron, whereas n represents electron concentration and p represents hole concentration. μ_n and μ_p give its mobilities. As with the increase in temperature, in ferrites the carrier concentration doesn't change much, so that, the temperature dependence of conductivity mainly arise because of the temperature dependence of mobilities of electrons as well as holes and the same can be expressed as follow

$$\mu_n = \frac{ed^2 f_n \exp -\frac{E_n}{kT}}{KT} \quad (14)$$

$$\mu_p = \frac{ed^2 f_p \exp -\frac{E_p}{kT}}{KT} \quad (15)$$

where ' d ' = octahedral sites jump length, f_n and f_p are the jumping process lattice frequencies, and E_n and E_p are the activation energies for electron and holes respectively. Jonker [22] and Elwell et. al [23] have applied the above stated model to analyze the Ni and Co ferrites.

6.2 Polaron Model

When an electron carrier is trapped in a site as a result of the displacement of adjacent atom or ion then a defect is created known as polaron defect. The entire defect is drifted by an activated hopping mechanism. The drift of small polaron is driven by hopping of both the electron from the nearest involved sites [24, 25]. The drift mobility for free lattice can be represented as;

$$\mu = \frac{(1 - c)ea^2R}{KT} \quad (16)$$

here ' e ', a and c are the electronic charge, lattice parameter and fraction of site having an electron ' n ' because $c = \frac{n}{N}$ is the number of electrons and ' N ' the number of sites/unit volume. The polaron jump rate ' R ' between two adjacent sites can be expressed as;

$$R = P\mu_o, \exp\left[\frac{-E}{KT}\right] \quad (17)$$

where, ' μ_o ', E and P are the appropriate optical mode phonon frequency, activation energy, and factor which gives the probability that the electron will transfer after the polarized configuration has moved to the adjacent site respectively. From above equations we get;

$$\mu = [p(1 - c)ea^2] \left[\frac{\mu_o}{KT} \right] \exp \left[\frac{-E}{KT} \right] \quad (18)$$

If we consider only electronic conduction, the conductivity can be expressed as;

$$\sigma = ne\mu \quad (19)$$

$$\sigma = [Npc(1 - c)e^2a^2] \left[\frac{\mu_o}{KT} \right] \exp \left[\frac{-E}{KT} \right] \quad (20)$$

$$\sigma = \frac{A}{T} \exp \left[\frac{-E}{KT} \right] \quad (21)$$

Low value of mobility and thermally activated hopping is explained by this model.

6.3 Phonon Induced Tunneling

Srinivasan and Srivastava gave detailed description about the electrical behavior of ferrites by using the concept of phonon induced tunneling [26]. They explained the electrical behavior by assuming that the electrons do tunneling from one site to another through the $Fe^{2+} = Fe^{3+} + e^{-1}$ exchange process and are firmly coupled to the crystal structure also. Using this explanation,

$$\sigma = \frac{\sigma_o \frac{u}{KT}}{\exp \frac{u}{KT} + \exp \frac{-u}{KT}} \quad (22)$$

The conductivity can be expressed as given above. Nearest neighbor distance of $Fe^{2+}-Fe^{3+}$ is given by factor σ_o and u represents the exchanged lattice energy by oxygen ions when they move between the two crystallographic sites situated iron ions.

7 Effect of Substitution on Magnetic Properties of Ferrites

From last two decades, many researchers have observed changes in magnetic behaviour in ferrites after doping different elements. For instance, G. Kumar et al. have observed decrease in magnetization at room temperature after doping with one of the rare-earth (Gadolinium) ion in the Mg–Mn Ferrite. They also confirmed that with rare earth ion doping, the magnetic saturation curve became super paramagnetic in nature. Author concluded that decrease in magnetization at B-site could be the possible reason for this decrease, which further concludes that the dopant ion has replaced iron ion at B-site and decreases the A–B site magnetization in the prepared

ferrites. The observed behaviour is in accordance to Neel's theory of ferromagnetism, as discussed in the earlier section of the chapter. They have also investigated the magnetization behaviour in analogy to temperature change and observed that Curie temperature values are decreasing with increase in dopant concentration [27]. In one of the similar studies S. Amiri et al. have synthesized rare earth doped Co ferrite and found that for different rare earth dopants, coercivity values are increases differently due to rise in magneto-crystalline anisotropy. Saturation magnetization and Curie temperature values decreases with rise in ionic radii of doped rare earth elements [28]. Transition elements are also found to show unique characteristics because of d-electrons present in outer shells. K. El Maalam and his co workers have synthesized transition metal doped Tin ferrite and investigated that for different dopants they show different behaviour. For manganese doped ferrites, the magnetization values are higher than Nickel and Cobalt doped ones [29]. Similarly, P. Kumar et al. prepared Lanthanum doped Co ferrite by precipitation method. They analysed that magnetic behaviour deteriorates with increase in concentration of transition metal in mother samples. As Co ferrite has inverse type structure, the doping of a non magnetic type of dopant results into decrease in overall magnetization [30]. Whereas, A. Fransco Jr. and his team prepared Bismuth doped Co ferrite and investigated low temperature magnetization behaviour. They analyzed that magnetic anisotropy and coercivity varies with dopant concentration and temperature. Coercivity found to increase with increase in dopant concentration and anisotropy rises with fall in temperature. These observed results are attributed to replacement of Co ions from octahedral sites by Bismuth ions [31]. M. Dhiman et al. have synthesized d-block element (Yttrium) and f-block element (Samarium) doped Mg ferrite and found decrease in magnetization after doping and concluded that this decrease is due to replacement of B site Iron by Diamagnetic dopants [32]. Same group of researchers has prepared Holmium doped Mg–Mn mixed ferrite and found decrease in magnetization with increase in doping [33]. Whereas, they have investigated the magnetic characteristics of Scandium doped Mg–Mn ferrite samples too and found increase in magnetization with doping concentration. The magnetic loop shows increase in superparamagnetic nature with scandium doping which is attributed to spin disordering in the magnetic structure of the prepared samples [34]. So, it can be concluded that magnetic behaviour of the ferrites immensely depends on the site preference of the doped element and its concentration (Fig. 3).

There have been abundant studies on effect of substitution on magnetic properties of Ni Zn doped ferrites, some of the very relevant ones are listed here. Venkatraman Manikandan et al. prepared Ru doped Nickel ferrite by co-precipitation technique and found rise in particle size with rise in preparation temperature. With rise in temperature, the enlargement in particle size leads to increase in saturation magnetization, coercivity and retentivity of the prepared samples, thus concludes dependence of magnetic parameters and spin ordering of ferrites on particle size and synthesis temperature [35]. M. R. Patil and his co-workers [36] synthesized Cd doped Ni Zn ferrite and found decrease in Curie temperature and magnetic saturation of the mother sample. This behavior is attributed to the replacement of magnetic ion in the crystal structure by non magnetic ions which further leads to decrease in net

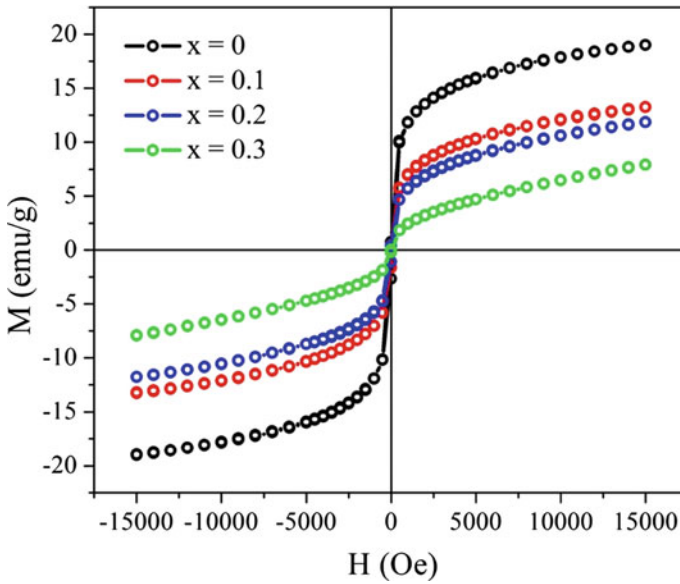


Fig. 3 M–H Loops for $\text{Mg}_{0.9}\text{Mn}_{0.1}\text{Fe}_{(2-x)}\text{Ho}_x\text{O}_4$ particles ($x = 0, 0.1, 0.2$ and 0.30) [33]. Reprinted with permission from Elsevier

magnetization of the structure. A. E. Virden et al. had synthesized and investigated various samples of Ni–Zn ferrite by co precipitation and found that their electrical behaviour is governed by electron hopping between A and B site which is dependent on the dopant concentration and their site preference [37]. K. Rama Krishna et al. has synthesized a series of doped NiZn ferrite samples by employing sol gel technique and analyzed the magnetic behavior of the samples. They found that the magnetic saturation rises with Zinc doping upto 80% replacement of nickel ions from the ferrite composition. This rise is attributed to the Zinc ion placement at A sites specifically, which leads to rise in net magnetization of the samples [38]. Recently Shiwen Li et al. prepared spherical shaped rare earth metal (Sc, Dy and Gd) substituted NiZn ferrite samples by co precipitation technique. They found magnetic behavior of the samples to vary with type of dopant and observed an increase in superparamagnetic nature of the same. The Gd doped samples are found to have maximum superparamagnetic characteristic depicted in hysteresis graph [39]. A. V. Knyazev and his co researchers have analyzed the magnetic behavior of NiZn and Co doped NiZn ferrite samples. They found increase in magneto crystalline anisotropy of the prepared sample with Co doping which increase the coercive field values also. The observed magnetic saturation results were less than the corresponding bulk values [40]. Jalel Massoudi et al. have synthesized Aluminium doped NiZn ferrite samples and studied them for magnetic properties by varying temperatures. They reported a fall in Curie temperature with rising sintering temperature of the synthesized materials. This change may be attributed to dependence of Curie transition on grain size which varies from nano

to micro scale [41]. B. S. Tewari and his group has prepared Sn doped NiZn ferrite and analysed EPR spectra to study magnetic behavior of the samples. The observed EPR spectra confirm the presence of Fe^{3+} ions in the structure and g values confirms superexchange interactions in the samples [42]. M. P. Ghosh et al. have synthesized Gd doped NiZn ferrite by co-precipitation method and found that the superparamagnetic behavior at 5 K temperature and decrease in magnetic saturation with dopant concentration. At both the temperatures 5 and 300 K, magnetic behavior deteriorates with doping which is due to decrease in particle size. The observed Mössbauer spectra shows sextet corresponding to both the sites and low isomer shift values also confirm Fe trivalent ions in the structure [43]. Y. Hong et al. have studied effect of doping of divalent magnesium ion in the NiZn ferrite prepared by high temperature sol gel technique. They investigated their magnetic behavior and found soft natured hysteresis curves for the prepared samples with minimal changes in the saturation values with change in doping. They also found increase in crystallite size and decrease in lattice parameter with doping concentration [44]. In the similar way, H. Moradmard et al. doped Magnesium in nickel ferrite and found decrease in magnetic saturation and increase in coercive field values with doping. This observed behavior is attributed to substitution of Fe trivalent ion by divalent non magnetic dopant and finite size and nanosurface effects observed in ferrites [45]. S. Nag and his team prepared Er doped NiZn ferrite samples by auto combustion technique and found decrease in the size of the prepared samples after doping. The prepared samples show superparamagnetic relaxation in the Mössbauer spectra with clear sextets. The hysteresis curves of the samples show soft magnetic nature with increase in coercive field values after doping which is explained due to increased anisotropy and spin canting in the samples [46]. As one of the earliest studies, N Rezlescu et al. have studied rare earth doped NiZn ferrites and investigated the magnetic results too. They observed dependence of magnetic behavior on the ionic radii of the dopant. They observed decrease in permeability due to internal stress created by rare earth dopants in the crystal structure [47]. Y. Köseoğlu et al. have prepared Cr doped NiZn ferrite samples by hydrothermal method and studied their magnetic behavior. The magnetic behavior of the doped samples is studied with temperature variation and it was reported that the magnetic saturation and blocking temperature values, both decreases after doping. The doped samples exhibit ferromagnetic and superparamagnetic like characteristics at low and high temperatures respectively [48]. Super-para-magnetism has been reported by Hashim et al. on substitution of varying concentrations of Indium in $\text{Ni}_{0.5}\text{Cu}_{0.25}\text{Zn}_{0.25}\text{Fe}_{2-x}\text{In}_x\text{O}_4$ at 325 K [49]. Apart from Mg–Mn and Ni–Zn, Mn–Zn, a very important class of soft ferrites has been studied intensively by researchers for magnetic behaviour on substitution of different types of dopants their magnetic behaviour by combustion synthesis method. P. P. Naik et al. has prepared Nd doped Mn–Zn ferrite by employing combustion technique. They found small shrinkage in the crystal structure with rise in dopant concentrations. This decrease in size is also related further to decrease in magnetic saturation results [50]. They found that with dopant concentration lattice parameters rises and produce strain in the structure which is due to large ionic size of the dopant. This produced strain leads to decrease in crystallite and grain size further. The rise in dopant concentration leads to increase

in A–B interactions followed by rise in magnetic saturation. The internal magnetic behaviour and presence of iron in trivalent state is justified by low isomer shift values found in Mössbauer spectra [51]. Recently V. Jagadeesha Angadi et al. has employed sol gel combustion technique to prepare Gd and Sm doped Mn Zn ferrite and found magnetic behaviour decrease with increase in dopant concentration [52]. E. De Fazio and his co-workers studied Li doped Mn–Zn ferrite and reported rise in saturation magnetization with dopant concentration [53].

8 Effect of Substitution on Electric Properties of Ferrites

Synthesis parameters and composition of ferrites greatly influence the electric characteristics of the ferrites [54]. To determine the effect of substitution on various electric properties of ferrites, such as electric conductivity (AC and DC), resistivity, temperature coefficient of resistance, dielectric strength, dielectric constant and dielectric loss tangent factors are studied and results are analysed. In ferrite nano-materials, there is electrons' hopping between ion pairs of same type of elements on equal sublattice with different valance state. Hoping in electrons and ions presents in different valance states cause the conductivity of material and this is circulated over the crystal lattice sites. In ferrites, electron hoping increases between Fe ions in B-site as Fe^{2+} and Fe^{3+} ions are produced during synthesis. Electric properties of various ferrites which are dopped with different metal ions and the effect of dopants on these properties are discussed below.

The resistivity of the material is explained using Verwey's hopping mechanism [20] that gives an insight on how electronic conduction in ferrites is largely due to electron hopping between same element ions, present in various valence states and arranged arbitrarily on crystal lattice. By virtue of having two crystal sites, the probability of hopping relies on the activation energy and inter-distance between the ions involve. As reported by Naik and Hasolkar, in nanocrystalline material $\text{MnFe}_{2-x}\text{Gd}_x\text{O}_4$ the DC resistivity of materials increases for all the samples within the range of 300–773 K. Resistivity of the samples at room temperature was found to be 10^6 – $10^7 \Omega$ [55]. In this material, the grain size was reported as 8–24 nm, and due to this, there is an increase in grain boundaries. As grain boundaries are generally non conducting, so they contribute an increase in electric resistance. Also, as Fe^{3+} ions are replaced by Gd^{3+} , which is a source of charge carriers, and Gd^{3+} has large ionic radii, electron hopping also decreases and further due to that, lattice constant increases. As in the lower range of temperature, resistivity decreases slowly as thermal charges are released slow [56] but as temperature approaches 441 K, an extreme reduction in resistivity is noted, which shows semiconductor behaviour of material as per Arrhenius equation [57]. This indicates that secondary electrons also support the conduction process by decreases the resistivity of the material [58]. The activation energy is evaluated by incorporating the dc-resistivity results with the Arrhenius relation, i.e.

$$\rho = \rho_0 \exp\left(\frac{E_a}{KbT}\right) \quad (23)$$

Chhaya and Kulkarni also reported resistivity-temperature dependence for Al-Cr substituted ferrite [59]. On similar basis, M. J. Iqbal et al. also reported that at room temperature resistivity of magnesium ferrite with different concentration of Co-Cr increases from 7.50×10^8 to 1.47×10^9 [60] which is 100 times higher than previously doped spinal ferrites resistance for Ca^{2+} , Zn^{2+} , Zr-Mn, Co-Ni, and Zr-Ni [61–66]. $\text{Mg}_{1-x}\text{Co}_x\text{Cr}_x\text{Fe}_{2-x}\text{O}_4$ shows lowest value for $x = 0.0$ gives 0.75×10^9 and for $x = 0.5$ value of resistivity is 3.47×10^9 [60]. For $\text{Mg}_{1-x}\text{Tb}_x\text{Fe}_2\text{O}_4$, with the increase in concentration from 0.02 to 0.2 of Tb, the resistivity also increases from 2.33×10^6 Ω cm to 5.71×10^7 Ω cm [67]. $\text{Mg}_{1-x}\text{Cu}_x\text{Cr}_x\text{Fe}_{2-x}\text{O}_4$ ($x = 0.0$ –0.7) gives minimum value for resistance at $x = 0.0$ is 0.553×10^5 and maximum value at $x = 0.7$, with observed resistivity of 0.105×10^8 Ω cm [68]. Electrical conductivity also depends upon temperature and frequency. At lower frequencies, conductivity also increases slowly but at higher frequencies, conductivity increases rapidly. At high frequencies, conductive nature of grain boundaries is more active [69, 70]. $\text{Mg}_{1-x}\text{Co}_x\text{Cr}_x\text{Fe}_{2-x}\text{O}_4$ shows lowest value for activation energy at $x = 0.0$, which is reported to be 0.35 and for $x = 0.5$ value of activation energy is 0.58 [60], For $\text{Mg}_{1-x}\text{Cu}_x\text{Cr}_x\text{Fe}_{2-x}\text{O}_4$ ($x = 0.0$ –0.7) gives minimum value for activation energy at $x = 0.0$ which is 0.0391 and a maximum value at $x = 0.7$ which is equals to 0.45 [68]. U. R. Ghodake et al. have synthesized doped Mg Zn ferrites for electrical studies and found that with Manganese doping, the electrical resistivity increases with temperature. The dielectric studies confirm the interfacial polarization in the samples and show decrease in dielectric constant values with rise in frequency in the beginning, then remain constant and similar behaviour was observed for all the samples [71]. The dielectric loss factor decrease with rise in dopant concentration initially and then rises gradually. J. Z. Msomi and his co-workers have studied the electrical properties of different samples of MgMn ferrite and found that the I–V graph have negative slope which shows resistance rises with dopant concentration. The electrical resistivity is found to vary inversely with temperature which also confirms the semiconducting behaviour of the prepared ferrites [72]. S. Mahalakshmi et al. have prepared rare earth doped Nickel ferrite samples. They found Nd and Gd doped samples have higher conductance than others, which is attributed to the free electrons of their f-shells. The dielectric results of the ferrites depend on the electron exchange phenomena through iron ions. After doping with rare earth ions, dielectric constant value decrease with both dopant concentration and frequency and the dielectric loss values rises with frequency for all compositions [73]. H. K. Fadafan et al. have studied changes in the electrical behavior of Mn–Zn ferrites after Co doping. They found that DC resistivity attains a peak which is attributed to cation reordering and spin canting in the ferrite structure. The resistivity value rises with dopant concentration which is also supported by the change in lattice parameters and hopping length due to size of dopant [74]. Shyam K. Gore et al. have studied Mg–Zn ferrite system and analyzed that their dielectrical behavior is temperature and dopant concentration dependent.

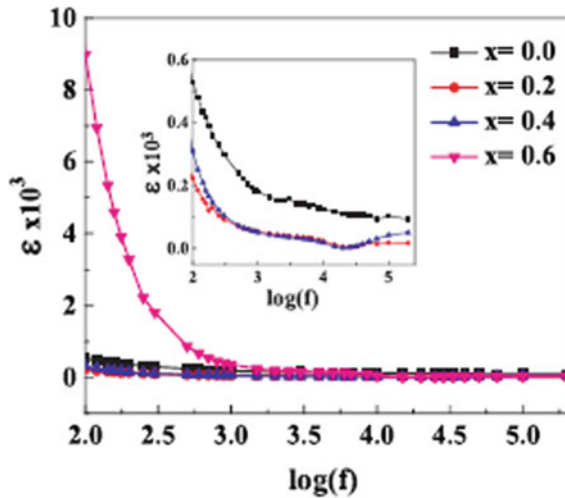


Fig. 4 Variation of dielectric constant (ϵ) with frequency in $\text{Ni}_{0.8-x}\text{Cu}_x\text{Zn}_{0.2}\text{Fe}_2\text{O}_4$ ferrites [77]. Reprinted with permission from Elsevier

For all the samples, dielectric constant varies in accordance with temperature change and loss tangent decreases with temperature for all the dopants [75]. P. P. Hankare et al. have synthesized various Cr doped Mg ferrite by co-precipitation technique and found that DC resistivity varies inversely with rise in temperature which is justified by hopping mechanism between A and B sites of the ferrite structure. The values of electrical resistivity are also found to depend on the dopant concentration [76]. M. Houshiar et al. have used auto-combustion technique to prepare Copper doped NiZn ferrite. They analyzed their electrical nature and found that the dielectric constant and tangent loss factors increase at low frequency values which is due to change in the crystal density and size [77] (Fig. 4).

C. Venkataraju et al. have studied effect of Ni doping in MnZn ferrite and found direct dependence of resistivity on dopant and inverse behavior with rise in temperature. They also investigated dielectric behavior and found that the dielectric constant value varies inversely with dopant concentration for most of the samples [78]. A. D. Sheikh and his co-workers have prepared and investigated NiZn ferrite system for electrical behavior. They performed electrical study for two different temperature sintered samples and found that the dielectric loss decreases with frequency [78]. L. George et al. reported a linear rise in AC conductivity with frequency of applied field indicating small polaron hopping mechanism in Mn substituted Ni-Zn mixed ferrite doped with Gd ions [78].

9 Conclusion

It is understood that the unusual variation in structural properties, electrical and magnetic behaviour, in ferrites is dependent not only on the concentration and nature of the dopant but also on the distribution of substituted metal ion. The preference of site, whether octahedral or tetrahedral, has a bigger role in deciding the developed magnetic properties in the ferrite apart from the magnetic nature of the substituent itself. Similarly, the presence of dopant cations with multiple oxidation states, by virtue of free available electrons for hopping play a significant role in tailoring the electrical properties in the ferrite. Subsequently, cation distribution is one of the most effective and determining factor to study the electric and magnetic behaviours of doped ferrites.

References

1. A. Sharma, K.M. Batoo, O.M. Aldossary, S. Jindal, N. Aggarwal, G. Kumar, J. Mater. Sci.: Mater. Electron. **32**, 313 (2021)
2. R.S. Waldron, *Ferrites—An Introduction for Microwave Engineers* (D. Van Nostrand Company Ltd., Canada, 1961)
3. K. Yogoro, T. Takeshi, Jpn Patent **98**, 844 (1932)
4. J.L. Snoek, *New Developments in Ferromagnetic Materials* (Elsevier, New York, 1947)
5. L. Neel, Ann. de Phys. **3**(12), 137 (1948)
6. W.H. Bragg, Nature **95**, 561 (1915)
7. S. Nishikawa, Proc. Tokyo Math. Soc. 2nd Ser. **8**, 199–209 (1915)
8. F.W. Barth, E. Posnjak, Zeitschrift Für Kristallographie-Cryst. Mater. **82**, 379 (1932)
9. N. Rezlescu, E. Rezlescu, C. Pasnicu, M.L. Craus, J. Phys. Condens. Matter **6**, 5707 (1994)
10. H.A. Kramers, Physica **1**, 182 (1934)
11. P.W. Anderson, Phys. Rev. **79**(2), 350 (1950)
12. J.B. Goodenough, Prog. Solid Suppl. **3**, 96 (1964)
13. J. Kanamori, J. Phys. Chem. Solids **10**(2–3), 87 (1959)
14. R. Pauthenet, J. Appl. Phys. **30**(4), S290 (1959)
15. Y. Yafet, C. Kittel, Phys. Rev. **87**, 290 (1952)
16. E.W. Gorter, F.K. Lotgering, J. Phys. Chem. Solids **3**, 238 (1957)
17. R.R. Powar, V.D. Phadtare, V.G. Parale, S. Pathak, K.R. Sanadi, H.-H. Park, D.R. Patil, P.B. Piste, D.N. Zambare, Mater. Sci. Eng. B Solid-State Mater. Adv. Technol. **262**, 114776 (2020)
18. J. Shah, M. Arora, L.P. Purohit, R.K. Kotnala, Sens. Actuat. A Phys. **167**(2), 332 (2011)
19. J.H. Verwey, E.J.W. De Boer, Recl. des. Trav. Chim. des Pays-Bas **55**(6), 531 (1936)
20. A. Lakshman, P.S.V.S. Rao, B.P. Parvatheeswara Rao, K.H. Rao, J. Phys. D. Appl. Phys. **38**(5), 673 (2005)
21. G.H. Jonker, J. Phys. Chem. Solids **9**, 165 (1959)
22. D. Elwell, B A Griffiths R Parker. Br. J. Appl. Phys. **17**, 587 (1966)
23. E.H. Snow, A.S. Grove, B.E. Deal, C.T. Sah, J. Appl. Phys. **36**(5), 1664 (1965)
24. R.H. Walden, J. Appl. Phys. **43**(3), 1178 (1972)
25. G. Srinivasan, C.M. Srivastava, Phys. Status Solidi **103**(2), 665 (1981)
26. G. Kumar, J. Shah, R.K. Kotnala, V.P. Singh, Sarveena, G. Garg, S.E. Shirsath, K.M. Batoo, M. Singh, Mater. Res. Bull. **63**, 216 (2015)
27. S. Amiri, H. Shokrollahi, J. Magn. Mater. **345**, 18 (2013)
28. K. El Maalam, M.B. Ali, H. El Moussaoui, O. Mounkachi, R. Masrour, E.K. Hlil, A. Benyoussef, J. Alloys Compd. **622**, 761 (2015)

29. P. Kumar, S.K. Sharma, M. Knobel, J. Chand, M. Singh, J. Electroceramics **27**(2), 51 (2011)
30. A. Franco, F.L.A. MacHado, V.S. Zapf, F. Wolff-Fabris, J. Appl. Phys. **109**(7), 4 (2011)
31. M. Dhiman, S. Rana, K.M. Batoo, J.K. Sharma, M. Singh, Integr. Ferroelectr. **184**(1), 151 (2017)
32. M. Dhiman, S. Rana, Sanansa, N. Kumar, M. Singh, J.K. Sharma, J. Mater. Sci. Mater. Electron. **32**(7), 8756 (2021)
33. M. Dhiman, S. Rana, M. Singh, J.K. Sharma, Integr. Ferroelectr. **202**(1), 29 (2019)
34. V. Manikandan, A. Mirzaei, S. Vignesvelvan, S. Kavita, R.S. Mane, S.S. Kim, J. Chandrasekaran, ACS Omega **4**(7), 12919 (2019)
35. M.R. Patil, M.K. Rendale, S.N. Mathad, R.B. Pujar, Inorg. Nano-Metal Chem. **47**(8), 1145 (2017)
36. A.E. Virden, K. O'Grady, J. Magn. Mater. **290–291**(2), 868 (2005)
37. K.R. Krishna, K.V. Kumar, C.R. Gupta, D. Ravinder, Adv. Mater. Phys. Chem. **2**(3), 149 (2012)
38. S. Li, J. Pan, F. Gao, D. Zeng, F. Qin, C. He, G. Dodbiba, Y. Wei, T. Fujita, J. Mater. Sci.: Mater. Electron. **32**, 13511 (2021)
39. A.V. Knyazev, I. Zakharchuk, E. Lähderanta, K.V. Baidakov, S.S. Knyazeva, I.V. Ladenkov, J. Magn. Mater. **435**, 9–14 (2017)
40. J. Massoudi, M. Smari, K. Nouri, E. Dhahri, K. Khirouni, S. Bertaina, L. Bessais, El K. Hlil, RSC Adv. **10**, 34556 (2020)
41. B.S. Tewari, A. Dhyani, S.K. Joshi, S. Dubey, K. Pandey, Conf. Pap. Sci. **816970**, 2356 (2014)
42. M.P. Ghosh, S. Mandal, S. Mukherjee, Eur. Phys. J. Plus **135**, 41 (2020)
43. Y. Hong, W. Zhou, Z. Cheng, H. Huang, Z. Wu, S. Liao, G. Luo, J. Mater. Sci.: Mater. Electron. **31**, 16975 (2020)
44. H. Moradmard, S.F. Shayesteh, P. Tohidi, Z. Abbas, M. Khaleghi, J. Alloys. Compds. **48**(29), 116 (2015)
45. S. Nag, A. Roychowdhury, D. Das, S. Das, S. Mukherjee, J. Magn. Mater. **466**, 172 (2018)
46. Y. Köseoğlu, Ceram. Inter. **41**(5), 6417 (2015)
47. M. Hashim, S.E. Shirsath, S.S. Meena, R.K. Kotnala, S.Kumar, D. Ravinder, M. Raghasudha, P. Bhatt, E. Şentürk, Alimuddin, R. Kumar, J. Magn. Mater. **381**, 416 (2015)
48. A. Sharma, K.M. Batoo, E.H. Raslan, G. Kumar, J. Mater. Sci.: Mater. Electron. **31**, 16959 (2020)
49. P.P. Naik, R.B. Tangsali, S.S. Meena, S.M. Yusuf, Mater. Chem. Phys. **191**, 215 (2017)
50. V.J. Angadi, K. Manjunatha, K. Praveena, V.K. Pattar, B.J. Fernandes, S.O. Manjunatha, J. Husain, S.V. Angadi, L.D. Horakeri, K.P. Ramesh, J. Magn. Mater. **529**, 167899 (2021)
51. E. De Fazio, P.G. Bercoff, S.E. Jacobo, J. Magn. Mater. **323**(22), 2813 (2011)
52. S. Zahi, A.R. Daud, M. Hashim, Mater. Chem. Phys. **106**(2–3), 452 (2007)
53. P.P. Naik, S.S. Hasolkar, J. Mater. Sci. Mater. Electron. **31**(16), 13434 (2020)
54. S.S. Hasolkar, P.P. Naik, J. Alloys Compd. **823**, 153605 (2020)
55. R.A. Reddy, K.R. Rao, B.R. Babu, G.K. Kumar, C. Rajesh, A. Chatterjee, N.K. Jayothi, Structural, electrical and magnetic properties of cobalt ferrite with Nd³⁺ doping. Rare Met. (2019). <https://doi.org/10.1007/s12598-019-01285-4>
56. G. Kumar, J. Shah, R.K. Kotnala, P. Dhiman, R. Rani, V.P. Singh, G. Garg, S.E. Shirsath, K.M. Batoo, M. Singh, Ceram. Inter. **40**(9), 14509 (2014)
57. U.V. Chhaya, R.G. Kulkarni, Mater. Lett. **39**(2), 91 (1999)
58. M. Javed Iqbal, Z. Ahmad, T. Meydan, Y. Melikhov, J. Appl. Phys. **111**(3), 033906 (2012)
59. S.D. Chhaya, M.P. Pandya, M.C. Chhantbar, K.B. Modi, G.J. Baldha, H.H. Joshi, J. Alloys Compd. **377**, 155 (2004)
60. P.K. Roy, J. Bera, J. Mater. Proc. Tech. **197**(1–3), 279 (2008)
61. M.J. Iqbal, M.R. Siddiquah, J. Magn. Mater. **320**(6), 845 (2008)
62. I.H. Gul, F. Amin, A.Z. Abbasi, M. Anis-ur-rehman, A. Maqsood, Scripta Mater. **56**(6), 497 (2007)
63. M.N. Ashiq, S. Saleem, M.A. Malana, Anis-Ur-Rehan, J. Alloys Compds. **486**(1–2), 640 (2009)
64. J. Chand, G. Kumar, S. Thakur, S.K. Sharma, M. Singh, A.I.P. Conf. Proc. **1349**, 1169 (2011)

65. M.A. Khan, M.U. Islam, M. Ishaque, I.Z. Rahman, *Ceram. Inter.* **37**(7), 2519 (2011)
66. S. Yonatan Mulushoa, N. Murali, M. Tulu Wegayehu, S.J. Margarette, K. Samatha, *Results Phys.* **8**, 772 (2018)
67. C.G. Koops, *Phys. Rev.* **83**(1), 121 (1951)
68. L.G. Van Uitert, *J. Chem. Phys.* **24**(2), 306 (1956)
69. U.R. Ghodake, N.D. Chaudhari, R.C. Kambale, J.Y. Patil, S.S. Suryavanshi, *J. Magn. Magn. Mater.* **407**, 60 (2016)
70. J.Z. Msomi, T. Moyo, H.M.I. Abdallah, J.J. Dolo, *J Supercond Nov Magn* **26**, 1021 (2013)
71. S. Mahalakshmi, K. SrinivasaManja, S. Nithiyantham, *J Supercond Nov Magn* **27**, 2083 (2014)
72. H.K. Fadafan, R.L. Orimi, S. Nezhadeini, Effect of Co doping on the magnetic and DC electrical properties of Mn–Zn nanoferrites. *J. Magn. Magn. Mater.* **456**, 98–103 (2018). <https://doi.org/10.1016/j.jmmm.2018.02.025>
73. S.K. Gore, U.B. Tumberphale, S.S. Jadhav, R.S. Kawale, M. Naushad, R.S. Mane, *Phys. B: Condens. Matter* **530**, 177 (2018)
74. P.P. Hankarea, V.T. Vader, N.M. Patil, S.D. Jadhav, U.B. Sankpal, M.R. Kadam, B.K. Chougule, N.S. Gajbhiye, *Mater. Chem. Phys.* **113**, 233 (2009)
75. M. Houshiar, L. Jamilpanah, *Mater. Res. Bull.* **98**, 213 (2018)
76. C. Venkataraju, G. Sathishkumar, K. Sivakumar, *J. Alloys Compds.* **498**, 203 (2010)
77. A.D. Sheikh, V.L. Mathe, *J. Mater Sci* **43**, 2018 (2008)
78. L. George, C. Viji, M. Maheen, E.M. Mohammed, *Mater. Res. Bull.* **126**, 110833 (2020)

The Role of Nanoferrites in Bio-medical Applications



Sarveena

Abstract Magnetic nanoferrites have shown immense potential in the biomedical applications due to its ability to precisely control the behavior by application of external magnetic field. Superior magnetic properties of ferrites make them promising nanoagents in various applications like targeted drug delivery, magnetic separation, biosensors, MRI, antimicrobial agents and magnetic hyperthermia (MHT). The challenge is to maintain the high magnetization which decreases when size is reduced to nanoscale, hence the engineering of these nanoferrites is of prime importance, where selection of appropriate synthesis method plays very important role. Hence the parameters like morphology, biocompatibility, chemical and physical properties affect the efficiency of nanoferrites in biomedical applications.

Keywords Nanoferrites · Superparamagnetism · Toxicity · MRI · Targeted drug delivery · Magnetic hyperthermia

1 Introduction

Nanoferrites have numerous biomedical applications due to their size comparable to biological molecules and excellent magnetic properties, which are prerequisites for all biomedical applications. Due to the transparency of biological tissues to magnetic field, various properties can be tuned when nanoferrites interacts with magnetic field. These unique properties of magnetic nanoferrites along with the stability, sensitivity and easy functionalization makes them the future biomedical materials in numerous applications like targeted biosensors, drug delivery, MRI imaging, magnetic separation, antimicrobial agents, magnetic hyperthermia, detoxification, photoablation therapy [1, 2]. The magnetic characteristics of ferrite nanoparticles strongly affect its performance in biomedical applications. For example, saturation magnetization is

Sarveena (✉)

Department of Physics, Chandigarh University, Gharuan, Mohali, Punjab, India

one of the most prominent magnetic parameters closely linked to the thermal conversion efficiency of magnetic nanoferrites [3, 4]. Toxicity is another very crucial parameter for the use of the ferrite nanoparticles in the biomedical applications. Nanoparticles which are superparamagnetic at room temperature are preferred for the biomedical use. Among various nanomaterials iron oxide nanoparticles (Fe_3O_4) have been successfully applied in vivo (targeted drug delivery, MRI, and tissue engineering) and in vitro (magnetic transfection, magnetic separation and magnetic sensing/detection) due to their low toxicity and the superparamagnetism at the nanoscale [5]. Another effective method for enhancing the magnetic properties is to dope Fe_3O_4 with divalent cation (Ni^{2+} , Zn^{2+} , Mn^{2+} , Co^{2+} , Mg^{2+} , etc.). The various ferrites such as Co, Ni, Zn etc. shows the potential in numerous biomedical applications owing to their biocompatibility and large magnetic anisotropy [6–13].

The real challenge is to maintain the high magnetization which decline when size is reduced to nanoscale. Hence, the engineering of these nanoferrites for increased magnetic response in biomedical applications is very important where selection of appropriate synthesis method plays very important role. The surface engineered nanoferrites promote the chemical and biological functionalization for improved bioselectivity, biocompatibility, and drug encapsulation ability etc. to enhance the interaction with tissues or cells. The most commonly used methods for synthesis of metal oxide nanoparticles are sol–gel, thermal decomposition, solvothermal, reverse micelle, hydrothermal method, microwave assisted method, co-precipitation and flow synthesis etc. [14, 15]. The parameters like morphology, chemical and physical properties and biocompatibility are highly influenced by the synthesis method being used. Nanoferrites have widespread biomedical applications and each application requires nanoferrites with some special features. It is beyond the scope of this chapter to address all the biomedical applications, so we will mainly focus on the role of nanoferrites in MRI, targeted drug delivery and magnetic hyperthermia.

2 MRI (Magnetic Resonance Imaging)

MRI is among the most powerful and versatile techniques used for diagnostic radiology as well as for therapeutic purpose. It is the standard clinical methods which locate the position and size of tumour and also make distinction between pathological and healthy tissues [16]. MRI uses non ionizing radiation and magnetic field for three dimensional anatomical imaging of human body. The magnetic properties of the body help to create the complete image of any part of body. Hydrogen is present in abundance in fat and water and has a significant magnetic moment required for creating image. MRI images are better in quality, resolution and diagnostic accuracy. Major limitation of MRI is the time duration needed for issues associated with high-power magnetic field, imaging and claustrophobia (As the patient is placed in the MRI magnet with the position of head at the centre of magnetic field). Any movement of the patient can distort the quality of image [17].

The body part, whose image is to be recorded, is placed in strong magnetic field. When magnetic field is applied the proton gets excited and radio waves are released, which are measured by a receiving coil. These radio signals provide information of the position by changing magnetic field by gradient coils. The repeating noise characteristic of an MR scanner is produced when it is turned on and off alternately [18]. Figure 1 shows schematic of basic principles of MRI [19]. When an external magnetic field (B_0) is applied, the protons tend to align with the direction of the external magnetic field either in the direction of the field (parallel to the external field) or anti-parallel to the external field. If alternating magnetic field (B_1) is applied to static magnetic field (B_0), the magnetic moment of the proton is interrupted from the B_0 direction. Figure 1b, c shows that during relaxation, protons lose energy by longitudinal relaxation (T_1) and transverse relaxation (T_2). MRI is based on the dipole-dipole interaction between magnetic nanoferrite and surrounding water molecules to minimize the T_1 or T_2 of water protons. The contrast ability of the MR contrast agent is estimated by relaxivities i.e. longitudinal relaxation rate (r_1) and transverse relaxation rate (r_2) per millimolar of agent [3]. T_1 contrast agents are used in clinical applications as extracellular agents and T_2 contrast agents are used in imaging of blood pool. T_2 contrast agent can be used to differentiate normal and cancer tissues.

Relaxivity is affected by different relaxation mechanisms known as inner sphere and outer sphere mechanisms. The direct bonding of water molecules and paramagnetic ions is required in the relaxation of the protons of the inner sphere, while the relaxation of the external sphere protons is related to the dephasing of coherent proton spins. The contribution of the internal sphere mechanism cannot be overlooked when the size of the nanoparticle is below 5 nm, which indicates that the improvement of T_1 relaxation is affected by the relaxation of the protons of the external sphere and the internal sphere [20, 21].

Magnetic spinel nanoferrites are used as contrast agents as they have the ability to affect the relaxation process when accumulated on tissue. These ferrite materials help in accelerating the spin-spin relaxation (T_2 relaxation) rather than the spin lattice relaxation (T_1 relaxation) [22, 23]. Iron oxides like Fe_3O_4 and Fe_2O_4 have been extensively used as contrast agents on account of their chemical stability, biodegradability, non-toxicity [21]. Javid Muhamad Arshadet. al. [24] investigated cobalt ferrite nanoparticles as MRI contrast agent. Co-ferrite has the potential to be used as T_2 contrast agents of higher relaxivity. The relaxivity coefficient was found to increase with size. For comparing contrast enhancement on MRI images four rabbits of same weight were taken. Signal intensity generated by iron oxides (for liver, $I = 1433 \pm S.D = 111.5$, spleen, $I = 1009 \pm S.D = 96.5$) and cobalt ferrites (for liver, $I = 1513 \pm S.D = 102.2$, spleen $I = 1694 \pm S.D = 219.2$) contrast agents is shown in Fig. 2a-c. Cobalt ferrites were found to induce a high signal intensity of T_2 contrast agents in comparison to iron oxide nanoparticles. Metal doped MR contrast agents may be used for clinical purposes to diagnose various diseases in liver and spleen.

The shape and size of nanoparticle also affect the relaxivity coefficient. In case of the cobalt ferrite nanoparticles, there was increase in relaxivity coefficient with increase in size and the faceted irregular nanostructures showed higher relaxivity coefficient as compared to spherical nanostructures [25]. Zinc ferrite nanoparticles

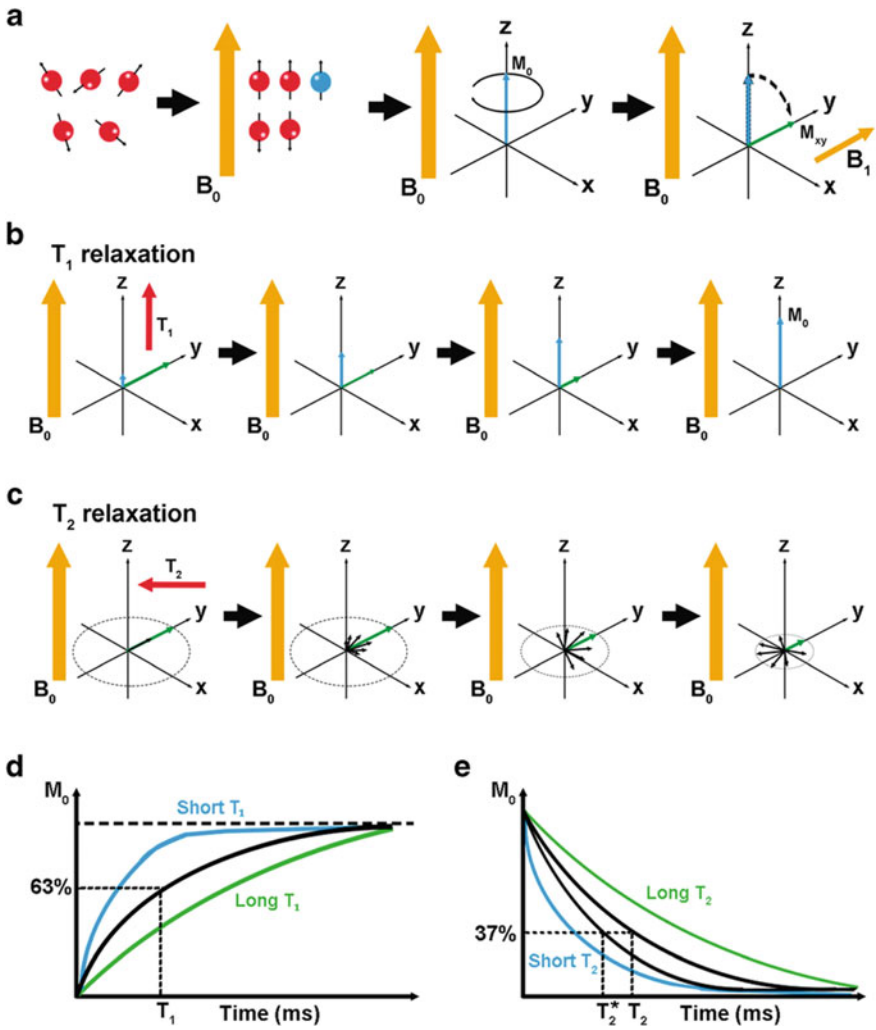


Fig. 1 Schematic representation of the fundamental principles of MRI. **a** Red balls represent the protons spinning around their own axis and orange arrow represents magnetic field B_0 . The difference between the protons aligned parallel and antiparallel to magnetic field B_0 (blue ball) represents the protons responsible for the MRI signal. The sum of these protons can be described using a magnetisation vector (M_0 , blue arrow). **b** T_1 and **c** T_2 relaxation are displayed respectively. **d** The time required to achieve the 63% of the original longitudinal magnetization is called T_1 relaxation. Tissues with short T_1 values are shown by blue curve and the tissues with long T_1 values are shown by green curve. The time it takes to de-phase up to 37% of the initial value is known as T_2 relaxation [19]. Reprinted with permission from Springer Nature

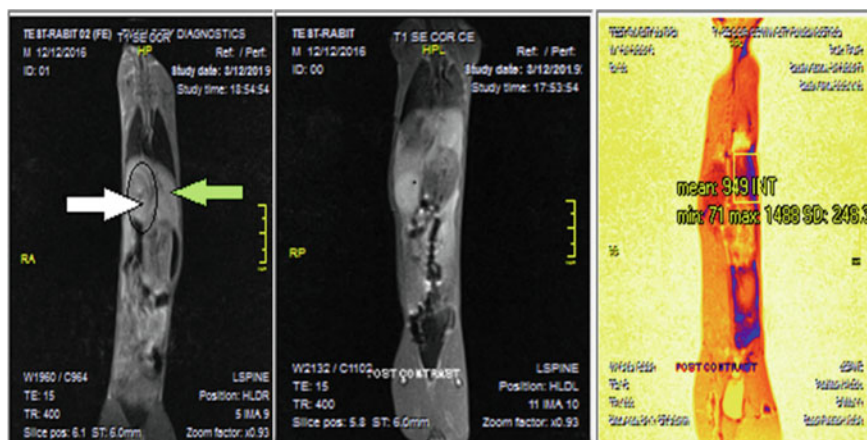


Fig. 2 MRI scans of the liver and spleen, **a** contrast agent Fe_3O_4 , **b** contrast agents Cobalt ferrites-20%wt, **c** contrast agents Cobalt ferrites-40%wt. [white arrow depicts the anatomy of stomach of rabbit, whereas the green arrow depicts the liver of rabbit] [24]. Reprinted with permission from Elsevier

$\text{Zn}_x\text{Fe}_{1-x}\text{OFe}_2\text{O}_3$ (up to $x = 0.34$) enclosed in polymeric micelles were also found to show increased T_2 relaxivity and improved detection sensitivity in MRI [26]. Manganese nanoferrites have high magnetic saturation and are superparamagnetic, which makes them suitable candidates as MRI contrast agents. The Manganese nanoferrites are capable of enhancing the transverse relaxivities as negative contrast agents (T_2 -weighted) and depend on particle size. The relaxivity is directly related to the particle size and magnetic moment of nanoparticles. In MnFe_2O_4 , the transverse relaxivity increases with particle size [27–29]. The T_1 and T_2 relaxivities of silica-coated manganese ferrite nanoparticles in water were 1.42 and $60.65 \text{ s}^{-1} \text{ mM}^{-1}$ respectively and r_2/r_1 was 48.91, which confirm that these nanoparticles have potential as highly efficient T_2 contrast agents [30].

Khairul Islam et. al. [31] explored chitosan (CS) coated MnFe_2O_4 nanoparticles in magnetic resonance imaging and relaxivity variation with concentration was linear (Fig. 3).

Figure 3a shows images obtained at echo times (TEs) of 14 ms of the nanoparticle of sizes 5, 6, 10, and 15 nm for chitosan coated manganese ferrites nanoparticles with different concentrations values of 0.17, 0.34, 0.51, 0.68 and 1.03 Mm. The degree of darkness increased with the increase of nanoparticle concentration. Figure 3b represents the dependence of concentration of relaxation at the different particle size = 5, 6, 10, 15 nm which is linear. 5.3c shows that relaxivity r_2 is linearly dependent on nanoparticle size. The size, surface, morphology and metal composition of nanoparticles plays important role in development of high-performance T_2 contrast agents [32, 33].

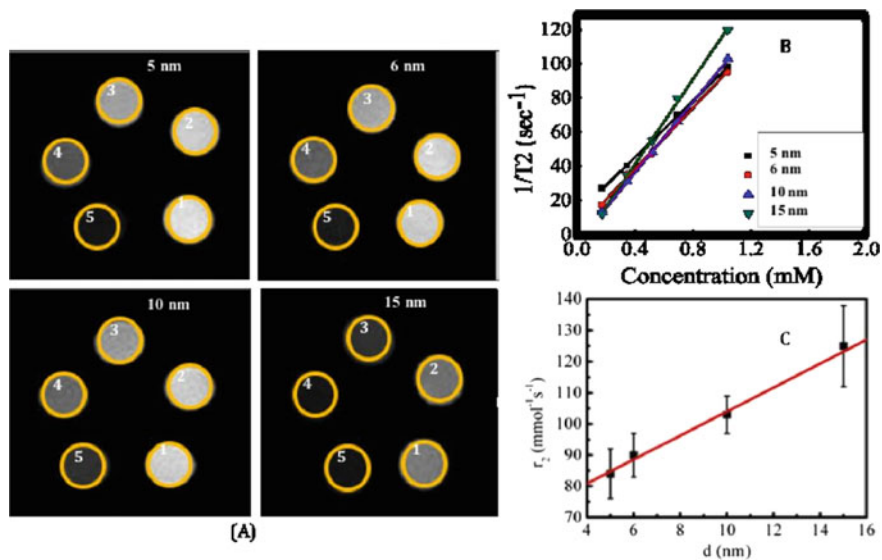


Fig. 3 MRI data of MnFe_2O_4 coated with chitosan spinel ferrites nanoparticles. **a** Images obtained at TE of 14 ms, **b** absolute R_2 (or $1/T_2$) mapping images for nanoparticles of sizes 5, 6, 10, and 15 nm at different concentrations. **c** Relaxivity (r_2) of chitosan coated MnFe_2O_4 nanoparticles as a function of nanoparticle size [31]. Reprinted with permission from MDPI

3 Targeted Drug Delivery

With the development of biomedical nanotechnology, traditional drug delivery systems have evolved into smart drug delivery systems with stimuli-responsive characteristics [34]. In the conventional way of any disease treatment, the drugs are usually orally taken or injected, which result in the distribution of the drug through the whole body to arrive the affected part. It can adversely affect the healthy part and can even cause serious problems to the person also. The challenge associate with conventional method can be overcome by targeted drug delivery; it reduces the side effects and dosage and hence improves the efficacy of treatment. Targeted drug delivery also known as smart drug delivery is a special form of drug delivery system in which medication is selectively delivered only to the affected site and not to the non-targeted tissues [35, 36]. Targeted drug delivery is potentially promising in applications for the treatment of diseases like nervous system diseases, cancers, sudden sensorineural hearing loss etc. [37].

Nanoparticles, drug and targeting molecules are three main components of targeted drug delivery systems. The nanoparticles are the promising drug delivery agent due to their unique properties and various nanostructures as delivery agents like polymers, nanotubes, nanowires, liposomes, quantum dots, monoclonal antibodies and fragments, mesostructures, dendrimers have been developed [38, 39]. When drug is loaded inside the nanostructure it results in the formation of drug-loaded structure

by forming a chemical bond with the surface. It is desired that the drug should arrive at the target site with minimal interaction with healthy tissues which is feasible only with the target molecule. Target molecule plays important role to prevent premature drug release from the nanocarriers during interaction with body fluid or blood cells. The bio-physicochemical properties of the delivery vehicle e.g. charge, size, nature and density of the ligands on their surface, surface hydrophilicity can affect the biodistribution and circulating half-life of the particles [40].

In general, there are two modes of targeting: active and passive targeting. In passive targeting accumulation of nanoparticles takes place on organ or tissue due to their physicochemical properties like size and surfaces. Active targeting on the other hand uses stimuli-responsive or surface-functionalized nanodevices with homing moieties for nanoparticles accumulation on the desired organ/tissue or cells by either [41, 42]. Figure 4 shows the active and passive targeting. In passive targeting extravasation of particles passively takes place through the leaky vasculature, which is attributing of inflamed tissue and solid tumors. When the particles have extra vasated in the target cell or tissue, the presence of ligands on the surface of particle result in active targeting of particles to receptors that are present on target cell or tissue resulting in improved accumulation and cell uptake through receptor mediated endocytosis.

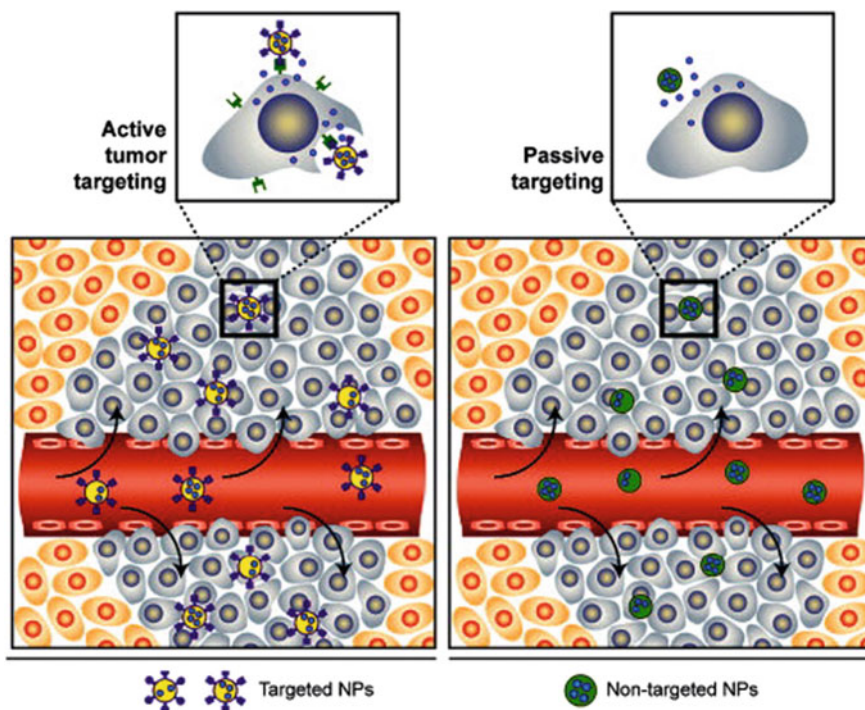


Fig. 4 Passive and active targeting [40]. Reprinted with permission from ACS

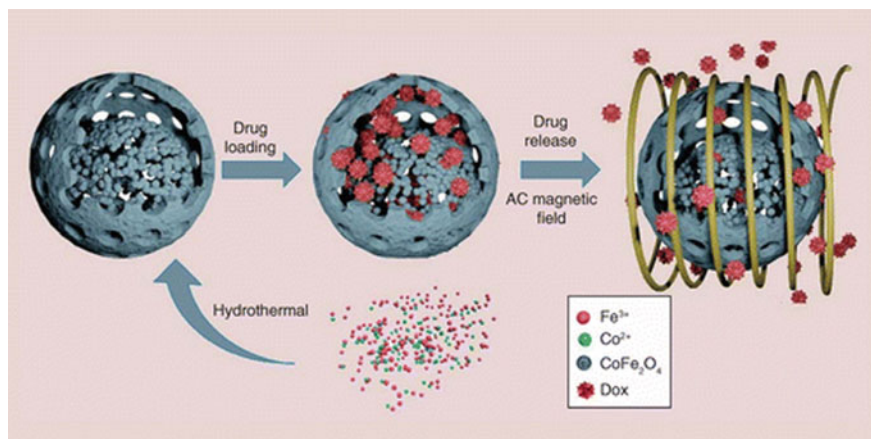


Fig. 5 Illustration of the drug loading and drug release features of the magnetically responsive system [46]. Reprinted with permission from ACS

Active targeting improves the therapeutic efficacy of drugs [40]. In most of the clinically approved nanotechnology products the passive targeting approach is used.

Magnetic nanoferrites have been widely used for targeted drug delivery. Cobalt ferrite (CoFe_2O_4) nanoparticle is a promising material as a drug delivery agent [43–45]. CoFe_2O_4 has the properties like large surface area for effective drug loading, capability to produce large number of multifunctional nanocomposites and externally applied magnetic field has the potential to control it when used in magnetic targeting. Magnetically responsive system's drug loading and drug release characteristics are depicted schematically in Fig. 5. For doxorubicin (DOX) delivery, magnetically driven and elion pollen-like CoFe_2O_4 nanostructures was proposed for controlled release of drug. Cobalt ferrite (CoFe_2O_4) nanoparticles have negligible cytotoxicity and high drug loading capacity.

Manganese ferrite/graphene oxide ($\text{MnFe}_2\text{O}_4/\text{GO}$) nanocomposites were evaluated for the controlled targeted drug delivery. Cytotoxicity of $\text{MnFe}_2\text{O}_4/\text{GO}$ was negligible on HeLa cells and drug loading capacity was found to increases with increase of the initial concentration of DOX and was as high as 0.97 mg/mg. The drug release characteristics of $\text{MnFe}_2\text{O}_4/\text{GO}$ were consistent and pH-responsive [47]. Drug delivery efficiency of zinc ferrite (ZnFe_2O_4) and silver substituted zinc ferrite ($\text{Ag}_{1-x}\text{Zn}_x\text{Fe}_2\text{O}_4$) nanoparticles was investigated under initial drug concentrations, pH and magnetic field [48]. Drug delivery effectiveness of the nanoparticle at constant pH = 6, magnetic field of 5mT and initial concentration of 8 mg was higher than reported by all other similar experiments. MnZn ferrite composite material could be a potential drug delivery system and also applicable as pH-stimuli responsive nanocarriers [49]. The calcium ferrite (CaFe_2O_4) nano-particles and its composites have also been analysed for targeted drug delivery [50–52].

4 Hyperthermia Application

Cancer is one of the most fatal diseases and a leading cause of death globally. There are various therapeutic modalities to treat cancer such as surgery, chemotherapy, immunotherapy, radiation and gene therapy [53]. These conventional modalities are often associated with the life long side effects and can adversely affect the healthy tissues which are in the vicinity of cancerous cell. Hence, it is crucial to develop novel and effective cancer treatment with improved efficacy to overcome the drawbacks of conventional treatments. Magnetic hyperthermia has emerged as a promising therapeutic method to treat cancer. The term “hyperthermia” is derived from the two Greek words, “hyper” means rise and “therme” means heat [54]. Hyperthermia refers to the increase of the temperature of body or selected tissues to achieve a precise therapeutic effect. Hence in hyperthermia, body tissues are exposed to clinically adequate temperatures to damage or kill the cancerous cells or to make these cells more prone to the radiation effects and anticancer drugs [55]. Magnetic nanoparticles have tremendous potential in providing effective treatment of cancer due to the selective binding of functionalized magnetic nanoparticles with tumor cells and by using alternating magnetic field.

The heating efficiency produced by magnetic nanoparticles is expressed in terms of specific absorption rate (SAR) or specific loss power (SLP). SAR is defined as the amount of heat emitted by a unit weight of the material per unit time during the exposure to an AC magnetic field of defined frequency and field strength [56]:

$$SAR = C \frac{\nabla T}{\nabla t} \quad (1)$$

where C is sample-specific heat capacity calculated as a mass of magnetic carriers per equivalent of medium and is determined by the rate of temperature rise, expressed as mean absorbed power per mass (W/g). The temperature increase per unit time ($\Delta T/\Delta t$) or initial slope of the temperature versus time dependence. SLP/SAR should be higher in the hyperthermia application to achieve the required enhancement in temperature rise in order to reduce the dose concentration to a minimal level. SLP/SAR is proportional to the rate of the temperature increase ($\Delta T/\Delta t$) and depends upon various parameters like particle size, shape, viscosity of the dispersive medium and magnetic field parameters [57].

Heating occurs when AC magnetic field is applied to magnetic nanoparticles due to hysteresis, Néel and Brown mechanisms [58]. The heat generation mechanisms are shown in Fig. 6. These heat generation mechanisms depend upon microstructure, size and shape of nanoparticles. Hysteresis loss occurs in both single and multi-domain magnetic nanoparticles and larger particles of the order 100 nm or higher [59].

Brownian and Néel relaxation are predominant mechanism than the hysteresis mechanism and it occur in single-domain magnetic nanoparticles, as single-domain superparamagnetic nanoparticles are mostly employed in magnetic hyperthermia. Néel mechanism is the rotation of magnetic moment within a stationary magnetic

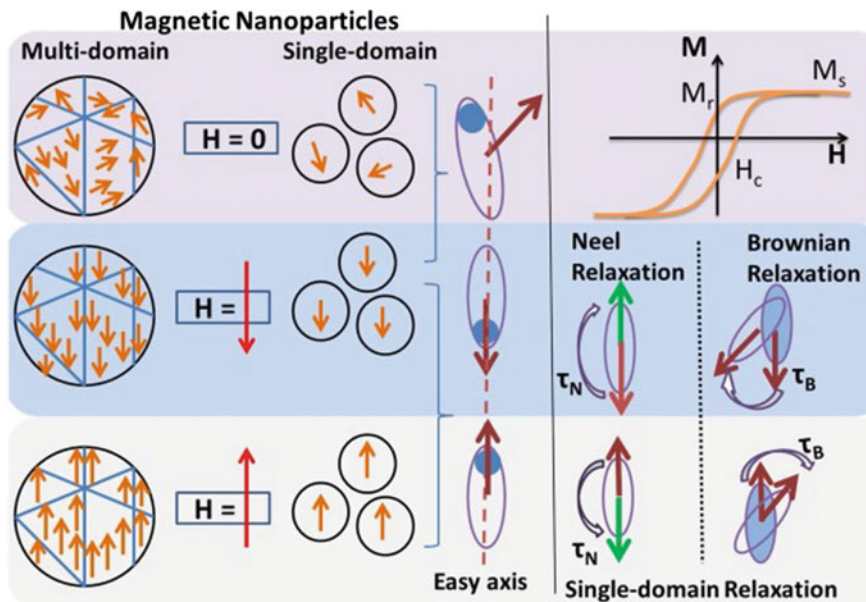


Fig. 6 Different heat generation mechanism in magnetic nanoparticles [60]. Reprinted with permission from Elsevier

nanoparticle, whereas Brownian mechanism is due to the rotation of entire magnetic nanoparticle as well as the magnetic moment. Brownian mechanism occurs in larger nanoparticles dispersed in low viscosity media; if the particle size is less than 15 nm then Néel mechanism overcomes Brownian mechanism. In general, both Néel and Brownian mechanisms can exist at the same time [61, 62]. Heat generation mechanism mainly depends on the particle size. In large particles (>100 nm) hysteresis mechanism dominates, but for many clinical applications this size range of particles is very high. It is evident from the *in vivo* and *in vitro* experiments that it is better if nanoparticle undergoes relaxation by Néel mechanism, since in the cells change in the viscosity medium and free rotation of the particles can be averted [63, 64].

In hyperthermia most effective heating agents are very crucial as it would facilitate localized heating of tumour cells by preventing any harm to healthy tissue. To produce more energy per cycle of heating more coercivity is required which can be obtained by metal nanoparticles. In this regard magnetic nanoferrite and its composites have received special attention as superior heating agents; hence a variety of magnetic nanoparticles has been developed accordingly. The magnetic and morphological parameters are influenced by the synthesis methods, so it becomes very important to choose an appropriate synthesis method which has the ability to control the size, shape and composition of magnetic nanoparticles. To overcome the limitations like low stability of these hyperthermia agents, the surface is coated with targeting moieties which increases their therapeutic efficacy and also reduces the side effects

of nanoparticles [65]. Particle size, exchange interaction and interparticle interaction play a pivotal role in controlling the heating efficiency [66].

For efficient magnetic hyperthermia, nanoferrite should be superparamagnetic with high magnetic moment, high SAR and biocompatible. Minhong Jeun et. al. [67] analysed $Mg_xMn_{1-x}Fe_2O_4$ superparamagnetic nanoferrites (SPFs) as a magnetic hyperthermia agent. Figure 7a shows schematic of magnetic hyperthermia heating and $Mg_xMn_{1-x}Fe_2O_4$ superparamagnetic nanoferrites pass through the tumor cell due to their increased permeability and retention ability. Figure 7b shows the AC magnetically induced heating temperature ($T_{AC,mag}$) characteristics of the $Mg_{0.285}Mn_{0.715}Fe_2O_4@lipid$ SPNFs in D.I water, high $T_{AC,mag}$ of 52.1 °C and SLP value of 2170 W/g was achieved at a low concentration and AC magnetic field. These superparamagnetic nanoferrites $Mg_{0.285}Mn_{0.715}Fe_2O_4@lipid$ as an MHF agent in vivo not only show high SLP and $T_{AC,mag}$ but retains its superparamagnetic phase and it also had a high cell viability.

The biocompatible zinc ferrites nanoparticles are also promising therapeutic agent due to higher SAR values, long term stabilization and moderate curie temperature [68–71]. Heating efficiencies are also affected by the dipolar interactions which depend upon the intrinsic parameters. Study conducted on zinc substituted magnetite nanoparticles showed that heating efficiency does not depend only on a one intrinsic property, it depends upon various parameters. If the interactions increase the heating efficiency can also increase [72]. The increase of the zinc content in zinc cobalt nanoferrite has found to increase the magnetization and hence the heating efficiency [73, 74].

Cobalt ferrite ($CoFe_2O_4$) nanoparticles have been used in many biomedical applications owing to the unique properties like large magnetocrystalline anisotropy, high Curie temperature, large magnetostriction coefficient, non-toxicity and good chemical stability; hence they have the potential as magnetic hyperthermia agent [75–83]. In addition to this property, unique tendency of cobalt ferrite nanoparticles is to form growing chains on the application of an alternating magnetic field. The magnetic anisotropy facilitates this chain like structure. This chain formation, along with intrinsic cobalt toxicity and mild hyperthermia leads to complete tumor regression and result in improved survival in an vivo murine xeno graft model, all under clinically approved alternating magnetic field conditions [84]. Hence cobalt ferrite nanoparticles can be used as non-conventional synergistic multimodal cancer therapy based magnetic hyperthermia.

Surface functionalization plays crucial role in biomedical application to prevent the toxicity issues. Nickel ferrite nanoparticles ($NiFe_2O_4$) are potential candidate for hyperthermia application with considerably high saturation magnetization but the major problem is their known cytotoxic effect. The toxic ion leakage to the biological media can be prevented by using suitable surface coating ligands, and permits the use of nickel ferrite nanoparticles in hyperthermia application [85–87]. Çiğdem E. Demirci Dönmez et. al. [88] carried out comparative study of heating efficiencies of EDT-coated $CoFe_2O_4$, $MnFe_2O_4$ and $NiFe_2O_4$ nanoparticles. $CoFe_2O_4$ shows poor heating efficiency at low field as compared to $MnFe_2O_4$, and $NiFe_2O_4$. The maximum value of SLP was approximately 315 W/g for $CoFe_2O_4$ nanoparticles and

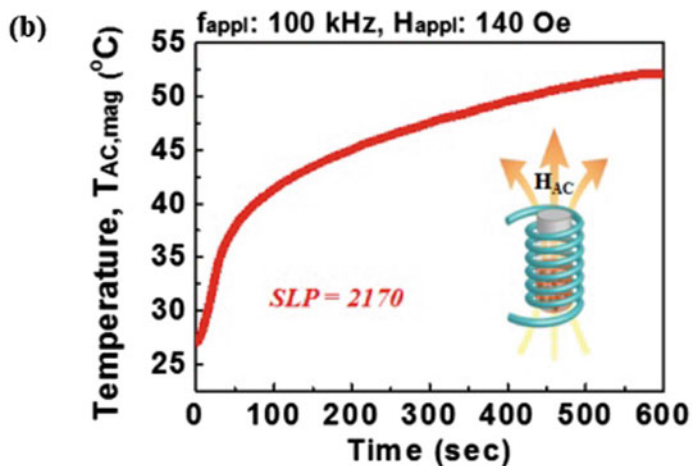
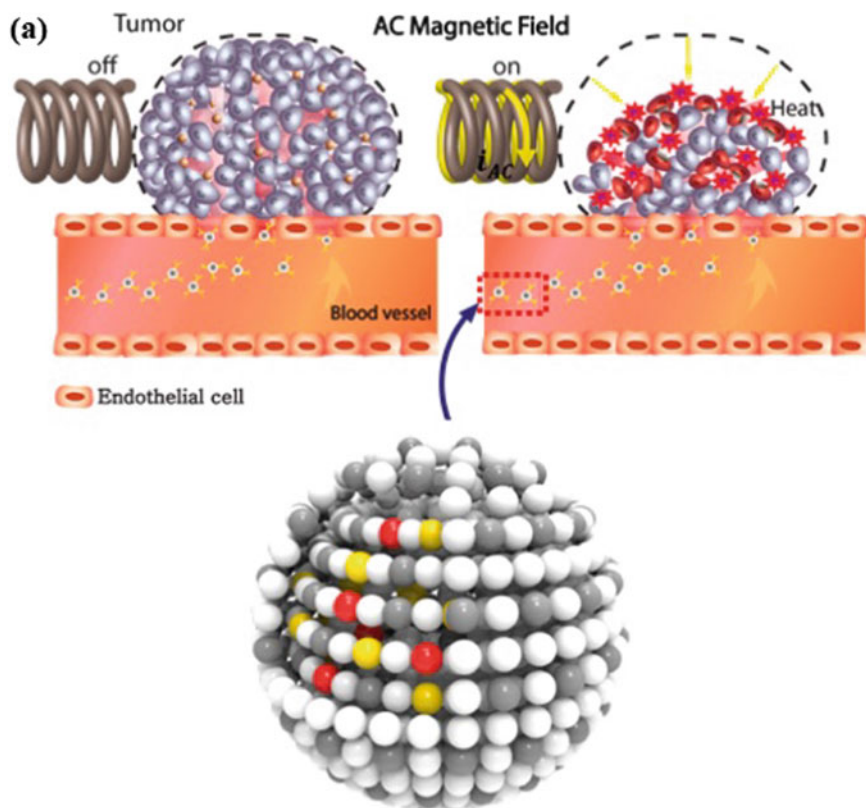


Fig. 7 **a** In Vivo MFH using tailored $\text{Mg}_x\text{Mn}_{1-x}\text{Fe}_2\text{O}_4$ superparamagnetic nanoferrites. **b** $T_{\text{AC,mag}}$ and SLP of $\text{Mg}_{0.285}\text{Mn}_{0.715}\text{Fe}_2\text{O}_4$ @lipid SPNFs measured in D.I water [67]. Reprinted with permission from ACS

for NiFe_2O_4 and MnFe_2O_4 nanoparticles the value was approximately 295 W/g, which represents the efficacy of these nanoferrites as hyperthermia agents.

5 Conclusion

The role of nanoferrite in MRI, targeted drug delivery and magnetic hyperthermia application was briefly discussed in this chapter. The tunable magnetic behavior and magnificent properties of nanoferrites makes them promising candidate for all these biomedical applications. Stability and biocompatibility are the major concerns which require attention while using various nanoferrites for biomedical applications to improve the efficacy. Despite the fact that nanoferrites have been widely investigated in vitro, clinical trials of nanoferrites are still lacking.

References

1. P. B. Kharat, S. B. Somvanshi, P. P. Khirade, K. M. Jadhav, J. Phys. Conf. Ser. **1644**, 012028 (2020)
2. S. Amiri, H. Shokrollahi, Mater. Sci. Eng. C **33**, 1 (2013)
3. Y. Wang, Y. Miao, G. Li, M. Su, X. Chen, H. Zhang, Y. Zhang, W. Jiao, Y. He, J. Yi, X. Liu, H. Fan, Mater. Today Adv. **8**, 100119 (2020)
4. D. García-Soriano, R. Amaro, N. Lafuente-Gómez, P. Milán-Rois, Á. Somoza, C. Navío, F. Herranz, L. Gutiérrez, and G. Salas, J. Colloid Interface Sci. **578**, 510 (2020)
5. C. Wang, C. Xu, H. Zeng, S. Sun, *Recent Progress in Syntheses and Applications of Dumbbell-like Nanoparticles* (2009)
6. N. Sanpo, C.C. Berndt, C. Wen, J. Wang, Acta Biomater. **9**, 5830 (2013)
7. J. Giri, P. Pradhan, V. Somani, H. Chelawat, S. Chhatre, R. Banerjee, D. Bahadur, J. Magn. Magn. Mater. **320**, 724 (2008)
8. A.B. Salunkhe, V.M. Khot, N.D. Thorat, M.R. Phadatare, C.I. Sathish, D.S. Dhawale, S.H. Pawar, Appl. Surf. Sci. **264**, 598 (2013)
9. E. Peng, E.S.G. Choo, P. Chandrasekharan, C.T. Yang, J. Ding, K.H. Chuang, J.M. Xue, Small **8**, 3620 (2012)
10. R.A. Bohara, N.D. Thorat, H.M. Yadav, S.H. Pawar, New J. Chem. **38**, 2979 (2014)
11. M. Tada, T. Kanemaru, T. Hara, T. Nakagawa, H. Handa, M. Abe, J. Magn. Magn. Mater. **321**, 1414 (2009)
12. A.K. Tangra, S. Singh, G. Singh, Mater. Today Proc. **36**, 621 (2019)
13. S.M. Hoque, M.S. Hossain, S. Choudhury, S. Akhter, F. Hyder, Mater. Lett. **162**, 60 (2016)
14. A.V. Nikam, B.L.V. Prasad, A.A. Kulkarni, CrystEngComm **20**, 5091 (2018)
15. D. Nunes, A. Pimentel, L. Santos, P. Barquinha, L. Pereira, E. Fortunato, R. Martins, in *Metal Oxide Nanostructures*, edited by D. Nunes, A. Pimentel, L. Santos, P. Barquinha, L. Pereira, E. Fortunato, and R. Martins (Elsevier, 2019), (pp. 21–57)
16. H. Shokrollahi, Mater. Sci. Eng. C **33**, 2476 (2013)
17. F. Rabai, R. Ramani, *Magnetic Resonance Imaging: anesthetic Implications. Anesthetic Implications* (Elsevier Inc., 2017)
18. H. Anwar, I. Arif, H. Mushtaq, in *Magnetic. Nanoheterostructures, Nanomedicine Nanotoxicology*, edited by S. K. Sharma and Y. Javed (Springer Nature Switzerland, 2020).
19. S. Mastrogiacomo, W. Dou, J.A. Jansen, X.F. Walboomers, Mol. Imaging Biol. **21**, 1003 (2019)

20. Zijian Zhou, L. Yang, J. Gao, X. Chen, *Adv Mater.* **8**, e1804567 (2019)
21. N. Lee, T. Hyeon, *Chem. Soc. Rev.* **41**, 2575 (2012)
22. M. Ravichandran, G. Oza, S. Velumani, J.T. Ramirez, F. Garcia-Sierra, N.B. Andrade, M.A. Garza-Navarro, D.I. Garcia-Gutierrez, R. Lara-Estrada, E. Sacristán-Rock, J. Yi, *RSC Adv.* **5**, 17223 (2015)
23. F. Javed, M.A. Abbas, M.I. Asad, N. Ahmed, N. Naseer, H. Saleem, A. Errachid, N. Lebaz, A. Elaissari, N.M. Ahmad, *Magnetochemistry* **7**, 1 (2021)
24. J. Muhamad Arshad, W. Raza, N. Amin, K. Nadeem, M. Imran Arshad, M. Azhar Khan, Synthesis and characterization of cobalt ferrites as MRI contrast agent. *Mater. Today Proc.* (2020)
25. H.M. Joshi, Y.P. Lin, M. Aslam, P.V. Prasad, E.A. Schultz-Sikma, R. Edelman, T. Meade, V.P. Dravid, *J. Phys. Chem. C* **113**, 17761 (2009)
26. C. Bárcena, A.K. Sra, G.S. Chaubey, C. Khemtong, J.P. Liu, J. Gao, *Chem. Commun.* **19**, 2224 (2008)
27. U.I. Tromsdorf, N.C. Bigall, M.G. Kaul, O.T. Bruns, M.S. Nikolic, B. Mollwitz, R.A. Sperling, R. Reimer, H. Hohenberg, W.J. Parak, S. Förster, U. Beisiegel, G. Adam, H. Weller, *Nano Lett.* **7**, 2422 (2007)
28. J.A. Peters, *Prog. Nucl. Magn. Reson. Spectrosc.* **120–121**, 72 (2020)
29. M. Ravichandran, S. Velumani, *Mater. Res. Express* **7**, 016107 (2020)
30. A. Ahmad, H. Bae, I. Rhee, *AIP Adv.* **8**, 055019 (2018)
31. K. Islam, M. Haque, A. Kumar, A. Hoq, F. Hyder, S.M. Hoque, *Nanomaterials* **10**, 1 (2020)
32. L. Yang, L. Ma, J. Xin, A. Li, C. Sun, R. Wei, B.W. Ren, Z. Chen, H. Lin, J. Gao, *Chem. Mater.* **29**, 3038 (2017)
33. J.H. Lee, Y.M. Huh, Y.W. Jun, J.W. Seo, J.T. Jang, H.T. Song, S. Kim, E.J. Cho, H.G. Yoon, J.S. Suh, J. Cheon, *Nat. Med.* **13**, 95 (2007)
34. D. Liu, F. Yang, F. Xiong, N. Gu, *Theranostics* **6**, 1306 (2016)
35. G. Manish, S. Vimukta, *Res. J. Chem. Sci.* **1**, 160 (2011)
36. K. Rani, S. Paliwal, *Sch. J. Appl. Med. Sci.* **2**, 328 (2014)
37. Y.L. Liu, D. Chen, P. Shang, D.C. Yin, *J. Control. Release* **302**, 90 (2019)
38. B. Sahoo, K.S.P. Devi, S. Dutta, T.K. Maiti, P. Pramanik, D. Dhara, *J. Colloid Interface Sci.* **431**, 31 (2014)
39. M. S. Dahiya, V. K. Tomer, S. Duhan, *Metal-Ferrite Nanocomposites for Targeted Drug Delivery* (Elsevier Inc., 2018)
40. O.C. Farokhzad, R. Langer, *ACS Nano* **3**, 1 (2007)
41. N.N. Al-Rawi, B.A. Anwer, N.H. Al-Rawi, A.T. Uthman, I.S. Ahmed, *Saudi Pharm. J.* **28**, 876 (2020)
42. L.H. Reddy, J.L. Arias, J. Nicolas, P. Couvreur, *Chem. Rev.* **112**, 5818 (2012)
43. S.Y. Srinivasan, K.M. Paknikar, D. Bodas, V. Gajbhiye, *Nanomedicine* **13**, 1221 (2018)
44. Z. Shi, Y. Zeng, X. Chen, F. Zhou, L. Zheng, G. Wang, J. Gao, Y. Ma, L. Zheng, B. Fu, R. Yu, *J. Magn. Magn. Mater.* **498**, 166222 (2020)
45. P. Chen, B. Cui, X. Cui, W. Zhao, Y. Bu, Y. Wang, *J. Alloys Compd.* **699**, 526 (2017)
46. B. Cai, M. Zhao, Y. Ma, Z. Ye, J. Huang, *A.C.S. Appl. Mater. Interfaces* **7**, 1327 (2015)
47. G. Wang, Y. Ma, L. Zhang, J. Mu, Z. Zhang, X. Zhang, H. Che, Y. Bai, J. Hou, *J. Magn. Magn. Mater.* **401**, 647 (2016)
48. R. Jose, J. Rinita, N.S.N. Jothi, *Mater. Technol.* **36**, 347 (2021)
49. W. Montha, W. Maneepakorn, I.M. Tang, W. Pon-On, *RSC Adv.* **10**, 40206 (2020)
50. S. Kamaraj, U. M. Palanisamy, M. S. B. Kadhhar Mohamed, A. Gangasalam, G. A. Maria, R. Kandasamy, *Eur. J. Pharm. Sci.* **116**, 48 (2018)
51. Y. Jumril, S. Noor Humam, G. Mariyam Jameelah, *Key Eng. Mater.* **775 KEM**, **115** (2018)
52. B. K. Purushothaman, M. Harsha S, P. U. Maheswari, K. M. M. Sheriffa Begum, *J. Drug Deliv. Sci. Technol.* **52**, 509 (2019)
53. A. van der Horst, E. Versteijne, M.G.H. Besselink, J.G. Daams, E.B. Bulle, M.F. Bijlsma, J.W. Wilmink, O.M. van Delden, J.E. van Hooft, N.A.P. Franken, H.W.M. van Laarhoven, J. Crezee, G. van Tienhoven, *Int. J. Hyperther.* **34**, 969 (2018)

54. Z. Hedayatnasab, F. Abnisa, W.M.A.W. Daud, *Mater. Des.* **123**, 174 (2017)
55. M. Bañobre-López, A. Teijeiro, J. Rivas, *Reports Pract. Oncol. Radiother.* **18**, 397 (2013)
56. A.B. Salunkhe, V.M. Khot, S.H. Pawar, *Curr. Top. Med. Chem.* **14**, 572 (2014)
57. A. Rajan, N.K. Sahu, *J. Nanoparticle Res.* **22**, 1 (2020)
58. A. López-Ortega, M. Estrader, G. Salazar-Alvarez, A.G. Roca, J. Nogués, *Phys. Rep.* **553**, 1 (2015)
59. Ç. E. D. Dönmez, A. Dönmez, in *Academic Studied Science and Mathematics Science*, edited by S. I. Ucuncu, T. V. Soldatović (Livre de Lyon Address, 2020)
60. S. K. Sharma, N. Shrivastava, F. Rossi, L. D. Tung, N. T. K. Thanh, *Nano Today* **29**, 100795 (2019)
61. M. Saeed, W. Ren, A. Wu, *Biomater. Sci.* **6**, 708 (2018)
62. K. Wu, J. Liu, Di. Su, R. Saha, J. P. Wang, *ACS Appl. Mater. Interfaces* **11**, 22979 (2019)
63. S. Laurent, D. Forge, M. Port, A. Roch, C. Robic, L. V Elst, R.N. Muller, *Chem. Rev.* **108**, 2064 (2008)
64. A. Hervault, N.T.K. Thanh, *Nanoscale* **6**, 11553 (2014)
65. J.K. Kang, J.C. Kim, Y. Shin, S.M. Han, W.R. Won, J. Her, J.Y. Park, K.T. Oh, *Arch. Pharm. Res.* **43**, 46 (2020)
66. P. Thandapani, M. Ramalinga Viswanathan, M. Vinícius-Araújo, A. F. Bakuzis, F. Béron, A. Thirumurugan, J. C. Denardin, J. A. Jiménez, A. Akbari-Fakhrabadi, *J. Am. Ceram. Soc.* **103**, 5086 (2020)
67. M. Jeun, S. Park, G.H. Jang, K.H. Lee, A.C.S. Appl. Mater. Interfaces **6**, 16487 (2014)
68. D. Lachowicz, W. Górka, A. Kmita, A. Bernasik, J. Zukrowski, W. Szczerba, M. Sikora, C. Kapusta, S. Zapotoczny, *J. Mater. Chem. B* **7**, 2962 (2019)
69. H. Ghayour, M. Abdellahi, N. Ozada, S. Jabbrzare, A. Khandan, *J. Phys. Chem. Solids* **111**, 464 (2017)
70. S.O. Aisida, A. Ali, O.E. Oyewande, I. Ahmad, A. Ul-Hamid, T. Zhao, M. Maaza, F.I. Ezema, *J. Nanopart. Res.* **23**, 47 (2021)
71. S. B. Somvanshi, R. V. Kumar, J. S. Kounsalye, T. S. Saraf, K. M. Jadhav, *AIP Conf. Proc.* **2115**, 030522 (2019)
72. Y. Hadadian, A.P. Ramos, T.Z. Pavan, *Sci. Rep.* **9**, 1 (2019)
73. V. Marneli, A. Musinu, A. Ardu, G. Ennas, D. Peddis, D. Niznansky, C. Sangregorio, C. Innocenti, N.T.K. Thanh, C. Cannas, *Nanoscale* **8**, 10124 (2016)
74. P. Appa Rao, K. Srinivasa Rao, T. R. K. Pydi Raju, G. Kapuseti, M. Choppadandi, M. Chaitanya Varma, K. H. Rao, *J. Alloys Compd.* **794**, 60 (2019)
75. Z. Mahhouti, H. El Moussaoui, T. Mahfoud, M. Hamedoun, M. El Marssi, A. Lahmar, A. El Kenz, A. Benyoussef, *J. Mater. Sci. Mater. Electron.* **30**, 14913 (2019)
76. A. L. SHA, H. RA, A. AA, A. T, A. H, *Int. J. Adv. Technol.* **08**, 1000196 (2017)
77. E.L. Verde, G.T. Landi, J.A. Gomes, M.H. Sousa, A.F. Bakuzis, *J. Appl. Phys.* **111**, 123902 (2012)
78. E. Demirci, P.K. Manna, Y. Wroczynskij, S. Aktürk, J. van Lierop, *J. Magn. Magn. Mater.* **458**, 253 (2018)
79. P.H. Nam, L.T. Lu, P.H. Linh, D.H. Manh, L.T. Thanh Tam, N.X. Phuc, P.T. Phong, I.J. Lee, *New J. Chem.* **42**, 14530 (2018)
80. E. Mazarío, N. Menéndez, P. Herrasti, M. Cañete, V. Connord, J. Carrey, *J. Phys. Chem. C* **117**, 11405 (2013)
81. S.W. Lee, S. Bae, Y. Takemura, I.B. Shim, T.M. Kim, J. Kim, H.J. Lee, S. Zurn, C.S. Kim, *J. Magn. Magn. Mater.* **310**, 2868 (2007)
82. S. Gandhi, S. Issar, A. K. Mahapatro, I. Roy, *J. Mol. Liq.* **310**, 113194 (2020)
83. B.E. Kashevsky, V.E. Agabekov, S.B. Kashevsky, K.A. Kekalo, E.Y. Manina, I.V. Prokhorov, V.S. Ulashchik, *Particuology* **6**, 322 (2008)
84. P.B. Balakrishnan, N. Silvestri, T. Fernandez-Cabada, F. Marinaro, S. Fernandes, S. Fiorito, M. Miscuglio, D. Serantes, S. Ruta, K. Livesey, O. Hovorka, R. Chantrell, T. Pellegrino, *Adv. Mater.* **32**, 1 (2020)

85. G. Stefanou, D. Sakellari, K. Simeonidis, T. Kalabaliki, M. Angelakeris, C. Dendrinou-Samara, O. Kalogirou, *IEEE Trans. Magn.* **50**, 1 (2014)
86. E. Umut, M. Coşkun, F. Pineider, D. Berti, H. Güngüneş, *J. Colloid Interface Sci.* **550**, 199 (2019)
87. M. Menelaou, K. Georgoula, K. Simeonidis, C. Dendrinou-Samara, *Dalt. Trans.* **43**, 3626 (2014)
88. C. E. Demirci Dönmez, P. K. Manna, R. Nickel, S. Aktürk, J. Van Lierop, *ACS Appl. Mater. Interfaces* **11**, 6858 (2019)

Ferrite Materials for Microwave and High Frequency Antenna Applications



Pankaj Sharma, Vineet Sharma, Nikhil Thakur, Pawan Kumar, and Ashok Kumar

Abstract Ferrite nanoparticles have a significant impact in determining the dielectric behaviour and are promising materials for microwave and high frequency antenna applications. Thus chapter presents the frequency as well as temperature reliant dielectric properties of Mn^{2+} doped $\text{Mg}_{0.5}\text{Zn}_{0.5-x}\text{Mn}_x\text{Fe}_2\text{O}_4$ (where, $x = 0.125, 0.250, 0.375, 0.500$) nano-ferrites synthesized by co-precipitation. In comparison to that at higher frequencies, the dielectric constant falls dramatically at low frequencies. For every sample, the loss tangent was found to be minimal. The temperature reliant dielectric analysis of prepared samples reveals that the dielectric relaxation occurs at higher temperatures of approximately 531–667 K. The nano-ferrites being studied have minimal loss tangent values, making them potential candidates for microwave device applications.

Keywords Nanomaterials · Ferrites · $\tan \delta$ loss · Dielectric constant

1 Introduction

Magnetic nanoparticles are of great scientific importance compared to their bulk counterparts because of the influence of their size on numerous physical characteristics [1, 2]. Magnetic nanoparticles have advantages in memory storage, medicinal research as well as in microwave devices [1]. As a topic of interest, why ferrites are important is demonstrated in Fig. 1. Among various magnetic nanoparticles, spinel ferrites are the most promising [3–9]. Most spinel ferrites with the generic chemical formula MFe_2O_4 , where M may be Mn (manganese), Fe (iron), Co (cobalt), Ni

P. Sharma (✉) · A. Kumar

Applied Science Department, National Institute of Technical Teachers Training and Research, Sector 26, Chandigarh 160019, India

V. Sharma

Department of Physics & Materials Science, Jaypee University of Information Technology, Waknaghat, Solan, HP 173234, India

N. Thakur · P. Kumar

School of Physics and Materials Science, Shoolini University, Solan 173229, India

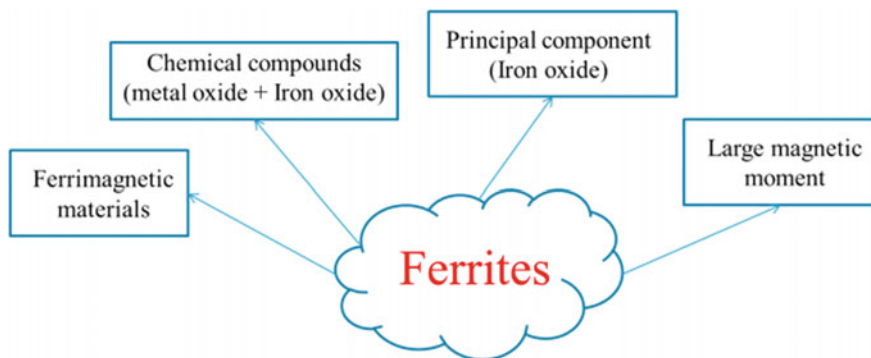


Fig. 1 Why ferrites are important?

(nickel), Cu (copper) and Zn (zinc), that display superparamagnetic characteristics at nanoscale level of size less than or equal to 20 nm [3–9]. The capacity of spinel ferrites to allocate cations across accessible tetrahedral A-sites as well as octahedral B-sites gives these compounds their special physical characteristics [10].

Spinel ferrites are used in the photocatalytic degradation of dyes, Manikandan et al. discovered that Mn doped ferrites have improved photocatalytic dye degradation [11]. Spinel ferrites are utilised in the electronic applications for various purposes including microwave systems, memory storage systems, high frequency systems, and several more electronic devices [12]. The dielectric characteristics of ferrite nanoparticles are appropriate in electronic device purposes [13]. Mg–Zn ferrites occur naturally in the environment and have an economical synthesis [14] and exhibit strong electrical resistivity as well as minimal dielectric loss at specific frequencies. Mg–Zn ferrite nanoparticles have unusual dielectric characteristics, making them a significant material in a variety of technologically essential device applications [15, 16]. The replacement of various transition metal ions plays a key role in determining the frequency dependent dielectric behaviour of ferrite nanoparticles [15–17]. The diamagnetic Zn^{2+} and Mg^{2+} metal ions in Mg–Zn ferrite reduce A–B super-exchange interaction and diminish the magnetic properties. Transition metal ions such as Co^{2+} , Ni^{2+} and Mn^{2+} enhance the magnetic properties of spinel ferrites [18–20]. The magnetic properties of spinel ferrites depend on the distribution of metal ions at crystallographic lattice sites. In Mg–Zn ferrite system, the replacement of Zn^{2+} ions with transition metal ions will create anti-parallel arrangement of metal ions and enhance the A–B super-exchange interaction. For defining the frequency based dielectric behaviour of ferrites, size of crystallite as well as grain is a crucial characteristic [21].

The shape and surface area of nanoparticles influences the physical attributes [22]. The synthesis method as well as reaction mechanism play a key role in the variation of grain or crystallite size. Co-precipitation method, sol–gel method, hydrothermal method, is a few of the wet chemical processes that may be used to make ferrite nanoparticles [23]. Because of its numerous advantages, the co-precipitation

approach is the most suited of these methods. One of the most significant benefits of the co-precipitation approach is the ability to adjust nucleation as well as growth rates, which determines not only the size distribution but determines the grain size of nanoparticles [24]. The dielectric characteristics of $Mg_{0.5}Zn_{0.5-x}Mn_xFe_2O_4$ (Here, $x = 0.125, 0.250, 0.375, 0.500$) ferrites produced via co-precipitation are elucidated in detail.

2 Experimental Details

The coprecipitation technique is an economical and easy technique for the synthesis of $Mg_{0.5}Zn_{0.5-x}Mn_xFe_2O_4$ ferrites. $MgCl_2 \cdot 6H_2O$, $ZnCl_2$, $MnCl_2 \cdot 4H_2O$ and $FeCl_3 \cdot 6H_2O$ have been used for the synthesis. The schematic of the synthesis can be seen in Fig. 2 [24]. The proposed reaction scheme is described below [25]:

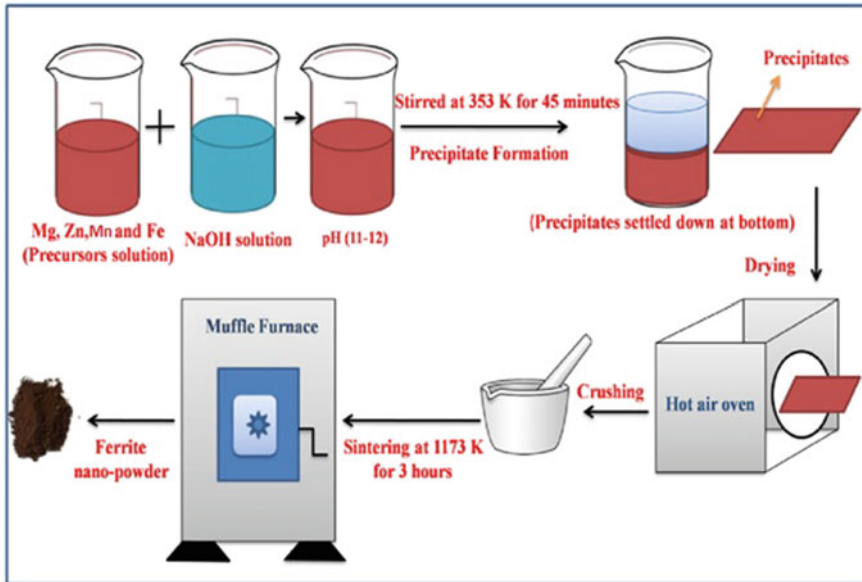
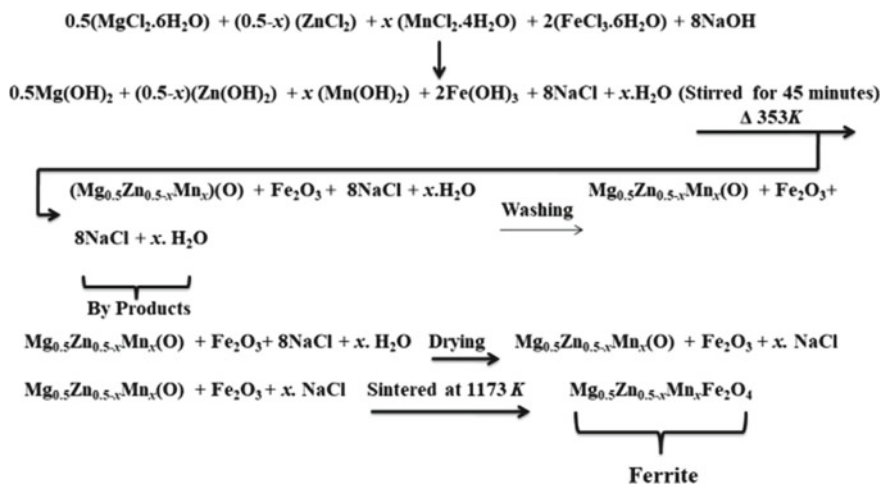


Fig. 2 Schematic for the synthesis of $Mg_{0.5}Zn_{0.5-x}Mn_xFe_2O_4$ nanoferrites by co-precipitation method [24]. Reprinted with permission from Elsevier



X-ray diffraction (XRD) study has been conducted on the synthesized samples using Shimadzu 6000 diffractometer. The XRD data have been obtained in the range 10° – 80° at a scan speed of $2^\circ/\text{min}$ with Cu $K\alpha$ radiation ($\lambda = 1.5406 \text{ \AA}$). At 300 K, a Keithley 6487 electrometer has been employed for the I–V characterization in the range 0–100 V. Using an impedance analyzer, in the frequency range 10^4 – 10^6 Hz as well as temperature range 313–723 K, the dielectric characteristics of produced samples have been investigated.

The round pellets have been made by crushing the powdered samples in a stainless-steel dye by utilizing a hydraulic press at a pressure of 3–8 ton/inch². I–V and dielectric characterization have been conducted on pellets having diameters of 0.50 cm and thicknesses ranging from 0.20 to 0.25 cm. To establish effective electrical connections, pellets have been coated on the top and bottom with silver paste. Two terminal capacitance and sometimes even equivalent parallel circuit have been used to estimate various dielectric properties.

3 Results and Discussions

Figure 3 shows the X-ray diffraction patterns for $\text{Mg}_{0.5}\text{Zn}_{0.5-x}\text{Mn}_x\text{Fe}_2\text{O}_4$ ferrites. For samples having composition $x \geq 0.250$, a hematite phase has been observed.

The formation of hematite phase is due to the heating of iron-hydroxides in air [26]. The crystallite size has been calculated from the most intense (311) peak. The crystallite size values are given in Table 1 [25].

The relationship between I and V is shown in Fig. 4a for Mn^{2+} doped $\text{Mg}_{0.5}\text{Zn}_{0.5-x}\text{Mn}_x\text{Fe}_2\text{O}_4$ ($x = 0.125, 0.250, 0.375, 0.500$) ferrite samples has been determined for measuring resistivity (ρ) as shown in Table 1 by using the equation $\rho = RA/d$, where d represents the thickness, A represents the surface area of the pellets' flat surfaces, and R represents resistance. Resistivity is inversely proportional to grain size. Particles with lower crystallite sizes, as shown in Table 1, have

Fig. 3 XRD patterns of $Mg_{0.5}Zn_{0.5-x}Mn_xFe_2O_4$ ferrites [25]. Reprinted with permission from Elsevier

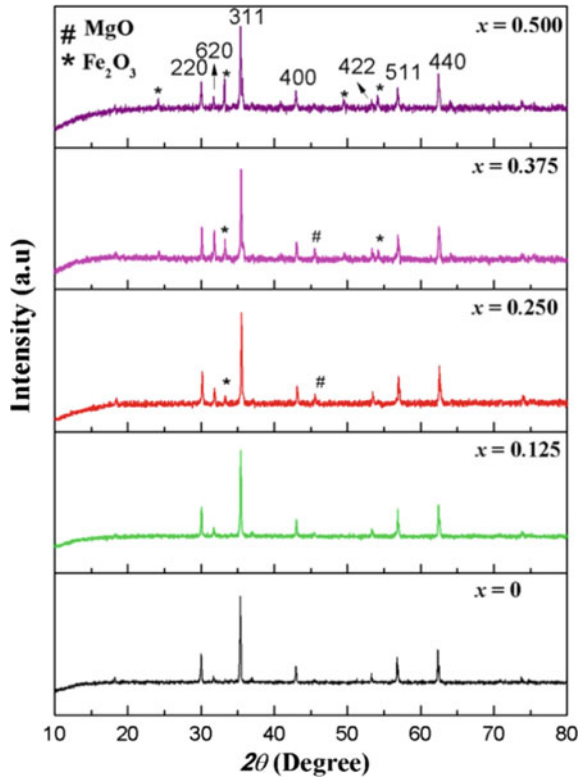


Table 1 Resistivity [27], size of crystallite [25] and $\tan \delta$ [27] with temperature for Mn^{2+} doped $Mg_{0.5}Zn_{0.5-x}Mn_xFe_2O_4$ ferrite nanoparticles

x	Resistivity (ohm m)	The crystallite size (nm)	$\tan \delta$ (At 6×10^6 Hz)
0.125	4.595×10^4	57.05	0.065
0.250	2.155×10^5	53.31	0.080
0.375	4.497×10^4	55.50	0.054
0.500	6.115×10^4	48.68	0.044

Reprinted with permission from Elsevier & IEEE

smaller grains that further behave as a barrier to electron passage and hence enhance resistivity. Using the equation $\epsilon' = Cd/\epsilon_0 A$, (here, C represents the capacitance and ϵ_0 represents permittivity of free surface) the quantities of the dielectric constant (ϵ') have been derived. The identical parallel circuit required to determine the dielectric properties is seen in the inset of Fig. 4b. For all prepared samples, the dielectric constant reduces with increasing frequency (Fig. 4b). Insulating grain boundaries outnumbering conducting grain boundaries at lower frequency. The detected change

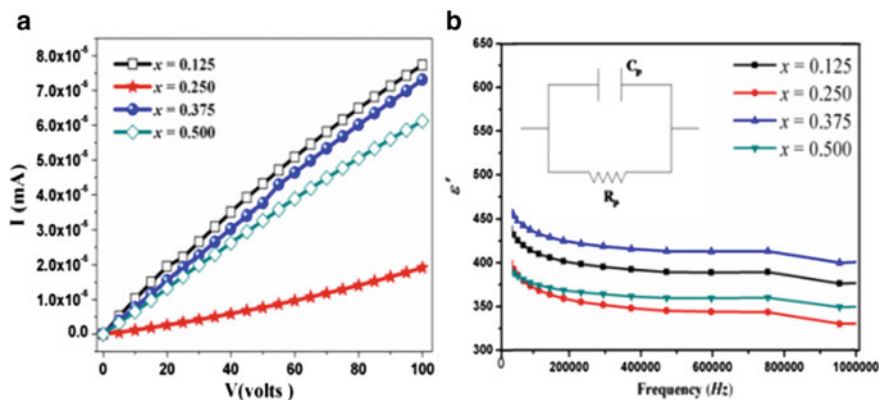


Fig. 4 **a** Relationship between I and V. **b** Dielectric constant variation for Mn^{2+} doped $\text{Mg}_{0.5}\text{Zn}_{0.5-x}\text{Mn}_x\text{Fe}_2\text{O}_4$ ferrite nanoparticles. In this figure illustrates an inset of analogous parallel circuit used to test dielectric properties [27]. Reprinted with permission from IEEE

of ϵ' with frequency for prepared materials is consistent with the Wagner interfacial polarization and Koop's phenomenological hypothesis [28]. Druc et al. discovered comparable dielectric behaviour in Co-doped Mg-ferrite [29]. Koop's theory states that ferrites have heterogeneous compositions consisting of good conducting grains as well as insulating grain edges. Polarization occurs as a result of electron hopping between various metal ions across the lattice locations [16]. When a low-frequency alternating field is applied, electrons concentrate at insulating grain boundaries, resulting in interfacial polarization, which is entirely responsible for the greater values of dielectric constant at lower frequency. The difference in dielectric constant with Mn^{2+} is mainly due to electrons hopping across Mn^{2+} as well as Fe^{3+} ions only at B region. In this situation, the crystallite size (as shown in Table 1) effects electron hopping, also shorter crystallites give higher resistivity and minimise the electron hopping. Sun et al. recently found that the grain structure of nanoparticles has a significant impact in determining the dielectric behaviour of spinel ferrites [21]. The dielectric constant (ϵ') changes inversely with resistivity, and this has been found for the currently prepared samples [30].

The calculation of $\tan \delta$ loss (Table 1) is a significant component in the use of ferrite nanoparticles in numerous technological purposes. $\tan \delta$ loss denotes the energy loss in the device when an alternating current field is applied. $\tan \delta$ losses reduce with increasing frequency until 6×10^5 Hz, then rise slightly for all investigated samples as shown in Fig. 5a.

The ac conductivity has been calculated using the formula; $\sigma_{ac} = \epsilon' \epsilon_0 \omega \tan \delta$, where ω represents the angular frequency. The frequency reliant ac conductivity (as shown in Fig. 5b) of all prepared materials exhibits the same trend as that of the $\tan \delta$ losses. The replacement of Mn^{2+} moves Fe^{3+} ions from octahedral locations to tetrahedral locations [25], which reduces electron hopping across Fe^{3+} and Fe^{2+} just at location B and results in a reduction in the ac conductivity. Farea et al. similarly

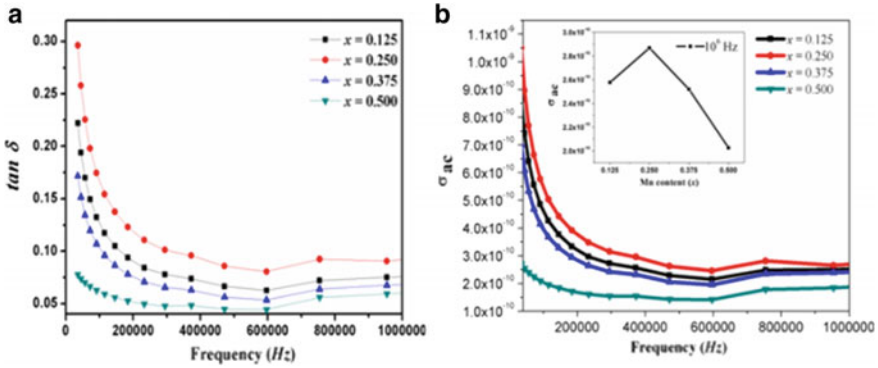


Fig. 5 a $\tan \delta$ loss, b ac conductivity versus frequency for Mn^{2+} doped $Mg_{0.5}Zn_{0.5-x}Mn_xFe_2O_4$ nano-ferrites. At 10^6 Hz, the inset in this figure illustrates the change in ac conductivity with Mn^{2+} concentration [27]. Reprinted with permission from IEEE

observed similar ac conductivity- dependence behaviour on the composition [31]. The measured ac conductivity behaviour might be explained by the lowest value of resistivity at $x = 0.250$.

Figure 6a depicts the change of ϵ' between temperature 313–723 K at 10^6 Hz. For all prepared samples, ϵ' rises with temperature, indicating the existence of dielectric relaxation peaks between 531 and 667 K. The heat effect increases the charge carrier hopping, which raises the dielectric constant. Ionic, electronic, dipolar, as well as interfacial polarization are the primary contributors to polarization in ferrites. The ionic and electronic polarization are independent of temperature, whereas dipolar and interfacial polarization depends on the temperature, which are responsible for increasing the ϵ' with the increase in temperature [32]. The occurrence of relaxation

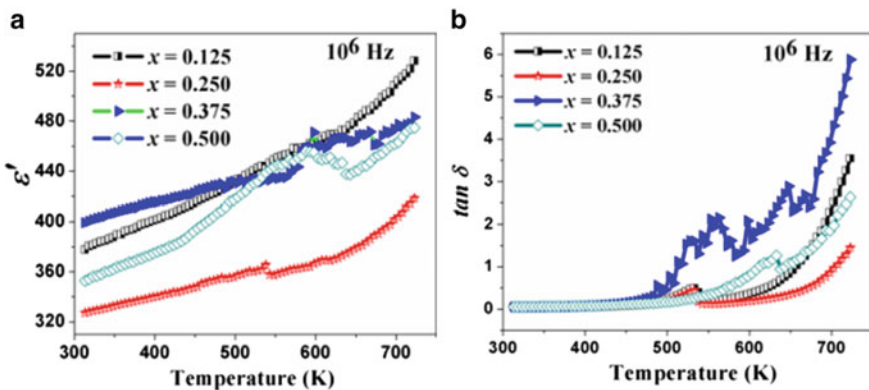


Fig. 6 a Dielectric constant variation, b $\tan \delta$ loss with temperature for Mn^{2+} doped $Mg_{0.5}Zn_{0.5-x}Mn_xFe_2O_4$ ferrite nanoparticles at 10^6 Hz [27]. Reprinted with permission from IEEE

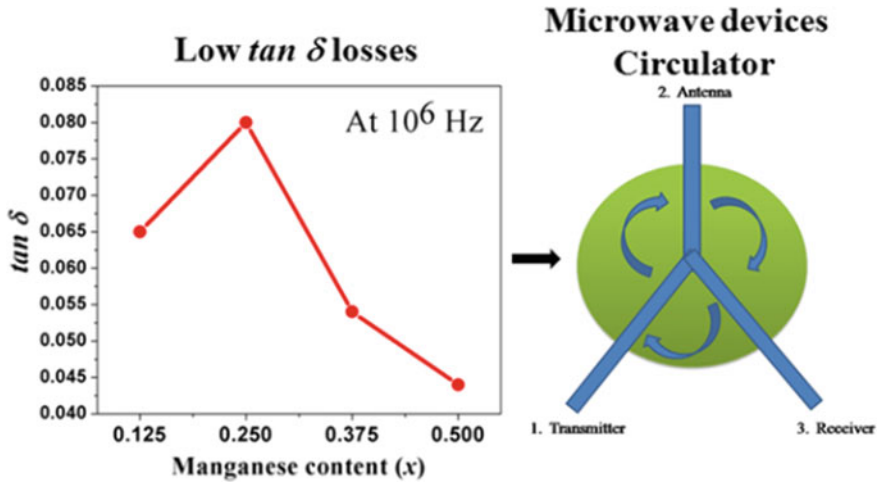


Fig. 7 A diagram illustrating the potential applications of nanomaterials [27]. Reprinted with permission from IEEE

peaks is due to the existence of various metal ions within spinel ferrites, which provide varying inertia to the applied field.

The existence of relaxation peaks indicates that the various metal ions available in spinel ferrites contribute to determining the dielectric behaviour. The change of $\tan \delta$ losses over temperature at 10^6 Hz is being examined for prepared samples (as shown in Fig. 6b). $\tan \delta$ losses rise, with rising temperature and relaxation peaks have indeed been found for all prepared samples. Hashim et al. similarly found comparable temperature-dependent $\tan \delta$ loss behaviour [32]. The observed values of different dielectric parameters for prepared samples indicate that they can be explored for microwave device applications (as shown in Fig. 7).

4 Conclusion

Coprecipitated $\text{Mg}_{0.5}\text{Zn}_{0.5-x}\text{Mn}_x\text{Fe}_2\text{O}_4$ nano-ferrites show the formation of cubic spinel structure. For samples having composition $x \geq 0.250$, a hematite phase has been observed. The crystallite size varies between 59.40 and 48.68 nm. Resistivity measurements are performed on the produced samples. It ranges between $2.15 \times 10^5 \Omega \text{ m}$ and $4.497 \times 10^4 \Omega \text{ m}$. For all prepared samples, the dielectric constant falls with increasing frequency. Minimal $\tan \delta$ loss of 0.04 is found for $x = 0.5$ at 6×10^5 Hz. Because of the minimal $\tan \delta$ losses in the synthesized samples that they are a viable contender for microwave device purposes. For the temperature dependent dielectric research, dielectric relaxation peaks for all synthesized samples

are detected. The observed values of different dielectric parameters for prepared samples indicate that they can be explored for microwave device applications.

References

1. D. Lisjak, A. Mertelj, *Prog. Mater. Sci.* **95**, 286 (2018)
2. J. Arul Mary, A. Manikandan, L. John Kennedy, M. Bououdina, R. Sundaram, J. Judith Vijaya, *Trans. Nonferrous Met. Soc. China* **24**, 1467 (2014)
3. Z. Yan, J. Gao, Y. Li, M. Zhang, M. Guo, *RSC Adv.* **5**, 92778 (2015)
4. R.T. Olsson, G.S. Alvarez, M.S. Hedenqvist, U.W. Gedde, F. Lindberg, S.J. Savage, *Chem. Mater.* **17**, 5109 (2005)
5. A.H. Latham, M.E. Williams, *Acc. Chem. Res.* **41**, 411 (2008)
6. H. El Moussaoui, A. Benyoussef, *J. Magn. Mater* **405**, 181 (2016)
7. D.S. Mathew, R.-S. Juang, *J. Chem. Eng.* **129**, 51 (2007)
8. D. Carta, M.F. Casula, A. Falqui, D. Loche, G. Mountjoy, C. Sangregorio, A. Corrias, *J. Phys. Chem. C* **113**, 8606 (2009)
9. Q. Song, Y. Ding, Z.L. Wang, Z.J. Zhang, *Chem. Mater.* **19**, 4633 (2007)
10. M.K. Fayek, S.S. Ata-Allah, H.A. Zayed, M. Kaiser, S.M. Ismail, *J. Alloys Compd.* **469**, 9 (2009)
11. H. Harzali, A. Marzouki, F. Saida, A. Megrache, A. Mgaidi, *J. Magn Magn Mater* **460**, 89 (2018)
12. T. Tatarchuk, M. Bououdina, J.J. Vijaya, L.J. Kennedy, *ICNNFC* **305** (2016)
13. M. Ahmed, K. Rady, M. Shams, *J. Alloys Compd.* **622**, 269 (2015)
14. A. Manikandan, J. Judith Vijaya, M. Sundararajan, C. Meganathan, L. John Kennedy, M. Bououdina, *Superlattices Microst.* **64**, 118 (2013)
15. S.F. Mansour, M.A. Abdo, *J. Magn. Mater.* **428**, 300 (2017)
16. R. Sharma, P. Thakur, M. Kumar, N. Thakur, N.S. Negi, P. Sharma, V. Sharma, *J. Alloys Compd.* **684**, 569 (2016)
17. K. Verma, A. Kumar, D. Varshney, *J. Alloys Compd.* **526**, 91 (2012)
18. M. Shahid, S. Shafi, M.F.A. Aboud, M.F. Warsi, M. Asghar, I. Shakir, *Ceram. Int.* **43**, 14096 (2017)
19. K. El Maalam, M. Ben Ali, H. El Moussaoui, O. Mounkachi, M. Hamedoun, R. Masrour, E.K. Hlil, A. Benyoussef, *J. Alloys Compd.* **622**, 761 (2015)
20. P. Shikha, T.S. Kang, B. Randhawa, *J. Alloys Compd.* **701**, 788 (2017)
21. L. Sun, J. Guo, Q. Ni, E. Cao, Y. Zhang, W. Hao, L. Ju, *J. Mater. Sci. Mater. Electron.* **29**, 5356 (2018)
22. P. Bhavani, A. Manikandan, S.K. Jaganathan, S. Shankar, S.A. Antony, *J. Nanosci. Nanotechnol.* **18**, 1388 (2018)
23. K.K. Kefeni, T.A. Msagati, B.B. Mamba, *Mater. Sci. Eng. B* **215**, 37 (2017)
24. R. Sharma, P. Thakur, P. Sharma, V. Sharma, *J. Alloys Compd.* **704**, 7 (2017)
25. R. Sharma, P. Thakur, M. Kumar, P.B. Barman, *Ceram. Int.* **43**, 13661 (2017)
26. R. Jayaprakash, M.S. Seehra, T. Prakash, S. Kumar, *J. Phys. Chem. Solids* **74**, 943 (2013)
27. R. Sharma, P. Thakur, P. Sharma, V. Sharma, *IEEE Electron Device Lett.* **39**, 901 (2018)
28. K. Wagner, *Ann. Phys.* **345**, 817 (1913)
29. A.C. Druc, A.I. Borhan, A. Diaconu, A.R. Iordan, G.G. Nedelcu, L. Leontie, M.N. Palamaru, *Ceram Int.* **40**, 13573 (2014)
30. B.P. Rao, K. Rao, *J. mater sci.* **32**, 6049 (1997)
31. A. Farea, S. Kumar, K.M. Batoo, A. Yousef, *Phys. B Condens. Matter* **403**, 684 (2008)
32. M. Hashim, M. Raghasudha, J. Shah, S.E. Shirsath, D. Ravinder, S. Kumar, S.S. Meena, P. Bhatt, R. Kumar, R.K. Kotnala, *J. Phys. Chem. Solids* **112**, 29 (2018)

Ferrites for Water Purification and Wastewater Treatment



Pankaj Chamoli, Ravi K. Shukla, Achintya N. Bezbaruah, Kamal K. Kar, and K. K. Raina

Abstract This chapter defines the features of ferrites for the application of wastewater treatment and water purification. The structural, magnetic properties and synthesis routes of ferrites are described and special attention is paid to the spinel ferrites. The adsorption of organic and inorganic contaminants is presented, and the adsorbent/adsorbate systems are discussed based on available published reports. The applications of ferrites in photocatalytic activity are also examined for its pollutant degradation behavior in wastewater. Furthermore, the possible separation and recovery methods for ferrites used as an adsorbent and photocatalyst in wastewater treatment are addressed.

Keywords Ferrites · Adsorption · Photocatalysis · Recycling · Wastewater treatment

P. Chamoli (✉)

School of Basic & Applied Sciences, Department of Physics, Shri Guru Ram Rai University, Dehradun 248001, Uttarakhand, India

R. K. Shukla

Advanced Functional Smart Materials Laboratory, School of Physical Sciences, Department of Physics, DIT University, Dehradun 248009, Uttarakhand, India

A. N. Bezbaruah

Nanoenvirology Research Group, Civil, Construction and Environmental Engineering, North Dakota State University, Fargo 58105, ND, USA

K. K. Kar

Advanced Nanoengineering Materials Laboratory, Materials Science Programme, Indian Institute of Technology Kanpur, Kanpur 208016, India

K. K. Raina

MS Ramaiah University of Applied Sciences, Bangalore Urban, Karnataka 560054, India

1 Introduction

An essential element for life on the earth is water. While water covers a large percentage of the Earth's surface, less than one percent of this water is suitable for human and industrial uses. Industrial developments have marked improved the lives of human but also polluted our environment, specifically the aquatic ecosystem system. An enormous amount of wastewater is generated daily by various industries including leather, pharmaceuticals, and packaging, which include organic dyes, heavy metals, and other harmful chemicals, and such wastes are dumped to our aquatic ecosystem without any meaningful treatment [1]. This is a serious threat to life as they lead to various deceases in human [2]. Thus, the effective removal of such contaminants is needed. Most contaminants such as harmful metal ions and emerging organic contaminants can be removed using modern treatment techniques. Several technologies have been used which include chemical precipitation, coagulation, extraction, membrane filtration, ion exchange, chemical oxidation, and electrochemical technique [3]. Among the emerging methods, nanotechnology-based treatments are becoming popular. Such technologies use nanomaterials and they are very effective due to their high specific surface areas and high adsorption capacities. The most extensively studied nanomaterials for water and wastewater treatment include metal oxide nanoparticles (NPs), carbon nanomaterials [e.g., carbon black, carbon nanotube (CNT), graphene oxide (GO)], and a number of nanocomposites (NCs). This chapter will focus on the use of magnetic NPs (especially ferrites, their properties and synthesis methods) for the treatment of different pollutants present in wastewater.

2 Materials for Water Purification

Various NPs have been studied for water purification including zero-valent metal NPs, metal oxides NPs, CNTs, GO, reduced GO (rGO) and their NCs. Among these nanomaterials, magnetic NPs and their NCs not only offer various beneficial properties but they are also easy to removed/recovered from water. The separation/recovery of the magnetic NPs involves an application of a simple magnetic field on the system. Herein, special focus has been given to the ferrites, their classification, and synthesis for the application in water purification and wastewater treatment [4].

2.1 Ferrites

Ferrite was discovered by ancient human as naturally present magnetic stone "lode-stone". In 1600, it was first documented and reported by Dr. William Gilbert [5, 6]. Later on, in 1930, ferrites were synthesized for first time [7]. Iron oxide and bivalent

elements (e.g. Ni, Mg, Mn, Cu, Zn, Fe) are the main constituents of ferrites [5]. Due to this combination, ferrites exhibit excellent properties including high electrical resistivity, high permeability, wide frequency range, low eddy current loss, shape versatility and time–temperature properties [8]. These excellent properties of ferrites make them usages in a multitude of applications which include uses in magnetic shielding, magnetic recordings, magnetic sensors, information storage, medical devices, electronic devices, mobile communication, gyromagnetic device, transformers, catalysis, and pigments. Especially, ferrites own a wide range of applications as semiconductors for energy storage, drug delivery and in various biomedical applications in addition to their use as optics, photo-catalyst, ferrofluids, and gas sensors [9–14].

2.2 Ferrites Properties

As ferrites display existence of spontaneous magnetization and they can be classified into two different groups according to their properties such as soft ferrites and hard ferrites. Low coercivity of magnetism is the main characteristics of soft ferrites, whereas, hard ferrites have a high coercivity of magnetism (shown in Fig. 1). Other properties (Table 1) also make ferrites very desired Ferrimagnetism is a permanent type of magnetism exhibited by ferrites and proposed by Neel to define the magnetic order phenomenon in ferrites [15]. Magnetic moments align in both parallel (called “ferromagnetism”) and antiparallel (called “anti-ferromagnetism”) directions in ferrimagnetic materials. Due to partial cancellation of magnetic field, ferrites show overall magnetic fields which are less strong than that of ferromagnetic materials [16]. Similar to ferromagnetic materials, the ferrimagnetic materials exhibit spontaneous magnetic moments in the absence of a magnetic field. The magnetic properties of magnetic materials can be learned by studying their hysteresis loop (Fig. 1). The paramagnetic behavior of ferrimagnetic materials is similar to that of ferromagnetic materials above the Curie temperature. Ferrites show substantial

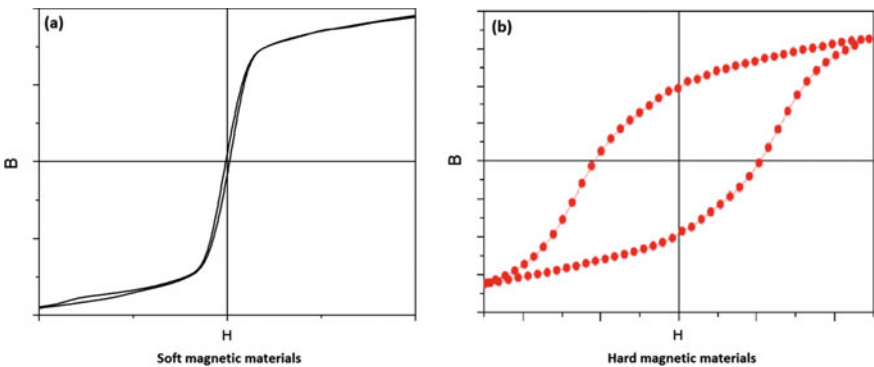


Fig. 1 B–H curve, a soft ferrites and b hard ferrite

Table 1 Comparison of the properties of magnetic materials

Properties	Soft ferrites		Hard ferrites	
	Value	Range	Value	Range
Saturation magnetization	High	1–2 T	High	0.3–6 T
Coercivity	Low	~100 Oe	High	~250 Oe
Permeability	High	900–15,000 μ	Low	–
Anisotropy	Low	~10 ² erg/cm ³	High	~10 ⁶ erg/cm ³
Curie temperature	High	200–250 °C	High	450 °C
Electrical resistivity	High	~10 ⁸ Ω cm	High	~10 ⁶ Ω cm

Reprinted with permission from Elsevier

excellent properties such as low eddy current, high electrical resistivity, high saturation magnetization, high permeability, low dielectric losses, spontaneous magnetization, moderate permittivity, and conductivity (Table 1) [17]. Ferrites show high saturation magnetization in comparison to diamagnetic or paramagnetic materials. Ferrimagnetic materials exhibit saturation magnetization lower than ferromagnetic materials.

2.3 Ferrites Classification

Ferrites show a variety of crystal structures and classified into four categories, viz., spinel, garnet, ortho, and hexagonal ferrites (Table 2) [17]. Out of these, spinel ferrite (Fig. 2) is broadly viewed as non-toxic and shows excellent chemical and mechanical stability, and displays interesting magnetic properties.

The general composition of spinel ferrite is AB_2O_4 where, A could be Fe, Ni, Mg, Zn, Mn, and B could be Cr, Fe, or Al, and O is oxygen. Magnetite (Fe_3O_4) is a classic example of this family where A site is occupied with spinel space group (Fd3m, no 227). In AB_2O_4 , a face-centered cubic (FCC) packing of oxygen ions takes place and tetrahedral and octahedral voids are occupied by divalent and trivalent cations, respectively. A schematic representation of the spinel structure is shown in Fig. 2. This type of arrangement is commonly found in zinc ferrite ($ZnFe_2O_4$)

Table 2 Crystal structure of ferrites [17]

Types	Molar ratio	Representation
Spinel	Fe_2O_3 –MO	MO: Transition metal oxide
Garnet	$5Fe_2O_3$ – $3M_2O_3$	M_2O_3 : Rare earth metal oxide
Ortho	AFe_2O_3	A: Rare earth metal oxide (e.g., Dy, Er, Y)
Hexagonal	$6Fe_2O_3$ –MO	MO: Divalent metal oxide (e.g., BaO, CaO, SrO)

Reprinted with permission from Elsevier

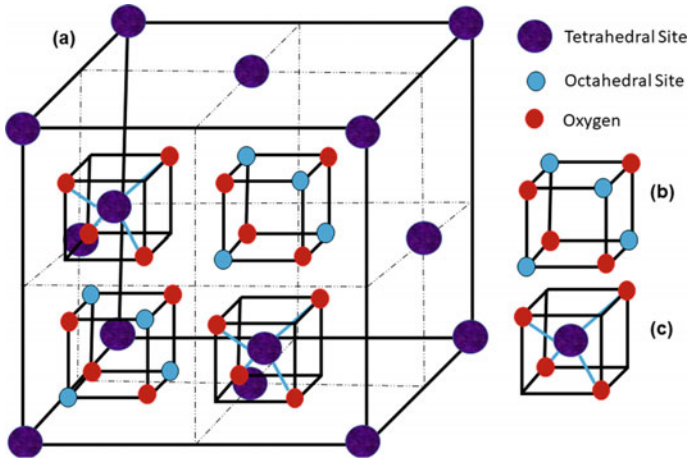


Fig. 2 **a** Unit cell of Spinel ferrite, **b** octahedral interstice (B-site: 32 per unit cell, 16 occupied), and **c** tetrahedral interstice (A-site: 64 per unit cell, 8 occupied) [17]. Reprinted with permission from Elsevier

and manganese ferrite (MnFe_2O_4). Aluminum-spinel, chromium-spinel and iron-spinel are three different series of spinel group. For example, aluminum spinel can be found as spinel (MgAl_2O_4), gahnite (ZnAl_2O_4), hercynite (FeAl_2O_4), and galaxite (MnAl_2O_4); chromium spinel includes chromite (FeCr_2O_4), and magnesiochromite (MgCr_2O_4). These spinel's are harder and found as masses in igneous, granite pegmatites, metamorphic, stony meteorites, and high-temperature sulfide veins [18].

2.4 Ferrites Synthesis Methods

Ferrites can be synthesized by various methods. The synthesis method plays a vital role in the properties of ferrites. The common synthesis methods for ferrites include inert gas condensation, electrochemical method, micro-emulsion, thermal decomposition, and electro-spinning. The most widely used methods are sol-gel, hydrothermal, co-precipitation, and solid-state method. The sol-gel method is a chemical route for the synthesis of isotropic and anisotropic phase material [19]. This process involves multi-steps of chemical and physical processes related to polymerization, hydrolysis, condensation, gelation, drying, and densification. However, hydrothermal method is a simple, cost-effective and common method for the preparation of ferrites. This is a solution reaction-based approach in which solutions of metal salts and the base material are autoclaved under pressure and temperature which offers an improved reaction rate to harvest multi-metal oxide compounds [20, 21]. In

the solid-state synthesis method, the material mixture is kept at a high temperature (50–200 °C) in a furnace and baked to obtain the resultant compounds [22, 23].

3 Water Treatment

3.1 Adsorption

Metallic ion (e.g., Pb, As, Co) contaminants have harmful effects on the human body and lead to major public health concern. Magnetic NPs are specifically appropriate as cost-effective adsorbents for the removal of heavy metal ions owing to their excellent properties such as large specific surface area, ease of separation from water, non-toxicity, and recyclability. A magnetic filter (eco-fabricated) with mesh architectures constituted (Fig. 3) of soft magnetic material (Ni, Zn- Fe_2O_4) and poly (acrylic acid) (PAA)-coated quasi-superparamagnetic Fe_3O_4 nanoparticles (NPs) has been utilized for heavy metal removal including Pb, Ni, Co, and Cu [24].

Carbon-based ferrites composition has shown excellent properties for MB dye and As (V) from aqueous solution [25]. Various radio-nuclides have been successfully removed from the solution via their adsorption onto nickel ferrite/rGO composites [26]. NPs of CaFe_2O_4 displayed speedy absorption of organic dyes [27]. Table 3 shows published reports on metal pollutant and organic contaminant adsorption performance of various ferrites.

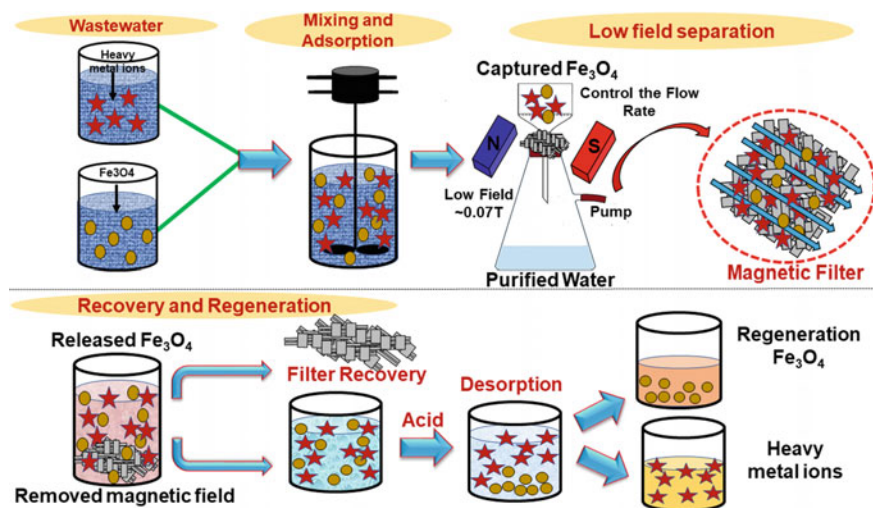


Fig. 3 Schematic of heavy metal ions removal and low-field separation technique [24]. Reprinted with permission from ACS

Table 3 Various ferrites against different metal and organic pollutants

Ferrite adsorbent	Specific area (m ² /g)	Pollutant	Adsorption capacity (mg/g)	References
Fe ₃ O ₄	109	U(IV)	52.6	Li et al. [29]
CoFe ₂ O ₄	–	Cs(I)	75	Hassan and Aly [30]
NiFe ₂ O ₄ /rGO	167	Th (IV)	100	Lingamdinne et al. [31]
MnFe ₂ O ₄ /GO	67	As(V)	240	Lan Huong et al. [32]
CuFe ₂ O ₄ /DC	17	PB(II)	921	Khan et al. [33]
CoFe ₂ O ₄	31.2	RR195	91.7	Nassar and Khatab [34]
CaFe ₂ O ₄	41.8	CR	40.9	An et al. [35]
MnFe ₂ O ₄ /GO	67	MB	177.3	Khan et al. [33]

The aforementioned removal mechanisms are versatile for metal ions and organic pollutants removal from aqueous solution. Moreover, photodegradation is another process that degrades various organic contaminants in the presence of ferrites NPs and considered an eco-friendly cost-effective process [28].

3.2 Photocatalysis

Photocatalysis is a clean and environmentally friendly technique for the removal of organic contaminant present in wastewater. Semiconducting metal oxide and ferrites have been employed as photocatalysts for contaminant removal (Fig. 4) [36]. Fenton and photo-Fenton processes are generally used for organic contaminant removal, and they need the addition of H₂O₂ and a ferrous ion (Fe²⁺) for the treatment process to progress. In this process, ferric ion (Fe³⁺) is formed with the breakdown of the peroxide into OH radicals (\cdot OH), and they react with organic matter to decompose them. When ultra-violet (UV) irradiation is used, UV photons accelerate the decomposition of the peroxide (photo-Fenton process). Here, magnetic NP catalysts contain iron and the iron utilized in the treatment process. Table 4 shows available literature on organic contaminant degradation in the presence of various ferrites.

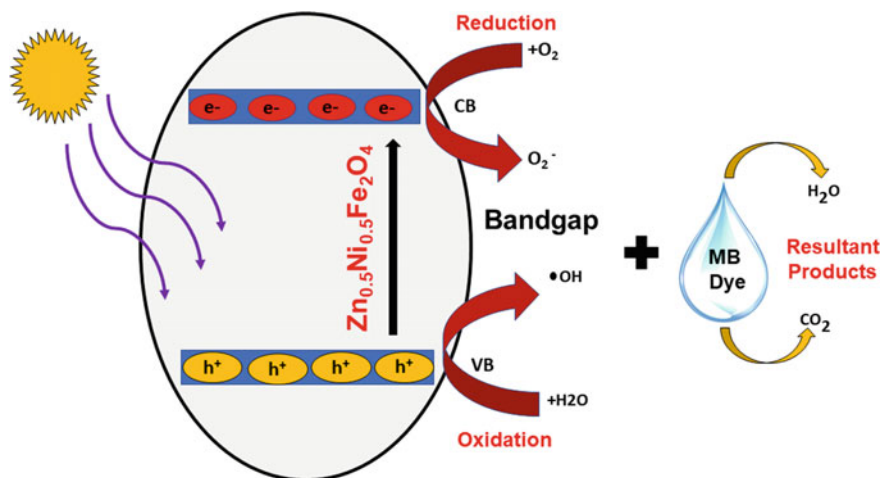


Fig. 4 Schematic of degradation of MB organic dyes [36]. Reprinted with permission from Elsevier

Table 4 Photodecomposition of organic pollutants using various ferrites

Ferrite adsorbent	Specific area (m ² /g)	Organic pollutant	Reaction rate (min ⁻¹)	References
MgFe ₂ O ₄	141	RhB	0.0197	Diao et al. [37]
ZnFe ₂ O ₄	151	MB	0.267	Sharma et al. [38]
NiFe ₂ O ₄ /CNTs	54	Amaranth	0.017	Rigo et al. [39]
MgFe ₂ O ₄	14	MB	0.117	Ivanets et al. [40]
CoFe ₂ O ₄	48.6	DCP	0.0197	Nair and Kurian [41]

RhB: Rhodamine B (C₂₈H₃₁ClN₂O₃); MB: Methylene blue (C₁₆H₁₈ClN₃S); Amaranth: An anionic dye (C₂₀H₁₁N₂Na₃O₁₀S₃); DCP: 2,6-Dichlorophenolindophenol (C₁₂H₇Cl₂NO₂)

4 Separation and Recycling

The magnetic character of ferrites plays an important role in their utilization for water and wastewater treatment. After decontamination, the separation or recovery of non-magnetic materials solid adsorbents involves sedimentation or filtration. This process of recovery is time consuming and may involve the addition of chemicals, and thus involves major expenses and yet does not guarantee a hundred percent removal of the catalyst/adsorbent from the processed liquid. The use of magnetic particles (NPs and NCs) can circumvent these issues by offering an ease of separation from the liquid (Fig. 5). They can separate with the application of a magnetic field that can achieve very effective separation of the solid particles [42]. An adsorbed organics and metal contaminants can be desorbed from the adsorbents, and separated ferrite can be potentially reused for multiple treatment cycles (adsorption–desorption cycles).

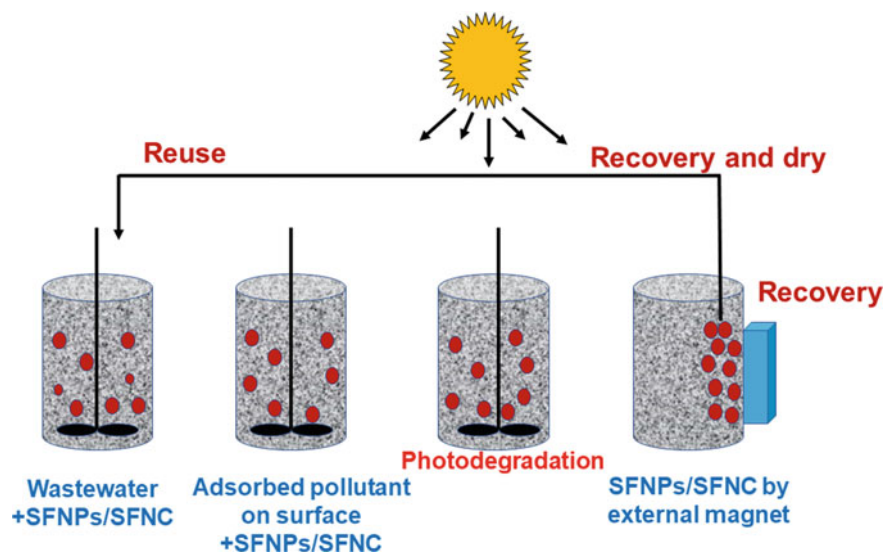


Fig. 5 Schematic illustration of the use of NPs/NCs for water/wastewater treatment and their recovery [42]. Reprinted with permission from Elsevier

Hao et al. [43] have utilized modified Fe_3O_4 NPs and reported adsorption stability over fifteen cycles for the removal of Cu (II) [43]. Xiong et al. [44] have synthesized cadmium sulfide-ferrite ($\text{CdS-MFe}_2\text{O}_4$, $\text{M}=\text{Zn, Co}$) NCs and reported adsorption stability over three cycles for the degradation of aqueous Rhodamine B (RhB) and 4-chlorophenol (4-CP) under visible-light irradiation (Fig. 6) [44–49].

5 Conclusion

Ferrite-based adsorbents have low toxicity, high chemical stability and economical to use as they can be easily separated from the purified liquid. Ferrites have shown great promise and are potential candidates for application for water and wastewater. Excellent magnetic properties make the use ferrites in water systems attractive as they can easily recovered at the end of the treatment train using a conventional magnetic field. While they can easily use in water treatment systems, their use in wastewater systems would need additional work given the complexity of wastewater (e.g., presence interfering ions and organic matters). As a result, ferrites adsorbents are a top choice due to their versatile properties, reasonability, and magnetic separation capability for water and wastewater purification.

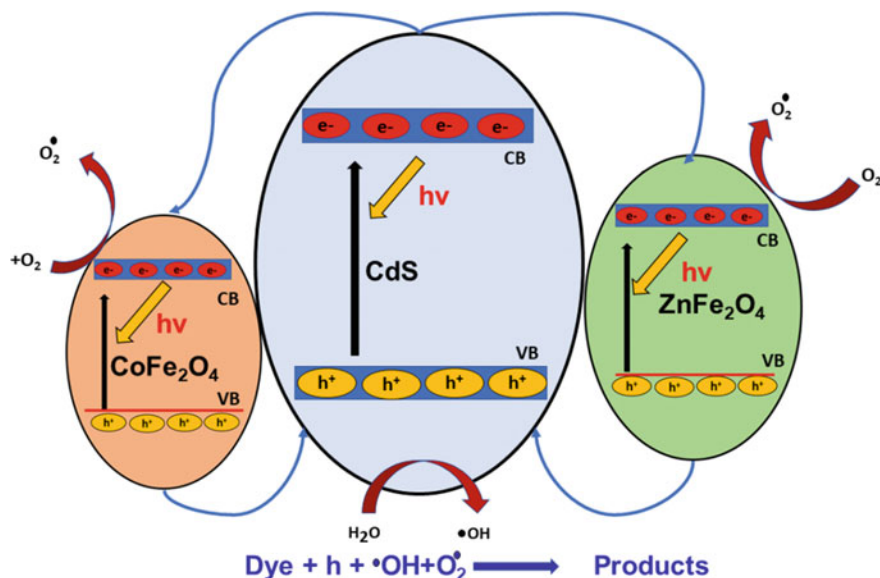


Fig. 6 Schematic of possible degradation mechanism by Cadmium sulfide-ferrite (CdS–MFe₂O₄, M=Zn, Co) NCs [44]. Reprinted with permission from ACS

References

1. G. Kaur, M. Kaur, A. Thakur, A. Kumar, FeS₂ pyrite nanostructures: an efficient performer in photocatalysis, in *Green Methods for Wastewater Treatment* eds. by M. Naushad, S. Rajendran, E. Lichtfouse (Springer Nature Switzerland AG, 2020), p. 55
2. H.A. Hasan, M.H. Muhammad, N.I. Ismail, J. Water Process. Eng. **33**, 101035 (2020)
3. T.W. Seow, C.K. Lim, M.H.M. Norb, M.F.M. Mubarak, C.Y. Lam, A. Yahya, Z. Ibrahim, Int. J. Appl. Environ. Sci. **11**(1), 111 (2016)
4. C. MartinezBoubeta, K. Simeonidis, Magnetic nanoparticles for water purification. in *Nanoscale Materials in Water Purification* eds. by S.Thomas, D. Pasquini, S.-Y. Leu, D. Gopakumar (Micro and Nano Technologies Elsevier, 2019), p. 521
5. J.D. Adam, L.E. Davis, G.F. Dionne, IEEE T Microw Theory **50**, 721 (2002)
6. R.C. Pullar, Prog Mater Sci **57**, 1191 (2012)
7. A.R.A. Dairy, L.A. Al-Hmoud, H.A. Khatatbeh, Symmetry **11**, 732 (2019)
8. J. Smit, H.P.J. Wijn, Ferrites (Philips Technical Library, Eindhoven, Netherland, 1959), p. 149
9. B. Issa, I. Obaidat, B. Albiss, Int. J. Mol. Sci. **14**, 21266 (2013)
10. S. Ammar, A. Helfen, N. Jouini, J. Mater. Chem. **11**, 186 (2001)
11. M. Veena, A. Somashekarappa, G.J. Shankaramurthy, J. Magn. Mater. **419**, 375 (2016)
12. G. Vaidyanathan, S. Sendhilnathan, Phys. B **403**, 2157 (2008)
13. R. Valenzuela, Phys. Res. Int. **59**, 2012 (1839)
14. M. Kaur, N. Kaur, V. Verma, *Ferrites and Ferrates: chemistry and Applications in Sustainable Energy and Environmental Remediation*, eds. by V.K. Sharma, R. Doong, H. Kim, R.S. Varma, D.D. Dionysiou (ACS Symposium Series, 2016), p. 113
15. V. Sechovsky, Magnetism in solids: general introduction, in *Encyclopedia of Materials: Science and Technology*, eds. by K.H. Jürgen Buschow, R.W. Cahn, M.C. Flemings, (Elsevier, 2001), p. 5018

16. E. Gregersen, *The Britannica Guide to Electricity and Magnetism* (Britannica Educational Publishing and Rosen Educational Services, New York, 2011)
17. V. Jadhav, S.D. Shirsat, U.B. Tumberphale, R.S. Mane, Properties of ferrites, in *Spinal Ferrite Nanostructures for Energy Storage Devices*, eds. by A. Mane, V. Jadhav (Elsevier, 2020), p.35
18. A. Vedrtnam, K. Kalauni, S. Dubey, A. Kumar, *AIMS Mater. Sci.* **7**(6), 800 (2020)
19. P.P. Phulé, T.E. Wood, Ceramics and glasses, sol–gel synthesis of, in *Encyclopedia of Materials: science and Technology*, 2nd edn, eds by K.H.J. Buschow, R.W. Cahn, M.C. Flemings, Oxford, Elsevier, 2001), p. 1090
20. G. Allaedini, S.M. Tasirin, P. Aminayi, *Int. Nano. Lett.* **5**, 183 (2015)
21. Y.X. Gan, A.H. Jayatissa, Z. Yu, *J. Nanomaterial* 8917013 (2020)
22. D. O'Hare, Hydrothermal synthesis, in *Encyclopedia of Materials: science and Technology*, eds. by K.H.J. Buschow, R.W. Cahn, M.C. Flemings (Oxford, Elsevier, 2001), p. 3989
23. A. Kumar, D. Nanda, Methods and fabrication techniques of superhydrophobic surfaces, in *Superhydrophobic Polymer Coatings*, eds. by S.K. Samal, S. Mohanty, S.K. Nayak (Elsevier, 2019), p. 43
24. X. Wei, P.J. Sugumaran, E. Peng, X.L. Liu, J. Ding, *A.C.S. Appl. Mater. Interfaces* **9**(42), 36772 (2017)
25. P. Thi, L. Huong, N. Tu, H. Lan, L.H. Thang, N.V. Quy, P.A. Tuan, N.X. Dinh, V.N. Phan, A.T. Le, *RSC Adv.* **8**, 12376 (2018)
26. M.B. Askari, P. Salarizadeh, *Int. J. Hydrog. Energy* **45**(51), 27482 (2020)
27. X. Liu, S. An, Y. Wang, *Chem Eng. J.* **262**, 517 (2015)
28. T.K. Das, A.N. Bezbaruah, *Sci. Total Environ.* **764**, 142914 (2021)
29. M. Li, H. Liu, T. Chen, *Sci. Total Environ.* **651**, 1020 (2019)
30. M.R. Hassan, M.I. Aly, *Part Sci. Technol.* **1** (2019)
31. L.P. Lingamdinne, Y.L. Choi, I.S. Kim, *J. Hazard. Mater.* **326**, 145 (2017)
32. P.T. Lan Huong, N. Tu, H. Lan, *RSC Adv.* **8**, 12376 (2018)
33. M.A. Khan, M. Otero, M. Kazi, *J. Hazard. Mater.* **365**, 759 (2019)
34. M.Y. Nassar, M. Khatab, *RSC Adv.* **6**, 79688 (2016)
35. S. An, X. Liu, L. Yang, L. Zhang, *Chem. Eng. Res. Des.* **94**, 726 (2015)
36. A. Nawaz, A. Khan, N. Ali, N. Ali, M. Bilal, *Environ. Technol. Innov.* **20**, 101079 (2020)
37. Y. Diao, Z. Yan, M. Guo, X. Wang, *J. Hazard. Mater.* **344**, 829 (2018)
38. R. Sharma, S. Bansal, S. Singhal, *RSC Adv.* **5**, 6006 (2015)
39. C. Rigo, E.D.C. Severo, M.A. Mazutti, *Mater. Res.* **20**, 311 (2017)
40. A. Ivanets, M. Roshchina, V. Srivastava, *Colloids Surf. A Physicochem. Eng. Asp.* **571**, 17 (2019)
41. D.S. Nair, M. Kurian, *J. Environ. Chem. Eng.* **5**, 964 (2017)
42. K.K. Kefeni, B.B. Mamba, *Sustain. Mater. Technol.* **23**, e00140 (2020)
43. Y.M. Hao, C. Man, Z.B. Hu, *J. Hazard. Mater.* **184**, 392 (2010)
44. P. Xiong, J. Zhu, X. Wang, *Ind. Eng. Chem. Res.* **52**, 17126 (2013)
45. Y.K. Penke, G. Anantharaman, J. Ramkumar, K.K. Kar, *RSC Adv.* **6**, 55608 (2016)
46. Y.K. Penke, A.K. Yadav, I. Malik, A. Tyagi, J. Ramkumar, K.K. Kar, *Chemosphere* **267**, 129246 (2021)
47. P. Benjwal, M. Kumar, P. Chamoli, K.K. Kar, *RSC Adv.* **5**(89), 73249 (2015)
48. P. Chamoli, R.K. Shukla, A.N. Bezbaruah, K.K. Kar, K.K. Raina, *Appl. Surf. Sci.* **555**, 149663 (2021)
49. N. Duklan, P. Chamoli, K.K. Raina, R.K. Shukla, *Inorg. Chem. Commun.* **116**, 107924 (2020)

Basics of Multiferroic Materials and Their Types



Samta Manori and Ramesh Chandra

Abstract The co-existence and interplay between multiple ferroic orders in a single material have been already known for many decades. These materials have been explored only theoretically on a large scale because the coupling between these orders is found to be very weak and rare in single-phase materials. However, advancements in fabrication techniques have made it possible to synthesize these materials in low dimensional structures like thin films or wires and also in the form of compound structures e.g. laminates and heterostructures. In these types of structures, coupling between multiple ferroic orders becomes stronger due to new degrees of freedom. In addition, the miniaturization of devices in electronic and computer-based industries has reached a limit beyond which size reduction is difficult to achieve. One possible solution to meet the requirements of increased memory storage and computer power without size reduction is to use these multifunctional or multiferroic materials which would definitely improve device performance and capabilities. This chapter will familiarize the reader with the basics of multiferroic materials and their types based on different structures.

Keyword Multiferroics · Single-phase multiferroics · Composite multiferroics

1 A Brief Historical Journey

The journey of multiferroic materials started right from 1820 when Hans Christian Oersted observed the deflection in a magnetic compass needle when the current in a battery placed nearby to it was switched on and off. This coexisting relation between electricity and magnetism kept scientists and engineers fascinated for centuries [1]. After following Oersted's observation, André Marie Ampère and Michael Faraday

S. Manori (✉)

Department of Physics, School of Physical Sciences, DIT University, Dehradun 248009, Uttarakhand, India

R. Chandra

Nanoscience Laboratory, Institute Instrumentation Centre, Indian Institute of Technology Roorkee, Roorkee 247667, Uttarakhand, India

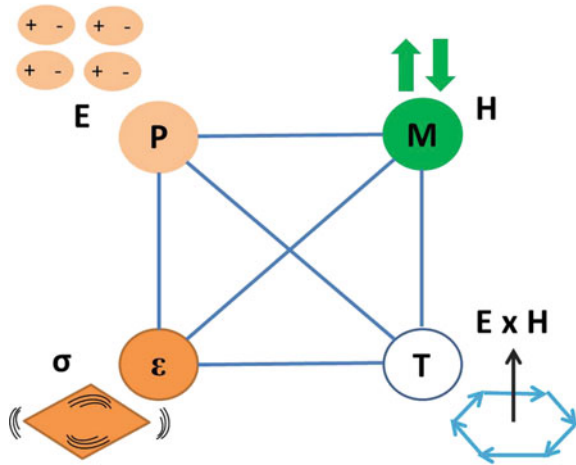
gave their contributions to work out the classical theory of electromagnetism which was finally culminated in the 1860s with James Maxwell's unified theory. These discoveries proved to be a milestone for the benefit of society on a large scale. A promising novelty in materials can be created by combining different physical properties in a single material to achieve multi-functionality. A successful attempt in this direction was made in the 1960s predominantly by two groups in the then Soviet Union: Smolenskii in St.Petersburg (then Leningrad) and by Venevtsev in Moscow, by combining both ferromagnetic and ferroelectric properties in a single system [2]. This idea of combining different physical properties in a single material has emerged vastly over the last few years, as many of the issues of material science and solid state chemistry which were once inundated have been fixed, and hence, some relevant physical phenomena can be studied. The development of a new class of materials called "Multiferroics" added a feather into the wings of these multifunctional systems. This chapter discuss the multiferroics in a little depth!

2 What are Multiferroics?

Any material that possesses the property of spontaneously switching its internal alignment by its conjugate applied field is termed *ferroic*. In a magnetic material, this ferroic order could be any one of ferromagnetic, antiferromagnetic, or ferrimagnetic, and the alignment of electronic spins can be switched by applying an external magnetic field; in a ferroelectric material, the alignment of electron's dipole moment can be switched by an applied electric field and in the case of ferroelastic materials, external stress can switch the strain alignment. Another promising ferroic order of toroidal moments is possible in ferrotoroidics, which can be switched by crossed electric and magnetic fields [1]. These ferroic materials have already gained their importance both because of the rich physics involved and for their technological applications. For example, the application of ferroelectrics and ferromagnetic materials in memory storage media is very well known, as the opposite orientations of both polarization and magnetization can represent binary "1" and "0" data bits. Thus, a multiferroic material can be designed to give mixed memory and logic operations.

As the name suggests, the term *multiferroic* stands for the class of materials in which any two or more of the ferroic orders can co-exist in a single phase (Fig. 1). In multiferroics, a ferroic order, in addition to its conjugate field, can also be switched by the conjugate field of any other coexisting ferroic order. The most appealing aspect of multiferroics is the magnetoelectric coupling, which so far has been explored in a much broader way. In a magnetoelectric material, the electric and magnetic ferroic ordering co-exist and the electric polarization can be changed by an applied magnetic field while the magnetization in the material can be changed by an applied electric field. Hence, a magnetoelectric material can effectively create a four-state logic device with (P+, M+), (P-, M+), (P+, M-), and (P-, M-) [3]. However, the coexistence of both these orders in the same material is fascinating from the physics point of view as, magnetization and polarization being represented by an

Fig. 1 Interactions in a multiferroic material



axial and polar vector respectively, have quite different symmetry properties. Therefore, it doesn't sound immediately possible to switch one by the other's conjugate field. The next section discusses the reason behind the scarcity of multiferroic or magnetoelectric materials.

2.1 Multiferroics: Why Are they so Few?

As discussed in the previous section, multiferroic materials are those which possess multiple ferroic orders in the same phase. This section discusses the scarcity of multiferroic and more specifically magnetoelectric materials. The first obvious reason behind the rare existence of these materials is that to sustain polarization a ferroelectric material should be a perfect insulator while most of the magnetic materials are conductors. And even if some magnetic materials are formally insulating, any leakage current arising due to the presence of impurities is highly unfavorable to give ferroelectricity. The second reason is more like a mysterious challenge. In ferroelectric materials, the non-magnetic cations are centered at their surrounding anions and give rise to polarization as they shift from their center. This noncentrosymmetry between cations and anions gives birth to what is known as electric dipole moment. Exactly opposite happens in the case of magnetic materials, where magnetic cations maintain centrosymmetry by sitting at the center of surrounding anions, and hence, no electric dipole moments are formed. This vast difference in the behavior of magnetic and non-magnetic cations can now be considered as an outcome of the competition between energy-lowering covalent bond formation (which is larger for cations with empty d shells) and energy-raising electronic Coulomb repulsion (which is larger for cations with occupied d shells) [4]. In view of the fact that magnetism and ferroelectricity tend to exclude each other, certain systems are already developed

with co-existing magnetic and ferroelectric properties and many more are likely to be discovered in near future. The next section discusses the history of magnetoelectric materials that are made with different structures and compositions. Thereafter, we will see the limiting factors for these materials to exist and how they can be made in spite of several restricted conditions.

2.2 History of Magnetoelectric Multiferroic Materials

(a) *Boracites*

Nickel iodine boracite, $\text{Ni}_3\text{B}_7\text{O}_{13}\text{I}$ is the first-ever discovered magnetoelectric material. This discovery was then followed by many other multiferroic boracite compounds. The boracite compounds are complex in structure and there are a large number of atoms in each formula unit and each unit cell contains more than one formula unit [5]. The inter-ionic interactions are so strong in these materials that it becomes almost impossible to isolate the factors which are responsible for multiferroic behavior and the strength of coupling between different order parameters. Nickel iodide boracite is basically “Rochelle salt” of magnetoelectric materials, helpful for validating proof of concept, but does not have any wide application and contribution in understanding the field deeply.

(b) *Mixed Perovskite Materials*

In the 1950s, the search for other magnetoelectric materials started when the magnetic cations with d^n electronic configuration replaced the B-site cations in ferroelectric perovskite materials with d^0 electronic configuration [6]. The first-ever synthesized magnetoelectric perovskite material using this approach was $(1 - x) \text{Pb}(\text{Fe}_{2/3}\text{W}_{1/3})\text{O}_3 - x \text{Pb}(\text{Mg}_{1/2}\text{W}_{1/2})\text{O}_3$ which was synthesized in 1960s [7]. Where, the Mg and W ions are responsible for ferroelectricity as they are diamagnetic and the Fe^{3+} ion with d^5 configuration is responsible for the magnetic ordering. Other examples for perovskite-based magnetoelectric materials are: B-site ordered $\text{Pb}_2(\text{CoW})\text{O}_6$ which possesses both ferroelectric and ferromagnetic ordering, B-site disordered $\text{Pb}_2(\text{FeTa})\text{O}_6$ which shows ferroelectric and antiferromagnetic orderings, with a weak ferromagnetic order below 10 K [8]. The dilution of magnetic ions in these double perovskite structures lowers their Néel or Curie temperatures.

(c) *Other Perovskite Materials*

Many other perovskite materials are there which show magnetoelectric behavior, but most of them possess antiferromagnetic ordering, for example, Yttrium manganite and other small rare earth manganites and few other compounds with Bismuth as the large cation.

2.3 *Magnetoelectric Multiferroic Materials: How they Can Be Made?*

As we are well aware now that, a magnetoelectric material is simultaneously magnetic and ferroelectric. Therefore, all the allowed physical, chemical, and structural characteristics of a magnetoelectric material are confined to those that are found in both magnetic and ferroelectric materials. This section discusses different properties that limit the choice of potential candidates for making a magnetoelectric material.

(a) *Symmetry*

As discussed earlier in Sect. 2.1, for a material to be ferroelectric, noncentrosymmetry is the primary requirement, i.e. there should be a distortion in the structure of the material from the high symmetry phase followed by removal of the center of symmetry and hence allowing the electric polarization. It is to be noted here that, there are 31 point groups that show spontaneous electric polarization, and 31 point groups that give spontaneous magnetic polarization [9]. Among these, 13 point groups (*1, 2, 2', m, m', 3, 3 m', 4, 4 m'm', m'm2', m'm'2', 6, and 6 m'm'*) are common to both groups, which allow both magnetism and ferroelectricity to exist together in the same phase. Even though this set is quite small in comparison to the total number of crystal structures available i.e. 122, but still it can be considered as a significant number. Also, many materials that are not ferromagnetic or ferroelectric follow one of these allowed symmetries. Hence, it can be said here that symmetry properties do not restrict the co-existence of magnetic and ferroelectric properties in a magnetoelectric material.

(b) *Electrical Properties*

A ferroelectric material by definition has to be an insulator so that the applied electric field can create electric polarization and not induce an electric current. Ferromagnets, on the other hand, do not require any specific electrical property but are metals. Thus, one can attribute the lack of these two properties to co-exist in a single material simply to the scarcity of magnetic insulators. However, if one broadens the search of magnetic materials to ferrimagnets and weak ferromagnets such as those having canted antiferromagnetic ordering, then the quest for magnetoelectric materials can be ended, as most of the ferrimagnets and antiferromagnets are insulators. Thus, the blame for the scarcity of magnetically ordered ferroelectrics cannot be put on the shoulders of rarely available magnetically ordered insulators [4].

(c) *Chemical-d⁰ness*

Mostly, the perovskite ferroelectric materials have a B-site cation with d^0 electron configuration, which is responsible for the formal charge distribution. Hence, none of the magnetic ordering like ferromagnetism, ferrimagnetism, or antiferromagnetism is possible in such materials as empty d shells cannot create localized magnetic moments. However, if the d shell on the small B-site cation is partially occupied, then

the removal of the center of symmetry becomes quite difficult. Many effects could be responsible for this, which includes the size of the B-site cation, some dominant structural distortion, electronic or magnetic properties, or any combination of all these properties. Let us now discuss the effect of all these factors.

1 *Size of Cation*

To see the role of size of cation, comparison of the ionic radii of d^0 cations present in perovskite ferroelectrics with those of d^n cations present in non-ferroelectric perovskite materials, is required. This comparison will help find whether the transition metal ions with filled/partially filled d shells are large enough to prevent its movement through space created at the center of oxygen octahedron. The Shannon ionic radii [10] of some ferroelectric perovskite materials having small cations with d^0 shells are Ti^{4+} , 74.5 pm; Nb^{5+} , 78 pm; and Zr^{4+} , 86 pm. Also, the ionic radii of some small size cations with d^n shells found in non-ferroelectric perovskite materials are $\text{Mn}^{3+}(d^4)$, 78.5 pm; $\text{Ti}^{3+}(d^1)$, 81 pm; and $\text{V}^{4+}(d^1)$, 72 pm. A quick comparison of the above two categories gives the impression that B-site cations with occupied d shells do not have any systematic increase in radii as compared to B-site cations with empty d shells. Thus, it can be concluded here that, the size of B-site cation is not a judging factor for the existence of these materials.

2 *Structural Distortions*

The ferroelectric materials are accompanied by a low-temperature phase transition that is devoid of any center of symmetry. In conventional perovskite ferroelectric materials, this is commonly achieved by displacement of B-site cation from the center of oxygen octahedron. On the other hand, cations having occupied d shells will show some dominant structural effects as they have more chances to undergo strong Jahn–Teller distortion. And this is to mention here that a material having Jahn–Teller distorted structure could have a lower driving force for the off-center displacement of cation as compared to the undistorted structure. Lanthanum manganite (LaMnO_3) and Yttrium titanate (YTlO_3) are well-known examples of this effect, where Mn^{3+} ion in LaMnO_3 has d^4 and Ti^{3+} ion in YTlO_3 has d^1 configuration. Both of them show d -type Jahn–Teller distortion, where the oxygen octahedron has elongated axes which are parallel to each other along the direction of the crystallographic c axis [11]. Also, in addition to Jahn–Teller ordering, orbital ordering is observed in these systems. LaMnO_3 is an insulating material with A-type antiferromagnetic behavior, where, the planes containing ferromagnetically aligned Mn^{3+} ions are antiparallel to each other. On the other hand, YTlO_3 is a strongly correlated ferromagnetic Mott–Hubbard insulator. Neither LaMnO_3 nor YTlO_3 is ferroelectric. However, the significance of the formal charge on B-site cation has to be noted here, as in BaTiO_3 , the $3d$ electrons have a configuration that is closer to d^1 than to d^0 resulting from the charge density contributed by oxygen ligands [12]. A cation with d^1 configuration should undergo a Jahn–Teller distortion. But, no such distortion is seen in BaTiO_3 , which is applicable for cations with empty d shells.

Since we have now arrived at a point, where we have gained some knowledge about the scarcity of multiferroic materials and how a multiferroic material can be made or what are the specific requirements to design a multiferroic material, Let us now look into the types of multiferroic materials based on their structure and strength of coupling between various order parameters.

3 Types of Multiferroic Materials

Magnetism in all the magnetic materials arises from the localized electrons in partially filled d or f shells corresponding to transition metal or rare earth ions giving a net magnetic moment. Magnetic ordering arises as the exchange interaction takes place between these localized magnetic moments. On the other hand, in the case of ferroelectric materials, there are different sources of the microscopic origin of ferroelectricity. Hence, depending upon the source of ferroelectricity, there can be various types of multiferroics. Broadly, they are divided into two categories: Single Phase Multiferroics and Composite Multiferroics. Single Phase multiferroics are further divided into Type I and Type II multiferroics. Type I multiferroic materials are the ones in which ferroelectricity and magnetism originate from different sources, and both the orders do not depend upon each other and hence are coupled weakly. Ferroelectricity in these materials occurs at high temperatures as compared to magnetism, the magnitude of spontaneous polarization P is quite large ($\sim 10\text{--}100\text{ mC/cm}^2$). Examples of type-I multiferroics are BiFeO_3 ($T_{\text{FE}} \sim 1100\text{ K}$, $T_N = 643\text{ K}$, $P \sim 90\text{ mC/cm}^2$) and YMnO_3 ($T_{\text{FE}} \sim 914\text{ K}$, $T_N = 76\text{ K}$, $P \sim 6\text{ mC/cm}^2$). Type-II multiferroics are comparatively recently discovered materials, here, magnetism is the source of ferroelectricity, thus indicating a strong coupling between the two orders [13, 14]. In addition to these two categories, various groups are working on the possibility to create composite multiferroics which comprise some well-studied magnetic and ferroelectric materials designed as multilayers and self-assembled nanostructures [15]. Let us discuss these types of multiferroics in more detail.

3.1 Single Phase Multiferroics

Single phase multiferroics are those which possess ferroelectric and ferromagnetic orders in a single phase. Following are the details about the types of single phase multiferroics.

(a) Type-I Multiferroic Materials

Type-I multiferroic materials are rather older and are large in number. The good thing about them is that the critical temperatures for both ferroelectric and magnetic transitions are well above room temperature. But, unfortunately, the magnetic and

ferroelectric orders are weakly coupled in these materials. Therefore, the challenging task for this category of multiferroics is to improve this coupling while keeping all other positive features as they are. Type-I multiferroics can be further divided into subcategories depending upon the source of ferroelectricity. Figure 2 summarizes type-I multiferroics.

(a-1) *Multiferroic Perovskite Materials*

Perovskite structured materials like BaTiO_3 or $\text{Pb}(\text{ZrTi})\text{O}_3$ (PZT) are well-known ferroelectric materials. Among perovskite materials, there exist many magnetic materials and also many ferroelectric materials [3, 16]. However, as discussed earlier in Sect. 2, there is a mutual exclusion of both magnetism and ferroelectricity in perovskite materials. For a material to show magnetic properties, the transition metal ion should have partially filled d shells, while ferroelectric perovskite materials contain transition metal ions like Ti^{4+} , Ta^{5+} , W^{6+} which have empty d shells. Ferroelectricity in these materials arises due to off-center displacement of transition metal ions that forms strong covalent bonds with one or three oxygen atoms, via the empty d shells. On the other hand, the presence of d^n configuration in magnetic transition metals suppresses the process of off-center displacement and hence prevents the

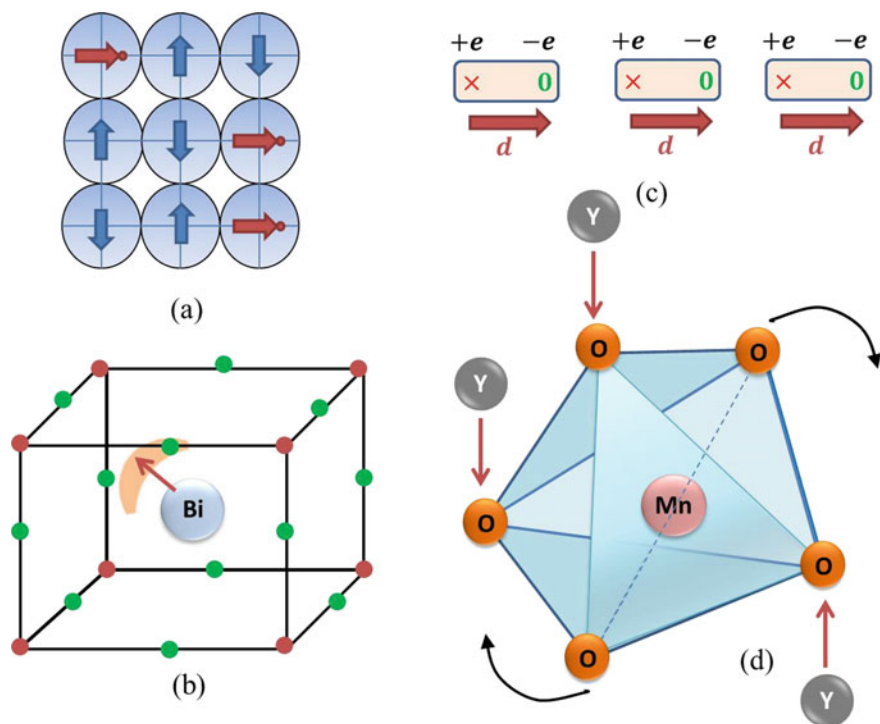


Fig. 2 Type-I multiferroics. **a** Perovskites, **b** ferroelectricity due to lone pairs, **c** ferroelectricity due to charge ordering, **d** ferroelectricity due to geometric structure

origin of ferroelectricity. This problem related to d^0 versus d^n issue in these materials was studied theoretically on a larger scale, but no satisfactory solution could be attained [3, 4, 16]. However, one promising solution could be to design a mixed perovskite with both d^0 and d^n ions (Fig. 2a). But, the drawback of doing so is that the coupling between both magnetic and ferroelectric counterparts in these mixed perovskite materials is very weak.

(a-2) *Ferroelectricity due to lone pairs*

Lone pairs are formed by those ions which do not contribute to the formation of chemical bonds. Figure 2b shows the origin of ferroelectricity that arises because of lone pairs. In perovskite materials like BiFeO_3 , BiMnO_3 , and PbVO_3 , Bi^{3+} and Pb^{2+} give major contributions towards the origin of ferroelectricity, as the two outer 6s electrons in these ions form lone pairs or dangling bonds. Thus, they have large electric polarization—which is the required condition for ferroelectricity. The microscopic origin of ferroelectricity in these materials arises due to the ordering of lone pairs in one direction. This type of ordering is observed in many ferroelectric materials which are based on Bi and Pb such as BiFeO_3 . This ordering also helps in improving the ferroelectric properties of $\text{Pb}(\text{Zr}_x\text{Ti}_{1-x})\text{O}_3$ compounds [3].

(a-3) *Ferroelectricity due to charge ordering*

Ferroelectricity in certain materials can also be achieved by charge ordering and is observed generally in transition metal compounds with transition metal ions having different valence. As shown in Fig. 2c, if both sites and bonds are imbalanced after charge ordering in these compounds, then it can give rise to ferroelectricity [17]. An equivalent phenomenon can take place in materials like $\text{Pr}_{0.5}\text{Ca}_{0.5}\text{MnO}_3$ and also in Nickel compounds (RNiO_3) with charge ordering [18]. Most commonly, there exist materials where the ions have different charges as the elements are different; furthermore, dimerization is also observed in these compounds. The compounds that belong to this category are TbMn_2O_5 [14] and newly discovered multiferroic $\text{Ca}_3\text{CoMnO}_6$ [19]. Another situation that is likely possible is the inequivalent bond formation because of the structure of the materials, along with site-centered charge ordering. The examples for this category are organic ferroelectric $(\text{TMTTF})_2\text{X}$ [20] and multiferroic LuFe_2O_4 [21].

(a-4) *Ferroelectricity due to Geometric Structure*

In certain compounds, ferroelectricity arises due to certain changes in the geometry of the structure (Fig. 2d). The famous example for this category is Yttrium Manganite (YMnO_3), where ferroelectricity has nothing to do with magnetic ion Mn^{3+} [22]. In this case, the tilting of the MnO_5 block occurs to provide a close packing of the structure which results in the movement of oxygen ions towards smaller Y ions and hence gives ferroelectricity.

(b) *Type-II Multiferroic Materials*

The Discovery of a novel class of multiferroic materials where ferroelectricity arises due to the presence of a particular magnetic state has created the biggest interest in developing multiferroics. Examples of such categories are TbMnO_3 , in which magnetic ordering occurs at a temperature of 41 K, and at a still lower temperature of ~ 28 K, there is a change in magnetic structure. It is observed that at a lower temperature the electric polarization becomes non-zero. A similar thing happens in the compound TbMn_2O_5 . The first study on TbMnO_3 revealed that electric polarization has a strong dependence on an external applied magnetic field, where, the electric polarization rotates by 90° as a critical magnetic field is applied along a fixed direction [13]. In the case of TbMn_2O_5 , there is an even stronger dependence of polarization on the magnetic field [14]. It is observed that the polarization changes its polarity with the applied magnetic field. As the magnetic field is altered between ± 1.5 T, the electric polarization begins to oscillate. After these two compounds, a large number of type-II multiferroics, with even stronger coupling between magnetic and ferroelectric orders, have been synthesized and studied. Further, type-II multiferroic materials can be divided into two categories: firstly, when ferroelectricity arises due to magnetic spiral, and secondly when ferroelectricity is observed in collinear magnetic structures. Let us now discuss them separately.

(b-1) *Spiral type-II multiferroics*

These are the most commonly found type-II multiferroic materials. In these materials, ferroelectricity arises along with cycloid type spiraling magnetic phase. Examples are TbMnO_3 , MnWO_4 , and $\text{Ni}_3\text{V}_2\text{O}_6$. In the case of TbMnO_3 , the magnetic state is represented by a spin-density wave that varies sinusoidally below 41 K. Here, all the magnetic spins are pointed in the same direction, but there is a periodic variation in the size of the local moment. However, below 28 K, the Mn spins order in such a way that their tip sweeps out a cycloid. A microscopic [23] and phenomenological [24] approach revealed that in the case of a cycloidal spiral magnetic structure, the polarization \mathbf{P} can be represented by the equation:

$$P \sim r_{ij} \times [S_i \times S_j] \sim [Q \times e] \quad (1)$$

where, r_{ij} connects two neighboring spins S_i and S_j , Q is the wave vector which describes the spiral, and $e \sim [S_i \times S_j]$ is the axis of spin rotation. The spin-orbit interaction is mainly responsible for the origin of this polarization.

In any insulating material, magnetic frustration arises due to the presence of spiral magnetic ordering. Hence, type-II multiferroicity is most commonly observed in frustrated magnetic systems. The findings of these materials have potential applications in different fields.

Thus, from the above discussion, it is clear that the magnetic field plays an important role. The effect of applied magnetic field \mathbf{H} on a cycloid can be seen similar to well famous spin-flop transition in an antiferromagnetic material. When an external

magnetic field is applied, the sublattice magnetic moments are preferably oriented in a plane that is perpendicular to the applied field so that these magnetic moments are able to cant in the direction of an applied field with a lesser loss of exchange energy between adjoining spins. Subsequently, when the applied field forces the magnetic cycloid plane to switch by 90° , the electric polarization \mathbf{P} also flips, as given by Eq. (1), \mathbf{P} lies in the plane of spins but is perpendicular to the wave vector \mathbf{Q} . It is to be noted here, that the derivation of Eq. (1) is valid for a particular crystal structure like simple cubic or tetragonal. Therefore, in such cases, Polarization \mathbf{P} of a proper screw, where the plane of spin rotation is perpendicular to the wave vector \mathbf{Q} , will be zero. Nonetheless, recent studies show that the above-mentioned effect may not be observed for other crystal structures, where a non-zero polarization may appear even for a proper screw spiral [25]. This is observed experimentally in various systems like $\text{RbFe}(\text{MoO}_4)_3$ [26], CuFeO_2 , and ACrO_2 ($A=\text{Cu, Ag, Li, Na}$) [27].

(b-2) *Type-II multiferroics with collinear magnetic structures*

In collinear magnetic structures, all the magnetic moments are oriented in a specific direction along an axis without any requirement of spin–orbit coupling. These materials can show electric polarization as a result of exchange striction as the coupling between the magnetic spins varies with the position of the atoms. The most common example of this category is $\text{Ca}_3\text{CoMnO}_6$ [19], which is made up of Co^{2+} and Mn^{4+} ions forming a one-dimensional chain with alternate positions. At elevated temperatures, these ions in the chain maintain a fixed distance and hence it possesses inversion symmetry with zero polarization. This inversion symmetry is broken by the magnetic ordering with spins forming a magnetic structure of the type $\uparrow\uparrow\downarrow\downarrow$. Now, ferroelectricity results as distortion in ferro ($\uparrow\uparrow$) and anti-ferro ($\downarrow\downarrow$) bonds is different due to exchange striction. This observation is also confirmed by theoretical studies [28]. In $\text{Ca}_3\text{CoMnO}_6$, exchange striction is caused by the different valence of transition metal ions (Co^{2+} and Mn^{4+}). It is also observed that a similar effect can be obtained for materials with identical magnetic ions, by considering the fact that in transition metal oxides, exchange striction generally arises through intermediate oxygens and depends on two factors: distance between the metal ions and the metal–oxygen–metal bond angle. In perovskite materials like RMnO_3 , where R is a small rare earth ion, the magnetic state of the Mn ion in the basal plane is of the type $\uparrow\uparrow\downarrow\downarrow$. In such cases, the exchange striction can make the oxygen ions move in a direction perpendicular to the Mn–Mn bonds which produce an electric polarization along the direction of the shift [29–32].

Another phenomenon by which ferroelectricity can arise in frustrated magnetic systems with a collinear magnet is *electronic ferroelectricity*, where the polarization of a triangular spin structure is proportional to the spin correlation function, $\mathbf{S}_1(\mathbf{S}_2 + \mathbf{S}_3) - 2\mathbf{S}_2\mathbf{S}_3$ (the subscripts denote the positions on the vertices of the triangle) [33]. Also, the polarization is zero if the spin correlation function is zero.

3.2 Composite Multiferroics

Composite multiferroics are a better alternative due to the scarcity of single phase multiferroics. In this case, multiferroicity is due to a combination of two separate materials which are ferroelectric and ferromagnetic/antiferromagnetic, respectively. As there are many ferromagnetic/antiferromagnetic and ferroelectric materials at room temperature, it's easy to make a composite of them that behaves as multiferroic at room temperature. The properties of composite multiferroics can be described on the basis of phase connectivity. To explain this concept, a notation like d_1-d_2 is used, where the subscripts represent the dimensionality of the respective component. On the basis of dimensionality, these composites are described as 0–3 which denotes granular compounds i.e. ferromagnetic particles embedded in a ferroelectric matrix, 1–3 structures with columns of ferromagnetic material in a ferroelectric matrix, and 2–2 planar structures with alternate layers of ferromagnetic and ferroelectric materials [34].

4 Conclusion

In this chapter, we discussed the origin of multiferroics and their historical journey. Basically, multiferroics materials are those which show multiple ferroic orders and coupling between them. Magnetoelectric multiferroic materials are the most studied materials that fall in the category of multiferroics. For a material to show magnetoelectric effect, it is discussed that the requirements are concerned with symmetry properties, electrical properties, and chemical d^0 -ness. Multiferroics can be divided into single-phase and composite materials, based on the structure. Single-phase multiferroics being those which can show the coupling between various ferroic orders in the same phase without being combined with any other material. Composite multiferroics are those which overcome the scarcity of single phase multiferroics, as they comprise a combination of different ferroelectric and ferromagnetic materials to show a strong multiferroic behavior. Single Phase multiferroics can be further divided into Type-I and Type-II multiferroics, depending upon the strength of coupling between various ferroic orders. Composite multiferroics comprise 0–3 type granular compounds, 1–3 structures, and 2–2 planar structures. The studies on improving the multiferroic properties and strengthening the magnetoelectric coupling are proving these materials as potential candidates for applications in multiple logic state devices, spin-valves as well as energy harvesting devices.

References

1. N.A. Spaldin, S.-W. Cheong, R. Ramesh, Phys. Today **63**, 38 (2010)
2. D.I. Khomskii, J. Magn. Magn. Mater. **306**, 1 (2006)

3. D. Khomskii, *Physics* **2**, 20 (2009)
4. N.A. Hill, *J. Phys. Chem. B* **104**, 6694 (2000)
5. E. Ascher, H. Rieder, H. Schmid, H. Stössel, *J. Appl. Phys.* **37**, 1404 (1966)
6. V.A. Smolensky, G.A. Agranovskaya, A.I. Isupov, *Sov. Phys. Solid State* **1**, 149 (1959)
7. A.I. Smolensky, G.A. Isupov, V.A. Krainik, N.N. Agranovskaya, *Izvest Akad Nauk SSSR, Ser. Fiz.* **25**, 1333 (1961)
8. W. Brixel, J.P. Rivera, A. Steiner, H. Schmid, *Ferroelectrics* **79**, 201 (1988)
9. H. Schmid, *Ferroelectrics* **162**, 317 (1994)
10. R.D. Shannon, *Acta Cryst. A* **32**, 751 (1976)
11. T. Mizokawa, D.I. Khomskii, G.A. Sawatzky, *Phys. Rev. B Condens. Matter Mater. Phys.* **60**, 7309 (1999)
12. R.E. Cohen, H. Krakauer, *Ferroelectrics* **136**, 65 (1992)
13. T. Kimura, T. Goto, H. Shintani, K. Ishizaka, T. Arima, Y. Tokura, *Nature* **426**, 55 (2003)
14. N. Hur, S. Park, P.A. Sharma, J.S. Ahn, S. Guha, S. Cheong **429**, 392 (2004)
15. R. Ramesh, N.A. Spaldin, *Nat. Mater.* **6**, 21 (2007)
16. D.I. Khomskii, *J. Magn. Magn. Mater.* (2004)
17. D.V. Efremov, J. Van Den Brink, D.I. Khomskii, *Nat. Mater.* **3**, 853 (2004)
18. S.-W. Cheong, M. Mostovoy, *Nat. Mater.* **6**, 13 (2007)
19. Y.J. Choi, H.T. Yi, S. Lee, Q. Huang, V. Kiryukhin, S.-W. Cheong, *Phys. Rev. Lett.* **100**, 047601 (2008)
20. P. Monceau, F.Y. Nad, S. Brazovskii, *Phys. Rev. Lett.* **86**, 4080 (2001)
21. N. Ikeda, *J. Phys. Condens. Matter* **20** (2008)
22. B.B. Van Aken, T.T.M. Palstra, A. Filippetti, N.A. Spaldin, *Nat. Mater.* **3**, 164 (2004)
23. H. Katsura, N. Nagaosa, A.V. Balatsky, *Phys. Rev. Lett.* **95**, 057205 (2005)
24. M. Mostovoy, *Phys. Rev. Lett.* **96**, 067601 (2006)
25. T.H. Arima, *J. Phys. Soc. Jpn.* **76**, 1 (2007)
26. M. Kenzelmann, G. Lawes, A.B. Harris, G. Gasparovic, C. Broholm, A.P. Ramirez, G.A. Jorge, M. Jaime, S. Park, Q. Huang, A.Y. Shapiro, L.A. Demianets, *Phys. Rev. Lett.* **98**, 2 (2007)
27. T. Kimura, J.C. Lashley, A.P. Ramirez, *Phys. Rev. B Condens. Matter Mater. Phys.* **73**, 1 (2006)
28. H. Wu, T. Burnus, Z. Hu, C. Martin, A. Maignan, J.C. Cezar, A. Tanaka, N.B. Brookes, D.I. Khomskii, L.H. Tjeng, *Phys. Rev. Lett.* **102**, 026404 (2009)
29. A. Malashevich, D. Vanderbilt, *Phys. Rev. Lett.* **101**, 1 (2008)
30. B. Lorenz, Y.-Q. Wang, C. Chu, *Phys. Rev. B* **76**, 104405 (2007)
31. I.A. Sergienko, C. Şen, E. Dagotto, *Phys. Rev. Lett.* **97**, 227204 (2006)
32. S. Picozzi, K. Yamauchi, G. Bihlmayer, S. Bluegel, *Phys. Rev. B* **74**, 12 (2006)
33. L.N. Bulaevskii, C.D. Batista, M.V. Mostovoy, D.I. Khomskii, *Phys. Rev. B Condens. Matter Mater. Phys.* **78**, 1 (2008)
34. J.P. Velez, S.S. Jaswal, E.Y. Tsymlal, *Philosophical transactions of the Royal society A: mathematical. Phys. Eng. Sci.* **369**, 3069 (2011)

Multiferroic Material Bismuth Ferrite (BFO): Effect of Synthesis



Ritesh Verma, Ankush Chauhan, Neha, and Rajesh Kumar

Abstract This chapter has a focus on multiferroics in particular bismuth ferrite and its production techniques (BiFeO₃, BFO). BFO is recognized to be the major ABO₃ perovskite-type single-stage compound that has multiferroic at room temperature and is therefore seen as the most encouraging up-and-comer for applications in next-generation storage, information and spintronics. Since, ferroelectric and antiferromagnetic characteristics are included concurrently; BFO has started to draw attention to it. BFO exhibits an electrical and antiferromagnetic ordering of the cycloid spin structure ($T_c = 850$ °C). In ABO₃ multiferroic, bismuth has B sites with Fe³⁺ ions and 6 neighboring anions of oxygen, forming FeO₆ octahedra linked by a sharing of their corners. Unfilled space between FeO₆ and the A-site is mainly occupied by the Bi³⁺ ions. There are numerous methods to synthesize BFO nanoparticles like sol–gel auto-combustion, solid-state, co-precipitation etc. In this chapter, we discuss the various methods of synthesis in detail.

Keywords Multiferroics · Perovskite · Ferroelectric · Antiferromagnetic · Solid-State · Sol–gel Auto-combustion

1 Introduction

Nanotechnology is an interdisciplinary field of research dealing with very small particles of one billionth of a metre in size. In arithmetic, 10^{−9}, known as a nanometer (nm), may be defined in mathematics [1]. The nanoscale is the size that plays a major role as a material's element of atoms and molecules. The scientific and technological area in which the complex macromolecules are inside the nanometric range is nanotechnology. First, in his first classical speech “A challenge for the introduction of a new field of physics, A great deal of ground” the father of nanotechnology “Richard Feynman” presented the notion of nanotechnology to the world [2]. In 1974 the first

R. Verma · A. Chauhan · Neha · R. Kumar (✉)

School of Physics and Materials Science, Shoolini University, Bajhol, Solan, HP, India

R. Verma · A. Chauhan · R. Kumar

Himalayan Centre of Excellence in Nanotechnology, Shoolini University, Bajhol, Solan, HP, India

coincided with the word Nanotechnology was Norio Taniguchi of Tokyo University. In the realm of conceptual design and in the case of intelligent materials that may protest worldwide concerns, nanotechnology and nanoscience now-a-days are essential. Nanotechnology has been increasing day after day in the class of smart materials and has taken them to the next level forcefully. Smart materials can be classified as high-quality, specifically sized nanoparticles. The next-generation materials are regarded as intelligent and are capable of changing their characteristics, such as thermal, mechanical, electromagnetic and optical inputs, automatically [3]. These materials may be regarded as intelligent materials that adapt to the changes in the environment and explore their functions in the environment accordingly [4].

Between smart materials, ferroic and multiferroic materials attract more attention. New and inventive materials that bring changes in building and manufacturing represent the growth of nanotechnology and intelligent materials. We need to grasp the link between synthesis, structure and their characteristics to find novel materials of desirable features. One of the greatest methods to accomplish multifunctionality is by expanding novel materials in an individual phase by lining up their different physical features. Due to its basic and technical applications, the topic of multiferroics captivated more researchers with itself.

2 Ferroics

The Latin term “Ferrum,” which signifies iron, is used to refer to the word ferroic. The term ferroic encompasses such properties as ferromagnetic, ferroelastic and ferroelectric. It can be ferromagnetic and ferroelectric. One of the most essential characteristics is that ferroic materials tend to a well-defined hysteresis circuit. The material is magnetically, electrically or physically switched for a specified hysteresis loop. A spontaneous M magnetization can be converted to a hysteresis loop with an application of a magnetic field. Likewise, the electric polarization P can be converted to hysteresis again by the application of an electric field and the last one, mechanical stress application, can be converted to ferroelastic deformation. Ferroics are the kinds of products in which it changes its physical characteristics by applying external variables such as temperature, stress, pressure, electric and magnetic fields. Figure 1 shows the ferroic materials hysteresis loop. The reason for this shift is because the transition to phase beyond critical temperature. Overhead, no physical characteristics change and the material was discovered in a non-ferroic state over this critical temperature.

A domain is an important factor in the case of ferroic materials. A domain is an area inside the material in which the parameters aligned themselves naturally in the uniform direction. In the absence of applied fields, no order parameters take place. When we apply magnetic (M), stress (σ) or electric (E) fields then the domain starts to orientate in a uniform direction. At higher applied fields, the saturation of polarization (P_s), magnetization (M_s), strain (ϵ_s) is observed. After removing the applied field, it will come back to zero and hence possess a noticeable range of order

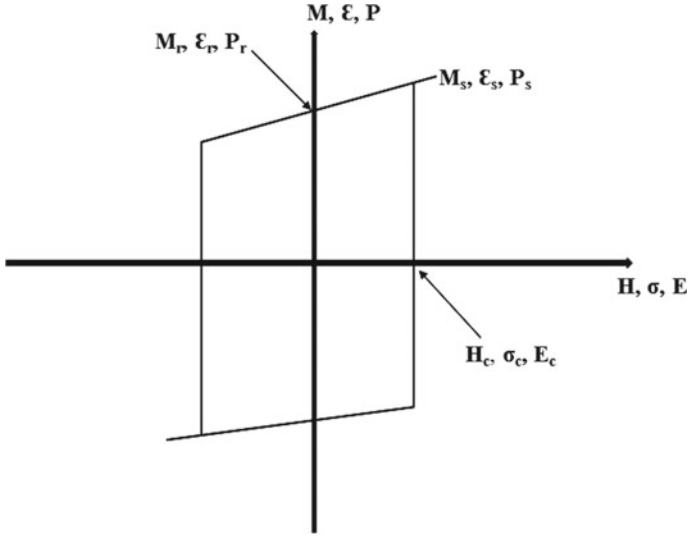


Fig. 1 Hysteresis loop of ferroic materials

parameter at a specific field called retentivity ($P_r, M_r,$ and ϵ_r) while if we reverse the field the net order parameter become zero known as coercive field (H_c, E_c, σ_c).

2.1 Ferromagnetism

Ferromagnetism was originally found in Chinese in the traditional period about 100 B.C. In the context of ferromagnetic material, the atomic magnetic moment, as seen in Fig. 2, is parallel to each other because of the intense interplay between the neighboring magnetic moment. For example, gadolinium, alloys, alnico, nickel and iron, etc. Ferromagnetic compounds are.

The valence electrons of the neighboring atoms show interaction with each other in such a way that the magnetic moment of these neighboring atoms aligned in the same direction [5] under a specific area called a magnetic domain. Inside these magnetic domains, the number of atoms is very large (10^{17} – 10^{21} m^3) but the occupied volume of these domains is very less (10^{-12} – 10^{-15} m^3). The theory of ferromagnetism was first theorized by Pierre Weiss in 1906.

According to Weiss theory, there are main two important postulates (i) their spontaneous magnetization (ii) their domain distribution. The variation of temperature varied the magnetic susceptibility (χ) of the ferromagnetic substances is given by Curie–Weiss law,

$$\chi = C/T - T_c \tag{1}$$

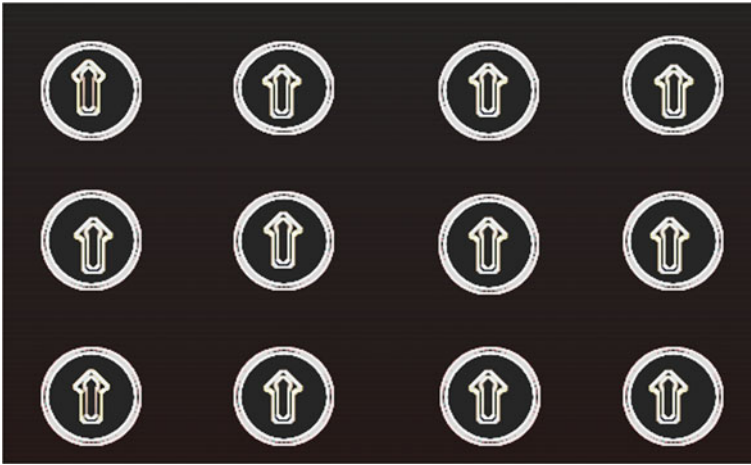


Fig. 2 Ferromagnetic ordering

where C = Curie point, T_c = Curie temperature. Above the Curie temperature, the phase transition of materials from ferromagnetic to paramagnetic takes place and with temperature rise their susceptibility decreases. Ferromagnetism arises due to the unpaired d electrons associated with transition metals. According to domain theory, all the magnetic moments are aligned in the same direction, resulting in net magnetic dipole moment in the case of ferromagnetic substances. The alignments are in different directions in different domains. No existence of magnetism took place in the absence of a magnetic field. When the ferromagnetic material is placed in an external magnetic field then the domain having magnetic moment parallel to the applied field enlarge at the expenditure of neighboring domains, called Bloch walls and arrangements of boundaries as displaced in Fig. 3.

2.2 Antiferromagnetism

Neel and Bitter firstly invented antiferromagnetism. In 1938, it was experimentally first observed in MnO by Squire, Bizette and Tsai. In certain materials at very little temperature, the neighboring ions act like teeny magnets, align themselves in the opposite direction as shown in Fig. 4 and result in no magnetism because they cancel out each other magnetization effect. MnO, Cr, CuO, NiO are some examples of antiferromagnetic materials.

Above a certain temperature, antiferromagnetic material becomes paramagnetic materials known as Neel temperature. Above Neel temperature, the susceptibility is given by the equation,

$$\chi = \frac{2C}{T + T_N} \quad (2)$$

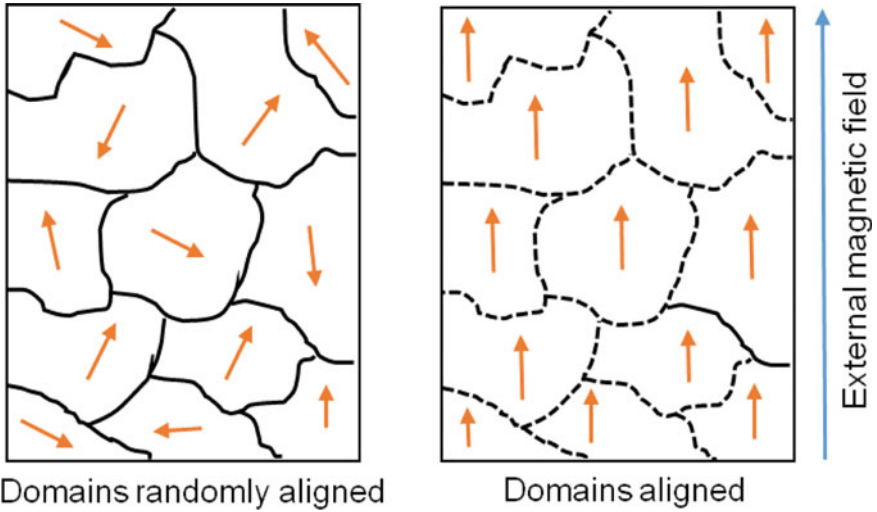
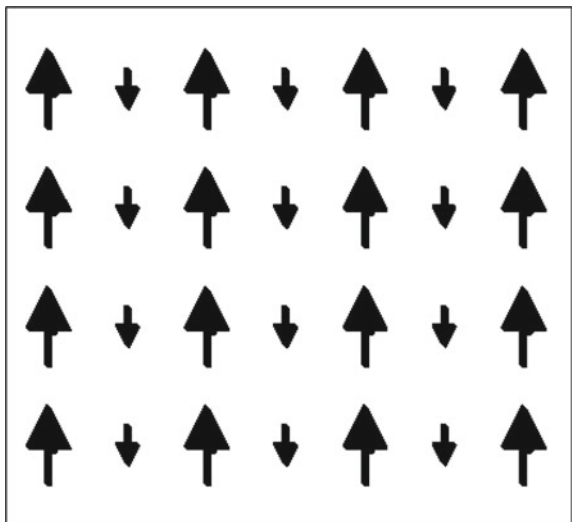


Fig. 3 Ferromagnetic substances in an external magnetic field. Reprinted with permission from MDPI

Fig. 4 Antiferromagnetic order



where T_N stands for Neel temperature. The susceptibility is closely independent in the direction of the field concerning spin axis, at and above Neel temperature. Whereas, the antiferromagnetic susceptibility is greatly dependent upon the orientation of the magnetic field below the Neel temperature.

3 Ferroelectrics

J. Valasek also gave the notion of ferroelectricity in 1920 when he examined the dielectric characteristics of Rochelle salt [6]. Ferroelectric materials are a form of polar material consisting of a spontaneous electrical polarization, which may be reversed by the application of an outside electric field. The centre of the positive charge does not match the centre of the negative charge [7–9] in case of a ferroelectric condition. At some time, ferroelectricity, known as the temperature transition, is gone and overhead, the material becomes paraelectric.

3.1 Polarization

In a polarized material, polarization may be defined as the dipole moment per unit volume and in mathematically form

$$P = p/V \quad (3)$$

where volume and dipole moment of the dielectric material is denoted as V and p . The polarity of a molecule can be measured by dipole moment. We can define the dipole moment as the vector sum from the center of negative charge to the center of positive charge written in the equation as,

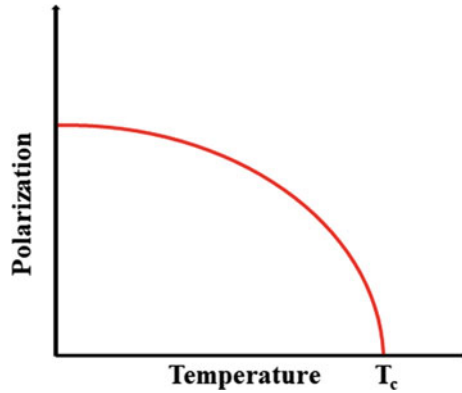
$$p = \sum q_n r_n \quad (4)$$

where r_n is the position vector of q_n .

3.2 Spontaneous Polarization

Spontaneous polarization may be defined as that type of polarization that a material possesses in the lack of an external electric field. When the interaction between the adjacent permanent dipoles occurs then they align themselves in the same direction. In ferroelectrics, the spontaneous polarization may be reorientation able and reversible. The phase transitions in the case of these materials occur at a temperature T_c . Above this temperature; the electric dipoles are randomly oriented and go to a paraelectric state. Below temperature T_c ($T < T_c$) the substance goes to spontaneous polarization where the interaction between the dipoles took place. The interaction between dipoles tends to an internal field that regulates the dipoles. The regulation of dipoles gives

Fig. 5 Temperature dependence of polarization



rise to spontaneous polarization (P_s). The dropping of temperature tends to the steady increase in polarization until it disappears at Curie temperature (T_c) [10], as shown in Fig. 5.

3.3 *Ferroelectric Domains*

In a ferroelectric material, all the electric dipoles are arranged in a uniform direction lies in a small region called domain while in the case of polar polarization these domains are aligned in a different direction. The difference in the number of the downward and upward-directed domains results in net polarization. The crystal is spontaneously strained with $a_T \leq a_C \leq c_T$ in the ferroelectric phase where a_T and a_C are the a-axis of the tetragonal and cubic unit cell. The polarization along with the direction will arise and develop on the mechanical and electrical boundary situations introduced on the sample. The areas between the two separated domains are known as domain walls displayed in Fig. 6a, b. We can represent domains walls by the angle between the directions of polarization on another side of the wall. Ordinarily, to minimize the walls energy domains are formed results in a change in the direction. The boundary wall which isolates the domain acquire perpendicular polarization is called the “90° walls” and having opposite polarization called the “180° wall” (Fig. 6b). 90° domain walls are much broad than that of the domain wall of 180°.

Grain size, sample geometry, crystal symmetry, defect structure and synthesis method are certain factors that affect the structure and size of these domains [11, 12]. The interior domains (the neighboring domain between the materials) are different from the properties of the domain making them more conductive, capable to be electrically charged or display mechanical strain. Hence the properties of the surrounding material may affect by the stationary domain walls if their density is very large. By applying electric field and pressure on the ferroelectric the domain wall make move.

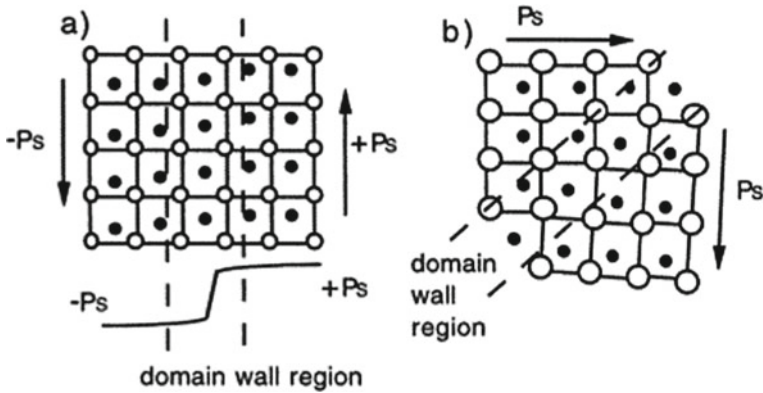


Fig. 6 Illustrations of the tetragonal perovskite structure of **a** 180° and **b** the domain and domain wall areas. For a 180° wall, the schematic polarization shift over the domain wall is illustrated (a). (b) is exaggerated by tetragonal distortion. Reprinted with permission from IOP

This will tend to a large contribution to the electrical, mechanical, and electromechanical properties of the ferroelectrics, called domain wall contribution [13, 14]. The movement of the domain walls is afflicted by certain parameters such as grain boundaries, point defects and dislocations [15].

3.4 Ferroelectric Hysteresis Loop

In the case of ferroelectric material, the hysteresis loop shows the relation between polarization P and applied field E . When the substance gets polarized in a certain direction and after that comes back to the opposite direction is known as the hysteresis loop shown in Fig. 7. On applying an electric field to a ferroelectric material, the randomly oriented domains get polarized to a certain direction i.e., positive axis. At an appropriate large electric field, all the electric domains are polarized along the applied electric field and hence obtain a maximum value called saturation point (P_{max}) [16]. Then the material is described as single domain material. On decreasing the applied field, the rate of polarization decreases but for zero electric fields, the value of polarization does not return to zero, at this point the material is spontaneously polarized thus achieving a remnant polarization (P_r). In the absence of field, this polarization would remain. When we apply the electric field in the opposite direction up to a coercivity value (E_c) the remnant value gets disappear. Further, on reversing the applied field, the material again acquires the saturation polarization but in the reverse direction. The area inside the loop shows the amount of energy that is necessary to switch the direction of polarization 180° .

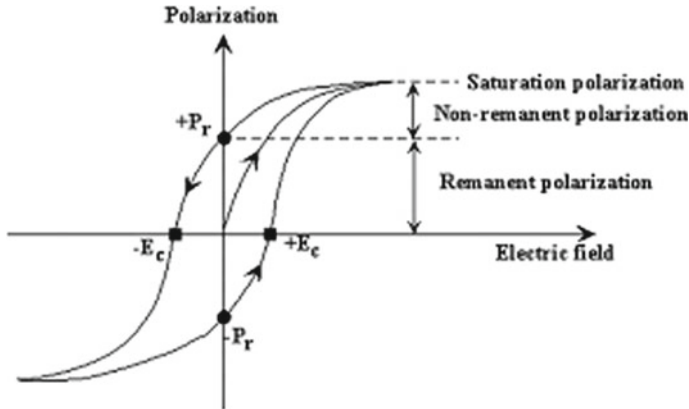


Fig. 7 P-E hysteresis curve of ferroelectric materials. Reprinted with permission from Taylor and Francis

4 Ferroelastics

Ferroelastic materials are kinds of materials where mechanical switching takes happen by the application of stress between two orientation states of a material. We may do a broader study on Ferro, ferromagnetic and multiferroic switching behaviour by knowing ferroelastic properties [17]. A visible form change in the material arises during mechanical switching. We may thus claim that there is a phase shift while applying stress. The transition of the Ferroelastics stage generates an elastic hysteresis that depends on temperature [18].

5 Multiferroic Materials

Multiferroic material is a type of operating material including concurrently two or more “ferroic” orders such as ferroelectricity (anti), ferromagnetism (anti), ferroelasticity and ferrotoroidism. The presence of up to two switchable states (for example strain, magnetization and polarization) has garnered great interest in itself because they are relevant to the many applications of multifunctional devices. Furthermore, owing to the combination of the different factors in the sequence, physical effects like the magnetic polarization field or vice versa can be injected. For device applications, one of the most adorable factors for multiferroic material is to attain two or more ‘ferroic’ orders at room temperature [19]. In the case of solid-state physics and different types of technological fields, these materials have great importance. Potential applications in spintronic devices, data storage devices and multiple state memories make more curious these in the study field [20]. There are certain parameters that on coupling describes the multiferroic behaviour is illustrated in Fig. 8.

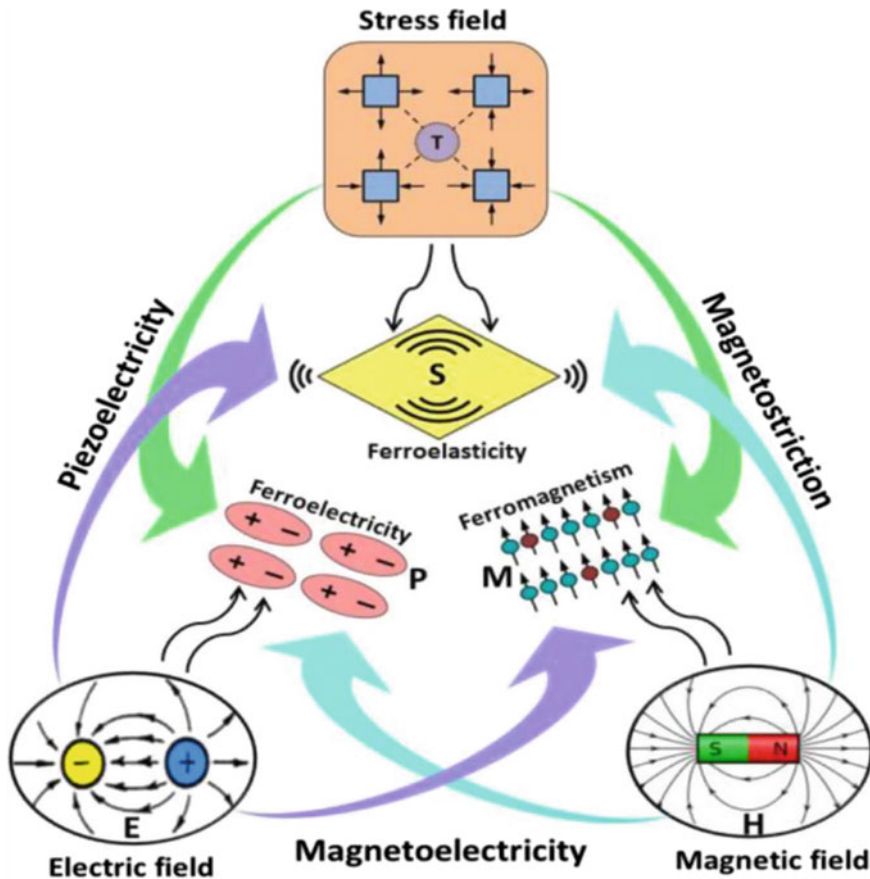


Fig. 8 Schematic illustration of the coupling between magnetic-elastic-electric in multiferroics [21]. Reprinted with permission from MDPI

- **Magnetolectric coupling:** The coupling takes place between the ferromagnetism and ferroelectricity which enables the magnetic field to change polarization and vice-versa.
- **Piezoelectricity:** It associates with the change in polarization as a function of applied strain.
- **Piezomagnetism:** It associates with the change in magnetization as the function of applied strain.
- **Electrostriction:** It associates with the change in the strain as a quadratic function of an applied electric field.
- **Magnetostriction:** It associates with the change in the strain as a quadratic function of an applied magnetic field.

The magnetolectric coupling material is one of the most sought features among all these multiferroic materials. The magnetolectrical coupling will produce a novel

design and be used for practical applications of electronic materials. Chemically, single-phase magnetoelectric are homogenous and magnetoelectric couplings are provided by isotropic compounds, which need magnetic moments and long-range electric dipoles simultaneously. Miserably, there are relatively few materials that show multimedia [22], and the presence of multiferroic materials is, of course, quite small. For ferroelectric behaviour, the transition ions with empty d shells are responsible. The positive loading ions contain combined to form molecules with oxygen ions (negative load). The transition ion movement towards oxygen ions hence encourages electric polarization takes place at electrical dipole moment. Then it is stabilized between O2p and vacant d-orbitals by strong covalent interactions. Vice versa, magnetism is responsible for transition metals using partly filled d-orbitals. The filled orbitals with electron spin are not carried out in magnetic order. Interaction between the uncompensated spins of various ions generates a lengthy magnetic order and causes the electrons to hop. These variables are responsible for ferromagnetism and ferroelectricity, which makes them trendy [23].

5.1 Type-1 Multiferroics

The first group of multiferroic materials comprises those types of materials in which ferroelectricity and magnetism take place independently. For these materials, polarization has a high value and at high temperature, ferroelectricity appears. Examples are YMnO₃, BiFeO₃ etc.

5.2 Type-2 Multiferroics

The second group of multiferroic materials comprises those types of materials in which ferroelectricity and magnetism depend on each other (polarization caused by magnetism and vice-versa). These materials show a low value of polarization. Examples are: TbMnO₃, MnWO₄ [24, 25].

6 Mechanism of Multiferroicity

6.1 Multiferroicity Due to Lone Pair

In BFO ferroelectricity is mainly caused by Bi³⁺ ions. These ions contain two electrons, called solitary pairs, which are not used for bond formation. The materials are highly polarized and the formation of ferroelectricity may be described by organizing these pairs in a unidirection, as illustrated by Khomskii [26].

6.2 Multiferroicity Due to Charge Ordering

Ferroelectricity due to charge ordering is another mechanism that tends to ferroelectricity. It occurs in materials by accommodating ions with mixed valence. After charge ordering both bonds and sites become unequal as illustrated by Khomskii [26].

7 Applications of Multiferroics

Multiferroics have a large range of potential applications that are given below as:

- **Magnetic recording read heads:** These are based on magnetoelectric effect so used in multiferroic materials.
- **Spintronics:** MRAM is the most trending spintronic device that has MTJ (Magnetic Tunneling Junction). MTJ tends to 4 or 8 stage logic used in multiferroic materials. It consists of large memory density, non-volatility and less use of power rather than ordinarily used memory devices.
- **Photovoltaic solar cell:** Multiferroic materials show coupling effect so used in photovoltaic solar cells.
- **Thermal energy harvesting:** Multiferroic materials like $\text{Ni}_{45}\text{Co}_5\text{Mn}_{40}\text{Sn}_{10}$ contain inter-metallic multiferroic alloy that changes heat into electromotive work. So, these materials also have been used for energy harvesting.

8 BiFeO₃ (BFO) as a Multiferroic

BFO is known to be the main single-stage ABO_3 -type perovskite compound which has multiferroic properties at room temperature and is therefore viewed as the most encouraging up-and-comer among different multiferroic materials for applications in next-generation memories, information storage and spintronics. BFO has started to pull much attention towards itself due to the presence of ferroelectric and antiferromagnetic properties simultaneously [27]. As per our previous study, we found that with a cycloid spin structure BFO has ferroelectric ordering ($T_c = 850\text{ }^\circ\text{C}$) and antiferromagnetic ordering ($T_N = 370\text{--}380\text{ }^\circ\text{C}$) [28]. BiFeO_3 is one of the lead free multiferroic materials with narrow band gap so counted in an environmentally friendly material. Thin and bulk film form of BiFeO_3 can be prepared. In bismuth ferrite, reason behind the ferroelectric behaviour is the presence of 6s electron pair of Bi and for the magnetic behaviour partially filled d -orbitals of Fe is responsible [29].

8.1 Structure of BFO

Among the multiferroic materials, BiFeO_3 has a rhombohedral distorted perovskite structure with space group $R3c$ at room temperature [30]. The compound formula of perovskite is regularly expressed as ABO_3 . From the structure of BFO shown in Fig. 9, we came to know that Fe^{3+} ions occupy the centered position, Bi^{3+} ions occupy the corner position and O_2 -conquers all the face centered position. In ABO_3 perovskite Bismuth multiferroic has B-sites occupied by Fe^{3+} ions surrounded by six adjacent oxygen anions and form FeO_6 octahedra that are connected by sharing their corners. A-site consumes the unfilled space between FeO_6 i.e., consumed by Bi^{3+} particles. BFO in a hexagonal unit cell contains six equation units having cross-section parameters $a = 5.587 \text{ \AA}$, $b = 5.587 \text{ \AA}$ and $c = 13.867 \text{ \AA}$ with $\alpha = \beta = 90^\circ$ and $\gamma = 120^\circ$ [31]. The antiferromagnetic property of BFO contains G-type arrangement in which Fe^{3+} ions having spins up are enclosed by six adjacent neighbours of Fe ions by spin down. Due to this, there is distortion found in the oxygen octahedron related to Fe–O–Fe angle, resulting a weak canting moment. A significant basic parameter is the rotation angle of the oxygen octahedral. This angle would be 0° for a cubic perovskite with consummately coordinated ionic sizes. How the ions into a perovskite unit cell fit well the ratio for this is $(r_{\text{Bi}} + r_{\text{O}})/l = 1$, where ‘ l ’ is the length of the octahedral edge and the ionic radius of the individual particle is denoted by ‘ r ’.

This is relatively related to the Goldschmidt tolerance factor which is defined as, $t = \frac{r_{\text{A}} + r_{\text{O}}}{\sqrt{2}(r_{\text{B}} + r_{\text{O}})}$ can be introduced to show the extent of coordination between r_{A} , r_{B} and r_{O} where r_{A} , r_{B} and r_{O} represent the ionic radius of A-site, B-site and oxygen

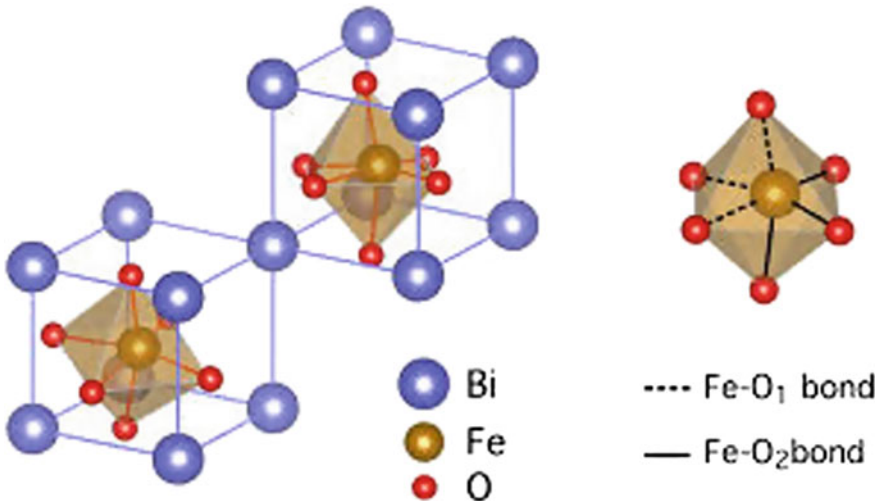


Fig. 9 Schematic representation of BFO structure in the hexagonal unit cell [32]. (Reprinted with kind permission from Springer Nature)

ions respectively. Ideally, the tolerance factor should be equal to or less than one. Using the ionic radii of Shannon, the value of tolerance factor for BiFeO_3 we obtain $t = 0.88$, with Bi^{3+} in eightfold coordination (the value for 12-fold coordination is not reported) and Fe^{3+} in six-fold coordination and high spin. For the oxygen octahedra must buckle in order to fit into a cell this ratio is smaller than one [19]. The temperature is one of the most important factors which affects the crystal structure and lattice spacing of bismuth ferrite. Between the temperature of 5 and 300 K, the unit cell atomic coordinates of BFO are nearly unaffected. The Fe and O ions have z atomic coordinates, increase significantly above 300 K which determine the polarization of the BiFeO_3 unit cell. Commonly, an increase in temperature leads to an increase in the bond length of Fe–Bi and bond angle Fe–O–Fe, O–Fe–O, and subsequently leads to a reduction in magnetization and polarization. The ferroelectric structure $R3c$ and the idyllic perovskite structure are related to each other in two dissimilar crystal distortions by freezing. The symmetry to the polar space group $R3m$ reduced along $[0\ 0\ 1]$ by the polar displacements Bi^{3+} and Fe^{3+} . Antiferro distortive turn of the oxygen octahedra about $[0\ 0\ 1]$ hub yields the nonpolar space bunch $\bar{R}3c$. The combination of these two distortions results into $R3c$ [33].

8.2 Drawbacks of BFO

For non-volatile memories and high-performance electronics use BiFeO_3 is one of the suitable candidates. Despite superior benefits, BiFeO_3 has major limitations also which obstruct the applications of BFO. These are given below as:

- **Occurrence of Impurity Phase:** Bi has volatile nature due to which the synthesis of a pure phase of BFO is a tough task. Impurity phases like $\text{Bi}_2\text{Fe}_4\text{O}_9$, $\text{Bi}_{25}\text{FeO}_{39}$ take place due to the formation of Bi_2O_3 – Fe_2O_3 system.
- **High Leakage Current:** Existence of oxygen vacancies and valence variation of Fe^{2+} and Fe^{3+} tends to the high current leakage in BFO and thus high conductivity slow down its electric properties.
- **High Dielectric Loss:** Bouncing of Fe^{3+} and Fe^{2+} ions and occupancy of impurity phase also the reason behind high dielectric loss.
- **Small Remnant Polarization:** High leakage of current also results in small value of remnant polarization.
- **Weak Magnetic Properties:** BFO shows antiferromagnetic nature in which magnetic ordering shows a partially modulated spiral spin structure within the range of 62 nm long-wavelength results in cancelling of macroscopic magnetization. This spin canting effect is the main reason behind the weak magnetization of BFO.

All these factors are collectively responsible for the weak magnetoelectric effect in BiFeO_3 and restrict the use of BiFeO_3 for the construction of multifunctional devices. These issues can be efficiently overwhelmed by:

- To reduce the limitations of BFO, doping on A-site or B-site or both sites can be done e.g., doping of transition metal ions (Cr, Co, Mn etc.) on B-site and doping of rare earth ions (Gd, Pr, Ho, Nd etc.).
- By improving the synthetic techniques, a pure single phase BFO can be obtained without any secondary phase.
- For improving the magnetic properties size of nanoparticles can be reduced below the periodicity of spin helical structure within wavelength of 62 nm.
- The problem of non-stoichiometry can be solved by fabricating high quality single crystal.

9 Synthesis Methods of BFO

For the synthesis of multiferroic BiFeO_3 , several methods were used such as solid-state route, sol-gel, co-precipitation, hydrothermal and combustion method. All the properties of BFO like structural, magnetic and electric depends upon the factors like size of crystal, pressure, temperature, dopant and chemical composition etc. These factors can be controlled by applying a suitable synthesis method under optimized conditions. For the synthesis and to have a pronounced effect on magnetic, structural and electrical properties of BFO it is necessary to choose an appropriate method. Among all these methods sol-gel, co-precipitation and solid-state method are suitable methods for the required conditions. All these synthesis methods are discussed below as.

9.1 Sol-Gel Method

This process is a chemical-based solution used for the synthesis of metal oxides. In this method evaporation of sol takes place and the chelating agent plays an important role. Citric acid, oxalic acid, tartaric acid and malic acid are the most commonly used chelating agents. Nitrates are dissolved on a stoichiometric ratio in deionized water and after that addition of a chelating agent take place on a hot plate. Heat the solution with constant stirring at low temperature till the formation of gel and allowed it to evaporate. After some time, the precursor form. Grind it and sintered it at the required temperature to get the final result. The main advantages of this method are easy to handle, required low temperature, cost-effectiveness etc.

9.2 Co-precipitation Method

In this technique, metallic salts are dissolved in the aqueous solution. Small-sized nanoparticles result in this process at a low annealing temperature. Single pure phase

BiFeO_3 were synthesized by Muneeswaran et al. by using this method. Bismuth and iron nitrate in the stoichiometric ratio were dissolved in deionized water [30]. A mixture of deionized water (10 M) and ammonia (2.5 M) was then added drop wise to the solution. After sometimes the formation of precipitates take place and is washed many times with distilled water to remove the impurities. Then, the obtained product was dried in a hot air oven and crushed in a mortar pestle to obtain the homogeneous powder. Sinter the obtained powder at the required temperature.

9.3 Solid-State Method

The solid-state method is one of the most commonly used methods for the synthesis of BFO. In the case of the solid-state method, the precursors such as bismuth nitrate, iron nitrate have been weighed in the required amount. An agate mortar and pestle are used for the proper mixing of these reactants. Acetone or alcohol is added to the homogeneous mixture. This mixture forms a paste. After 10–15 min of continuous mixing, this liquid gets evaporated. To obtain the fine powder the same process we have to repeat 10–15 times. Then the powder is calcinated at different temperatures.

10 Applications of BFO

- BiFeO_3 is a room temperature multiferroic material that has potential applications in the field of spintronics, magnetism, and photovoltaics due to its ferroelectric photovoltaic effect.
- BiFeO_3 is also a type of multiferroic material which can also be used in the case of communication devices.
- Due to its low bandgap property BiFeO_3 can also be used in the case of an optical fiber.

11 Review Related to the Synthesis of BFO

In the mid 50s, by using conventional solid-state method BFO was firstly prepared in Russia [34]. Many authors at that time reported that by using solid state method BFO could only be synthesized at 700–800 °C annealing temperature. In 1967, Achenbach observed a difficult task to obtain a pure single phase BFO [10]. Many researchers did not get success to achieve a pure phase of BFO without any impurity. Certain modification in time, temperature, synthesis techniques was made. Morozov [32] described that BiFeO_3 is not achievable by solid state method as its disintegration temperature is lesser than the activation one. In 2004, Wang [35] synthesized a pure

single phase BFO, by using rapid liquid phase sintering process without any impurity. In this method, annealing temperature ($\sim 880^\circ\text{C}$) is larger than the melting point of Bi_2O_3 ($\sim 825^\circ\text{C}$). In rapid liquid phase method further modification was done by Pradhan [36]. He suggested that for the synthesis of pure BFO crystal annealing temperature should be 880°C . Many authors described that structural, microscopic, thermal, magnetization, and dielectric properties of BFO. Accordingly, incomplete reaction takes place at annealing temperature 850°C whereas formation of multi-phase took place at higher temperature (890°C) due to the vaporization of Bi_2O_3 . Side by side the impact of the particle size was studied by Yuan. By using different synthesis techniques six types of BFO ceramics pattern was prepared and their electrical resistivity, porosity and phases was compared. Particle size lies in nm range was observed by authors which was annealed at 855°C for 5 min at $100^\circ\text{C}/\text{s}$, tends to the production of the pore less single phase BFO having electrical resistivity $5 \times 10^{12} \Omega \text{ cm}$ [37]. A heavy crystalline BFO nanoparticle was synthesized by Chen using co-precipitation method for 3 h under different sintering temperature $750\text{--}850^\circ\text{C}$. It was observed that secondary phase arises when the sample sintered at 750°C . Further, the sample acquire low leakage current and highest density when sintered at 800°C with grain size $2 \mu\text{m}$ whereas high leakage current was acquired by the sample when sintered at 850°C with a grain size $7 \mu\text{m}$. The activation energy determined for the sample sintered at 800°C are 0.126 and 1.26 eV at room temperature of 290 and $350\text{--}430^\circ\text{C}$ [38]. By using ethylene diaminetetraacetic acid composite sol-gel process a new way was reported by Wei et al. to prepare BFO nanoparticles [39]. As compared to solid state method, pure phase of BFO was observed with no impurity phases at 600°C . SEM images displayed nanoparticles with cubic morphology having average size of $110\text{--}160 \text{ nm}$ and show better homogeneity. Due to the size confinement effects of BFO nanoparticles, at room temperature a weak ferromagnetic order has been observed. They farther showed that for the preparation of BFO nanoparticles with the use of EDTA as a chelating agent at a low temperature leads to the formation of heterometallic polynuclear complexes [39]. By using sol-gel process BFO nanoparticles was obtained under the calcination temperature $450\text{--}700^\circ\text{C}$. Under different calcination temperature, size of the crystalline particles lied in the range of $26\text{--}120 \text{ nm}$. SEM images showed that with the increase in the thermal treatment the average size of the particles increases. The BFO sample sintered at 500°C at room temperature showed weak ferromagnetism with the value of remanent magnetization of 0.004 emu/g and coercivity of 145 Oe . The coupling between the magnetic and electric order was indicated by dielectric anomaly at around 330°C . With the differential thermal analysis (DTA) ferroelectric transition temperature as observed at around 827°C [40]. The BFO nanoparticles with the average size of $60\text{--}80 \text{ nm}$ was reported by Wang by using sol-gel method using tartaric acid as a chelating agent. XRD, SEM, TG-DTA and TEM techniques has been performed for the detailed thermal and microstructural analysis. At 500°C calcination temperature a pure single crystal was observed due to the production of heterometallic polynuclear complexes in the tartaric acid. Ferroelectric nature of BFO nanoparticles was indicated at Curie temperature of around 851°C . The weak ferromagnetic behavior of as-prepared BFO was indicated using VSM [41]. Hu reported that by using wet

chemical route method narrow sized distribution of nanoparticles has been done by using citric and tartaric acid as chelating agent under the thermal treatment. The structural analysis like the phase and size of the BFO nanoparticles were characterized by using TG/DSC, XRD and TEM techniques. The magnetic properties of the sample were studied by VSM. They showed that using tartaric acid as chelating agent nanoparticles are crystallized at 450 °C whereas using citric acid nanoparticles crystallizes at 350 °C. With the increase in temperature the grain size was found to be increased [42]. The dielectric behavior of BFO was investigated by Ke using rapid heating and quenching technique sintered in the presence of argon and oxygen. Pure rhombohedral structure of both the samples was confirmed by XRD. The microstructure of oxygen and argon were found to be dense and uniform with average grain size lie in the range from 500 to 1500 nm sintered at 700°C temperature. The large dispersion and high dielectric loss were observed in case of argon as compared to oxygen sintered samples. This is because more Fe²⁺ and oxygen vacancies in argon sintered samples. From this author terminated that in the evaporation of the Bi there is important role of Fe²⁺ [43]. Polycrystalline BFO synthesis by solid state method was studied by Pillai. The structural and phase purity of the BFO samples was confirmed by XRD, Raman spectroscopy SEM and XPS. The Rietveld Refinement confirmed the rhombohedral (R3c) structure. The pure BFO with single phase containing no impurities and 4A1 and 6E modes with frequency range of 100–700 cm⁻¹ was confirmed by Raman spectroscopy. In the extension of this, the oxidation states tell through XPS the phase purity of the sample. For the magnetic behavior of the sample, SQUID was used which shows typical G-type antiferromagnetic behavior [44]. Fu examined BiFeO₃ single crystal nanoparticles at sintering low temperature method. BET surface area and BFO structures were established using techniques BET adsorption and XRD techniques individually. It has been evaluated that BET particles size are calculated as 67 nm and by XRD it is calculated about 39 nm. Ferromagnetism which was weak detected using remnant magnetization $M_r = 0.033$ emu/g, and coercive field, $H_c = 395$ Oe [42]. Godara observed BiFeO₃ nanoparticles size around 50 nm by using auto-combustion route method and studied its electrical, thermal, structural and optical properties [45]. Highly crystalline and spherical shaped BFO nanoparticles were observed by TEM. Thermal examination improved the calcinated temperature as 500 °C and displayed Curie temperature at around 834 °C. The dielectric studies indicated the magneto-electric coupling at Neel temperature. With low leakage current highly resistive BFO resistivity was observed i.e. $\rho = 3 \times 10^9$ Ω cm. P-E loop determined unsaturated loops with large coercive field and remnant polarization i.e. 25 kV/cm, 0.4 μC/cm², respectively. The energy difference between direct band gap found to be 2.2 eV utilized for photocatalysis applications. The retentivity and coercivity of the BFO nanoparticles was found to be 0.067 emu/g and 185 Oe on applying a magnetic field of 22 kOe [46]. Vijayasundaram described the Pechini-type sol–gel method with modification by using Malonic acid as a chelating agent. Malonic acid is a type of dicarboxylic acid which show co-ordination with two cations i.e., Bi and Fe, thus, tends to the preponderance of the two cations resulting heteronuclear complex formation. This way reducing the synthesis time and results into rapid formation of

gel. In this method two samples were prepared by using ethylene glycol (EG) in malonic acid and without it. For the phase formation of BFO nanoparticles EG plays an important role which was confirmed by Rietveld refinement. Magnetic properties of the prepared samples studied through VSM at low temperature shows a relation between the magnetic property and their size. By their analysis it was found that the sample exhibit ferromagnetic behavior calcinated at 500 °C which the characteristic of the uncompensated spin moment and decreased size of the sample [47]. Sowmya discussed the synthesis of pure BFO by using citrate sol-gel method. With the help of XRD and SEM size and phase purity of particle were confirmed. A decrease in the value of remanent magnetization from 0.025 to 0.003 emu/g was found with the increase in the sintering temperature which is associated with size—confinement effect. Dielectric properties in the frequency range 8.2–12.4 GHz were studied when the sample sintered at 700 °C. Better microwave absorption properties with smallest reflection exhibited by hexagonally shaped BFO nanoparticles [48]. Manzoor reported the optical and dielectric properties of BFO nanoparticles by using evaporation method. Structures regarding properties were determined by XRD and TEM. In order to examine the impact of oxygen vacancies on the phase and behavior of system samples were annealed at different temperature under two different environments (air and oxygen). For air annealed samples crystalline size was found to be in between 11 and 21 nm whereas 20–29 nm for oxygen annealed samples. The mean diameter of the sample was also confirmed by TEM in the range of 18–30 nm. With the increase in frequency the dielectric constant and loss decreases in the frequency range 1 kHz–1 MHz [49]. Dias examined synthesise of BiFeO₃ nanoparticles by using method high energy ball-milling followed by quenching and sintering at room temperature. By experiments of XRD it has been concluded that there is formation of BiFeO₃ nanoparticles which has no impurity and second phase. The sample which has resistance more than 10¹² Ωm was examined at room temperature. Conduction process indication was started at around 350 K which can be characteristic of hopping of charge carrier by grain boundaries and grain-grain. Magnetoelectric coupling strong evidences have been shown by measuring dc and dielectric samples respectively. It has been observed that stringing protocol; is highly effective and a powerful way for BFO samples which are highly resistive [50]. Wu reported on the synthesis of high purity BFO nanoparticles with the help of sol-gel method. The distorted rhombohedral perovskite structure of BiFeO₃ with space group R3c was demonstrated by XRD, Raman and IR spectra. With the help of TEM images, it was revealed that the size of BFO nanoparticles lies in the range of 30–200 nm. The bandgap between the BFO nanoparticles was 2.21 eV displayed through UV-Visible absorption spectra. At low temperature magnetic hysteresis loops display the weak ferromagnetic behavior of BFO nanoparticles. Furthermore, with decreasing temperature a sudden increase in magnetization has been experienced at ~10 K in both ZFC and FC measurements [38]. Authors described nickel doped bismuth ferrite powders annealed at 700 °C synthesized by high-energy ball milling method. The presence of rhombohedral structure was revealed with the help of X-ray diffraction patterns with small amounts of secondary phase such as Bi₂Fe₄O₉. As the amount of Ni²⁺ increases the stabilization of Bi₂₅FeO₄₀ reached up to 95.23% of sillenite for $x =$

0.5. The presence of small amount of Ni^{2+} ($x < 0.1$) caused the frustration of the G-antiferromagnetic order. With increasing Ni content (up to $x = 0.1$) a little increment was exhibited by DC conductivity. For nickel concentrations from 0.2 to 0.5, the conductivity increases. When the concentration of nickel is increased, the behavior modifications like permittivity, electrical conductivity takes place which are related to crystal structure modification [51]. Moghadam on his paper focused on different sintering methods for the synthesis of bulk $\text{Bi}_2\text{Fe}_4\text{O}_9$ ceramic prepared by chemical co-precipitation method. On the morphological and magnetic properties of BFO bulk samples, the effect of various types of sintering such as two-step sintering (TSS), conventional sintering (CS) and microwave sintering (MS) with various heating cycles was studied in detail. An orthorhombic crystal structure of BFO sample has been detected with the help of XRD which belongs to the pbam space group. TEM images showed the crystal size approximately 72 nm. By using field emission scanning electron microscope (FESEM) the morphology of bulk samples was studied. For the best heating cycles of CS, TSS and MS the average grain sizes were about 260, 295 and 210 nm. With the help of vibrating sample magnetometry (VSM) the M-H curve of the sintered samples confirmed antiferromagnetic behavior in all samples. An increase in grain boundaries and decrease in the particles size resulted in more compensated spins [52]. Authors in this paper reported that the crystal structure and magnetic properties of the BiFeO_3 regarding compounds co-doped with Ca and transition metals ions was calculated with vibrating sample magnetometer (VSM) and XRD. In this paper it has been observed that the chemical substitution tends to vary its structural parameters, therefore changes its magnetic state from parent cycloidal antiferromagnet. The transition metals i.e. their chemical composition results into a lattice compression lessen rhombohedral distortions and stabilize into a paraelectric state from a non-polar orthorhombic structure. Maximal remnant magnetization of about 0.07 emu/g was found when the compound doped with Ca and Mn ions [53]. Satyanarayana reported BFO nanoparticles i.e. $\text{Bi}_{(1-x)}\text{Tb}_x\text{FeO}_3$ ($x = 0, 0.03, 0.04, 0.06, 0.09, 0.12$) synthesized by sol-gel method. The formation of perovskite structure of the prepared samples was analyzed with the help of XRD and the size of crystal lies in the range of 15 nm. With the help of Fourier Transform Infrared Spectroscopy measurements strong absorption peak observed at 545 cm^{-1} . The BFO cycloid spin structure found to be suppressed in case of particles that are fewer than 62 nm across enhancing the ferromagnetic nature. With the change in Tb doping the magnetic behavior of $\text{Bi}_{(1-x)}\text{Tb}_x\text{FeO}_3$ particles found to be change anomalously. The maximum magnetic moment for Tb doping at $x = 0.03$ is revealed by VSM studies. The magnetization decreases with increase in x beyond 0.03, while magnetization increases again for a further increase beyond $x = 0.04$ [54, 55].

12 Conclusion

This chapter mainly focuses on bismuth ferrite and its manufacturing processes Multiferroics (BiFeO_3 , BFO). BFO is known to be the main single-stage ABO_3 perovskite compound with multiferroic content at room temperature, which is thus the most encouraging upcoming compound for storage, information and spintronic applications of the future generation. Because ferroelectric and anti-ferromagnetic properties are simultaneously incorporated, BFO has been attracting attention. BFO has a cycloid spin structure ($T_c = 850\text{ }^\circ\text{C}$) electrical and anti-ferromagnetic arrangement. Also, the synthesis methods to obtain BFO nanoparticles have been studied in detail. BFO is one of the most suitable multiferroic materials for application in the electronic industry. However, the major drawback of BFO comes during its synthesis. Bismuth is a highly volatile compound and at high temperature, it is responsible for impure phase formation. Thus, it can be concluded that modifying the synthesis methods or synthesizing BFO at low temperatures can be used to obtain the pure single-phase BFO nanoparticles.

Acknowledgements Authors would like to thank Chancellor Shoolini University for his continuous support.

References

1. C. Demetzos, *Pharma. Nanotechnol.* **142**, 702–705 (2016)
2. R. P. Feynman, *Eng. Sci. Mag.* **23** (1960)
3. S. Kamila, *Amer. J. Appl. Sci.* **10**, 876 (2013)
4. T. Takagi, *J. Intel. Mater. Sys. Struct.* **1**, 149–156 (1990)
5. R. Nistico, F. Cesano, F. Garelli, *Inorganic* **8**(1), 6 (2020)
6. J. Valasek, *Ferroelectricity* **2**, 239–244 (1971)
7. R. Verma, A. Chauhan, K.M. Batoo, R. Kumar, M. Hadi, E.H. Raslan, *Ceram. Inert.* **47**, 15442–15457 (2021)
8. R. Verma, A. Chauhan, K.M. Batoo, M. Hadhi, E.H. Raslan, R. Kumar, M.F. Ijaz, A.K. Assaifan, *J. Alloy. Compd.* **869**, 159520 (2021)
9. K.M. Batoo, R. Verma, A. Chauhan, R. Kumar, M. Hadhi, O.M. Aldossary, Y.A. Douri, *J. Alloy. Compd.* **18**, 160836 (2021)
10. G.D. Achenbach, W.J. James, R. Gerson, *J. Amer. Ceram. Soc.* **50**, 437 (1967)
11. D. Damjanovic, *Rep. Prog. Phys.* **61**, 1267 (1998)
12. Y. Xu, *Ferroelectric Materials and their Applications* (North-Holland, Elsevier Science Publisher B. V., 1991), p. 112
13. A.K. Tagantsev, L.E. Cross, J. Fousek, *Domains in Ferroic Crystals and Thin Films* (Springer, Berlin Heidelberg New York, 2010)
14. A. Pramanick, D. Damjanovic, D.E. Daniels, J.C. Nino, J.L. Jones, *J. Amer. Ceram. Soc.* **94**, 293–309 (2011)
15. D.M. Marincel, H. Zhang, A. Kumar, S. Jesse, S.V. Kalinin, W.M. Rainforth, *Adv. Funct. Mater.* **24**, 1409 (2014)

16. N. Izyumskaya, Y.-I. Alivov, S.-J. Cho, H. Morkoc, H. Lee, Y.-S. Kang, *Crit. Rev. Solid State Mater. Sci.* **32** (2007)
17. E.K. Salje, *Ferroelastic Mater. Ann. Rev. Mater. Sci.* **42**, 265–283 (2012)
18. J.E. Massad, R.C. Smith, *J. Intel. Mater. Syst. Struct.* **14**, 455–471 (2003)
19. G. Catalan, J.F. Scott, *Adv. Mater.* **21**, 2463–2485 (2009)
20. M. Čebela, D. Zagorac, K. Batalović, J. Radaković, B. Stojadinović, V. Spasojević, R. Hercigonja, *Ceram. Inter.* **43**, 1256–1264 (2017)
21. H. Palneedi, V. Annapureddy, S. Priya, *Jungho. Actuators* **5**, 9 (2016)
22. N.A. Hill, *J. Phys. Chem. B* **104**, 6694–6709 (2000)
23. S.W. Cheong, M. Mostovoy, *Nat. Mater.* **6**, 13–20 (2007)
24. T. Kimura, T. Goto, H. Shintani, K. Ishizaka, T.H. Arima, Y. Tokura, *Nature* **426**, 55–58 (2003)
25. N. Hur, S. Park, P.A. Sharma, J.S. Ahn, S. Guha, S.W. Cheong, *Nature* **429**, 392–395 (2004)
26. D. Khomskii, *Physics* **2**, 20 (2009)
27. G.A. Smolenskii, V. Yudin, E.S. Sher, Y.E. Stolypin, *J. Exp. Theo. Phys.* **16**, 622 (1963)
28. R. Seshadri, N.A. Hill, *Chem. Mater.* **13**, 2892–2899 (2001)
29. A. Mukherjee, M. Banerjee, S. Basu, M.D. Mukadam, S.M. Yusuf, M. Pal, *Mater. Chem. Phys.* **162**, 140–148 (2015)
30. M. Muneeswaran, P. Jegatheesan, N.V. Giridharan, *J. Exp. Nanosci.* **8**, 341–346 (2013)
31. R. Verma, A. Chauhan, K.M. Batoo, R. Kumar, M. Hadhi, E.H. Raslan, *Ceram. Inter.* **47**, 3680–3691 (2021)
32. D. Carranza-Celis, A. Cardona-Rodríguez, J. Narváez et al., *Sci. Rep.* **9**, 3182 (2019)
33. S.M. Selbach, T. Tybell, M.A. Einarsrud, T. Grande, *Adv. Mater.* **20**, 3692–3696 (2008)
34. G.A. Smolenskii, A.I. Agranovskaya, S.N. Popov, V.A. Isupov, *Sovt. Phys. Tech. Phys.* **10**, 2152–2153 (1958)
35. Y.P. Wang, L. Zhou, M.F. Zhang, X.Y. Chen, J.M. Liu, Z.G. Liu, *Appl. Phys. Lett.* **84**, 1731–1733 (2004)
36. A.K. Pradhan, K. Zhang, D. Hunter, J.B. Dadson, G.B. Loiutts, P. Bhattacharya, *J. Appl. Phys.* **97**, 1–4 (2005)
37. G.L. Yuan, S.W. Or, Y.P. Wang, Z.G. Liu, J.M. Liu, *Solid State Commun.* **138**, 76–81 (2006)
38. H. Wu, P. Xue, Y. Lu, X. Zhu, *J. Alloy. Compd.* **731**, 471–477 (2018)
39. J. Wie, D. Xue, *Mater. Res. Bull.* **43**, 3368–3373 (2008)
40. D.C. Jia, J.H. Xu, H. Ke, W. Wang, Y. Zhou, *J. Eur. Ceram. Soc.* **29**, 3099–3103 (2009)
41. X. Wang, Y.G. Zhang, Z. Wu, *Mater. Lett.* **64**, 486–488 (2010)
42. Y. Hu, L. Fei, Y. Zhang, J. Yuan, Y. Wang, H. Gu, *J. Nanomater.* **2011**, (2011)
43. H. Ke, W. Wang, Y. Wang, H. Zhang, D. Jia, Y. Zhou, X. Lu, P. Withers, *J. Alloy. Compd.* **541**, 94–98 (2012)
44. S. Pillai, D. Bhuwal, T. Shrepatti, V. Shelke, *J. Mater. Sci.: Mater. Electron.* **24**, 2950–2955 (2013)
45. C. Fu, X. Long, W. Cai, G. Chen, X. Deng, *Ferroelectricity* **460**, 157–161 (2014)
46. S. Godara, N. Sinha, G. Ray, B. Kumar, *J. Asia. Ceram. Soc.* **2**, 416–421 (2014)
47. S.V. Vijayasundaram, G. Suresh, R. Kanagadurai, *Appl. Phys. A* **121**, 681–688 (2015)
48. N.S. Sowmya, A. Srinivas, P. Suresh, A. Shukla, S.V. Kamat, *J. Mater. Sci.: Mater. Electron.* **26**, 5368–5372 (2015)
49. A. Manzoor, A.M. Afzal, N. Amin, M.I. Arshad, M. Usman, M.N. Rasool, *Ceram. Inter.* **42**, 11447–11452 (2016)
50. G.S. Dias, I.B. Catellani, L.F. Cótica, I.A. Santos, V.F. Freitas, F. Yokaichiya, *Integ. Ferro.* **174**, 43–49 (2016)
51. H. Maleki, S. Zare, R. Fathi, *J. Supercond. Nov. Mag.* **31**, 2539–2545 (2018)
52. E. Chandrakala, J.P. Paul, A. Kumar, A.R. James, D. Das, *J. Amer. Ceram. Soc.* **99**, 3659–3669 (2016)
53. A.K. Moghadam, O. Mirzaee, H. Shokrollahi, S.A. Lavasani, *Ceram. Inter.* **45**, 8087–8094 (2019)

54. D.V. Karpinsky, M.V. Silibin, A.V. Trukhanov, A.L. Zhaludkevich, T. Maniecki, W. Maniukiewicz, V. Sikolenko, J.A. Paixão, V.A. Khomchenko, *J. Phys. Chem. Solids* **126**, 164–169 (2019)
55. S. Satyanarayana, S.C. Sarma, S.C. Peter, S. Bhattacharya, *J. Magn. Magn. Mater.* **491**, 165–171 (2019)

Multiferroic Phenomenon in Bulk, Nanostructures and Thin Films



Samta Manori and Ramesh Chandra

Abstract The development of composite systems of multiferroic or magnetoelectric materials made from magnetic and ferroelectric subsystems has attracted interest as well as increased a large number of research activities. Multiferroics have found a special place in various technological applications based on novel multifunctional devices, like multi-state memories, spintronics, sensors, and transducers. Single phase multiferroics are rare and the coupling between various ferroic orders is either weak or occurs at low temperatures in these materials. The composite multiferroic materials, however, combine both ferroelectric and ferromagnetic phases and show a giant magnetoelectric effect even at high temperatures that are well above room temperature. In this view, various bulk composites have been studied and developed both experimentally and theoretically. Also, the high demand for on-chip integration in electronic and memory devices has accelerated the development of nanostructured ferroelectric and magnetic oxide materials in the form of thin films. With a high-quality thin film, it becomes easy to tailor the properties by epitaxial strain and interfacial coupling. This chapter will take the reader through the journey of evolution of multiferroic materials starting from the bulk form to nanostructures and thin films.

Keyword Bulk composites · Thin film · Epitaxial strain · Sputtering · Pulsed laser deposition

S. Manori (✉)

Department of Physics, School of Physical Sciences, DIT University, Dehradun 248009, Uttarakhand, India

R. Chandra

Nanoscience Laboratory, Institute Instrumentation Centre, Indian Institute of Technology Roorkee, Roorkee 247667, Uttarakhand, India

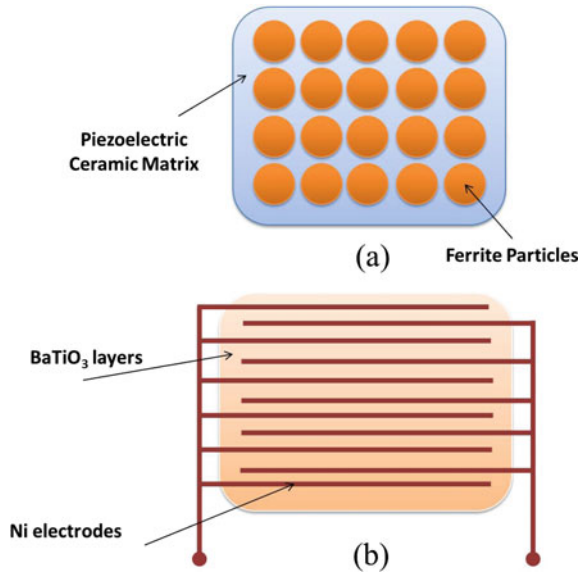
1 Multiferroism in Bulk Materials

The development of bulk multiferroic structures started in the form of bulk composites of magnetoelectric materials started in 1972 and was first proposed by van Suchtelen [1]. Experimental findings further accelerated the theoretical work on magnetoelectric composite structures and hence most of the work on these systems was theoretical before 2000 [2]. These theoretical modelings provided a quantitative knowledge of the magnetoelectric effect in bulk ceramic compounds. At the onset of the year 2000, a sudden rise in the research related to multiferroic magnetoelectric composite structures was observed. And the biggest turning point in the development of these composites in bulk form came in 2001 with the findings of materials with a giant magnetostrictive rare-earth alloy like Terfenol-D $Tb_{1-x}Dy_xFe_2$. The giant magnetoelectric effect observed in bulk materials of Terfenol-D was studied both theoretically [3] and experimentally [4, 5]. Let us now discuss some of the different types of bulk forms of multiferroic or magnetoelectric materials.

1.1 Composite of Ceramic Materials

Bulk magnetoelectric materials of ceramic composites can be made by various possible combinations of ferroelectric and magnetic oxides (especially ferrites), more commonly by co-sintering at high temperatures. It is to be noted here, that bulk magnetoelectric ceramic composites were expected to show a larger magnetoelectric effect, but on the contrary composites of ceramic materials co-sintered at high-temperature show magnetoelectric effect that is around ten times lower than expected. This results largely from the problems during their preparation, like reaction problems, and mismatch between thermal expansions of two ceramic phases during high-temperature treatment. In the case of ceramic composites with 0–3 type particulate structure, it is better to use a piezoelectric ceramic matrix in which ferrite particles are dispersed with high concentration (Fig. 1a). This is desired for the reason that mostly ferrites are conducting or semiconducting, this property can degrade the insulation of the composites with a leakage problem. A core–shell structure is an effective solution to this problem, with ferrite core and piezoelectric shell [6, 7], this approach can prevent the ferrite core particles from direct contact with the shell during sintering. However, because of the difficulties faced in preparing a core–shell structured system, such microstructured ceramics have not yet been attained. Recently developed techniques like chemical solution processing and sintering methods e.g. spark plasma sintering [8] and microwave [9] sintering have made it possible to fabricate improved quality of these particulate ceramics. However, there is still some more work is to be done to get adequate dispersion of ferrite particles with high concentration in the matrix of piezoelectric ceramic, coherent interfaces, and adequate bulk density while escaping any reaction or diffusion at the interface between the two ceramic phases.

Fig. 1 **a** 0–3 type bulk magnetoelectric composite with magnetic (Ferrite) particles immersed in a piezoelectric matrix, **b** 2–2 type alternate layers of ferroelectric (BaTiO_3) and ferromagnetic (Ni) materials



The 2–2 type laminate composite ceramics have high magnetoelectric coefficients as compared to particulate composite ceramics. This is attributed to the structure of these composites which comprises alternate layers of ferrite and piezoelectric oxide materials, which eliminates any leakage problem. However, the ferrite layers in these laminate composite ceramics do not perform as a good conductive electrode which results in the loss of magnetoelectric output signal induced by the alternate piezoelectric layers. This signal loss can be greatly reduced by introducing internal electrodes made up of materials like Ag, Ni, and Ag–Pd, between the alternate layers of piezoelectric and magnetic materials. These interface electrodes can improve the response by directly collecting the output charges that are produced from the piezoelectric layers. The phenomenon is well explained in a trilayered NCZF/PZT/NCZF (NCZF: $\text{Ni}_{0.6}\text{Cu}_{0.2}\text{Zn}_{0.2}\text{Fe}_2\text{O}_4$, PZT: $\text{Pb}(\text{ZrTi})\text{O}_3$) with the internal electrodes made up of Ag–Pd at the interface [11]. The multilayer ceramic capacitors (MLCCs) are made up of precisely fabricated magnetoelectric sensors [12] which consist of thin layers of BaTiO_3 (BTO) and ferromagnetic Ni internal electrodes (Fig. 1b). The magnetoelectric coupling is enhanced due to the laminar structure which further simplifies the strain field, and the magnetically induced output charge is increased by their large capacitance. The greatest advantage of these MLCC magnetoelectric sensors which are produced on a massive scale is that they can be operated at room temperature with highly reproducible cross-field cycles and temperature cycles [12]. The sensitivity of these magnetoelectric materials can be improved in a significant manner by connecting these capacitor plates in series. In this way, these MLCCs can be used as magnetic field sensors in various fields due to their low cost. As discussed in the case of 0–3 type particulate composites, the biggest challenge in the case of bulk magnetoelectric laminate composites is their processing by controlled cofiring of ferrite

and piezoelectric layers at high temperatures so as to obtain an interfacial contact without any inter-diffusion or reactions. Thus, to get rid of these problems, low temperature processing of these ceramics is desirable. Recently, various techniques used for the deposition of thin films have been employed to overcome the challenges imposed by high temperature sintering [13]. When ferroelectric films are deposited on dense ferrite ceramics by methods like pulsed laser deposition (PLD) or spin coating technique, then the ceramics can be easily annealed at much lower temperatures ($\sim 600\text{--}700\text{ }^\circ\text{C}$) than co-sintering temperatures. Also, with these methods, an improved interfacial bonding between the ferroelectric and ferrite layers is obtained which gives a large direct magnetoelectric effect. However, the obtained values of the magnetoelectric coefficient are still much lower than that calculated using the theoretical continuum model [14]. On the other hand, as mentioned earlier, the ferrite ceramics are not good enough to be used as conductive electrode because of their not so low resistance, and hence a bottom electrode in between the layers of ferrite and ferroelectric materials would be beneficial to improve the magnetoelectric response of these systems made up of layers-on-ceramics composites via low temperature processing.

1.2 Composite Materials from Magnetic Alloys

Bulk magnetoelectric composites which are based on magnetostrictive alloys like Terfenol-D and Metglas are reported to show a strong magnetoelectric effect. The modified Terfenol-D based ME composites, like a piezoelectric transformer with a Rosen-type structure, can magnify the input signal by more than 100 times [15]. Some better configurations of these bulk composites can also be made by considering their mechanical properties. However, magnetoelectric composites based on Terfenol-D are not so promising for low field applications because of their low permeability and high saturation field. As an alternate option, soft magnetic alloys, like Ni (Mn–Ga), Permendur and Metglas, can also be utilized. Among these alloys, Metglas is the widely used alloy. It is an amorphous alloy ribbon prepared by a rapid solidification process [16]. The process of rapid annealing is advantageous from the perspective that it creates remarkable properties in the ribbon alloy so that it can undergo magnetization and de-magnetization swiftly and effectually, giving low coercivity and saturation fields, and high magnetic permeability. A large magnetoelectric response of about $10\text{ Vcm}^{-1}\text{ Oe}^{-1}$ at low frequency and several hundred $\text{Vcm}^{-1}\text{ Oe}^{-1}$ at resonance have been observed, when the applied magnetic field is low, in a laminate of Metglass ribbon and a PZT-fiber actuator layer [5]. The optimization of some structural parameters of metglas based composites can be done to improve the magnetoelectric response and the sensitivity towards the applied field. Metglas is also advantageous as it shows magnetic flux concentration effect ascribed to its high permeability which in turn affects magnetostriction. In addition, the planar aspect ratio of the metglas ribbon is large enough that it can remarkably enhance the flux density near the central region [17]. The high permeability of metglas allows

it to be used as a third phase in the Terfenol-D/piezoelectric laminates, which in turn significantly increases the effective permeability of the resulting three-phase system, thus giving a strong magnetoelectric response at lower applied fields. The piezoelectric layer and the magnetic alloys in these magnetic alloy-based magnetoelectric composites are joined together with polymer binders. These binders affect the magnetoelectric response in a significant manner [18]. The aging effect and adhesive fatigue of these composites are mainly determined by the interfacial binders. Another alternative to prevent these issues is to deposit the magnetic alloys directly onto the piezoelectric layer by using magnetron sputtering or electro-deposition [19–21].

1.3 Composite Materials from Polymers

Polymer based magnetoelectric composites are easy to fabricate as compared to ceramic and magnetic alloy based composites. They can be produced in various forms like thin sheets and molded shapes using conventional low-temperature processes and give improved mechanical properties. It has been reported that a single PZT ceramic rod embedded in Terfenol-D/epoxy (TDE) matrix can give a much larger magnetoelectric response as compared to other polymer based magnetoelectric composites, due to effective coupling interaction between PZT rod and TDE medium [22, 23]. The studies on this magnetoelectric composite confirm that smaller (micro)-sized rods with large magnetoelectric response can be processed using a single PZT fiber which can prove to be a promising future micro-magnetoelectric device. The aging test performed on these composites shows that the response remains the same even for two years duration, thus indicating that no degradation occurred under the normal environment. Fatigue measurements also show good stability of the magnetoelectric response. Moreover, magnetoelectric composites which are derived from polymer based compounds with magnetic particles like CoFe_2O_4 (CFO), NiFe_2O_4 (NFO), Fe_3O_4 , Ni, and Terfenol-D, that are embedded in a matrix of polymers such as PVDF and Polyurethane, are technologically important for their easy processing. Some experimental investigations reveal that in these polymer-based composites, the magnetostriction produced by magnetic nano-fillers does not have any direct effect on the magnetoelectric response. However, the source of magnetoelectric coupling in these nanocomposites is still not clear.

1.4 Converse Magnetoelectric Effect in Bulk Composites

The Sects. 1.1, 1.2 and 1.3 mainly discussed the direct magnetoelectric effect, where the electric polarization is induced by an applied magnetic field. A converse magnetoelectric effect, in which magnetization is controlled by applied electric field is also another fascinating and technically important phenomenon in bulk composites [24–26]. Also, the magnetic hysteresis loops of some composite materials reveal

the dependence of magnetic anisotropy on applied electric field. Magneto-optical Kerr effect (MOKE) measurements in PZT/metglas laminate show that the local magnetization vector can be easily switched by an applied electric field [27]. The ferromagnetic resonance frequency can be easily tuned by applying a bias voltage through the converse magnetoelectric effect by controlling the magnetic response at high frequencies in these magnetoelectric structures. The electrostatically tunable microwave multiferroic devices are more energy-efficient, less noisy, compact in size, and lightweight as compared to their conventional tunable microwave magnetic devices.

2 Multiferroism in Nanostructures and Thin Films

With the advancement in techniques for thin film deposition and with improved theoretical calculations, the studies on nanostructured thin films of multiferroic materials have taken a new height. These deposition techniques provided a new path to grow different structures with the characteristics of parent functional materials which are tailored by strain engineering. The last few years have seen a surge in the number of studies on composite magnetoelectric thin films. Various physical deposition methods like sputtering, PLD, molecular beam epitaxy, and chemical methods like spin coating, metal–organic chemical vapor deposition (MOCVD) have been used to grow a large number of multiferroic thin films with ferroelectric materials like BTO, PbTiO_3 (PTO), PZT, and BFO and magnetic materials like CFO, NFO, Fe_3O_4 , $\text{La}_{1-x}\text{Sr}_x\text{MnO}_3$ (LSMO), and also certain metals with different types of composite structures (0–3 type, 2–2 type and 1–3 type). Multiferroic thin films are far superior to their bulk counterpart owing to their unique properties. The main advantage of multiferroic thin films is the ease of combining different phases at the atomic level, and the possibility to grow epitaxial and superlattice composite films by precisely controlling the lattice match between different layers. This way, the understanding of magnetoelectric coupling becomes more simplified at an atomic level. Multiferroic thin films have proved to be promising candidates for applications in integrated magnetoelectric devices, high-density memory systems, microelectromechanical systems, and spintronics. This can be achieved by synthesizing high-quality thin films of multiferroic materials using the techniques mentioned above.

Among these techniques, spin coating is a simple and low-cost chemical method to produce polycrystalline or textured films with some preferred orientations and is also flexible enough to develop thick films with large areas [28–31]. But, these conventional techniques are unable to provide high structural perfection, epitaxy, and growth of atomic level layers. The physical vapor deposition techniques, on the other hand, provide the flexibility to produce epitaxial thin films on an atomic scale with coherent interfaces. In the growth of thin films using physical vapor deposition techniques (PLD, sputtering, etc.), there is a large number of factors that need to be controlled for a better quality thin film. The most important factor is the choice of the substrate as it controls the orientation and strain in the epitaxial films. Orientation of

the substrate with respect to the thin film decides the inherent properties of multiferroic materials and also affects the crystallization and morphology of nanostructures with multiple components. These deposition techniques allow the atoms to acquire low-energy configurations so that the single crystal substrate can be extended to an epitaxial layer.

Another deciding factor for thin film growth, specifically for 2–2 type heterostructures, is strain-induced because of differences in the lattice constants and thermal expansion coefficients between the film and substrate. In heteroepitaxial structures, film and substrate are of different materials which usually have the same type of structure with a difference in their lattice parameters. To grow an ideal heteroepitaxial structure, one can select a suitable substrate with a little mismatch between lattice parameters of the substrate and desired materials to be grown. This way, a fully coherent and epitaxial film can be deposited with only a little structural distortion across the interface of substrate and film. However, if the mismatch between the lattice parameters of film and substrate is slightly higher, then it results in a strained or relaxed epitaxial layer, depending upon the lattice parameters [32]. These conditions can create some defects such as dislocations at the interface which in turn degrades the ferroelectric or other properties of the film.

For a good quality thin film, another important factor is the pre-treatment of substrates before deposition. For successful growth of epitaxial thin film with controllable atomic layers, the substrate must undergo specific chemical treatment at the surface. In addition to these factors, other deposition parameters like energy density and frequency of laser beam in PLD, target-substrate distance, rate of arrival of adatoms, the temperature of substrate, pressure, etc. in techniques like PLD and sputtering and surface diffusion also need to be monitored for the deposition of thin films with desired compositions, morphology, and other properties. However, as compared to their bulk counterpart, there is still a narrow understanding of physics involved in multiferroic thin films. There are still many questions that remain unanswered, like, what is the exact effect of a stiff substrate on the multiferroic properties of a thin film? How to improve the magnetoelectric response in a multiferroic thin film? Is the magnetoelectric coupling strain-mediated in multiferroic thin films like a bulk counterpart? Let us try to find the answers to these questions in the next section!

2.1 Magnetic Field Controlled Electric Polarization

(a) Direct Magnetoelectric Coupling

In bulk multiferroic composites, the magnetoelectric coupling is strain mediated where strain induced in the magnetic or ferroelectric component by an applied magnetic or electric field, respectively, is transferred mechanically to the ferroelectric

or magnetic component, which further induces a direct polarization or magnetization. However, the source or mechanism behind the observed magnetoelectric effect in multiferroic thin films is still not determined in an absolute manner.

To understand the origin of the direct magnetoelectric effect in multiferroic thin films, it is worth considering some properties of the film like residual stress or strain which results from the mismatch between lattice parameters or thermal expansion coefficient between film and substrate. Theoretical calculations on the magnetoelectric coupling and magnetic field induced polarization in the nanostructured multiferroic thin films done using Green's function technique [33] revealed the following observations: If leakage problem is prevented, then 1–3 type heterostructures can show larger magnetoelectric response as compared to their bulk counterpart, and by assuming complete in-plane constraint effect, the 2–2 type alternate layered heterostructures give a weaker response. Other theoretical calculations suggested that the magnetic field-induced polarization depends on the thickness of the film, morphology, and substrate stiffness. Some studies on the effect of constraint stress on the magnetoelectric response suggest that in magnetoelectric thin films, the strain-mediated magnetoelectric coupling is suppressed due to mechanical clamping imposed by the substrate [33, 34]. And if somehow this mechanical clamping is relaxed in these layered structures, then the strain-mediated coupling is still not vanished.

(b) *Methods to Enhance Direct Magnetoelectric Response*

It is always desired to have a high output signal from the magnetoelectric effect for various practical applications. In the previous section, we have already discussed that the direct magnetoelectric coupling in the case of multiferroic thin films does not depend only on its structural parameters (thickness of the layers, ratio of thickness between ferroelectric and magnetic layers, orientation of the grown films, etc.), but is highly modified by the interfaces and constraint imposed by the substrate. Thus, to get high output, it is well desired to control the growth orientation of ferroelectric and magnetic layers as well as coherent interfaces and relaxation of strain constraint in the magnetic layer. In the case of two-layered composite thin films made by a ferroelectric material like PZT or BTO and a magnetic material like spinel ferrites, with both the materials having different lattice match with the substrates due to their different crystal structures, the sequence of deposition of these layers on the substrates greatly influences the properties of the resulting composite thin films [31, 35]. It is found that the relaxation of constraint from the magnetic layer imposed by the substrate can largely enhance the magnetoelectric response. This relaxation from substrate constraint can also be attained by deposition of a buffer layer. For this purpose, some conductive perovskite materials like LaNiO_3 (LNO), SrRuO_3 (SRO), and LSMO can be used preferably as their lattice parameters are close to various perovskite ferroelectric materials. These materials serve the purpose of both, buffer layer as well as the bottom electrode layer on which the thin films of desired magnetoelectric bilayers can then be deposited [29, 36]. In addition to bringing relaxation from the constraint imposed by the substrate, the buffer layer also helps in the growth of thin films with preferential orientation and further

improves the properties of the bottom ferroelectric layer. The mechanical transfer of strain between the layers becomes a major concern as magnetoelectric coupling is established at the interface. It is to be mentioned here that the deposition techniques like PLD and sputtering produce coherent interface in the magnetoelectric bilayered epitaxial films which enhances the magnetoelectric response as compared to the films deposited by sol-gel methods which produce incoherent interfaces. Interface density also plays an important role in enhancing the magnetoelectric response. One solution to increase the interface density is growing multilayers or superlattices [37–39]. The magnetic and ferroelectric properties are also influenced by interface density. As the interface density is increased, the ferroelectric hysteresis loops show less remanent polarization mainly due to the dilution created by the ferrite layer. The resistance of the ferrite layer is also not sufficiently low to act as conductive electrodes, and this prevents the effective transport of polarization charges which are induced by magnetoelectric coupling leading to loss of polarization charges in these films. The understanding of the nature of magnetoelectric coupling in multilayer thin films is still lacking and needs vast investigation. On the other hand, the choice of a suitable ferroelectric or magnetic layer and controlled orientation of bottom ferroelectric layer can greatly enhance the magnetoelectric coupling [26, 30]. A strong and efficient mechanical coupling across the interface gives an extraordinary magnetoelectric effect in heterostructures. The magnetostrictive properties of manganite crystals give a very strong temperature-dependent magnetoelectric effect.

The 1–3 type vertical heterostructures with magnetic spinel nanopillars embedded in the ferroelectric film matrix with an epitaxial structure are found to show a much larger magnetoelectric response as compared to thin films. Such a larger response in these structures could arise due to the following reasons [40, 41]: (i) the substrate clamping is reduced in the heterostructures, (ii) larger interfacial area gives stronger strain coupling. But, the measurement of direct magnetoelectric response is difficult to measure in these 1–3 type heterostructures due to leakage problems because of the low resistance of magnetic nanopillars embedded in the ferroelectric film matrix. However, the leakage problems can be reduced to a large extent by increasing the film thickness. Even after all these considerations, getting rid of the leakage problems in these heterostructures is still a challenging task.

After discussing all the approaches to improve the magnetoelectric response in a thin film, we conclude that irrespective of the type of structure one grows, the main challenge in enhancing the direct magnetoelectric response remains the large clamping effect due to substrate stiffness. Since the substrates that are usually used for depositing these thin films or heterostructures are macroscopic in size (~0.3–0.5 mm thickness) as compared to the thickness of film which lies in a range of 10–100 nm (~1000 times smaller), therefore, using substrates of smaller thickness can be an efficient way of enhancing magnetoelectric response in these structures.

2.2 *Electric Field Controlled Magnetism*

The direction of magnetization in any ferromagnetic material is always controlled by an applied magnetic field. In magnetoelectric multiferroic materials, the magnetization or magnetic anisotropy of a magnetic material can be directly controlled by an applied electric field. The electric field controlled magnetic properties are observed in semiconducting dilute magnetic semiconducting (Ga, Mn) As system [42] and ultra-thin ferromagnetic metal films [43, 44] at temperatures much lower than room temperature. The magnetic properties in a multiferroic magnetoelectric thin film can be controlled by the applied electric field through different phenomena such as charge-driven, exchange bias mediated and strain mediated magnetoelectric coupling. Let us discuss these in detail.

(a) *Charge-Driven Magnetoelectric Coupling*

In ultra-thin ferromagnetic films deposited as 2–2 type alternate layered heterostructures, the spin-polarized electrons or holes can build up at the interface by an applied electric field, which further changes the magnetization at the interface because of spin-dependent screening of the electric field. Theoretical modeling on surface magnetoelectric effect caused by direct effect of the applied electric field on magnetization of ferromagnetic thin film reveals that measurable change in surface magnetization and surface magnetocrystalline anisotropy can be created by a spin imbalance of the excess charge due to spin-dependent screening [45]. The first principle density functional calculations based on a model of Fe/BTO superlattice [46], explained the magnetoelectric effect produced by electron hybridization between Ti and Fe atoms and not by strain. The ferroelectric instability creates movement of atoms at the interface which modifies the overlap between atomic orbits resulting in the change in magnetization and hence a magnetoelectric effect.

(b) *Exchange-Bias Mediated Magnetoelectric Coupling*

Exchange bias is manifested as a horizontal or vertical shift in the magnetic hysteresis loops along the applied magnetic field axis or magnetization axis, respectively. It results from the exchange coupling between uncompensated spins of antiferromagnetic phase and spins of ferromagnetic layers. The exchange bias phenomenon has been used for controlling the magnetic properties by applied electric field in ferromagnetic thin films. The utilization of exchange bias for magnetoelectric coupling originated from the work on various single phase magnetoelectric multiferroic materials which are antiferromagnetic like Cr_2O_3 , YMnO_3 , and BFO. For example, the exchange bias in multilayer thin film of $\text{Cr}_2\text{O}_3/(\text{Co}/\text{Pt})_3$ can be easily reversed by applied electric field, but it needs thermal cycling [47], on the other hand, in the case of YMnO_3 /permalloy heterostructures, the exchange bias can be tuned directly by applied electric field [48].

The bilayer of some multiferroic (like BFO) and a ferromagnetic material can be easily used to modulate and control the magnetic properties by an applied electric field even at room temperature [49, 50]. For example, it is observed that the magnetization of the ferromagnetic layer can be tuned by electric field as it changes the ferroelectric

polarization and hence the antiferromagnetic ordering through quantum–mechanical exchange coupling. Another possible way to modify the magnetoelectric coupling is by applying an electric field to a material that is both ferroelectric and ferroelastic, the change in electric polarization in such a case produces a mechanical strain which is then transferred to the ferromagnetic layer. The mechanical deformation can change the magnetization of the magnetic layer by possibly changing the preferred orientation of the magnetic domains.

(c) *Strain-Mediated Magnetoelectric Coupling*

As discussed in the previous section, by the converse piezoelectric effect, the shape of a ferroelectric–ferroelastic material can be changed by an applied electric field, this strain produced would be passed on to the magnetic layer thus altering its magnetic anisotropy via magnetostriction. Thus, the electric field controlled magnetization can be achieved in such multiferroic materials through strain-mediated magnetoelectric coupling. In the case of 1–3 type heterostructures, this strain-mediated magnetoelectric coupling is attained by lattice coupling between the ferroic parts of the nanocomposite thin film. In these structures, an applied electric field changes the shape of the piezoelectric matrix, which further modifies the magnetic anisotropy of the ferromagnetic nanopillars embedded in the matrix via magnetostriction [51]. However, most of the reports on electric field control of magnetization involve 2–2 type structures, where a magnetic thin film is deposited on a ferroelectric substrate. The magnetic layer in these structures usually comprises of either metallic films like Fe, Ni, and Ni–Fe alloys, or oxide-based films like Fe_3O_4 , CFO, NFO, and LSMO, while the materials like BTO, PZT, PMN–PT, and PZN–PT single crystals or ceramics are used as ferroelectric substrates [52–55]. The magnetoelectric coupling in such structures is manifested by electric field-induced changes in the M–H hysteresis loops.

3 Conclusion

This Chapter discussed the development of multiferroic materials in the form of bulk materials, nanostructures, and thin films. The bulk multiferroic composites are well-studied systems and are ready for applications in magnetoelectric devices as they show large magnetoelectric coupling above room temperature. However, the advancement of multiferroic thin films is still underway and needs to cover up various falls coming in way of designing a good quality thin film ready for application in magnetoelectric devices. Some of the main things to be considered while developing a multiferroic thin film are; control of composition, atomic arrangements, and especially the interface between different ferroic phases, precise control over the domain and the domain wall structures/patterns in multiferroic hetero-films, mechanisms responsible for exchange-bias based and charge-driven magnetoelectric coupling, and size effects.

References

1. C. W. Nan, M. I. Bichurin, S. Dong, D. Viehland, G. Srinivasan, *J. Appl. Phys.* **103** (2008)
2. J.H.S.A.M.J.G. Van Run, D.R. Terrell, *J. Mater. Sci.* **9**, 1710 (1974)
3. C.W. Nan, M. Li, J.H. Huang, *Phys. Rev. B Condens. Matter Materials Phys.* **63**, 1 (2001)
4. J. Ryu, S. Priya, K. Uchino, H. Kim, *J. Electroceram.* **8**, 107 (2002)
5. S. Dong, J. Cheng, J.F. Li, D. Viehland, *Appl. Phys. Lett.* **83**, 4812 (2003)
6. G.V. Duong, G. Roland, R.S. Turtelli, *IEEE Trans. Magn.* **42**, 3611 (2006)
7. L. P. Curecheriu, M. T. Buscaglia, V. Buscaglia, L. Mitoseriu, P. Postolache, A. Ianculescu, and P. Nanni, *J. Appl. Phys.* **107**, 0 (2010)
8. Q.H. Jiang, Z.J. Shen, J.P. Zhou, Z. Shi, C.W. Nan, *J. Eur. Ceram. Soc.* **27**, 279 (2007)
9. S. Agrawal, J. Cheng, R. Guo, A.S. Bhalla, R.A. Islam, S. Priya, *Mater. Lett.* **63**, 2198 (2009)
10. J. Ma, J. Hu, Z. Li, C.-W. Nan, *Adv. Mater.* **23**, 1062 (2011)
11. R. A. Islam, Y. Ni, A. G. Khachatryan, and S. Priya, *J. Appl. Phys.* **104** (2008)
12. C. Israel, N.D. Mathur, J.F. Scott, *Nat. Mater.* **7**, 93 (2008)
13. J. Wang, Y. Zhang, J. Ma, Y. Lin, and C. W. Nan, *J. Appl. Phys.* **104**, 014101 (2008)
14. J. Wang, L. Wang, G. Liu, Z. Shen, Y. Lin, C.W. Nan, *J. Am. Ceram. Soc.* **92**, 2654 (2009)
15. Y. Jia, H. Luo, X. Zhao, F. Wang, *Adv. Mater.* **20**, 4776 (2008)
16. J. H. H. Liebermann and C. D. Graham, *IEEE Trans. Magn.* **MAG-12**, 921 (1976)
17. Z. Fang, S.G. Lu, F. Li, S. Datta, Q.M. Zhang, M. El Tahchi, *Appl. Phys. Lett.* **95**, 10 (2009)
18. C.W. Nan, G. Liu, Y. Lin, *Appl. Phys. Lett.* **83**, 4366 (2003)
19. Y.C. Chen, T.H. Hong, Z.X. Jiang, Q.R. Lin, *J. Appl. Phys.* **103**, 3 (2008)
20. S. Stein, M. Wuttig, D. Viehland, E. Quandt, *J. Appl. Phys.* **97**, 9 (2005)
21. D. Seguin, M. Sunder, L. Krishna, A. Tatarenko, P.D. Moran, *J. Cryst. Growth* **311**, 3235 (2009)
22. J. Ma, Z. Shi, C.W. Nan, *Adv. Mater.* **19**, 2571 (2007)
23. J. Ma, Z. Shi, and C. W. Nan, *J. Phys. D: Appl. Phys.* **41** (2008)
24. J.G. Wan, J.M. Liu, G.H. Wang, C.W. Nan, *Appl. Phys. Lett.* **88**, 86 (2006)
25. Y. Wang, F. Wang, S.W. Or, H.L.W. Chan, X. Zhao, H. Luo, *Appl. Phys. Lett.* **93**, 2006 (2008)
26. T. Wu, M.A. Zurbuchen, S. Saha, R.V. Wang, S.K. Streiffer, J.F. Mitchell, *Phys. Rev. B Condens. Matter Mater. Phys.* **73**, 1 (2006)
27. J. Ma, Y. Lin, and C. W. Nan, *J. Phys. D: Appl. Phys.* **43** (2010)
28. J.G. Wan, H. Zhang, X. Wang, D. Pan, J.M. Liu, G. Wang, *Appl. Phys. Lett.* **89**, 2 (2006)
29. H. C. He, J. Ma, Y. H. Lin, and C. W. Nan, *J. Phys. D: Appl. Phys.* **42** (2009)
30. H. C. He, J. Ma, J. Wang, and C. W. Nan, *J. Appl. Phys.* **103**, 0 (2008)
31. H.C. He, J. Wang, J.P. Zhou, C.W. Nan, *Adv. Func. Mater.* **17**, 1333 (2007)
32. Q. Zhan, R. Yu, S.P. Crane, H. Zheng, C. Kisielowski, R. Ramesh, *Appl. Phys. Lett.* **89**, 20 (2006)
33. C.W. Nan, G. Liu, Y. Lin, H. Chen, *Phys. Rev. Lett.* **94**, 1 (2005)
34. H. Zheng, J. Wang, S. E. Lofland, Z. Ma, L. Mohaddes-Ardabili, T. Zhao, L. Salamanca-Riba, S.R. Shinde, S.B. Ogale, F. Bai, D. Viehland, Y. Jia, D.G. Schlom, M. Wuttig, A. Roytburd, R. Ramesh, *Science* **303**, 661 (2004)
35. C. Deng, Y. Zhang, J. Ma, Y. Lin, C.W. Nan, *Acta Mater.* **56**, 405 (2008)
36. J. Wu, J. Wang, *J. Appl. Phys.* **106**, 1 (2009)
37. N. Ortega, P. Bhattacharya, R.S. Katiyar, P. Dutta, A. Manivannan, M.S. Seehra, I. Takeuchi, S.B. Majumder, *J. Appl. Phys.* **100**, 1 (2006)
38. J. Liu, Y. Zhang, Y. Lin, and C. W. Nan, *J. Appl. Phys.* **105** (2009)
39. R. Martínez, A. Kumar, R. Palai, R. S. Katiyar, and J. F. Scott, *J. Appl. Phys.* **107** (2010)
40. I. Vrejoiu, M. Alexe, D. Hesse, U. Gösele, *Adv. Func. Mater.* **18**, 3892 (2008)
41. L. Yan, Z. Xing, Z. Wang, T. Wang, G. Lei, J. Li, D. Viehland, *Appl. Phys. Lett.* **94**, 1 (2009)
42. D. Chiba, M. Sawicki, Y. Nishitani, Y. Nakatani, F. Matsukura, H. Ohno, *Nature* **455**, 515 (2008)
43. T. Maruyama, Y. Shiota, T. Nozaki, K. Ohta, N. Toda, M. Mizuguchi, A.A. Tulapurkar, T. Shinjo, M. Shiraishi, S. Mizukami, Y. Ando, Y. Suzuki, *Nat. Nanotechnol.* **4**, 158 (2009)

44. M. Weisheit, S. Fähler, A. Marty, Y. Souche, C. Poinsignon, D. Givord, *Science* **315**, 349 (2007)
45. C.G. Duan, J.P. Velev, R.F. Sabirianov, Z. Zhu, J. Chu, S.S. Jaswal, E.Y. Tsybal, *Phys. Rev. Lett.* **101**, 1 (2008)
46. C.G. Duan, S.S. Jaswal, E.Y. Tsybal, *Phys. Rev. Lett.* **97**, 13 (2006)
47. P. Borisov, A. Hochstrat, X. Chen, W. Kleemann, C. Binek, *Phys. Rev. Lett.* **94**, 1 (2005)
48. V. Laukhin, V. Skumryev, X. Martí, D. Hrabovsky, F. Sánchez, M.V. García-Cuenca, C. Ferrater, M. Varela, U. Lüders, J.F. Bobo, J. Fontcuberta, *Phys. Rev. Lett.* **97**, 1 (2006)
49. Y.H. Chu, L.W. Martin, M.B. Holcomb, M. Gajek, S.J. Han, Q. He, N. Balke, C.H. Yang, D. Lee, W. Hu, Q. Zhan, P.L. Yang, A. Fraile-Rodríguez, A. Scholl, S. X. Wang, R. Ramesh, *Nat. Mater.* **7**, 478 (2008)
50. H. Béa, M. Bibes, F. Ott, B. Dupé, X.H. Zhu, S. Petit, S. Fusil, C. Deranlot, K. Bouzehouane, A. Barthélémy, *Phys. Rev. Lett.* **100**, 3 (2008)
51. F. Zavaliche, H. Zheng, L. Mohaddes-Ardabili, S.Y. Yang, Q. Zhan, P. Shafer, E. Reilly, R. Chopdekar, Y. Jia, P. Wright, D.G. Schlom, Y. Suzuki, R. Ramesh, *Nano Lett.* **5**, 1793 (2005)
52. W. Eerenstein, M. Wiora, J.L. Prieto, J.F. Scott, N.D. Mathur, *Nat. Mater.* **6**, 348 (2007)
53. S. Sahoo, S. Polisetty, C.G. Duan, S.S. Jaswal, E.Y. Tsybal, C. Binek, *Phys. Rev. B Condens. Matter Mater. Phys.* **76**, 3 (2007)
54. C. Thiele, K. Dörr, O. Bilani, J. Rödel, L. Schultz, *Phys. Rev. B Condens. Matter Mater. Phys.* **75**, 1 (2007)
55. J.W. Lee, S.C. Shin, S.K. Kim, *Appl. Phys. Lett.* **82**, 2458 (2003)

Lead-Free BiFeO₃–BaTiO₃ Ceramics: An Overview



Naveen Kumar, Gulshan Dhillon, Ranvir Singh Panwar, Indu Sharma,
and Anupreet Kaur Bhatia

Abstract Multiferroic materials based on BiFeO₃ show properties like ferroelectricity and ferromagnetism at the same time. Inclination towards materials that are environment friendly, overcomes the problems related to lead-based materials. BiFeO₃–BaTiO₃ binary system entirely takes the charge over lead enrich materials. The binary system of BaTiO₃ and BiFeO₃ consists of lead-free materials having characteristic properties like high piezoelectric coefficient, high Curie temperature, and the existence of morphotropic phase boundary (MPB). The studies were carried on the BiFeO₃–BaTiO₃ multiferroic system from the last decade. BiFeO₃–BaTiO₃ system exhibits outstanding electrical applications in devices such as actuators, multilayer capacitors, flexible display, and memory devices. The present chapter discusses some basics of multiferroics, specially BiFeO₃ ceramic, misfortune related to BiFeO₃ and BiFeO₃–BaTiO₃ binary systems are addressed.

Keywords Multiferroic materials · BiFeO₃–BaTiO₃ binary system · Piezoelectricity · Ferroelectricity

N. Kumar (✉)

Department of Applied Sciences, Punjab Engineering College (Deemed To Be University), Chandigarh, India

G. Dhillon

Institute of Engineering and Technology, Chitkara University, Punjab, India

R. S. Panwar

Department of Metallurgical and Materials Engineering, Punjab Engineering College (Deemed To Be University), Chandigarh, India

I. Sharma

Department of Physics, Career Point University, Hamirpur, HP, India

A. K. Bhatia

Department of Physics, Goswami Ganesh Dutta Sanatan Dharma College, Chandigarh, India

1 Introduction

In the nineteenth century, Maxwell's four equations combined the electric and magnetic properties into a single discipline in spite of having no common origin [1]. The electrostatics in materials is attributed to the ions or charged atoms, whereas the magnetism is governed by the electronic spin. Both the phenomenon does exhibit a number of similarities as well, like hysteresis behavior on the application of external magnetic fields, the existence of domains, and phase transition at the critical temperature. Magnetism and ferroelectricity appear in a correlated form because of the availability of unpaired d- or f- orbital electrons or the existence of dipoles. This tie-in of charge and spin gives an extra edge in the electronics area by introducing an activity where the spin displays an excellent advantage on the transport properties, which permits the process to manage one by the other. Pierre Curie suggested the coupling between the degrees of freedom [2]. Landau and Lifshitz remarked about the concept in "Course of Theoretical Physics" in 1959 [3], and soon after Dzyaloshinskii gives the same concept [4]. Furthermore, the magnetoelectric effect was given by Astrov [5]. The search for a new material that displayed two orders out of four ferroic orders, was the further step. In the future, this was accomplished by Soviet scientists [6]. From the starting, there has been a dearth of such materials having both the orderings at the same time because of the contrasting requirement. For magnetism, there is a necessity of an electron in the d- or f- orbitals, whereas, for ferroelectricity, the central ion must have unfilled d or f orbitals. Under this antithetical condition, the linear magnetoelectric effect is avoided, i.e., magnetic and ferroelectric orders partially overlap with each other. As the availability of materials showing a linear magnetoelectric effect, the research in this area was terminated. Hereinafter Schmidt [7], a new class of materials known as 'Multiferroics', having simultaneous existence of ferromagnetism and ferroelectricity: i.e., spontaneous spin due to orbital motion and electron spin, and spontaneous polarization of the electric dipoles, even in the absence of external electric field simultaneously. Probably, the first-ever known multiferroic material was Boracite ($\text{Mg}_3\text{B}_7\text{O}_{13}\text{Cl}$) [8]. Thereby, the duration of the research in the field of multiferroic materials that occurred naturally or were synthesized was extended. There were three main points that revived the interest in the study of multiferroics. One of them was, in which material shows the magnetic and electric order coupling [9, 10]. The artificial synthesis of the material was the second reason, and the third one was the identification and classification on the basis of their behavior. In principle, the synthesis of this type of material is difficult as when the improvement in magnetic properties is done, the ferroelectric properties get reduced, and vice versa. The preparation of thin films of multiferroic BFO by Ramesh's group in 2003 surged the interest in the field [11]. The multiferroic properties of thin-film BFO were enhanced as compared to its bulk counterpart. The multiferroicity in TbMnO_3 was observed in the same year by Tokura and Kimura

[12]. The transfixing characteristic of ferroelectricity in this material was caused by magnetism which introduced an unconventional field of multiferroics.

2 Multiferroics

The existence of ferroelectricity and ferromagnetism simultaneously and sometimes the ferroelastic phenomenon is known as multiferroism, and the materials that exhibit such behavior are called multiferroic materials [7]. Several research articles have reported the phenomenon of multiferroism in single-phase or multiphase composites [13–18]. Pierre Curie discovered the existence of ferroelectric and ferromagnetic properties in the same material at the same time [2]. In some materials, the application of magnetic field gives the electric polarization and vice versa, which is known as ‘Magnetolectric (ME) effect’. The coupling between the ferromagnetic and ferroelectric orders is called ‘Magnetolectric coupling’. For the material to be categorized as a magnetolectric, the simultaneous existence of both these phenomena is essential. However, the magnetolectric polarization need not be displayed by the materials which are both electrically and magnetically polarized. Practically, this phenomenon occurs in materials that can be switched both electrically ($P \propto H$) and magnetically ($M \propto E$). Predominantly, the magnetolectric coupling is strain-mediated phenomenon, i.e., there is strain-induced variation in magnetic anisotropy with the application of electric field and vice versa. In multiphase materials, the existence of ME coupling results, due to piezoelectricity of the ferroelectric and ferromagnetic phase and also due to piezo magnetism that comes due to the coupling among mechanical strain and magnetic polarization.

2.1 Prerequisites for Multiferroicity

The experimental evidence of the multiferroic and magnetolectric properties was conducted in the starting of the twentieth century. There is a scarcity of materials that display the magnetolectric effect and the simultaneous occurrence of the ferroelectric and magnetic ordering is itself a demanding task. In 2000, the compatibility of the oxide materials for the simultaneous existence of ferromagnetism and ferroelectricity was reported by Hill [9]. The article also described the coexistence conditions to be contradictory and extremely difficult to achieve. The important conditions that restrict the coexistence of the ferroic orders are mentioned below.

2.2 Crystal Symmetry

Pierre Curie gives the concept of magnetoelectric effect on the basis of the symmetry of the crystal [2]. The existence of a non-centrosymmetric crystal structure is the initial requirement for ferroelectricity. There exist 31-point groups out of the 122 Shubnikov Heesch point groups that allow both, magnetization and spontaneous polarization [12]. Out of these 31-point groups, multiferroicity in the same phase is permitted by 13-point groups (1, $m'm2'$, $m'm'2'$, $2'$, 2, $3m'$, 3, $4m'm'$, 4, $6m'm'$, and 6). The existence of multiferroic materials is restricted by crystal symmetry.

2.3 d-Orbital Electron Occupancy

In ABO_3 multiferroic structure, transition metal generally occupies the B-site, having partially filled d -orbital that give rise to the electrical and magnetic properties. Ferroelectricity and ferromagnetism in these materials arise due to the partially filled and empty d -orbital, respectively. The electron occupancy effect in the d -orbital has been discussed as under:

(a) *Electron occupancy effect of d -orbital*

In transition metals and Lanthanide-based compounds, magnetism arises due to unpaired electrons in the d -orbital or the f -orbital. Due to unpaired electrons in most ferromagnets gives rise to magnetic behaviour with a high density of states. The insulating nature and the non-magnetic behavior of the transition metals are attributed to the empty or completely filled d -orbital electronic configuration. The insulating nature ensures the sustainability of materials against the applied electric field. Due to the contradictory requirement of the occupancy in d -orbital, there are a limited number of materials having electric and magnetic order in the same phase. This conflicting situation can be overcome by insulating magnets with weak ferromagnetism, ferrimagnetism, or antiferromagnetism, which has been used to increase the count of multiferroic materials. Materials showing these properties are good candidature for futuristic applications.

(b) Ferroelectricity is exhibited by crystalline materials which have a non-centrosymmetric structure below the transition temperature (T_C). In ABO_3 type perovskites, the structural distortion is due to shifting of cations at B-site in accordance with the oxygen octahedral. Perovskites, such as $BaTiO_3$ that have d^0 configuration (here Ti^{4+}) behave like ferroelectric materials. The compounds consisting of B-site cations with partially filled d -orbital have a robust inclination of undergoing Jahn–Teller distortion. These distortions have the main structural phenomenon for this type of compound (e.g.,

In LaMnO₃, d^4 configuration is exhibited by Mn and A-type antiferromagnetic insulating behavior is displayed, whereas in the case of YTiO₃, Ti exhibits d^1 configuration and shows ferromagnetic insulating behavior. Neither of the two materials mentioned shows ferroelectric characteristics and are both magnetic insulators.)

3 Multiferroic Types

All materials exhibit the same emergence of magnetism. The magnetic moment is attributed to the localized spin which itself is caused by the existence of partially filled d- and f- orbitals in the transition metals and rare earth ions respectively. The exchange interactions between different magnetic moments are dependent on the spatial distribution of the spin and result in different magnetic orders in these materials. Whereas, the condition is somewhat dissimilar in ferroelectric materials. Different kinds of multiferroic materials can be obtained by exploiting the phenomenon of ferroelectricity by various mechanisms.

On the basis of ferroelectricity, the multiferroic materials can be classified as:

- (i) Multiferroics of Type I
- (ii) Multiferroics of Type II.

4 Ferroelectricity

In ferroelectric materials, dipoles are bound to the crystal lattice. Therefore, any structural change in the system leads to variation in the electric dipoles. Due to this effect, in the absence of voltage, the electric lines flow in or out of the capacitor. Domains are the regions that exist in different orientations of polarizations before the application of the electric field. The ferroelectric domains are formed due to the polarization vector arrangement along a specific direction. The domain wall is the region between the domains [19]. Whereas, the direction of the dipoles changes and they bring into line themselves in the track of electric field. At a low electric field, the material behaves like a normal dielectric because the domains are incapable to shift their directions in the applied electric field. As polarization (P) and applied electric (E) field are related to each other by the relation:

$$P \propto E \quad (1)$$

With an increase in the electric field, the domains alignment starts and saturation arises when domains ranged themselves in an applied electric field. On removal of the electric field, the domains get randomized and misalign with respect to each other. Due to this, the degree of polarization decreases, and on complete removal of the electric field, some of the polarization remains because of the domain's irreversible

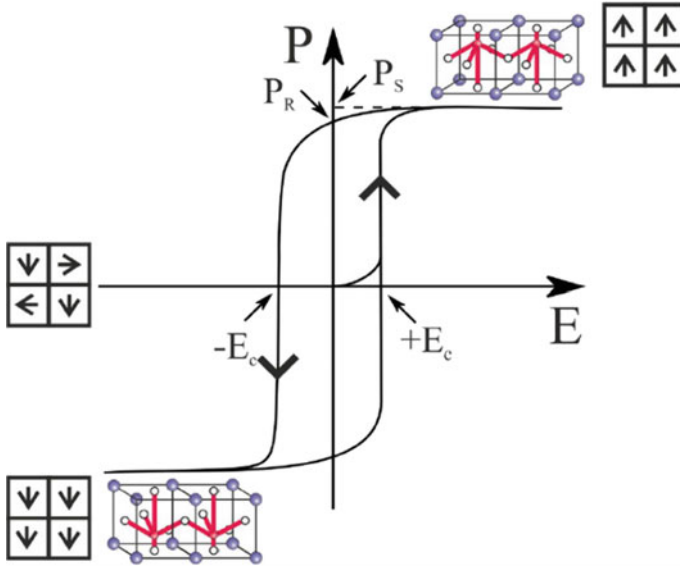


Fig. 1 Ferroelectric hysteresis curve between electric field and polarization

behaviour. At zero electric field, the polarization is named remnant polarization, whereas, the value of polarization extrapolated back from the remnant polarization is named spontaneous polarization. On increasing the field in the reverse direction, the polarization is removed and on more reversing the field, the polarization also changes in the reverse direction. In this manner hysteresis loop is formed as shown in Fig. 1.

The polarization produced in a dielectric material can be defined by the formula:

$$\vec{P} = \frac{\sum_i \vec{p}_i}{V} \tag{2}$$

where, \vec{P} is defined as electric polarization, \vec{p} is the dipole moment, and V is known as volume. The value of polarization can be increased by increasing polarization value or by decreasing volume. In another way, the more practical method is to increase the macroscopic polarization or the dipole moment per unit volume.

5 Barium Titanate (BaTiO₃)

In the year 1940, the ferroelectricity in BaTiO₃ (BTO) was observed and exhibit a high dielectric constant and a stable Curie temperature. It exhibits ABO₃-type structure in which corner positions are occupied by Ba²⁺ atoms, the center of the cube by Ti⁴⁺ cations and all the faces of the cube are occupied by O²⁻ ions. In case of inorganic perovskite oxides, transition elements, or an element from IVA or VA group are at B-site A site is occupied by alkaline earth metal or an alkali metal [20]. The tolerance factor is used for the determination of structural and thermal stability and is given by the formula [21]:

$$t = \frac{(r_a + r_o)}{\sqrt{2}(r_b + r_o)} \tag{3}$$

where, *r_a* and *r_b* are the radius of A site and B site cation, whereas, *r_o* is radii of oxygen anion [22].

For cubic symmetry or disturb three-dimensional configuration tolerance factor (*t*) lies between 0.8 and 1 [23]. For different molar fractions of BFO and BTO [(1 - *y*)BFO - *y*BTO; (*y* is the molar fraction of BTO)], the tolerance factor can be rewritten as:

$$t = \frac{[(1 - y)r_{Bi}^{+3} + yr_{Ba}^{+3} + r_O^{-2}]}{\sqrt{2}[(1 - y)r_{Fe}^{+3} + yr_{Ti}^{+4} + r_O^{-2}]} \tag{4}$$

By using the Shannon et al. values of effective ionic radius, the tolerance factor of a typical perovskite structure can be calculated [20]. At room temperature, BTO exhibits tetragonal crystal with Curie transition temperature of BTO is 120 °C (Fig. 2).

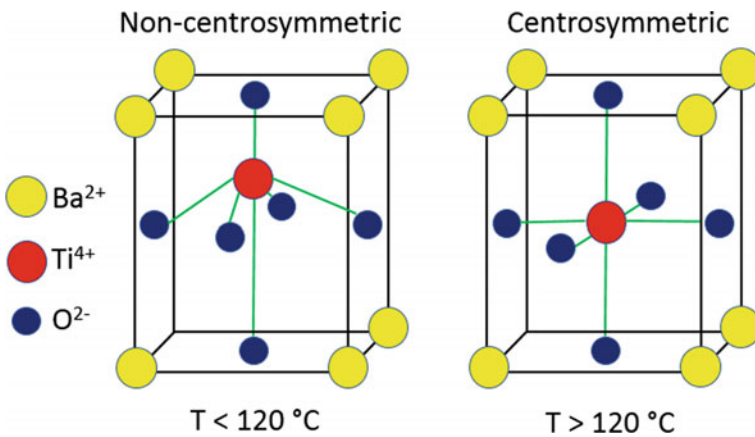


Fig. 2 BaTiO₃ structure below and above the Curie temperature

In literature, there are five crystallographic configurations of BTO namely tetragonal, cubic, rhombohedral, orthorhombic, and hexagonal. Above Curie temperatures, BTO exhibits cubic symmetry. The polarization results due to the hybridization between $3d$ states of 'Ti' and $2p$ states of 'O' which induced dipoles at room temperature.

The c/a ratio has the maximum value when the particle size was approximately $0.4 \mu\text{m}$ [24]. If the temperature is greater than the Curie temperature (393 K), BTO exhibits cubic symmetry ($Pm3m$). The tetragonal ($P4mm$) to orthorhombic ($Bmm2$) phase transition occurs at 298 K, whereas, at 183 K, transition from orthorhombic to rhombohedral ($R3m$) phase occurs [25, 26]. To explain the origin of ferroelectricity more theories are required for better understanding.

6 Bismuth Ferrite (BiFeO_3)

In 1960, Bismuth ferrite (BFO) was first discovered [27]. The BFO has a distorted rhombohedral cubic perovskite structure having space group $R3c$ and rhombohedral angle between 89.3° and 89.4° [28, 29]. The movement of Bi, O, and Fe ions as well as the cooperative alternation of FeO_6 , both along [111] direction, results in the distorted crystal structure [30].

In BFO, ferroic and antiferroic parameters exist along with two or more order parameters such as ferroelastic, ferroelectric, and ferromagnetism [31]. The simultaneous existence of two ferroic orders ferroelectric/magnetic and their control by the electric and magnetic field gives the existence of multiferroicity in BFO. In multiferroic materials, charges of ions and electrons control the electrical properties, whereas, electron spin controls the magnetic properties [32]. Empty d-orbitals are required for ferroelectricity which is necessary for cation off-center displacement, whereas, for ferromagnetism, empty d-orbitals are required [33, 34]. The simultaneous existence of ferroelectric and ferromagnetic orders is difficult to achieve at room temperature. The interactions between Fe–O–Fe are responsible for antiferromagnetic order. However, the canting of spins in the distorted structure is the reason for weak ferromagnetism in single-crystal BFO [35–39]. Spintronics and tunable waveguide devices are some of the broad applications of these materials [40].

The ferroelectricity in BFO can be enhanced by depressing its spiral spin structure. This can be achieved by [11, 41, 42]:

- By cation substitution or structural modification by doping.
- Formation of complexes by introducing ferrites.
- Size-dependent effects of nanocrystalline BFO.
- Stress-induced polarization and ferromagnetic properties.
- Release of the canted magnetic moment by the application of an intense magnetic field.

Hybridization between Bi-6*p* and O-2*p* orbitals in BFO is responsible for large polarization and piezoelectric response [43]. Due to the large extension of the 6*s* orbitals, the overlap of the 6-*p* orbitals of the cation and anion decreases, as a result, bond strength decrease. Due to hybridization, the ionic radius of Bi decreases, which separates out the 6*s* and 6*p* orbitals, and due to which 6*s* electrons get polarized. This makes the bonding and octahedral distortion stable [30].

7 Bismuth Ferrite-Barium Titanate (BFO-BTO)

The improvement in ferroelectricity of BFO-BTO ceramic system is done through substitution of different ions, for example Co³⁺, Cu²⁺, Mn²⁺, La²⁺, Nd³⁺, Dy³⁺, Er³⁺, Eu³⁺, Cr³⁺, Ni²⁺, Al³⁺, Ce²⁺, Gd³⁺, and Ga³⁺ [44–53]. The electrical properties are also improved in multiphase solution like BiMeO₃ (Me = Al, Ga, Y, Sc, Zn_{1/2}Ti_{1/2}, Mg_{2/3}Nb_{1/3}, Zn_{2/3}Nb_{1/3}), La_{0.7}Sr_{0.3}MnO₃, Na_{0.5}Bi_{0.5}TiO₃ [32, 54–58].

In BTO-BFO rhombohedral structure is evolved when BTO doping is less than 30%, and when the amount of BFO is 40–70% then, it shows cubic phase. In the case of a pure BTO-BFO system, the Curie temperature is 804 K, which can be varied by altering the BTO/BFO molar ratio [30, 44]. Rhombohedral phases in BTO-BFO are thermally stable in comparison to pseudocubic or a mixture of rhombohedral and pseudocubic phases [59]. Substitution of ions like Na, Al, Bi_{0.5}Na_{0.5}TiO₃, MnO₂–CuO, and La(Mg_{0.5}Ti_{0.5})O₃ is used to enhance the insulating properties as well as the thermal stability of BTO-BFO [57, 60–63]. Universal core–shell microstructures are also used to enhance thermal stability [64]. The crystalline phases for different substitution levelsof BTO in (1–Z)BFO-ZBTO are shown in Table 1 [65].

At 10 and 20% molar ratio of BTO, there is the existence of diffuse phase transition, whereas, when the composition of BTO ranges from 0.24 to 0.36, there is a simultaneous decrement in the coercive field and remnant polarization [66].

Table 1 Crystal structure of (1–Z)BFO-ZBTO at the varying substitution level

Composition(1–y)BFO-yBTO	Crystal structure
Z = 0	Rhombohedral
Z = 0.1	Rhombohedral
Z = 0.2	Rhombohedral
Z = 0.3	Rhombohedral
Z = 0.4	Cubic
Z = 0.5	Cubic

In the past few decades, research advancement is focused on the BTO-BFO crystal structure [67–70]. The simultaneous existence of pseudocubic, rhombohedral, and tetragonal phases was also reported [67]. Karpinsky et al. has studied the crystal structure around structural phase transition [69]. The improvement in electrical properties due to the coexistence of tetragonal and rhombohedral phases was also reported [71]. Lin et. al. supports the inclusion of rhombohedral ($y = 0-0.33$), pseudocubic ($y = 0.33-0.92$), and tetragonal ($y = 0.92-1$) phases in the $(1-y)$ BFO- y BTO solid solutions [29]. At 33% molar fraction of BTO, change from pseudocubic phase to rhombohedral phase was observed [27].

The cooling rate also affects the phase transitions. non-centrosymmetric orthorhombic structure ($Amm2$) has been observed in quenched samples, whereas, in tardily cooled sample's centrosymmetric orthorhombic structure ($Pbnm$) was observed. Ma Jian et. al. reported the effect of different cooling methods on the phase structure of BTO-BFO [72]. The variation in cooling methods does not affect the diffraction peak very much. Due to the longer cooling time in the furnace, the change in grain size is substantial. The orthorhombic structure is more favorable at intermediate temperatures between 773 and 923 K due to oxygen vacancies diffusion. A small rhombohedral distortion of 0.75BFO–0.25BTO occurs at room temperature [73]. Numerous works have been done till now, however, BTO-BFO structure is still a mystery. The various parameters of BFO-BTO ceramics and few lead-free ceramic solutions are given in Table 2.

8 Conclusion

In multiferroic materials, more than two ferroic orders exist at the same time such as ferroelasticity, ferroelectricity, and ferromagnetism. These materials exhibit great technological importance. Keeping in view the sustainability and environmental risks in mind, the search for lead-free materials is on topmost priority. Materials having comparable properties and performance as lead-based materials are going on. In literature, it has been suggested that BTO-BFO exhibits excellent magnetic and electrical properties, and is a good candidate for the aforementioned applications. The enhancement in piezoelectric properties still needs to be addressed and studied further as there is very little information about the structure of BTO-BFO. Scientists suggest that the future of the new generation of devices is based on spintronics. By understanding the domain structure, the ferroelectric and magnetoelectric properties can be altered. Moreover, ferroelectric materials can also be used in artificial intelligence.

Table 2 Piezoelectric coefficient (d_{33}), Curie temperature (T_c), remnant polarization (P_r) and crystalline phase of BFO-BTO ceramics, here, R = Rhombohedral and PC = Pseudocubic

Materials	d_{33} (pC/N)	T_c (°C)	P_r ($\mu\text{C}/\text{cm}^2$)	Phase structure	References
0.7BFO-0.3BTO 1 mol% MnO ₂	152	487	25	R-PC	Chen et al. [74]
0.97(0.67Bi _{1.05} FeO ₃ -0.33BTO)-0.03Bi _{1.05} (Zn _{0.5} Ti _{0.5})O ₃	324	466	-	-	Lee et al. [71]
0.725BFO-0.275BTO	136	485	21.4	R	Yang et al. [75]
0.99(0.675BFO-0.325BTO)-0.6 mol% MnO ₂ -0.4 mol% CuO-0.01 LiTaO ₃	145	~420	22.82	-	Akram et al. [76]
0.7(Bi _{0.991} Zn _{0.009})FeO ₃ -0.3BTO-0.3 wt.% MnO ₂	192	-	18.29	-	Tong et al. [77]
0.71BiFe _{0.9} (Zn _{1/2} Ti _{1/2}) _{0.1} O ₃ -0.29BTO	139	428	28.1	-	Sun et al. [78]
0.67Bi _{1.05} (Fe _{0.97} Ga _{0.03})O ₃ -0.33BTO	420	454	-	-	Lee et al. [71]
0.71BFO-0.29BaTi _{0.99} (Mg _{1/3} Nb _{2/3}) _{0.01} O ₃	158	453	-	-	Zhou et al. [79]
0.7BFO-0.3BTO	134	524	26.0	R-PC	Wei et al. [28]
0.75BFO-0.25BTO-1 mol% MnO ₂	114	635	23	R	Chen et al. [74]
0.67BFO-0.33BTO-Bi _{0.5} Na _{0.5} TiO ₃	183	467	24.2	PC	Cheng et al. [80]
0.7Bi _{1.05} Fe _{0.93} Sr _{0.07} O ₃ -0.3BTO	180	520	22	R-C	Zheng et al. [81]
0.96(Na _{0.52} K _{0.48})(Nb _{0.95} Sb _{0.05})O ₃ -0.04Bi _{0.5} (N _{0.92} K _{0.18}) _{0.5} ZrO ₃	490	227	-	-	Lee et al. [71]

References

1. J. C. Maxwell (ed.), *A Treatise on Electricity and Magnetism* (Clerndon Press Series, 1881)
2. P. Curie, *J. Phys. Theor. Appl.* **3**(1), 393 (1894)
3. L. D. Landau and E.M. Lifshitz, *Electrodynamics of Continuous Media*, 2nd edn. (Elsevier, Oxford, U.K., 1959)
4. I.E. Dzyaloshinskii, *Soviet Phys. JEPT* **10**, 628 (1959)
5. D.N. Astrov, *Soviet Phys. JEPT* **11**, 708 (1960)
6. G.A. Smolenskii, I.E. Chupis, *Soviet Phys. Uspekhi* **25**, 475 (1982)
7. H. Schmid, *Ferroelectrics* **162**, 317 (1994)
8. E. Asher, H. Rieder, H. Schmid, H. Stossel, *J. Appl. Phys.* **37**, 1404 (1966)
9. N.A. Hill, *J. Phys. Chem. B* **104**, 6694 (2000)
10. D. I. Khomskii, Magnetism and ferroelectricity; why do they so seldom coexist? in *Paper presented at American Physical Society, Annual March Meeting, Washington State Convention Center Seattle, Washington Meeting* (2001)
11. J. Wang, J.B. Neaton, H. Zheng, V. Nagarajan, S.B. Ogale, B. Liu, D. Viehland, V. Vaithyanathan, D.G. Schlom, U.V. Waghmare, N.A. Spaldin, K.M. Rabe, M. Wuttig, R. Ramesh, *Science* **299**, 1719 (2003)
12. T. Kimura, T. Goto, H. Shintani, K. Ishizaka, T. Arima, Y. Tokura, *Nature* **426**, 55 (2003)
13. N.A. Spaldin, M. Fiebig, *Science* **309**, 391 (2005)
14. W. Eerenstein, N.D. Mathur, J.F. Scott, *Nature* **442**, 759 (2006)
15. N. Hur, S. Park, P.A. Sharma, J.S. Ahn, S. Guha, S.-W. Cheong, *Nature* **429**, 392 (2004)
16. Y.H. Chu, L.W. Martin, M.B. Holcomb, M. Gajek, S.J. Han, Q. He, N. Balke, C.H. Yang, D. Lee, W. Hu, Q. Zhan, P.L. Yang, A.F. Rodríguez, A. Scholl, S.X. Wang, R. Ramesh, *Nat. Mater.* **7**, 478 (2008)
17. M. Bibes, A. Barthélémy, *Nat. Mater.* **7**, 425 (2008)
18. S. V. V. Khikhlovskiy, *Dissertation* (University of Groningen, 2010)
19. B. Jaffe, W.R. Cook, H.L. Jaffe, *Piezoelectric Ceramics*, 1st edn. (Academic Press, U.S., 1971)
20. R.D. Shannon, *Acta Crystallogr. Sect. A: Cryst. Phys. Diffr. Theor. Gen. Crystallogr.* **32**, 751 (1976)
21. C.F. Wang, H.J. Li, M.G. Li, Y. Cui, X. Son, Q.W. Wang, J.Y. Jiang, M.M. Hua, Q. Xu, K. Zhao, H.Y., Y. Zhang, *Adv. Funct. Mater.* **31**, 2009457 (2021)
22. M.L. Liang, W.H. Lin, Z.Y. Lan, J. Meng, Q. Zhao, X.S. Zou, I.E. Castelli, T. Pullerits, S.E. Canton, K.B. Zheng, *A.C.S. Appl. Electron. Mater.* **2**, 1402 (2020)
23. J. Rödel, W.J. Klaus, T.P. Seifert, E.M. Anton, T.J. Granzow, *Am. Ceram. Soc.* **92**, 1153 (2009)
24. T. Tunkasiri, G. Rujjanagul, *J. Mater. Sci. Lett.* **15**, 1767 (1996)
25. X.Z. Guo, Y.G. Wu, Y.N. Zou, Z.Y. Wang, *J. Mater. Sci.: Mater. Electron.* **23**, 1072 (2012)
26. R.E. Cohen, *Nature* **358**(136) (1992)
27. Q.M. Hang, Z.B. Xing, X.H. Zhu, M. Yu, Y. Song, J.M. Zhu, Z.G. Liu, *Ceram. Int.* **38S**, S411 (2012)
28. Y.X. Wei, X.T. Wang, J.T. Zhu, X.L. Wang, *J. Am. Ceram. Soc.* **96**, 3163 (2013)
29. Y. Lin, L.L. Zhang, J. Yu, *J. Mater. Sci.: Mater. Electron.* **26**, 8432 (2015)
30. M.M. Kumar, A. Srinivas, S.V. Suryanarayana, *J. Appl. Phys.* **87**, 855 (2000)
31. H.Z. Song, Y.X. Li, K.Y. Zhao, H.R. Zeng, S.X. Hui, G.R. Li, Q.R. Yin, *Mater. Lett.* **63**, 589 (2009)
32. S. Hajra, S. Sahoo, T. Mishra, P.K. Rout, R.N.P. Choudhary, *Appl. Ceram.* **12**, 164 (2018)
33. T. Park, S.S. Wong, G. Papaefthymiou, A.J. Viesacs, Y. Lee, H. Zhou, *Phys. Rev. B* **82**, 024431 (2010)
34. B. Madon, H.B. Kang, M.G. Kang, D.B. Maurya, A.M. Magill, J.P. Alves, J.E. Wegrowe, H.J. Drouhin, S. Priya, G.A. Khodaparast, *AIP Adv.* **8**, 105034 (2018)
35. A. Prasathetragarn, P. Jantaratana, N. Vittayakorn, B. Yotburut, R. Yimnirun, *R. Ferroelectr.* **451**, 109 (2013)
36. K.C. Verma, R.K. Kotnala, *Solid State Commun.* **151**, 920 (2011)

37. H.B. Yang, Q.Q. Ke, H.Y. Si, J.S. Chen, *J. Appl. Phys.* **111**, 024104 (2012)
38. N. Adhlakha, K.L. Yadav, R. Singh, *Smart Mater. Struct.* **23**, 105024 (2014)
39. R. Gotardo, E. Silva, R. Alonso, J. Rosso, D. Silva, G. Santos, K. Silva, L. Cótica, I. Santos, R.Y. Guo, A. Bhalla, *Ferroelectrics* **534**, 95 (2018)
40. S. Mallick, A. Vorobiev, Z. Ahmad, F. Touati, S. Gevorgian, *Ceram. Int.* **43**, 8778 (2017)
41. Z. Wen, Y. Lv, A.D. Li, *Appl. Phys. Lett.* **99**, 012903 (2011)
42. J. ñiguez, D. Vanderbilt, L. Bellaiche, *Phys. Rev. B* **67**, 224107 (2003)
43. S. Hajra, M. Sahu, V. Purohit, A. Kumar, R. Panigrahi, D. Sitikantha, R.N.P. Choudhary, *Iran. J. Sci. Technol. Trans. A: Sci.* **44**, 1251 (2020)
44. M.S. Mostari, N. Islam, M.A. Matin, *Ceram. Int.* **46**, 15840 (2020)
45. A. Kursumovic, W.W. Li, S. Cho, P.J. Curran, D.H.L. Tjhe, J.L. Macmanus-Driscoll, *Nano Energy* **71**, 104536 (2020)
46. H.N. Sun, X.J. Wang, Q.Z. Sun, X.X. Zhang, Z. Ma, M.Y. Guo, B.W. Sun, X.P. Zhu, Q.D. Liu, X.J. Lou, *J. Eur. Ceram. Soc.* **40**, 2828 (2020)
47. M.J. Tian, L. Zhou, X. Zou, Q.J. Zheng, L.L. Luo, N. Jiang, D.M. Lin, *J. Mater. Sci.: Mater. Electron.* **26**, 8840 (2015)
48. W. Zhou, Q. Zheng, Y. Li, Q. Li, Y. Wan, M. Wu, D.M. Lin, *Phys. Status Solidi A* **212**, 632 (2015)
49. D.J. Kim, M.H. Lee, T.K. Song, *J. Eur. Ceram. Soc.* **39**, 4697 (2019)
50. C. Behera, A. Pattanaik, *J. Mater. Sci.: Mater. Electron.* **30**, 5470 (2019)
51. J.S. Kim, C.I. Cheon, C.H. Lee, P.W. Jang, *J. Appl. Phys.* **96**, 468 (2004)
52. V.A. Khomchenko, D.V. Karpinsky, A.L. Kholkin, N.A. Sobolev, G.N. Kakazei, J.P. Araujo, I.O. Troyanchuk, B.F.O. Costa, J.A. Paixão, *J. Appl. Phys.* **108**, 074109 (2010).
53. V. Kumar, A. Gaur, R.J. Chaudhury, D. Kumar, *Superlattices Microstruct.* **98**, 54 (2016)
54. C.H. Yang, P.P. Lv, J. Qian, O.Y. Jun, X.J. Lin, S.F. Huang, Z.X. Cheng, *Adv. Energy Mater.* **9**, 1803949.1 (2019)
55. S. Murakami, N.T.A.F. Ahmed, D.W. Wang, A. Feteira, D.C. Sinclair, I.M.J. Reaney, *Eur. Ceram. Soc.* **38**, 4220 (2018)
56. X.L. Chen, X.X. Li, G.S. Huang, G.F. Liu, X. Yao, H.F. Zhou, *J. Adv. Dielectr.* **8**, 1850012 (2018)
57. S. Sahoo, S. Hajra, M. De, K. Mohanta, R.N.P. Choudhary, *J. Alloys Compd.* **766**, 25 (2018)
58. E. Stern-Taulats, P. Lloveras, M. Barrio, E. Defay, M. Egilmez, A. Planes, J.T. Tamarit, L. Manosa, N.D. Mathur, X. Moya, *APL Mater.* **4**, 091102 (2016)
59. Q.L. Fan, C.R. Zhou, Q.L. Li, J.W. Xu, *J. Mater. Sci.: Mater. Electron.* **26**, 9336 (2015)
60. H.B. Yang, C.G. Zhou, X.Y. Liu, Q. Zhou, G.H. Chen, W.Z. Li, H.J. Wang, *Eur. Ceram. Soc.* **33**, 1117 (2013)
61. Z.Y. Cen, C.G. Zhou, H.B. Yang, Q. Zhou, W.Z. Li, C.L. Yan, L. Cao, J. Song, L. Peng, *J. Am. Ceram. Soc.* **96**, 2252 (2013)
62. D.W. Wang, Z.M. Fan, W.B. Li, D. Zhou, A. Feteira, G. Wang, S. Murakami, S.K. Sun, Q.L. Zhao, X.L. Tan, I.M. Reaney, *A.C.S. Appl. Energy Mater.* **1**, 4403 (2018)
63. I. Calisir, A.A. Amirov, A.K. Kleppe, D.A. Hall, *J. Mater. Chem. A* **6**, 5378 (2018)
64. I.O. Owate, R. Freer, *J. Appl. Phys.* **72**, 2418 (1992)
65. S.O. Leontsev, R.E. Eitel, *J. Am. Ceram. Soc.* **92**, 2957 (2009)
66. S. Kim, G.P. Khanal, H.W. Nam, I. Fujii, S. Ueno, C. Moriyoshi, Y. Kuroiwa, S. Wada, *J. Appl. Phys.* **122**, 164105 (2017)
67. A. Singh, A. Senyshyn, H. Fuess, S.J. Kennedy, D. Pandey, *Phys. Rev. B* **89**, 024108 (2014)
68. D.V. Karpinsky, M.V. Silibin, S.V. Trukhanov, A.V. Trukhanov, *J. Nanomater.* **10**, 801 (2020)
69. A. Singh, A. Kumar, D. Pandey, *J. Appl. Phys.* **124**, 224101 (2018)
70. M.H. Lee, D.J. Kim, J.S. Park, S.W. Kim, T.K. Song, M.H. Kim, W.J. Kim, D. Do, I.K. Jeong, *Adv. Mater.* **27**, 6976 (2015)
71. M.A. Jian, Z. Bo-Ping, C. Jian-Yin, *J. Inorg. Mater.* **32**(10), 1035 (2017)
72. D.S. Kim, C.I. Cheon, S.S. Lee, J.S. Kim, *Appl. Phys. Lett.* **109**, 202902 (2016)
73. J.G. Chen, J.R. Cheng, J. Guo, Z.X. Cheng, J.L. Wang, H.B. Liu, S.J. Zhang, *J. Am. Ceram. Soc.* **103**, 374 (2020)

74. H.B. Yang, C.R. Zhou, X.Y. Liu, Q. Zhou, G.H. Chen, H. Wang, W.Z. Li, *Mater. Res. Bull.* **47**, 4233 (2012)
75. F. Akram, R.A. Malik, S. Lee, R.A. Pasha, M.H. Kim, *Korean. J. Mater. Res.* **28**, 489 (2018)
76. K. Tong, C.R. Zhou, Q.G. Li, J. Wang, L. Yang, J.W. Xu, G.H. Chen, C.L. Yuan, G.H. Rao, *J. Eur. Ceram. Soc.* **38**, 1356 (2018)
77. Y.Y. Sun, H.B. Yang, S.B. Guan, Y.H. Cao, M.H. Jiang, X. Liu, Q.H. Chen, M.J. Li, J.W. Xu, *J. Alloys Compd.* **819**, 153058 (2020)
78. X.J. Zhou, C.G. Zhou, Q. Zhou, H.B. Yang, *J. Electron. Mater.* **43**, 755 (2014)
79. S. Cheng, B.P. Zhang, L. Zhao, K.K. Wang, *J. Am. Ceram. Soc.* **102**, 7355 (2019)
80. T. Zheng, Z.G. Jiang, J.G. Wu, *Dalton Trans.* **45**, 11277 (2016)
81. G.A. Samara, *J. Phys.: Condens Matter* **15**, R367 (2003)

Applications of Multiferroics



**Rohit Jasrotia, Suman, Rohit Khargotra, Ankit Verma, Indu Sharma,
and Ritesh Verma**

Abstract This chapter gives a detailed expedition of multiferroic materials, from their inception as a theoretical interest to their current status as a centre of global research effort set to influence technology and moreover, it commences with the introduction of an overview of multiferroic materials along with their classification. After conferring the extensive advancement in the research field of multiferroics, a detailed overview of multifunctional applications of multiferroics materials is taken into account. This chapter emphasizes on the potential use of multiferroics in different research areas of science such as solar cells, gyrators, thermal and vibration energy harvesting, and many more.

Keywords Multiferroics · Single-phase and composite multiferroics · Fabrication · Multifunctional applications

1 Introduction

The study of new materials and their functions has been relatively widespread in current years, marked by the integration and shrinking of electronic components, and one of the vital goals is to be incorporated into present technologies, processors, and devices. Magnetic and ferroelectric (FE) materials have been the theme of research, ranging from large devices like electrical transformers to small devices

R. Jasrotia (✉) · R. Verma

School of Physics and Materials Science, Shoolini University, Bajhol, Solan, H.P, India

Suman

Yogananada School of AI, Computers and Data Sciences, Shoolini University, H.P Bajhol, Solan, India

R. Khargotra

Department of Engineering, University of Pannonia, Egyetem u., 10, Veszprem 8200, Hungary

A. Verma (✉)

School of Advanced Chemical Sciences, Shoolini University, H.P Bajhol, Solan, India

I. Sharma

Department of Physics, Career Point University, Hamirpur, India

like sensors used in integrated circuits or as a storage device, due to an inimitable arrangement of characteristics. Because of their intriguing characteristics and uses, multiferroic materials are progressively becoming the attention of current research [1]. The ferroics is categorized as those materials which contain small regions called domains that may exist in at least two different orientation states in equilibrium whereas typical ferroic confirm domains with varying orientation states unglued by domain barriers [2]. The multiferroic (MF) materials contain both ferroelectric and magnetic order, both of these have symmetry requirements that a multiferroic must meet at an identical time. In other words, we can say that, these are multifunctional materials in which at least two ferroic orders, such as ferromagnetism, ferroelectricity, and ferroelasticity, are present at the identical time and therefore, exchange interactions between magnetic dipoles, which originate from void shells of electron orbitals, are traditionally used to promote magnetic order [3]. The assembling of local electric dipoles produces electric order. The consequence of atomic displacements being ordered owed to strain is elastic order. The occurrence of magnetic and electric order at the identical time is particularly significant because it conglomerates features that could be used for data storage, processing, and transfer enables the interaction of magnetic and electric fields with magnetic and electric order. The simultaneous display of ferroelectric and ferromagnetic orders shows that magnetoelectric multiferroic materials are very promising for a variety of possible applications. This chapter emphasizes to multiferroics for useful tenacities, as they are homogeneous compounds that have both magnetic and electric dipoles ordered simultaneously.

Ferroelectric ordering pooled with Ferro or antiferromagnetic ordering is categorized under this family of materials [4]. For the first time, H. Schmid coined the word “multiferroics” in the year 1994 [5]. The multiferroics are classified into two components named “single-phase and composite”. Moreover, single-phase multiferroic materials are uncommon and display poor ferroelectric and ferromagnetic behavior along with weak coupling strength at 300 K [6, 7]. To be useful in advanced applications, multiferroic materials must have extremely high magnetoelectric coupling strength at and above 300 K. The electrical requirements of molecules to show ferroelectric and ferromagnetic ordering are opposed, which explains the paucity of single-phase multiferroic materials. For example, conventional ferroelectric materials like BaTiO_3 require an empty d-orbital of Ti, while unpaired electrons are necessary to display magnetism [7, 8]. In addition, symmetry criteria are a consideration and thus, only 13-point groups are capable of demonstrating the multiferroic characteristic. Multiferroic research has received minimal attention from the scientific community because of the shortage of single-phase materials [9]. There has been a surge in a study in this subject with the introduction of nanotechnology. The multiferroic characteristics of numerous single-phase structures can be changed via nano-level manipulation. By integrating the profits of the composite method, several novel systems with remarkable magnetoelectric coupling at 300 K have been created [10]. Excellent ferroelectric and magnetic characteristics are exhibited in BaTiO_3 at 300 K by decreasing the size of a particle to a range of nanometres [11]. The produced material should be in a phase with no additional phase's exhibit the outstanding multiferroic behavior but on the other hand, the development of the

secondary phase frequently leads in a decrease in the multiferroic characteristic. For example, in the fabrication of BiFeO_3 , additional phases of $\text{Bi}_2\text{Fe}_4\text{O}_9$ and $\text{Bi}_{25}\text{FeO}_{39}$ are obtained, which significantly degrade the multiferroic behavior of BiFeO_3 material [12]. Ferromagnetic materials are frequently utilized for data storage in cassettes, hard drives, and other devices whereas ferroelectrics are useful because of their high piezoelectric-coupling constant, which describes the connection between an electric field and strain due to which they can contribute their utilization in electronics like capacitors, microphones, and transducers. Now a day, a large amount of contribution along with scientific interest is created by multiferroics due to their potential applications in various research areas of science. The most significant use of multiferroics is in the area of a memory device, in which information may be recorded electrically and read magnetically [13]. To accomplish this application under microelectronic devices, the materials of large insulation, coupling between electric and magnetic order at 300 K along with varying polarization will require, but most of the multiferroics materials are not able to fulfill these boundary criteria. The multiferroics are also used on a large scale for the photocatalytic degradation of organic pollutants for wastewater remediation application [14, 15]. Figure 1 shows the number of publications in the research area of multiferroics from 2010 to 2021.

This chapter provides a summary of multiferroics, with a focus on the classification and fabrication of multiferroic, the data around the potential applications of multiferroics. Therefore, this chapter presents the latest text in this research field, which covers a wide spectrum of the potential use of multiferroics in different research areas, along with recent breakthroughs in this arena.

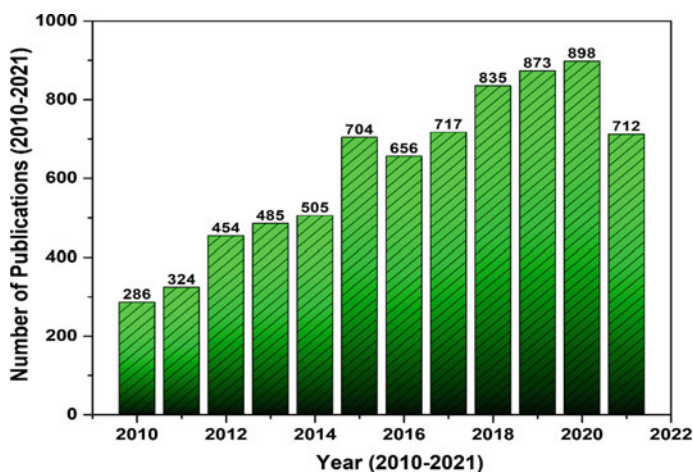


Fig. 1 Number of publications searched using the keyword “multiferroic” in science direct data source from 2010 to 2021

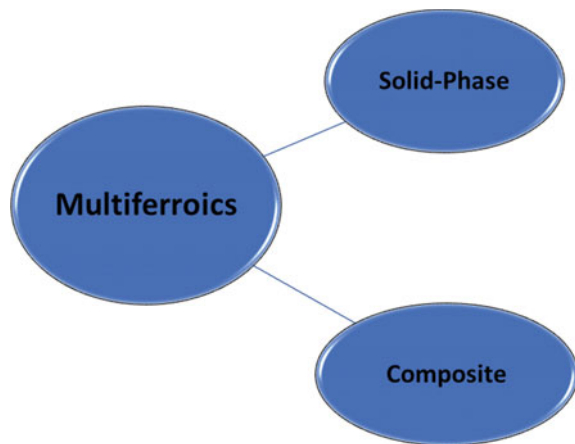
2 Classification of Multiferroics

The multiferroic materials are categorized into two broad components, as shown in Fig. 2, as single-phase and composite multiferroics.

2.1 Solid-Phase Multiferroics

The solid-phase multiferroics are again categorized into two further components-Type-I and Type II multiferroics. The type-I single-phase multiferroics comprising boracites, lone-pair, improper and proper geometric ferroelectrics whereas, type-II single-phase multiferroics contains the materials which show ferroelectricity because of magnetic or charge order. Under the lone pair ferroelectrics category, we have bismuth-grounded compounds whereas boracites are represented by the chemical formula, $M_3B_7O_{13}X$; M may be chromium, manganese, iron, cobalt, copper, nickel, etc. The proper, as well as improper geometric ferroelectrics, are represented by the chemical formula, $BaMF_4$; M = manganese, iron, cobalt, nickel, magnesium, etc., and $RMnO_3$; R = Lutetium, scandium, Ytterbium, etc. In addition to this, the category of materials that show ferroelectricity due to magnetic and charge order are exhibited by compounds as $TbMnO_3$, $TbMn_2O_5$, $Ni_3V_2O_8$, $CuFe_2O_4$, $CoCr_2O_4$, etc. and $LuFe_2O_4$, $Pr_{1-x}Ca_xMnO_3$. RFe_2O_4 ; R = Dysprosium, Lutetium and Ytterbium etc. [16].

Fig. 2 Schematic presentation of types of multiferroics



2.2 Composite Multiferroics

The combination of nanostructured ferroelectric and ferromagnetic materials at 300 K is an alternate method for producing multiferroic materials. As every phase performs independently, the magnetoelectric coefficient of composite multiferroics is significantly greater at 300 K than that of single-phase materials. Under the category of composite multiferroics, the magnetoelectric effect is extrinsic and can be arbitrated by the phenomenon of strain [17]. This is made feasible by the former's magnetostriction and the latter's piezoelectricity. When the magnetic phase is magnetized, the magnetostrictive action causes it to deform, straining the ferroelectric phase with which it is chemically linked along with a shared interface. Concurrently, the straining of the ferroelectric phase affects its polarisation because of the application of the piezoelectric effect. A magnetic field can cause a polarisation shift in the ferroelectric phase but, the inverse piezoelectric effect causes a distortion of the ferroelectric phase, on applying an electric field, and then, it is moved to the magnetic phase and changes its magnetic state via the inverse magnetostrictive effect [2].

3 Fabrication Methods of Multiferroics

Multiferroic nanoparticles can be prepared using a number of chemical techniques. Each approach has its own set of benefits and drawbacks. The synthesis technique determines the many features and properties of the developed multiferroic nanoparticles. As a result, choosing a specific technique for generating multiferroic nanoparticles is important. This chapter discusses the most common and straight forward ways for generating multiferroic nanomaterials as shown in Fig. 3.

3.1 Sol–Gel Method (SGM)

One of the most well-known approaches for the preparation of multiferroic nanomaterials is the SGM. It means the creation of a sol (colloidal dispersion of solid particles in a liquid media) followed by gelation, which results in the development of a gel [18–21]. Metal salts and metal alkoxides are commonly utilized as an initial precursor in this method. Additionally, in the precursors, SGM also needs a chelating agent [22]. Glycolic acid, citric acid, oxalic acid, tartaric acid, polyvinyl alcohol, and polyacrylic acid are examples of chelating agents that are widely used in SGM [23]. Several parameters influence the final product's properties, including the chelating agent used and its amount, pH of the sol [7–10] [24, 25], and dried gel's calcinations temperature. Nanostructures for specific purposes can be made by carefully regulating these parameters. The complete SGM may be broken down into five phases [18], which are as follows: (1) Hydrolysis and partial condensation of precursors to

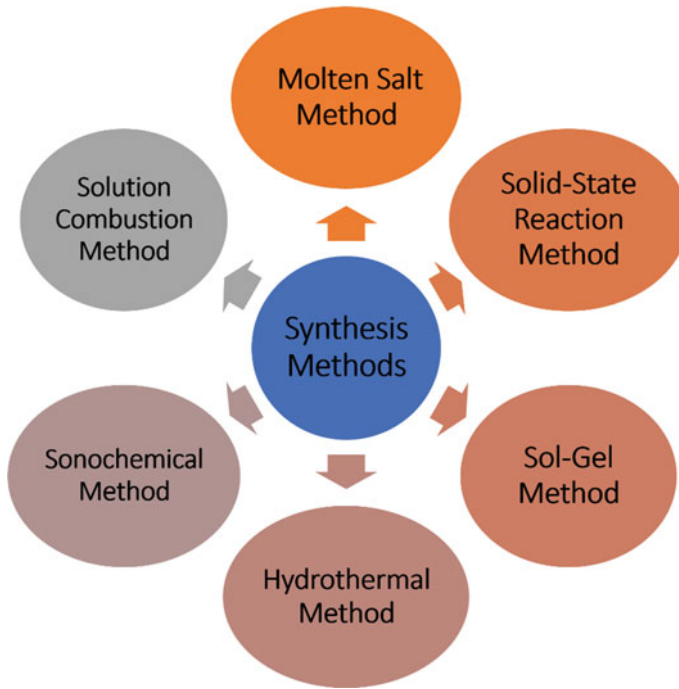


Fig. 3 Various synthesis methods for the fabrication of multiferroic nanomaterials

produce sol. (2) The polycondensation process gels the solution. (3) Syneresis, or ageing of the gel that has been produced. (4) The aged gel is dried. (5) Calcination or high-temperature treatment of the dried gel. The Pechini SGM technique is gaining a lot more interest these days for the production of multiferroic nanoparticles.

Maggio Pechini, an American scientist, developed it. In this technique, a metal/citrate complexes solution is made by combining a sufficient amount of precursors and citric acid, and poly-esterification is accomplished by heating the metal/citrate complexes solution in the existence of poly-hydroxyl alcohol, like ethylene glycol [26]. After the gel has dried, it can be exposed to a high-temperature process, which will result in the final product's formation [27, 28]. As for the synthesis of core-shell multiferroic materials, A. R. Abraham et al. and T. Woldu et al. used the sol-gel method.

3.2 Solid-State Reaction Method

“No reaction happens in the absence of a solvent,” according to Aristotle’s famous philosophy. This suggests that solid-state processes were not well studied in ancient times[29]. Recently, the situation has improved, and solid-state processes are now

receiving a lot of interest as a straight forward method for the preparation of different nanomaterials. Solids are chemically reacted in the absence of any solvent media to generate stable compounds in a solid-state method. But solid's reactions are not possible at room temperature [29]. High-temperature processing of the solid precursors is required to achieve solid-state reactions. Precursors are used for this technique like carbonates and oxides of different elements. M. Valant et al. produced single-phase polycrystalline BiFeO_3 from ultrapure starting oxides like Bi_2O_3 and Fe_2O_3 [30]. This technique can readily generate doped single-phase substances as compare to pure single-phase substances. Because of its simplicity, the solid-state reaction technique has gained importance in the production of composite systems.

3.3 Molten Salt Method

Molten salt is used as a reaction media in this technique. Salts have low toxic effects, are cheap, have great availability, low vapour pressure, making them a viable technique for the synthesis of nanomaterials [31, 32]. A typical method consists of three basic steps, which are: (1) Stoichiometric amounts of raw materials and salts are mixed; (2) The mixture is heated and (3) Washing and drying. The most frequent salts are sulphates and chlorides, whereas carbonates and oxides serve as the initial material in this method [31]. Individual salts have a high melting temperature; however, by employing a combination of salts, the melting temperature may be substantially reduced. For instance, the melting points of KCl and NaCl are 801 °C and 771 °C, respectively, whereas the melting point of KCl-NaCl salt with a 1:1 eutectic composition is around 650 °C. For example, J. Chen et al. synthesized the high-purity BiFeO_3 single-crystalline nanostructures with the help of precursors Fe_2O_3 and Bi_2O_3 as well as the salts Na_2SO_4 and NaCl within a particular temperature range 800 ± 10 °C. The impurity phases, $\text{Bi}_2\text{Fe}_4\text{O}_9$ and $\text{Bi}_{25}\text{FeO}_{40}$ were found at varied temperatures, like 840 and 820 °C [33]. Topo-chemical molten salt synthesis is gaining popularity as a variation of the molten salt technique. The Topo-chemical molten salt synthesis technique combines topochemical processes and molten salt to manufacture high-quality one-dimensional, two-dimensional, and three-dimensional perovskites nanostructures, and it is a very attractive technique.

3.4 Sonochemical Method

Some form of energy, such as heat, radiation, light, electric potential, is necessary to initiate a chemical reaction [34]. Ultrasound is used in the Sonochemical synthesis technique to form nanostructured materials. There are no direct interactions within the chemical species and ultrasound due to sonic wavelengths is significantly higher than the molecular dimensions. The transitory hot spots created during the creation,

growth, and collapse of bubbles in liquid are the indirect chemical impact of ultrasound [35]. For example, Dimple P. Dutta et al. used a Sonochemical technique to make Sc and Ti codoped multiferroic BiFeO₃ [36].

3.5 *Hydrothermal/Solvothermal Method*

Sir Roderick Murchison, a Scottish geologist, introduced the terminology hydrothermal. Chemical processes were performed in water at high pressures (above 1 bar) and temperatures (above 100 °C) in a hydrothermal technique. Water under high pressure and temperature serves a crucial part in the conversion of initial materials into an end product. The first work considered in hydrothermal technique was prepared crystals of strontium and barium carbonate at higher temperature (200 °C) and pressure (100 bars) by German scientist R. W. Bunsen in 1839 [37]. When other solvents are utilized as a reaction medium instead of water, the procedure is referred to as a solvothermal technique. The choice of solvent is important, because it allows you to regulate the nucleation and crystal formation processes by combining a variety of solvents. The method is particularly well suited to the production of nanomaterials with excellent purity, crystallinity, and particle size uniformity. The shape of materials produced with the solvothermal technique is largely controlled by additives. In the solvothermal technique, additives such as capping agents, mineralizers, and biomolecules are frequently utilized. For example, Jian-Tao Han et al. demonstrated that by adjusting the reaction temperature and pH in a hydrothermal procedure, distinct bismuth ferrite compounds with varied morphologies are produced using identical iron and bismuth precursors [38]. Besides the traditional hydrothermal technique, various multiferroic nanomaterials are currently produced using a mix of hydrothermal and microwave methods. A microwave-assisted hydrothermal technique is a name for this combined strategy. Sridhar Komarneni et al. were the first to employ the microwave-hydrothermal method to make unary oxides (like Fe₂O₃, TiO₂, and ZrO₂), as well as binary oxides (like BaTiO₃ and KNbO₃) [39]. Compared to traditional hydrothermal treatment, this technique provides several benefits. Crystallization kinetics is slower under traditional technique. As a result, to obtain the precise phase of the material, hydrothermal treatment may be required for an extended period. On the other hand, in microwave-hydrothermal technique uses fast and volumetric heating to achieve homogenous nucleation and crystallization in a limited period. Furthermore, the procedure is both energy-efficient and cost-effective [40]. For example, G. Biasotto et al. synthesized bismuth ferrite nanoparticles by heating at 180 °C for one hour. The results showed that a one-hour microwave processing period was effective in removing impurity phases from bismuth ferrite [41]. Remarkably, the hydrothermal technique may also be utilized to create various multiferroic nanostructures. For example, Shun Li et al. used a fast (1–2 min) microwave-hydrothermal technique to effectively manufacture single-crystalline bismuth ferrite nanoplates with thicknesses ranging from 20 to 160 nm and lateral sizes of sub micrometers [42].

3.6 *Solution Combustion Method*

The solution combustion technique is a form of self-propagating high-temperature synthesis technique, or simply combustion technique [43]. A. G. Merzhano introduced the self-propagating high-temperature synthesis technique idea. J. J. Kingsley et al. improved the process by combining it with a wet chemical approach, resulting in the solution combustion synthesis method [44]. Due to the method is based on a solution technique it offers all of the advantages of wet chemical processes, like doping and stoichiometry control. The high-temperature in a combustion process allows that the material develops the correct phase composition immediately in the solution combustion synthesis wave, eliminating the need for extra high-temperature products in the solution combustion synthesis method [44]. Furthermore, the required product is produced in a limited period and the creation of a high number of gases during solution combustion synthesis inhibits particle size expansion and permits the production of nano-size products. Metal salts like nitrates, carbonates and, sulphates are utilized as precursors in this procedure [45–47]. Additionally, the method also needs fuel for the combustion reaction. Urea, glucose, citric acid, sucrose and, glycine, are utilized as fuels in this experiment [48–50]. Jun Yang et al. discovered that the quantity and kind of fuel utilized in a combustion method had a significant impact on the end product's crystallinity and phase composition [51]. Jun Yang et al. used a variety of fuels for the formation of BiFeO_3 nanoparticles, including glycine, citric acid, ethylene glycol, urea, stearic acid, sucrose, ethanolamine, L-alanine, L-aspartic acid, L-leucine and, L-valine [52–55]. Glycine and L-alanine are acceptable fuels for the production of BiFeO_3 nanoparticles among the numerous fuels employed. Because of the high flame temperature, using too little fuel results in the production of amorphous phases, while using too much fuel results in the development of unwanted phases [51].

4 Applications of Multiferroics

The multiferroic materials are utilized in different research areas of science and engineering which are discussed as given below. The schematic presentation of multifunctional applicational of multiferroics is given in Fig. 4.

4.1 *Multiferroics for Microwave Phase Shifter (MPSs) Application*

The MPSs are considered as one of the significant electronic devices in various types of systems as radar, telecommunications, and phased array antenna. The semi-conducting, ferroelectric and, ferrite-based materials are mostly utilized in phase

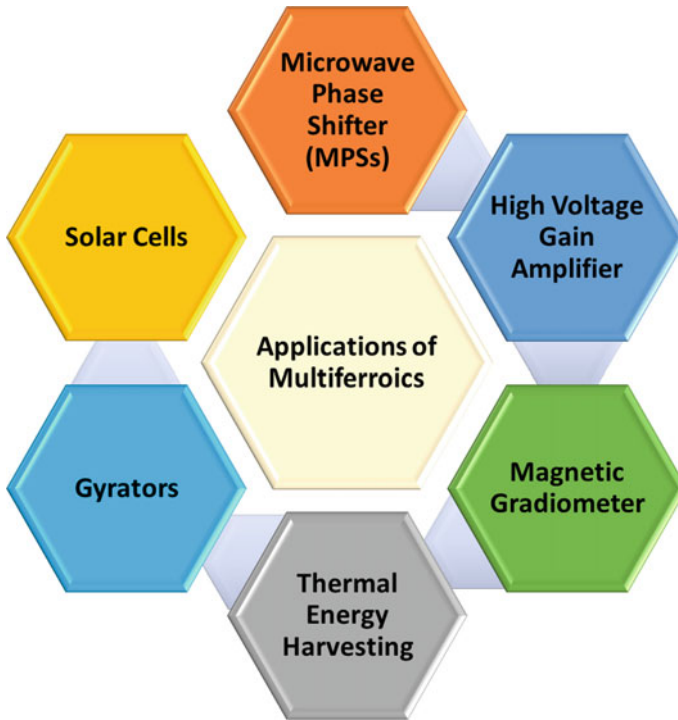


Fig. 4 Multifunctional applications of multiferroics

shifters. The operation of phase shifters made of ferrite-based materials is constructed on the phenomenon of Faraday spin of electromagnetic energy in magnetized ferrite, which is problematic. Another ferrite-based phase shifter operation is based on the propagation of spin waves in planar ferrites and this operation is working significant in planar ferrites because of its magnetic tunability in the high GHz frequency range of 1–26. Ferroelectric-based phase shifters, as opposed to magnetic ferrite-based phase shifters, have fast electric tunability, minimum power consumption, but very large loss of five GHz frequency. Therefore, a multiferroic composite can be constructed by mixing magnetic ferrite-based materials along with ferroelectrics so that the composite can be easily operated as a bi-phase microwave device above high GHz frequency (5 GHz). Ustinov and Srinivasan, (2007) reported the progress of these devices with a discussion of the concept of propagation of hybrid spin-electromagnetic waves in a ferrite-ferroelectric bilayer as this concept is used to create a dual, electric and, magnetic field adjustable MPS. A single-crystal of yttrium iron garnet film and barium strontium titanate slab is taken into consideration for making the bilayer and the electrical tunability of the differential phase shift is accomplished by passing a voltage across the barium strontium titanate. In the frequency range of 4.5–8 GHz, an insertion loss of 20 dB is recorded [56].

4.2 *Multiferroics for Thermal Energy Harvesting Application*

Heusler alloys belong to a category of inter-metallic multiferroic material which contains both ferromagnetic and ferroelastic phases and they are called shape memory alloys because they can modify their shape on the application of the applied magnetic field. The Heusler multiferroics are very fascinating to study because these types of multiferroics undertake phase transformations and under these phase transformations from the ferromagnetic austenite phase to non-ferromagnetic martensite phase, a large amount of distribution of lattice parameters takes place. The significant changes in lattice parameters that precede phase transitions are likewise linked with huge increases in entropy and internal energy. As a result, such materials are highly appealing for energy conversion, storage, shape memory actuation, and solid-state refrigeration applications. The NiTi shape memory alloy, which undergoes a reversible martensitic transition and transforms heat into mechanical work, is an excellent example [57]. In today world, $\text{Ni}_{45}\text{Co}_5\text{Mn}_{40}\text{Sn}_{10}$ Heusler alloys are extensively utilized as an energy conversion material but on the other hand, NiTi directly changes heat into the electromotive work [58]. In addition to this, when heated, $\text{Ni}_{45}\text{Co}_5\text{Mn}_{40}\text{Sn}_{10}$ Heusler alloys exhibit reversible martensitic phase change from non-magnetic to ferromagnetic along with minimal hysteresis [59]. Therefore, in this study, Srivastava achieved the phenomenon of the direct adaptation of heat into electricity with the use of $\text{Ni}_{45}\text{Co}_5\text{Mn}_{40}\text{Sn}_{10}$ Heusler alloys. In the year 2011, the development of the energy harvesting electronic device which consists of a $\text{Ni}_{45}\text{Co}_5\text{Mn}_{40}\text{Sn}_{10}$ multiferroic sample fixed to the extreme of a permanent magnet and encircled by a coil of copper having 2000 turns producing an output peak voltage of 0.6 MV [60].

4.3 *Multiferroics for Magnetic Gradiometer Application*

Magnetic gradiometers work similarly to sensors that measure magnetic field gradient, the sensitivity of which is defined by the capacity to enumerate the change regarding a reference value and therefore, in the year 2009, Bedekar et al. developed a magnetoelectric gradiometer (ME). For the development of the ME gradiometer, magnetoelectric composites were taken into utilization along with ring-dot piezoelectric transformer assembly. Here, the dot works as output whereas the ring works as input. A magnetostrictive disc, resembling a bilayer composite structure, was glued on top of the output portion. The sample's resonance frequency was discovered to be in the 91–94 kHz region. The produced magnetic field interacts with the externally applied magnetic field to produce a flux gradient, which is measured by the frequency shift and output voltage change of the gradiometer. The tests show that the suggested design has high sensitivity and may be utilized to detect magnetic field gradient [61].

4.4 Multiferroics for High Voltage Gain Amplifier

The multiferroics also have an attraction in the area of high voltage gain amplifier and therefore, in the year 2004, Dong made a multiferroic high voltage amplifier. The present study is created for a long-plate type piezoelectric and magnetostrictive laminate composite using the piezoelectric and piezomagnetic equations of state. Our investigation showed the potential of an exceptionally high magnetoelectric voltage gain, which would be ideal for applications as high-voltage minute transformers [62].

4.5 Multiferroics for Vibration Energy Harvesting Application

Energy harvesting from environmental vibrations is another area of the technical field where multiferroics show promising application. The devices that can harvest energy from the environment are of great economic interest because they can power wireless transducer and sensor networks, environmental conditions, structural health, securing care systems, and medical implants. The key heavy factor behind the energy harvesting business is the fact that the short lifespan of batteries raises maintenance costs in many applications, particularly in unfriendly surroundings where admittance is restricted or dangerous. Micro-energy harvesting devices, on the other hand, are cost-effective, have a maximum lifecycle, and need diminutive or exactly no maintenance cost. The primary technique for harvesting vibration energy is currently grounded on the piezoelectric devices but on the other hand, there are other ways of harvesting vibration energy which are based on the phenomenon of magnetostrictive vibration [63, 64]. Combining piezo-energy harvesting with magnetostrictive energy harvesting of mechanical vibrations in a single multiferroic device may result in the formation of an ultra-efficient vibration energy harvester made of multiferroic materials. This concept has previously been applied, with encouraging findings of hybrid piezoelectric/magnetostrictive multiferroic energy harvesters published [65].

4.6 Multiferroics for Gytrators Application

Four famous main electrical components are needed to manufacture an electronic device, such as condensers, inductors, resistance and, transformers. Bernard D. H. Tellegen, however, came up with the concept in 1948 that there was a fifth basic element of a gyrator [66] electrical device. A gyrator is an inductive and capacitive interface composed of a two-port four-wire circuit element. It is a voltage converter and vice versa. It is utilized. Gyrator's main benefit is that it can substitute a single instrument for the conversion process for the complicated circuit parts. An ideal two-port gyrator can be defined by the following equations;

$$I_1 = G \cdot V_2 \quad (1)$$

$$I_2 = G \cdot V_1 \quad (2)$$

where I and V are the instantaneous current and voltage respectively, and G is the constant called gyration constant and has the dimensions of 1/Ohm. With the aid of the stress transfer at the contact, the voltage-current conversion is done. Now that a gyrator is capable of performing an inductive circuit, its major use is to minimize the size and expense of a system by removing bulky, heavy and, expensive inducers. Filter design, miniaturization and telephone devices are extensively utilized in gyrators.

The magnetoelectric material is highly important in the gyrator since electric and, the magnet field are coupled with magnetoelectric material. In this context, the most suited materials for gyrators might be multiferroic materials. A multiferroic gyrator port was proposed by Zhai et al. The three components were developed in the layers of the composite of: the first layer, the terfenol-D/PZT/Terfenol-D-structure with a frequency of electromechanical resonance at a speed of 86 kHz; the second layer, the mechanical resonance structure at a frequency of 64 kHz; the third layer, the multiferroic composite Nickel/PZT/Nickel-structure at a frequency of 15 kHz [67]. A three-layered construction was wrapped in a belt around the laminated structure to function. They noticed the induction and the collection of electricity from the piezo-layer of stress-mediated connectors. This experimental check has shown and determined that, by replacing the electronic gyrator multi-component with a single multiferroic element, further downsizing of the instrument is achievable using a multiferroic composite.

4.7 Multiferroics for Solar Cells Application

The abundance of energy is solar power. Solar energy can meet the world's energy requirements. Solar energy is by far the best way to achieve this because it is renewable and ecological. This solar energy needs to be harvested differently and beneficially to meet demand. Photovoltaics are the tools that are utilized to generate electricity from solar energy. The three processes in photovoltaics are primarily used: pair creation of electron-holes; load separation and carriage of carriers and pairs recombination of electron-holes. Photovoltaics based on ferroelectrics were thoroughly researched. It was discovered that under the lighting, ferroelectric materials have a PV short circuit current that fluctuates abnormally much wider than the bandgap of a material, parallel to the directions of the rail polarization Axis and the photovoltages. In contrast, photo-excited photovoltaic transporters are carried without a gradient in electrochemical potential, due to their well-known PV effects of p - N junction-based solar cells. The polarization-induced internal electrical field typically promotes such an outcome. It has been proven recently that a change in the structure of a ferroelectric domain or a reduction of ferroelectric film's thickness can increase energy

conversion efficiency (PCE). It is predicted that the extra magnetic order will reduce the bandgap in the structure owing to the inherent strain connection by replacing the ferroelectric materials with a multiferroic material. This further decrease would increase the range of photovoltaic electromagnetic spectrums. A bulk photovoltaic cell with a lower bandgap (<1 eV) would ensure that the whole spectrum is utilized in the photon conversion process. Also, e-e interactions governing the magnetic order can lead to the smaller bandgap of typical 2.6–2.7 eV for bismuth ferrite (BiFeO_3 , BFO) multiferroic perovskites [68]. It has been experimentally demonstrated that multiferroic state contributes to the improvement of spectral response as well as the efficiency due to e-e interaction which lowers the bandgap to the useful level. In an ideal case, multiferroics can be tuned to harness the whole energy spectrum. This is possible because multiferroics can display coupling between electric and magnetic field. Thus, the properties of multiferroics can be modified or tuned by applying the external magnetic field, electric field, stress, strain, etc. which can be utilized to the harvesting of solar energy smartly.

4.8 Multiferroics for Multi-caloric Effect Application

A physical system's thermal reaction to changes in adiabatic variables such as volume, strain, magnetic or electric polarization produces a caloric effect like heating or cooling. These changes can be brought about by applying or deleting certain control settings that lead to the famous barocaloric, elastocaloric, magnetocaloric and electrocaloric impact [69–71]. Magnetocaloric or electrocaloric solid-state cooling is of great interest due to specific features such as vibration-free, noise-free, low energy requirements, etc. Because of its benefits, solid-state cooling is an excellent way of cooling at ambient temperature, ultra-low cryogenics and, solid-state collation of microelectronic components. However, the presence of two ferroic phases at the same time, providing a large number of applications for improved sensors, memories, and energy collection, magnetic recording and transformers, has given a new class of materials termed multiferroics significant attention [72, 73]. In his research, Vopson theoretically studied the multicaloric effect in multiferroic materials. He applied the numerical methods on NdCrTiO_5 multiferroic material and predicted the cooling of 6.88 K during an adiabatic demagnetization from applied fields of 5 to 0 T at its multiferroic transition temperature of 21 K. This effect offers a new perspective of multiferroic materials as a multicaloric effect due to its environmentally friendly solid-state refrigeration system. Thus, it can be concluded that multiferroic materials due to their simultaneous magnetic and electric effect which is crucial for the induced strain as induced strain, as induced strain, in particular, defines the application of multiferroic materials.

4.9 Multiferroics for AC/DC Magnetic Field Sensors Application

Magnetic sensors are equipment that can detect or evaluate the formation or modification of the surrounding magnetic field without being in real touch. Based on this change in the external magnetic field, the characteristics such as temperature, direction, location, angle and, speed of each item may be determined. Magnetic fields may have a major influence on our civilization and can be applied in scientific measures, weather analyses, microscopic imaging, magnetic field mapping and other cosmic phenomena, and geographical location. In this regard, multiferroic devices are the most suitable as they utilize a magnetic field to induce the magnetoelectric effect. This effect is well established by the following relation,

$$V = \alpha_H^V \cdot H \cdot t \quad (3)$$

where V is the induced voltage, H is the amplitude of applied magnetic field; t is the thickness of multiferroic material and α is the magnetoelectric coupling coefficient. This relation indicates that induced voltage in multiferroics varies linearly with the amplitude of the applied magnetic field. This relation applies to both single as well as composite phases of multiferroics. It is noted that output or induced voltage depends on the coupling coefficient. As all single-phase multiferroics have a very small coupling coefficient which limits their application in most of the devices. Thus, due to the large coupling coefficient at room temperature, composite multiferroics have gained much of the space as an application. In addition, large strain-mediated magnetoelectric effect occurs at room temperature, where magnetoelectric is related to the magnetostrictive properties of the magnetic phase. So, it again favors the use of composite multiferroics. The magnetic strain is well known to be non-linear to the magnetic DC field. This restricts the voltage generated to some value of the magnetic DC field supplied. In addition, the DC response of multiferroic composites further shows that it is not appropriate for the DC field. Surprisingly, most of the composites of multiferroics are thus employed for AC magnetic field sensing. The results indicated promising quality for multiferroic sensors with sensitive magnetic field detection varies from $10^{-13} < H_{ac} < 10^{-3}$ T experimentally and theoretically. Therefore, multiferroic materials may be inferred to be suitable as a contender to replace AC or DC magnetic field ferrites.

4.10 Multiferroics for Microwave Resonators Application

The ferromagnetic resonance (FMR) is seen with ferromagnetic materials that are susceptible to high frequencies, especially in the excited state [74]. This ferromagnetic resonance is achieved when the precision frequency equals the excitation field frequency and this usually happens in ferrite materials in microwave frequencies.

Also, in microwave signaling devices soft ferrites can be used as they need the operation of a DC magnetic field. However, the use of soft ferrite materials with microwave resonance might have certain disadvantages: sluggish operation, high noise level, high power consumption, and restricted miniaturization. Multiferroic composites are used for achieving multiferroic resonance to overcome these disadvantages [75]. Many scientists have used microwave resonance multiferroic materials. For the FMR electric field tuning, Fetisov et colleagues showed the YIG/PZT [76]. The results showed a well-defined FMR absorption of about 5 GHz with a line width of 3.4 GHz was found with the application of 2–10 Hz, 0.1 mW of power. The ferromagnetic resonance frequency also changed by 16 MHz to a higher frequency side with 10 kV/cm of an electric field, while with -10 kV/cm the resonance frequency changed by -18 MHz to a lower frequency side. During their measurements, they observed that with multiferroic materials, the shape of FMR response has not been attenuated, except its peak position. The application of an electric field has the effect of inducing a piezostain in the PZT, which is then transmitted to the YIG. This, in turn, will have the effect of changing the internal magnetization of the YIG. Therefore, the effect of the applied effect is viewed as the creation of an internal magnetic field, responsible for the shift in the FMR curve. It has therefore been discovered that multiferroics with many more enhancements have a microwave resonance identified. It can replace soft ferrites with multiferroics comprehensively [77].

5 Conclusion

In the concluding remarks, multiferroic materials have a wide range of technological applications due to their ability to exhibit adjustable mechanical, magnetic, dielectric, thermal, and optical features all at an identical time. These factors can also link to one other, resulting in intriguing cross-coupling phenomena that increase the adaptability of multiferroics for new applications. Different multiferroic material requirements apply to different applications depending on the area of applicability. However, in most situations, the following are typical conditions that must be rigorously adhered to for the applications of multiferroics:

1. These materials must exhibit strong magnetoelectric coupling effects, ideally at 300 K.
2. These materials must be simple to make and preferably composed of inexpensive chemical elements and compounds.
3. The structures of these materials must be suitable for large-scale production and integration at the chip and wafer level.
4. The structures of these multiferroic materials must be suitable for fabrication at micro and nanometer sizes without sacrificing operation.

Thus, it is not an exaggeration to say that multiferroic materials can profoundly change our civilization while still allowing present scientific and technical developments to continue. Furthermore, the combination of multiferroics with semiconductors and spintronic materials to produce multifunctional hybrid structures may pave the way for the creation of genuinely revolutionary new technologies.

References

1. B.D. Stojanovic, in *Introduction to Ferroics and Multiferroics: essential Background*, ed. by B. D. Stojanovic (Elsevier, 2018), pp. xxxi–xlii
2. M. Gich, Z. Ma, in *Multiferroic Oxide Thin Films*, ed. By M. Gich, Z. Ma (Elsevir, 2018), p. 253
3. J. Jin, F. Zhao, K. Han, M.A. Haque, L. Dong, Q. Wang, *Adv. Funct. Mater.* **24**, 1067 (2014)
4. A.J.C. Buurma, G.R. Blake, T.T.M. Palstra, U. Adem (ed.), *Multiferroic Materials: physics and Properties* (Elsevir, 2016)
5. H. Schmid, *Ferroelectrics* **162**, 317 (1994)
6. J. Ma, J. Hu, Z. Li, C.-W. Nan, *Adv. Mater.* **23**, 1062 (2011)
7. E.V. Ramana, F. Figueiras, M.P.F. Graca, M.A. Valente, *Dalton Trans.* **43**, 9934 (2014)
8. G. Schileo, C. Pascual-Gonzalez, M. Alguero, I.M. Reaney, P. Postolache, L. Mitoseriu, K. Reichmann, A. Feteira, *J. Am. Ceram. Soc.* **99**, 1609 (2016)
9. L.W. Martin, S.P. Crane, Y.H. Chu, M.B. Holcomb, M. Gajek, M. Huijben, C.-H. Yang, N. Balke, R. Ramesh, *J. Phys.: Condens. Matter* **20**, 434220 (2008)
10. R.M. Thankachan, R. Balakrishnan, in *Synthesis of Inorganic Nanomaterials*, eds. by S.M Bhagyaraj, O.S. Oluwafemi, N. Kalarikkal, S. Thomas (Elsevir, Woodhead Publishing, 2018), pp. 185–211
11. T. Woldu, B. Raneesh, M.R. Reddy, N. Kalarikkal, *RSC Adv.* **6**, 7886 (2016)
12. S. Vijayanand, H. S. Potdar, P. A. Joy, *Appl. Phys. Lett.* **94**, 182507 (2009)
13. W. Eerenstein, N.D. Mathur, J.F. Scott, *Nature* **442**, 759 (2006)
14. S. Kour, R. Jasrotia, P. Puri, A. Verma, B. Sharma, V. P. Singh, R. Kumar, S. Kalia, *Environ. Sci. Pollut. Res.* **1** (2021)
15. R. Jasrotia, N. Kumari, R. Kumar, M. Naushad, P. Dhiman, G. Sharma, *Earth Syst. Environ.* **5**, 399 (2021)
16. B. Raneesh, N. Kalarikkal, *Advanced Nanomaterials: synthesis, Properties, and Applications* (Vol. 24, 2014), p. 149
17. J. Kreisel, M. Kenzelmann, *Europhys. News* **40**, 17 (2009)
18. A.E. Danks, S.R. Hall, Z. Schnepp, *Mater. Horizons* **3**, 91 (2016)
19. C.J. Brinker, G.W. Scherer (ed.), *Sol-Gel Science: the Physics and Chemistry of Sol-Gel Processing* (Academic press, 2013)
20. M. Chandel, V.P. Singh, R. Jasrotia, K. Singha, R. Kumar, *AIMS Materials Science* **7**, 244 (2020)
21. R. Jasrotia, S. Kour, P. Puri, A.D. Jara, B. Singh, C. Bhardwaj, V.P. Singh, R. Kumar, *Solid State Sci.* **110**, 106445 (2020)
22. R. Jasrotia, V. P. Singh, R. Kumar, R. Verma, A. Chauhan, *Results Phys.* **15**, 102544 (2019)
23. R. Jasrotia, P. Puri, V.P. Singh, R. Kumar, *J. Sol-Gel. Sci. Technol.* **97**, 205 (2021)
24. M. Chandel, V. P. Singh, R. Jasrotia, K. Singha, M. Singh, P. Thakur, S. Kalia, *Phys. B: Condens. Matter* **595**, 412378 (2020)
25. K. Singha, R. Jasrotia, V.P. Singh, M. Chandel, R. Kumar, S. Kalia, *J. Sol-Gel. Sci. Technol.* **97**, 373 (2021)
26. M. P. Pechini, U.S. Patent 3,330,697, 11 July 1967

27. R. Jasrotia, V.P. Singh, R.K. Sharma, M. Singh, in *AIP Conference Proceedings* (AIP Publishing LLC, 2019), p. 090004
28. R. Jasrotia, V.P. Singh, R.K. Sharma, P. Kumar, M. Singh, in *AIP Conference Proceedings* (AIP Publishing LLC, 2019), p. 140004
29. F. Toda, *Acc. Chem. Res.* **28**, 480 (1995)
30. M. Valant, A.-K. Axelsson, N. Alford, *Chem. Mater.* **19**, 5431 (2007)
31. C. Sikalidis, *Advances in Ceramics: synthesis and Characterization, Processing and Specific Applications* (BoD-Books on Demand, 2011)
32. S. Zhao, Q. Li, L. Wang, Y. Zhang, *Mater. Lett.* **60**, 425 (2006)
33. J. Chen, X. Xing, A. Watson, W. Wang, R. Yu, J. Deng, L. Yan, C. Sun, X. Chen, *Chem. Mater.* **19**, 3598 (2007)
34. J.H. Bang, K.S. Suslick, *Adv. Mater.* **22**, 1039 (2010)
35. K.S. Suslick, T. Hyeon, M. Fang, A.A. Cichowlas, *Mater. Sci. Eng., A* **204**, 186 (1995)
36. D.P. Dutta, B.P. Mandal, M.D. Mukadam, S.M. Yusuf, A.K. Tyagi, *Dalton Trans.* **43**, 7838 (2014)
37. R. Feigelson, *50 Years Progress in Crystal Growth: a Reprint Collection* (Elsevier, 2004)
38. J.-T. Han, Y.-H. Huang, X.-J. Wu, C.-L. Wu, W. Wei, B. Peng, W. Huang, J.B. Goodenough, *Adv. Mater.* **18**, 2145 (2006)
39. S. Komarneni, R. Roy, Q.H. Li, *Mater. Res. Bull.* **27**, 1393 (1992)
40. B.L. Newalkar, S. Komarneni, H. Katsuki, *Mater. Res. Bull.* **36**, 2347 (2001)
41. G. Biasotto, A.Z. Simões, C.R. Foschini, M.A. Zaghete, J.A. Varela, E. Longo, *Mater. Res. Bull.* **46**, 2543 (2011)
42. S. Li, R. Nechache, I.A.V. Davalos, G. Goupil, L. Nikolova, M. Nicklaus, J. Laverdiere, A. Ruediger, F. Rosei, *J. Am. Ceram. Soc.* **96**, 3155 (2013)
43. A. Sharma, K.M. Batoo, E.H. Raslan, G. Kumar, *J. Mater. Sci: Mater. Electro.* **31**, 16959 (2020)
44. J.J. Kingsley, K.C. Patil, *Mater. Lett.* **6**, 427 (1988)
45. A. Sharma, K. Batoo, E.H. Raslan, S.F. Adil, *Vacuum* **157**, 422 (2018)
46. G. Kumar, S. Sharma, R.K. Kotnala, J. Shah, S.E. Shirsath, K.M. Batoo, M. Singh, *J. Mol. Struct.* **1051**, 336 (2013)
47. G. Kumar, R. Rani, S. Sharma, K.M. Batoo, M. Sing, *Ceram. Int.* **39**(5), 4813 (2013)
48. K.M. Somnath, E.H. Batoo, S.F. Raslan, I. Adil, G. Sharma, Kumar. *J. Mater. Sci.: Mater. Electron.* **31**, 7880 (2020)
49. G. Kumar, R.K. Kotnala, J. Shah, V. Kumar, A. Kumar, P. Dhiman, M. Singh, *Phys. Chem. Chem. Phys.* **19**, 16669 (2017)
50. R. Rani, G. Kumar, K.M. Batoo, M. Singh, *Appl. Phys. A* **115**(4), 1401 (2014)
51. J. Yang, X. Li, J. Zhou, Y. Tang, Y. Zhang, Y. Li, *J. Alloy. Compd.* **509**, 9271 (2011)
52. C.E. Ciomaga, M. Airimioaei, V. Nica, L.M. Hrib, O.F. Caltun, A.R. Iordan, C. Galassi, L. Mitoseriu, M.N. Palamaru, *J. Eur. Ceram. Soc.* **32**, 3325 (2012)
53. S.N. Tripathy, B.G. Mishra, M.M. Shirolkar, S. Sen, S.R. Das, D.B. Janes, D.K. Pradhan, *Mater. Chem. Phys.* **141**, 423 (2013)
54. S. Layek, S. Saha, H. C. Verma, *AIP Adv.* **3**, 032140 (2013)
55. X. Zhou, M. Chen, M. Xiang, H. Bai, J. Guo, *Ceram. Int.* **39**, 4783 (2013)
56. A. B. Ustinov, G. Srinivasan, B. A. Kalinikos, *Appl. Phys. Lett.* **90**, 031913 (2007)
57. Y. Song, C. Leighton, R.D. James, in *Heusler Alloys*, eds. by C. Felser, A. Hirohata (Springer, Cham, 2016), pp. 269–291
58. Y. Song, V. Srivastava, K. Bhatti, C. Leighton, R. James, in *10th International Energy Conversion Engineering Conference* (2012), p. 3709
59. V. Srivastava, X. Chen, R. D. James, *Appl. Phys. Lett.* **97**, 014101 (2010)
60. V. Srivastava, Y. Song, K. Bhatti, R.D. James, *Adv. Energy Mater.* **1**, 97 (2011)
61. V. Bedekar, R.A. Islam, H. Kim, M.I. Bichurin, S.N. Ivanov, Y.J. Pukinski, S. Priya, *Europ. Phys. J. B* **71**, 387 (2009)
62. S. Dong, J.-F. Li, D. Viehland, J. Cheng, L.E. Cross, *Appl. Phys. Lett.* **85**, 3534 (2004)
63. K. Dulta, G. K. Ağçeli, P. Chauhan, R. Jasrotia, P. K. Chauhan, *J. Clust. Sci.* **1** (2021)

64. K. Dulta, G. Koşarsoy Ağçeli, P. Chauhan, R. Jasrotia, P. K. Chauhan, J. Inorg. Organomet. Polym. Mater. **31**, 180 (2021)
65. M.M. Vopson, Crit. Rev. Solid State Mater. Sci. **40**, 223 (2015)
66. B.D. Tellegen, Philips Res. Rep. **3**, 81 (1948)
67. J. Zhai, J. Gao, C. De Vreugd, J. Li, D. Viehland, A.V. Filippov, M.I. Bichurin, D.V. Drozdov, G.A. Semenov, S.X. Dong, Europ. Phys. J. B **71**, 383 (2009)
68. S.R. Basu, L.W. Martin, Y.H. Chu, M. Gajek, R. Ramesh, R.C. Rai, X. Xu, J.L. Musfeldt, Appl. Phys. Lett. **92**, 091905 (2008)
69. L. Mañosa, D. González-Alonso, A. Planes, E. Bonnot, M. Barrio, J.-L. Tamarit, S. Aksoy, M. Acet, Nat. Mater. **9**, 478 (2010)
70. E. Bonnot, R. Romero, L. Mañosa, E. Vives, A. Planes, Phys. Rev. Lett. **100**, 125901 (2008)
71. K.A. Gschneidner Jr, V.K. Pecharsky, A.O. Tsokol, Rep. Prog. Phys. **68**, 1479 (2005)
72. J. Gao, L. Shen, Y. Wang, D. Gray, J. Li, D. Viehland, J. Appl. Phys. **109**, 074507 (2011)
73. M. Gajek, M. Bibes, S. Fusil, K. Bouzehouane, J. Fontcuberta, A. Barthelemy, A. Fert, Nat. Mater. **6**, 296 (2007)
74. C. Kittel, Phys. Rev. **73**, 155 (1948)
75. A. A. Semenov, S. F. Karmanenko, V. E. Demidov, B. A. Kalinikos, G. Srinivasan, A. N. Slavin, J. V. Mantese, Appl. Phys. Lett. **88**, 033503 (2006)
76. Y. K. Fetisov, G. Srinivasan, Appl. Phys. Lett. **88**, 143503 (2006)
77. R. Verma, A. Chauhan, K. M. Batoo, R. Jasrotia, A. Sharma, R. Kumar, M. Hadi, E. H. Raslan, J. P. Labis, A. Imran, ECS J. Solid State Sci. Technol. **10**, 073004 (2021)